

INSTITUTE OF GEOPHYSICS  
POLISH ACADEMY OF SCIENCES

PUBLICATIONS  
OF THE INSTITUTE OF GEOPHYSICS  
POLISH ACADEMY OF SCIENCES

MONOGRAPHIC VOLUME

M-29 (395)

MINING AND ENVIRONMENTAL GEOPHYSICS

Selected and Revised Contributions  
to the XXX Polish-Czech-Slovakian Symposium  
held at Łądek Zdrój on June 6-8, 2005

Editors: Adam Idziak and Ryszard Dubiel

WARSZAWA 2006

PUBL. INST. GEOPHYS. POL. ACAD. SC., M-29 (395), 2006

INSTITUTE OF GEOPHYSICS  
POLISH ACADEMY OF SCIENCES

Selected and Revised Contributions  
to the XXX Polish-Czech-Slovakian Symposium

**PUBLICATIONS**  
**OF THE INSTITUTE OF GEOPHYSICS**  
**POLISH ACADEMY OF SCIENCES**

MONOGRAPHIC VOLUME

**M-29 (395)**

**MINING AND ENVIRONMENTAL GEOPHYSICS**

Selected and Revised Contributions  
to the XXX Polish-Czech-Slovakian Symposium  
held at Łądek Zdrój on June 6-8, 2005

Editors: Adam Idziak and Ryszard Dubiel

WARSZAWA 2006

Editorial Committee

Roman TEISSEYRE (Editor), Jerzy JANKOWSKI (Deputy Editor),  
Janusz BORKOWSKI, Maria JELEŃSKA, Anna DZIEMBOWSKA (Managing Editor)

Editors of Issue:

Adam Idziak and Ryszard Dubiel

Editorial Office

Instytut Geofizyki Polskiej Akademii Nauk  
ul. Księcia Janusza 64, 01-452 Warszawa, Poland

**SUBSCRIPTION**

**Subscription orders should be addressed  
directly to the Editorial Office.**

**The list of issues to be published in 2006  
is on the inside back cover.**

© Copyright by Instytut Geofizyki Polskiej Akademii Nauk, Warszawa 2006

Publication was partly financed by the Ministry of Science and Informatization  
and the Committee of Geophysics, Polish Academy of Sciences

Circulation: 250 copies

ISBN-83-88765-67-1

ISSN-0138-015X

Camera ready copy prepared by:  
Dział Informacji i Wydawnictw Naukowych  
Instytutu Geofizyki PAN

Printed and bound by:  
PPH Remigraf sp. z o.o.  
Ratuszowa 11, 03-450 Warszawa

**Mining and Environmental Geophysics  
Selected and Revised Contributions  
to the XXX Polish-Czech-Slovakian Symposium**

**Preface**

The XXX Polish-Czech-Slovakian Symposium on Mining and Environmental Geophysics was held at Łądek spa (the Sudety Mts., Poland) from 6 to 8 June 2005. It was organized by the Faculty of Earth Sciences, University of Silesia, together with the Institute of Geophysics, Polish Academy of Sciences. The Symposium was attended by 71 participants which presented 44 original papers. The keynote lectures were delivered by the Symposium special guests, eminent geophysicists, Professor Roman Teisseyre and Professor Vladimir Rudajev. The important feature of the meeting was combination of formal scientific discussion and informal contacts among the researchers, engineers and technicians from participating countries.

The Symposium proceeded as usual in nice, friendly atmosphere. Participants were accommodated in the conference center localized at the foot of Mt. Śnieżnik in picturesque Kłodzka Valley near the Polish-Czech border. During the scientific excursion they had a possibility to visit glass work at Stronie Śląskie town, the old uranium mine and the Niedźwiedzia cave.

I would like to express my thanks for excellent arrangement of the Symposium to the members of the Local Organizing Committee:

- Waław M. Zuberek, Chairman
- Wojciech Dębski
- Lesław Teper
- Jolanta Pierwoła
- Ryszard Dubiel
- Radosław Tomaszewska
- Maria Dziurawicz

For a long time, the Polish-Czech-Slovakian Geophysical Symposia were dominated by problems of rockburst and induced seismicity in mines, but since the XXIX Symposium their important subjects have been geophysical methods in geotechnics and environmental engineering. Extension of the domain of research allowed to keep the interest in participation at our Symposia and presentation of papers.

The volume contains papers selected from those presented at the XXX Polish-Czech-Slovakian Symposium. Preliminary versions of the papers were verified by the authors and delivered for publication. They were peer reviewed and then revised according to the reviewers comments and suggestions. Finally, the papers which passed the full editorial procedure were accepted for publication in this monographic volume. The papers have been grouped into the following themes:

1. Induced seismicity
2. Seismic equipment
3. Engineering seismology
4. Geophysical methods in rock mechanics
5. Environmental geophysics.

I hope that the readers will find the volume interesting and useful for getting some information about the mining and environmental geophysical study carried out in Poland and Czech Republic.

I would like to express my sincere appreciation to the members of Scientific Committee which I had the honor to be in the chair:

- Sławomir J. Gibowicz
- Vladimir Rudajev
- Józef Dubiński
- Stanisław Lasocki
- Zdenek Kalab

for their valuable recommendations that improved scientific level of the Symposium.

I thank all the reviewers for their work, suggestions and comments.

I address special acknowledgements to Mrs. Anna Dziembowska, Managing Editor of "Publications of the Institute of Geophysics" for her help in preparing and publishing this volume.

Adam Idziak  
Editor

## **Seismic Effects and Rotation Waves\***

Roman TEISSEYRE

Institute of Geophysics, Polish Academy of Sciences  
ul. Księcia Janusza 64, 01-452 Warszawa, Poland  
e-mail: rt@igf.edu.pl

### **A b s t r a c t**

Modern approach to the theory and observations of seismic rotation waves is outlined. The spectacular development of the mechanics of continua, including defects, granular structure and other deviations from ideal linear elasticity, was followed by new technical achievements making it possible to detect the rotation waves with the help of very sensitive instruments. The ring laser and fiber coil interferometers concur with the systems of high precision seismographs, including those with the anti-parallel positions permitting to eliminate the displacement velocity motions.

### **1. Introduction**

Numerous observations pointed to macroscopic rotation effects at the ground surface; therefore, many attempts to detect seismic rotation waves were made at the end of XIX century and during the XX century, but without any success. Until the end of XX century a common view on these problems was that expressed by Mallet in his well-known book (Mallet 1862). The attention has been focused on surface rotation effects, namely, the rotation of some objects on the ground surface, especially those related to the rotation effects observed at different heights of a given object (an example is shown in Fig. 1). Mallet believed that such deformations are caused by a sequence of inclinations and returns to the vertical when an object is hit by a series of the emerging phases of seismic body or surface waves; the differences between the inertia tensor components of the considered object and the irregularities of friction and binding properties lead to the situation in which the position after the return is twisted as compared to the former place.

Seismology, despite its spectacular achievements, remains practically confined to ideal linear, isotropic or anisotropic elasticity. When returning to the old question of

---

\* **The Keynote Lecture**

the seismic rotation effects and waves, we shall go beyond this horizon; in terms of the ideal elastic theory any rotation motion, even if generated in a seismic source, should be immediately attenuated.

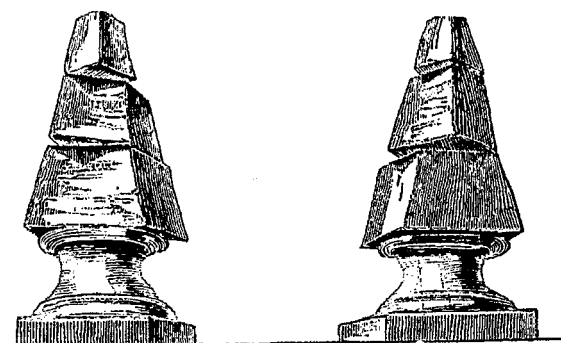


Fig. 1. An example of rotations at different heights; Stefano del Bosco, Calabria, 1783.

Seismic observations up to the end of last century were not accurate enough to detect any rotation waves. Of course, there still remains a displacement rotation component which differs from zero for shear motion. However, in an isotropic ideal-elastic body this component achieves only very small values and it is only in inhomogeneous and structural media that these values can be higher.

According to theory of continua containing defects and granular structure (including the micropolar and micromorphic category; cf. Eringen 1999), we can expect the rotation motions of spin and twist type; the latter corresponds to the oscillations of shear deformation of grains of the medium (point-grains in micropolar theories).

These theoretical achievements were followed by invention of new instruments: very sensitive rotation seismographs, based on anti-parallel seismograph systems (differential seismographs); and the laser ring and fiber coil interferometers, based on the Sagnac principle. Hence, the reliable recording techniques entered the seismological practice.

## 2. Some Macroseismic Observations

It is worth to stress the importance of historical designs and lithographs for seismic intensity evaluations and for studies of surface deformations.

Pioneers of seismology studied the surface rotation effects; their attention has been paid to some regularities observed, especially those related to the rotation effects at different heights of a given object.

## 3. Attempts to Construct Rotation-Type Seismographs

On the turn of XIX/XX centuries, several types of rotation seismographs have been constructed, but they failed to detect any rotation motions; the sensitivity of these historical instruments was too low.

#### 4. Rotation Waves: Theory

First, let us note that a non-zero rotation appears already in a seismic displacement field; it is equal to zero for the  $P$  waves, but different from zero for the  $S$  motion and some surface waves:

$$\omega^0 = \frac{1}{2} \left( \frac{\partial v}{\partial x} - \frac{\partial u}{\partial y} \right).$$

Such a rotation is very small for homogeneous media but may reach higher values for media contaminated by defects, inhomogeneities and internal structure (like in micromorphic/micropolar theories, continuum theories with dislocation and disclination densities).

Modern asymmetric theory of continuum (Teisseyre and Boratyński 2003, Teisseyre 2004) includes the constitutive relations for an interaction between stress moments (or antisymmetric part of stresses) and bonds between the particles (as schematically shown in Figs. 2 and 3).

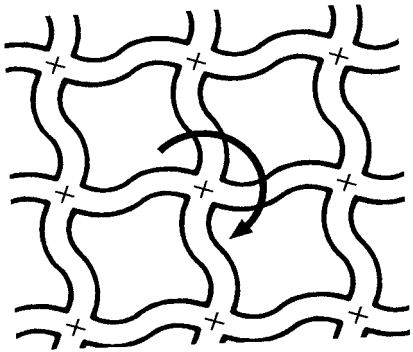


Fig. 2. Deformation of bonds between the particles – spin.

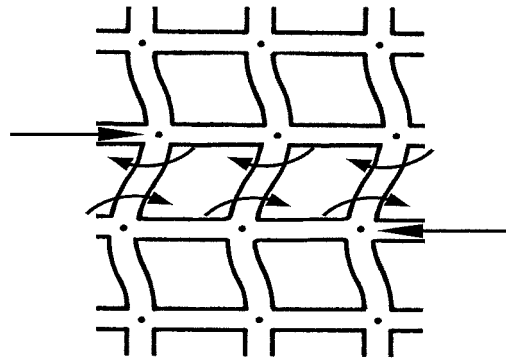


Fig. 3. Shear deformation of bonds between the particles – twist.

In such a way, there appear point rotations (such rotation motion varies from point to point, according to the respective field equations). Shimbo (1975, 1995), when studying friction processes, has introduced the constitutive law between the

point rotations  $\omega_{[ks]}$  and the antisymmetric stresses  $S_{[ks]}$  (or equivalently stress moments), involving a new constitutive rotation rigidity constant  $\mu^*$

$$S_{[ks]} = 2\mu^* \omega_{[ks]}$$

A similar law has been introduced for the twist motion (Teisseyre 2004).

In such a way, the sources of rotations related to internal frictions processes can be introduced and we shall include to our considerations both the rotation of displacements and the true spin and twist contributions. Thus, for spin and twist we can write:

$$\omega_{[i]}^0 = \frac{1}{2} \left( \frac{\partial v}{\partial x} - \frac{\partial u}{\partial y} \right) + \omega_{[i]}, \quad \omega_{(i)}^0 = \frac{1}{2} \left( \frac{\partial v}{\partial x} + \frac{\partial u}{\partial y} \right) + \omega_{(i)}$$

where the true, independent spin and twist motions are denoted by  $\omega_{[i]}$  and  $\omega_{(i)}$ , respectively.

### 5. First Seismogram of Rotation Waves

In the 1970s, a seismic azimuth station was installed in an Upper Silesian mine by a team from the Institute of Geophysics (Z. Droste, J. Hordejuk, M. Górski): six seismic channels permitted to discover some deviations from the azimuth as a function of time (the station–source distance was about 5 km). A sketch of the station is shown in Fig. 4.

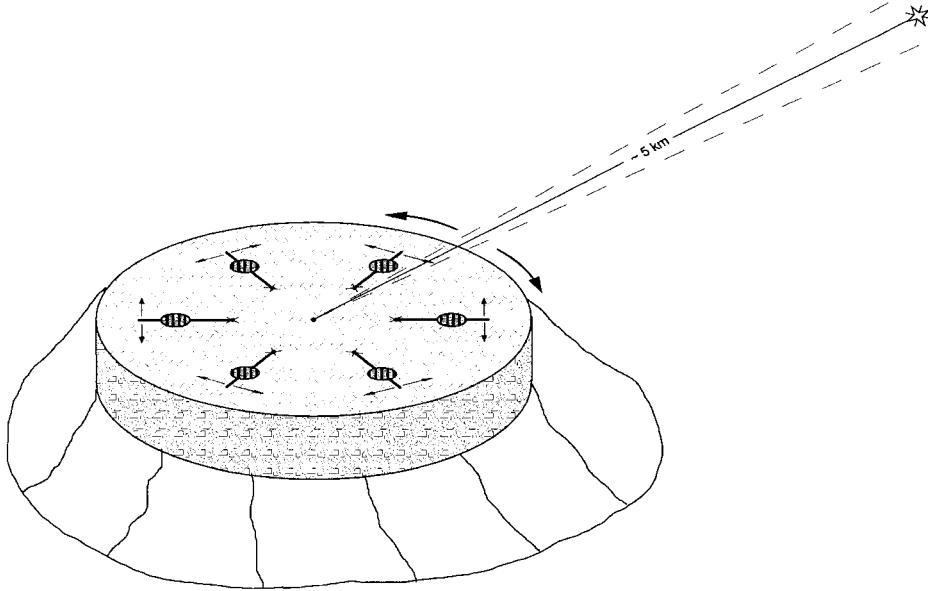


Fig. 4. Sketch of azimuthal seismic station installed in the 1970s.

With a special algorithm developed by Andrzej Kijko it became possible to find reliable estimates of the deviations from the known azimuth – such deviations were attributed to an influence of rotation waves. An example taken from Teisseyre (1973) is shown in Fig. 5.

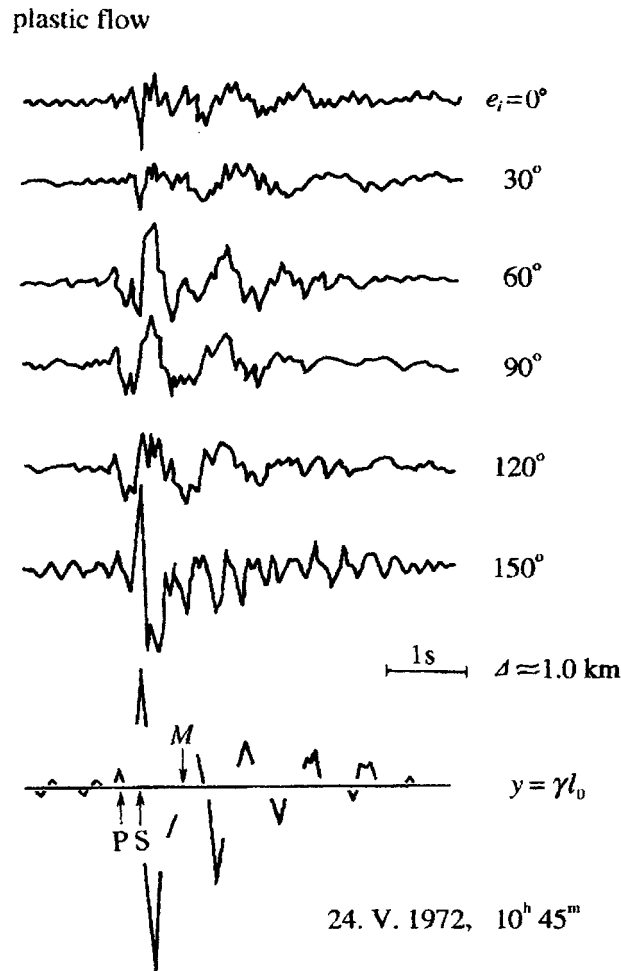


Fig. 5. Six-channel seismic records and rotation seismogram.

## 6. New Technologies of Spin Motion Recording

There have been several examples of the application of Sagnac's idea of interferometer (laser gyroscopes and fiber-optic interferometers) as inertia-less instruments to record spin. Such systems were first applied for aircraft navigation, then for the Earth's rotation measurements, and finally to seismology. In a fiber-optic system, its sensitivity increases with growing number of coils. The approximate orders of magnitude of the required sensitivities were the following:

- $10^{-3} - 10^{-4}$  rad/s in the case of aircraft navigation,
- $10^{-4} - 10^{-5}$  rad/s in the case of Earth's rotation,
- $10^{-5} - 10^{-9}$  rad/s in seismology.

The first 3-channel interferometric seismograph was constructed by Takeo (Takeo and Ito 1997). In our studies in the Ojców and Książ Observatories we used the interferometric seismograph designed by Jaroszewicz *et al.* (2001); its sensitivity was  $10^{-8}$  rad/s. Moriya and Morumo (1998) started to record seismic rotation waves using of two identical seismometers situated in anti-parallel position. This idea was modified at the Institute of Geophysics: two anti-parallel pendulums with a common rotation axis (for calibration, it is possible to put both pendulums of this seismograph into a parallel position). A sketch of the system is shown in Fig. 6.

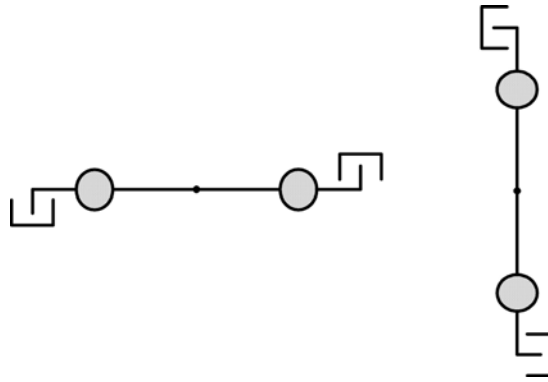


Fig. 6. System of two perpendicularly situated rotation seismographs.

From the system of rotation seismograph with the antiparallel pendulums we obtain the following relations (assuming identical seismograph responses):

$$U_1 = u + l\omega, \quad U_2 = u - l\omega \quad \text{and} \quad U_1 + U_2 = 2l\omega, \quad U_1 - U_2 = 2u.$$

where  $l$  is the reduced length of the pendulum,  $U_1$  and  $U_2$  are the recorded signals on sensors 1 and 2 as presenting the displacement field  $u$  disturbed by rotation  $\omega$ ; the sum of such signals results in rotation  $\omega$ , while their difference represents undisturbed displacement fields.

It was observed that the two perpendicular-oriented rotation systems bring different values of rotation: this is due to an influence of the twist component. Thus, instead of the above relation we shall write separate relations for each rotation seismograph, namely:

$$\tilde{U}_1 - \tilde{U}_2 = 2l\varphi, \quad \hat{U}_1 - \hat{U}_2 = 2l\psi \quad \text{and} \quad \tilde{U}_1 + \tilde{U}_2 = 2\tilde{u}, \quad \hat{U}_1 + \hat{U}_2 = 2\hat{u}.$$

The true rotation-spin is defined as a mean value from these two systems, while their difference defines the twist related to shear deformations of the rotating grains (see Fig. 7).

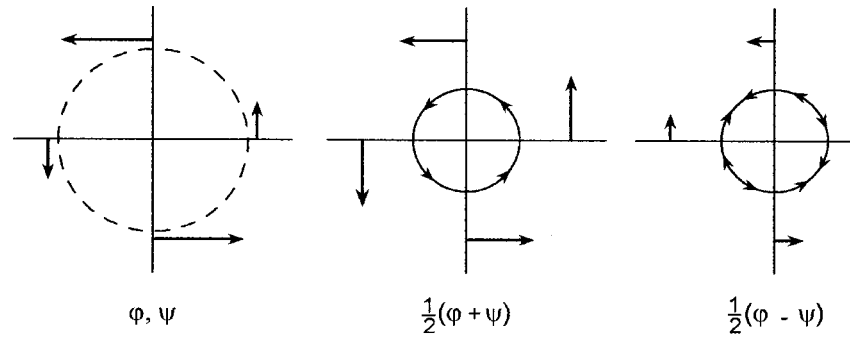


Fig. 7. Spin and twist motions; left: different values of rotation resulting from the perpendicular system of two rotation seismographs; middle: spin motion as their mean value; right: twist as their difference (note that the signs used depend on the assumed convention).

## 7. Sources of Rotation Motions and Waves

As mentioned above, the small rotation motions appear due to the inner friction properties even in a homogeneous medium; in such a way, propagation of rotation waves becomes possible (Teisseyre 2005). The above-mentioned effects become greater in inhomogeneous or structural media. However, in a source fracture zone the slip friction processes along micro-cracks contribute to producing much more remarkable rotation motions (see Figs. 8 and 9).

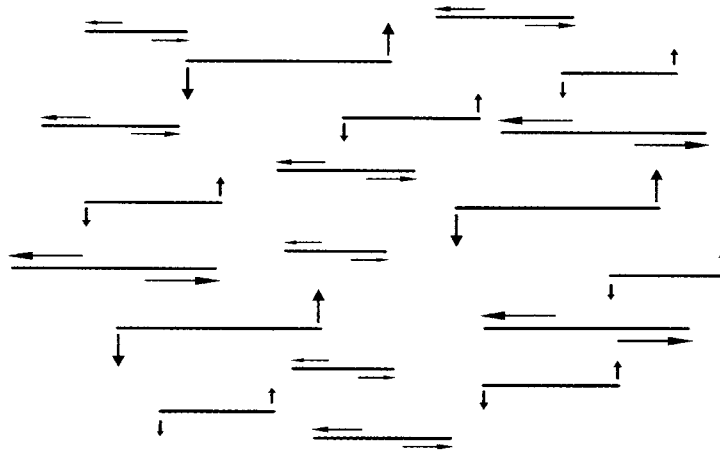


Fig. 8. Friction and moment formed at micro-fracturing.

## 8. Engineering Seismology and Rotations

In engineering, the rotation effects become especially important in the case of high buildings (Zembaty 2006). It is then useful to study both the rotation component along the vertical axis and the two rocking components (similar to tidal deformations):

$$\phi = \frac{1}{2} \left( \frac{\partial v}{\partial x} - \frac{\partial u}{\partial y} \right), \quad \theta_x = \frac{\partial w}{\partial x}, \quad \theta_y = \frac{\partial w}{\partial y},$$

where we marked only the components that are related to displacement motion, because this motion is really strongly amplified for high buildings.

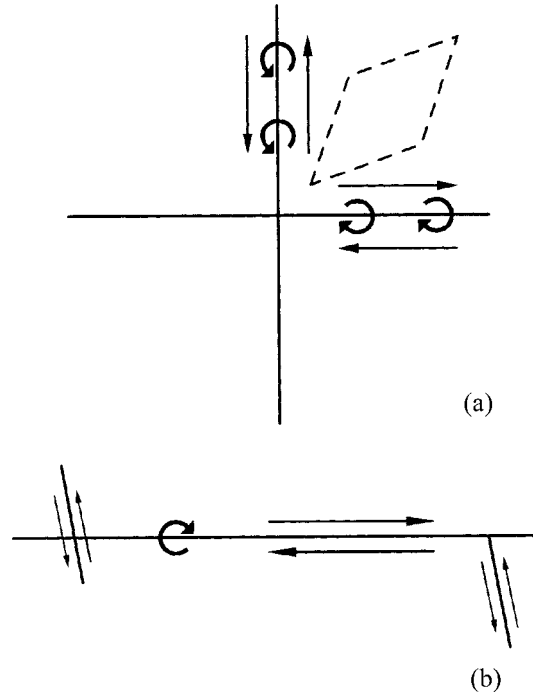


Fig. 9. Fracture and rotations: (a) symmetric case, (b) an asymmetric case as a real situation.

## 9. Conclusions

The study of rotation motion may be important near the source zones where we can assume that the true spin and twist motions may overpass the amplitudes of rotation of displacement and shear:

$$\omega_{[.] } \gg \frac{1}{2} \left( \frac{\partial v}{\partial x} - \frac{\partial u}{\partial y} \right), \quad \omega_{(\cdot)} \gg \frac{1}{2} \left( \frac{\partial v}{\partial x} + \frac{\partial u}{\partial y} \right).$$

In application to earthquake engineering, an opposite sense of these inequalities is expected.

Micro-rotation seismology opens new research areas, mainly related to the fracture processes, although some new applications may be also expected from the study of micromorphic properties of media.

## References

- Eringen, A.C., 1999, *Microcontinuum Field Theories*, Springer, Berlin.
- Mallet, R., 1862, *Great Neapolitan Earthquake of 1857. The First Principles of Observational Seismology*, vols. I-II, Chapman and Hall, London (Fasc. edit., SGA, Italy 1987).
- Moriya, T., and R. Marumo, 1998, *Design for rotation seismometers and their calibration* *Geophys. Bull. Hikkaido Univ.* **61**, 99-106.
- Shimbo, M., 1975, *A geometrical formulation of asymmetric features in plasticity*, *Bull. Fac. Eng., Hokkaido Univ.* **77**, 155-159.
- Shimbo, M., 1995, *Non-Riemannian geometrical approach to deformation and friction*. In: R. Teisseyre (ed.), "Theory of Earthquake Premonitory and Fracture Processes", 520-528, PWN, Warszawa.
- Takeo, M., and H.M. Ito, 1997, What can be learned from rotational motions excited by earthquakes?, *Geophys. J. Int.* **129**, 319-329.
- Teisseyre, R., 1973, *Earthquake processes in a micromorphic continuum*, *Pure appl. Geophys.* **102**, 15-28
- Teisseyre, R., and W. Boratyński, 2003, *Continua with self-rotation nuclei: evolution of asymmetric fields*, *Mech. Res. Com.* **30**, 235-240.
- Teisseyre, R., and J. Kozák, 2003, *Considerations on the seismic rotation effects*, *Acta Geophys. Pol.* **51**, 3, 243-256.
- Teisseyre, R., 2004, *Spin and twist motions in a homogeneous elastic continuum and cross-band geometry of fracturing*, *Acta Geophys. Pol.* **52**, 2, 173-183.
- Zembaty, Zb., 2006, *Deriving seismic surface rotations for engineering purposes*. In: R. Teisseyre, M. Takeo and E. Majewski (eds.), "Earthquake source Asymmetry Structural Media and Rotation Effects", Springer Verlag, 2006 (in print).

Accepted 10 April 2006



## Seismic Doublets and Multiplets in the Polish Copper Mines

Sławomir J. GIBOWICZ, Bogusław M. DOMAŃSKI and Paweł WIEJACZ

Institute of Geophysics, Polish Academy of Sciences  
Księcia Janusza 64, 01-452 Warszawa, Poland

### Abstract

A pair of earthquakes or seismic events of the same magnitude which occur close to each other during short time interval is called a seismic doublet. These events therefore should not be random. We accepted the following criteria for selection of doublets in the Polish copper mines: the difference in magnitude (based on seismic moment) of two events not larger than 0.15, the distance between their hypocenters not greater than 200 m, and the time interval between their occurrence not greater than 20 days. We considered seismic events from the Polkowice mine that occurred from 1994 to 1996 and from the Rudna mine that occurred between 1994 and 2003 studied previously; their source parameters and focal mechanisms were known, as well as their source time functions in some cases. Altogether, we found in the two mines about 100 doublets and several triplets and quadruplets. Spatial distribution of doublets in particular sections of mines display linear dominant trends, characteristic for a given area, which are often in conformity with the direction of nodal planes determined by focal mechanism of one or both events forming a doublet and with the direction of rupture propagation in their source. Such correlations imply a common origin of seismic doublets associated with dominant fault systems and discontinuities in mines.

### 1. Introduction

Earthquake interaction is a fundamental feature of seismicity, leading to earthquake sequences and clustering. An earthquake alters the shear and normal stress on surrounding faults. The observed seismicity rate may be influenced by both static and dynamic effects (Stein 1999). To study such stress interaction the computation of the stress field outside a rupturing fault is performed, and an interaction criterion that promises a better understanding of earthquake occurrence is Coulomb stress transfer (e.g., Stein 1999, King and Cocco 2001). Modelling results demonstrate that transient loads, such as stress changes associated with passing seismic waves, advance the time

of earthquakes that would have happened eventually as a result of constant background loading (Gomberg *et al.* 1997).

Global statistics of earthquake pairs reveal strong clustering in space and time, in which the occurrence of one earthquake increases the probability of a second earthquake. It should be noted that doublets or multiplets of large earthquakes are differently specified than those of small events, often micro-earthquakes observed locally. A doublet on a global scale may be defined as a pair of large events of the same magnitude (within its determination accuracy) with centroids (centre of the deformation release) closer than their rupture size and occurring within a time interval shorter than the recurrence time inferred from plate motion (Kagan and Jackson 1999).

Several studies show that earthquake doublets and multiplets occur in various parts of the Earth (e.g., Gibowicz and Lasocki 2005). The mechanism of their triggering is not well understood, but the generation of compound earthquakes indicates heterogeneity in the faulting process and has been attributed to a specific pattern of fault plane heterogeneity consisting of closely spaced asperities (areas with increased strength) on the fault contact plane such that the failure of one asperity triggers slip in immediately adjacent asperities (e.g., Ruff 1992, Horikawa 2001).

Recently Felzer *et al.* (2004) demonstrated that the statistics of earthquake data in several catalogues are consistent with a single triggering mechanism responsible for the occurrence of aftershocks, foreshocks, and multiplets; and that they are caused by the same physical process. They find that the high rate of multiplets in several subduction zones may be explained simply by a high regional aftershock rate and earthquake density.

A multiplet or a doublet on a local scale is a group or a pair of seismic events with similar waveforms, but different origin times, and is considered to be the result of stress release on the same fracture (e.g., Moriya *et al.* 2002). Events with such similar waveforms must occur in nearly the same position and share a similar source time function and focal mechanism (e.g., Poupinet *et al.* 1984, Lees 1998), but their magnitude needs not to be the same. Doublets/multiplets analysis is a powerful tool for detailed studies of seismotectonic structures and propagation characteristics of seismic waves (e.g., Augliera *et al.* 1995). It has been used to study the nature of ruptures in the geothermal field (Lees 1998), to monitor the post sealing behaviour of the caverns in a salt mine (Maisons *et al.* 1997), to investigate the underground reservoir structure (Moriya *et al.* 2002), and to strengthen a conceptual model for fluid-injection-induced seismicity at the KTB (Baisch and Harjes 2003).

In this paper a search for doublets and multiplets of seismic events induced by mining in the Polkowice and Rudna copper mines is presented. Special attention is paid to the discrimination of the rupture plane from two nodal planes described by fault plane solutions.

## **2. Data and Selection of Seismic Doublets and Multiplets**

In 1995 and 1997 we determined source parameters and in some cases focal mechanism of 173 seismic events that occurred between 1994 and 1996 in various

parts of the Polkowice copper mine. They are listed in two unpublished reports available at the Institute of Geophysics, Polish Academy of Sciences.

Similarly, during last ten years we determined, on the request of the Rudna mine management, source parameters and in some cases focal mechanism of 617 seismic events that occurred between 1994 and 2003 in various sections of the Rudna copper mine. They are listed in ten unpublished reports. For some of these events the source time function has been also determined (Domański *et al.* 2003) and in a number of cases directivity effects have been distinctly observed.

We specify a doublet of seismic events in mines in terms of their magnitude in a similar manner as doublets of large earthquakes; that is that the two events are of the same magnitude. It has been shown that such doublets in the Fiji-Tonga-Kermadec region are not connected by chance, that they are coupled (Gibowicz and Lasocki 2005). The degree of fault rupture overlap between two seismic events of the same magnitude is of special interest for a search of dominant fault systems in mines.

Moment magnitude (Hanks and Kanamori 1979) of seismic events from our copper mines is available and its internal consistency is expected to be high. We specify, therefore, a seismic doublet in our mines as a pair of seismic events with a magnitude difference of no more than 0.15 of magnitude unit, whose hypocentres are separated by no more than 200 m and whose difference in time of occurrence is not longer than 20 days. The distance separation was chosen taking into account the accuracy of location of at least 50 m for a single event. The selection of the time criterion is rather arbitrary, but it is significantly less important than the distance criterion (Gibowicz and Lasocki 2005).

At the Polkowice mine we selected seismic doublets and multiplets in 3 sections: G-21, G-31 and G-51. We found 24 doublets, 8 triplets and 2 quadruplets; altogether 46 seismic pairs. Similarly, at the Rudna mine we selected seismic multiplets in sections G-1/7, G-1/8, G-13/3, G-6/6, G-12/4, and G-12/5. We found 35 doublets, 6 triplets and 1 quadruplet; altogether 50 seismic pairs.

### 3. Characteristics of Seismic Doublets

From both mines we have 96 pairs of seismic events whose hypocentres are located at a distance ranging from 4 to 200 m, and whose time separation ranges from 0.7 minute to 19.6 days. The distance against the time interval is shown on a logarithmic scale in Fig. 1. The distance of 100 m and the time interval of 1 day are marked out to underline the pairs characterised by the shortest distance and time intervals. There are 17 such distinct pairs, that is 18% of all pairs. The distance between two events forming a doublet does not depend on their magnitude (Fig. 2). Similarly, their time separation is also not dependent on magnitude.

The degree of fault rupture overlap  $\eta$  in a pair (Kagan and Jackson 1999) was also calculated. It is the sum of the respective rupture lengths of the two earthquakes forming a pair divided by the double distance between their hypocentres. The values of  $\eta$  larger than 1.0 suggest that the rupture zones of both earthquakes overlap. The rupture lengths in our case were taken as double source radii known from previous

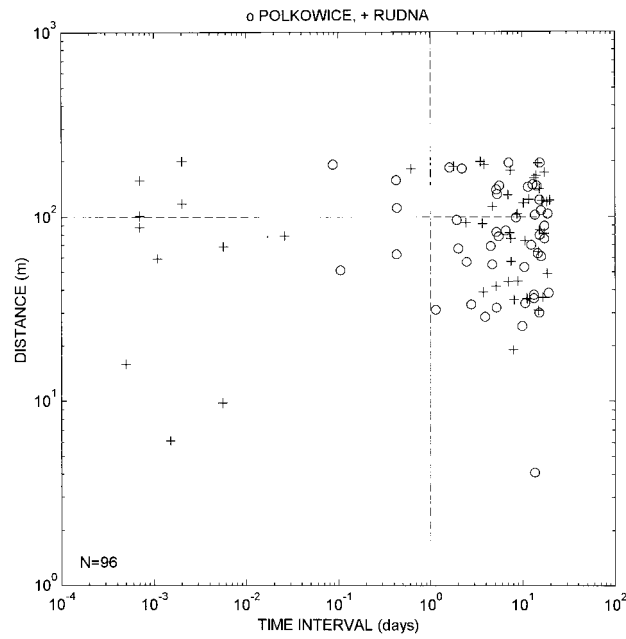


Fig. 1. The distance against the time interval between two seismic events forming a pair. Two dashed lines indicate the distance of 100 m and the time difference of 1 day, respectively.

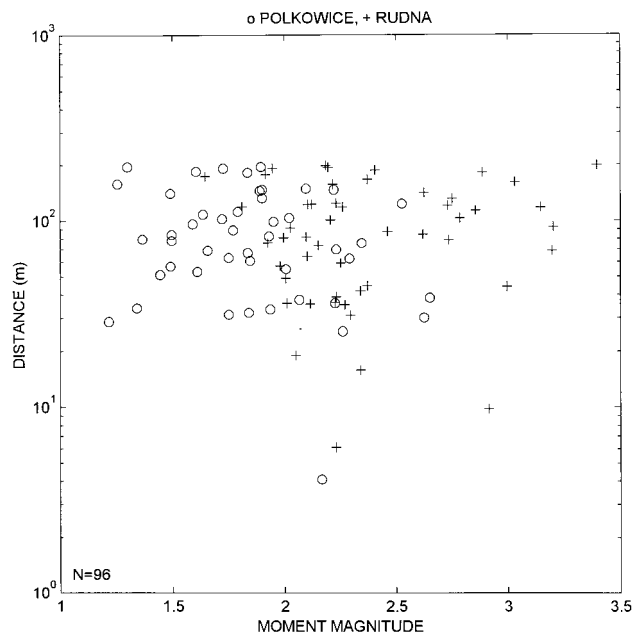


Fig. 2. The distance between two seismic events forming a pair against their average moment magnitude.

calculations for seismic events forming 92 pairs in both mines. We have 76 pairs (83% of all pairs) with the  $\eta$  values in excess of 1.0. They seem to increase with increasing magnitude (Fig. 3), but they are not dependent on the time interval between two events forming a pair.

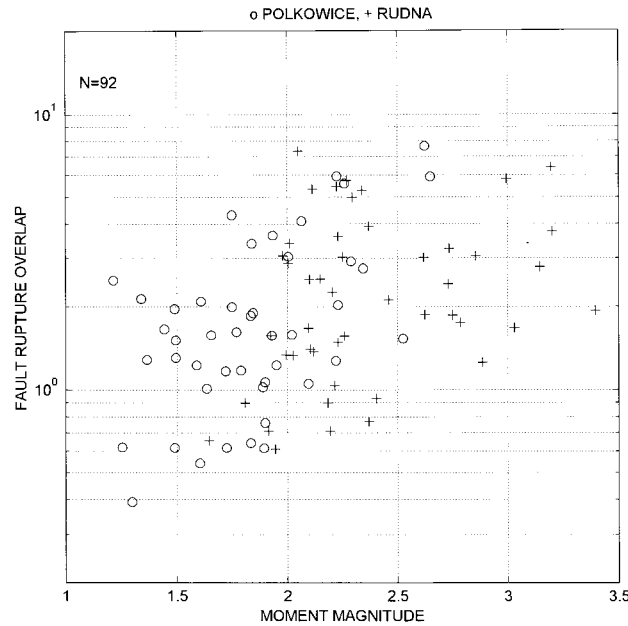


Fig. 3. The degree of fault rupture overlap between two seismic events forming a pair against their average moment magnitude.

The 3D angle of rotation (Kagan 1991) between focal mechanisms of two earthquakes forming a pair, that would transform the focal mechanism of one event into that of another event, is used to study their similarities and dissimilarities (e.g., Kagan 1992). The focal mechanism of seismic events in our copper mines is based on a moment tensor inversion described by Wiejacz (1992). The rotation angle ranges from  $6^\circ$  to  $108^\circ$ , but only about one third of pairs have the rotation angle smaller than  $30^\circ$  (Fig. 4), indicating that both events in these pairs have similar focal mechanism (Kagan and Jackson 1999). The rotation angle is not dependent on earthquake magnitude, on the time interval between the two events (Fig. 5), and on their distance.

The lines connecting the two events forming doublets, that originated in a particular section of mine, display quite uniformly dominant directions, indicating presumably dominant discontinuities in a given area. The spatial distribution of seismic doublets in sections G-21 and G-31 of the Polkowice mine is shown in Figs. 6 and 7, and in section G-6/6 of the Rudna mine is presented in Fig. 8. It seems that these dominant doublet directions could be used for discrimination of the rupture plane from the two nodal planes provided by fault plane solutions.

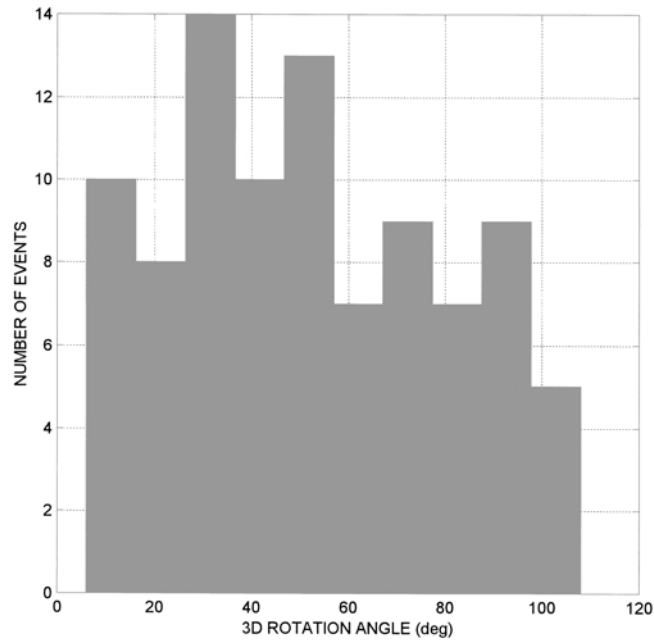


Fig. 4. Histogram of the 3D rotation angles that would transform the focal mechanism of one seismic event into that of another event forming a pair.

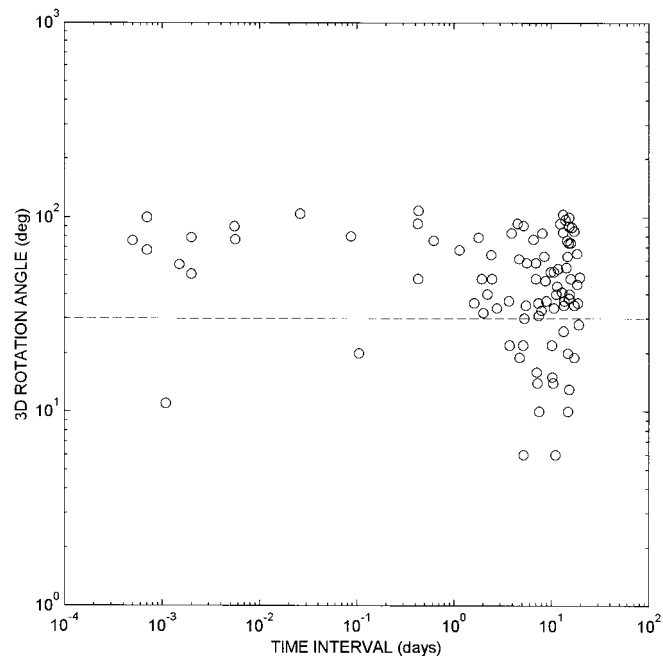


Fig. 5. The rotation angle against the time interval between two seismic events forming a pair. The dashed line indicates the rotation angle of  $30^\circ$ .

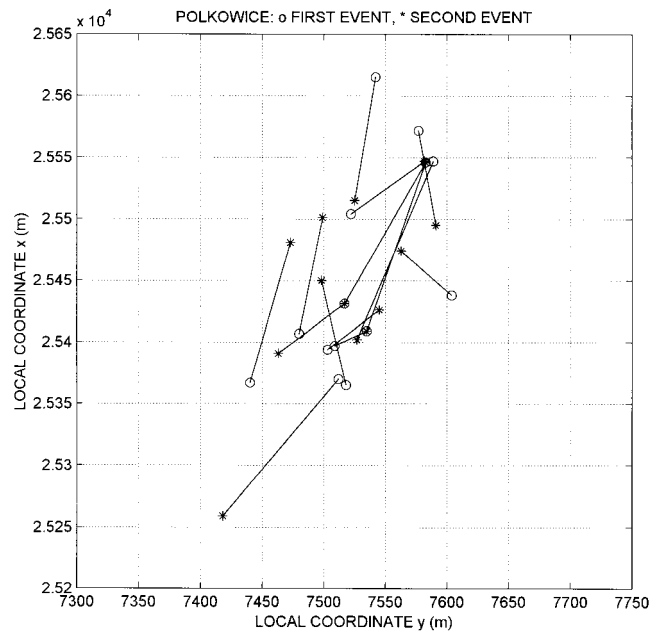


Fig. 6. Spatial distribution of seismic doublets in section G-21 of the Polkowice mine. The location of the first event of a doublet is marked by an open circle and of the second event by a star. Triplets are also indicated.

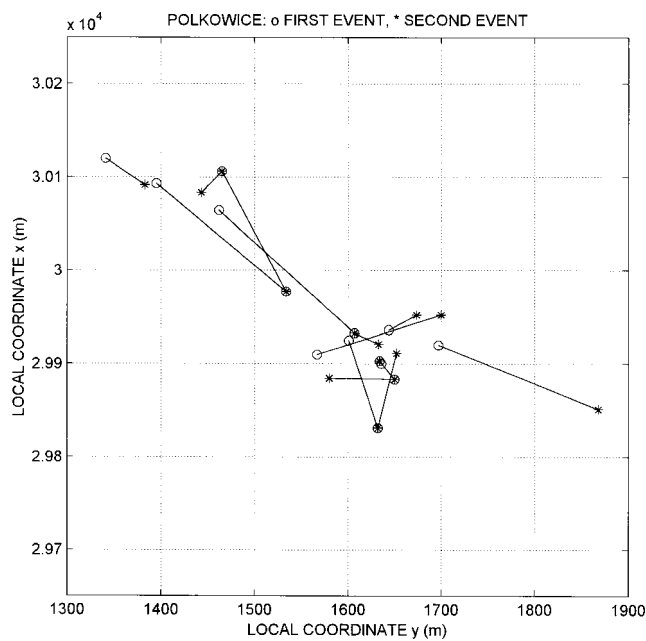


Fig. 7. Spatial distribution of seismic doublets in section G-31 of the Polkowice mine. The location of the first event of a doublet is marked by an open circle and of the second event by a star. Triplets are also indicated.

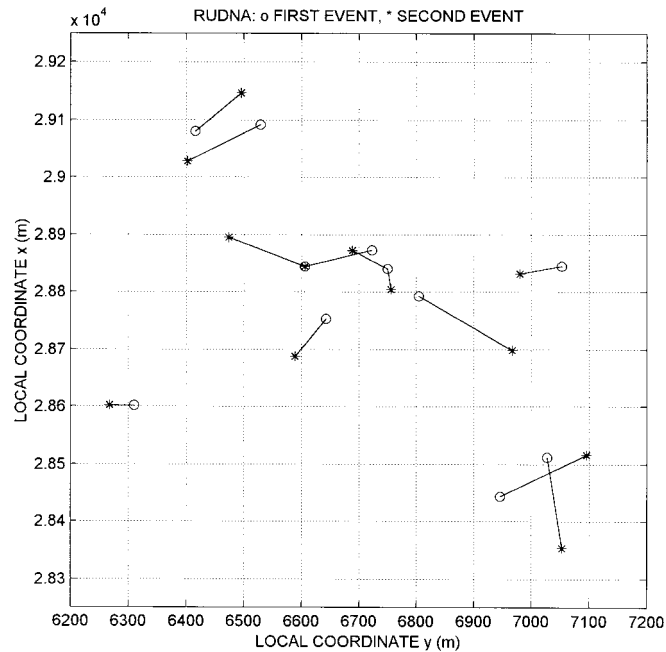


Fig. 8. Spatial distribution of seismic doublets in section G-6/6 of the Rudna mine. The location of the first event of a doublet is marked by an open circle and of the second event by a star. Triplets are also indicated.

#### 4. Determination of Rupture Plane

Discrimination of a rupture plane from nodal planes provided by fault plane solutions for seismic events forming pairs should be possible from comparison of the azimuths between the two events and the strikes of their nodal planes. Such comparison was made for each doublet azimuth and the strike of four nodal planes (two from the first and two from the second event). The smallest difference in absolute sense was considered separately for the first and the second event of a doublet. Additionally, the smallest differences between the doublet azimuth and the azimuth of the rupture propagation direction at the source, determined from the spatial distribution of relative source time functions, were also considered. A histogram of these differences for the first event (65 observations) is shown in Fig. 9, and for the second event (67 observations) is presented in Fig. 10. For about 60% of the cases the differences are smaller than  $30^\circ$ , implying that the determination of the rupture plane was at least partially successful.

A direct comparison of the strike of nodal plane or the azimuth of the rupture propagation direction with the azimuth between two events forming a doublet is shown for the first event in Fig. 11 and for the second event in Fig. 12. The continuous straight line shows an approximation of the data under an assumption that both the angles are equal; they are bound by the values of standard deviation of  $37-38^\circ$ , marked by dashed lines.

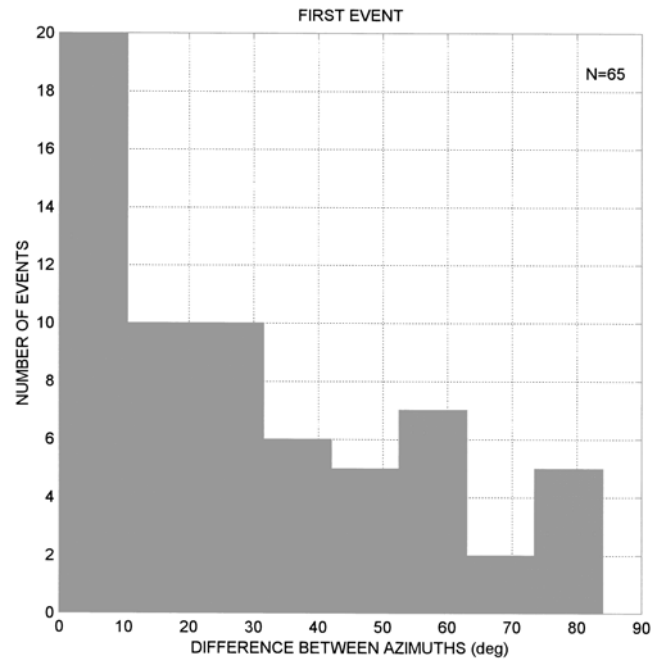


Fig. 9. Histogram of differences between the nodal plane strike or the rupture propagation direction azimuth and the azimuth between two events forming a doublet for the first event.

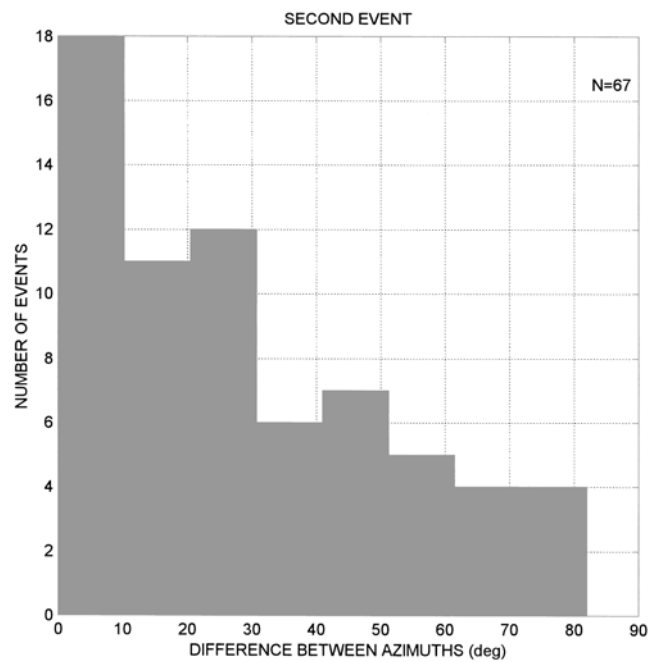


Fig. 10. Histogram of differences between the nodal plane strike or the rupture propagation direction azimuth and the azimuth between two events forming a doublet for the second event.

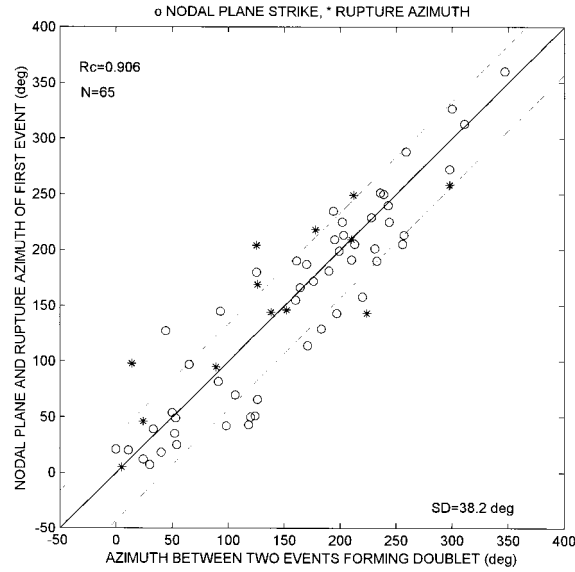


Fig. 11. The nodal plane strike (open circles) and the rupture propagation direction azimuth (stars) against the azimuth between two events forming a doublet for the first event. The continuous straight line shows the equal values of both angles within an interval defined by the standard deviation SD, marked by two dashed lines. The correlation coefficient Rc and the number of observations are also given.

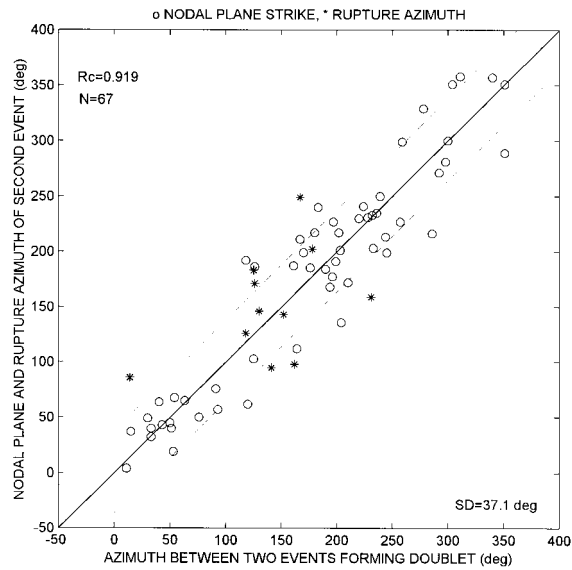


Fig. 12. The nodal plane strike (open circles) and the rupture propagation direction azimuth (stars) against the azimuth between two events forming a doublet for the second event. The continuous straight line shows the equal values of both angles within an interval defined by the standard deviation SD, marked by two dashed lines. The correlation coefficient Rc and the number of observations are also given.

## 5. Conclusions

Seismic doublets and multiplets at Polish copper mines are often observed within the studied range of moment magnitude between 1.2 and 3.4.

The distance and time intervals between two events forming a pair is not dependent on their magnitude.

In 35% of cases the rotation angle, that would transform the focal mechanism of one event into that of another event forming a pair, is smaller than  $30^{\circ}$ , indicating similar focal mechanisms of the two events.

The lines connecting the two events forming pair that occurred in a particular section of the mine display dominant directions, characteristic for this given area.

These lines define the azimuth between the two events that can be used to discriminate the rupture plane among two nodal planes known from fault plane solutions. This approach can be used for determination of seismogenic faults and discontinuities in mines.

**A c k n o w l e d g e m e n t s.** We are grateful to our colleague Dr. Wojciech Dębski for calculation of 3D rotation angles used for the comparison of fault plane solutions of seismic events forming pairs.

## References

- Augliera, P., M. Cattaneo and C. Eva, 1995, *Seismic multiplets analysis and its implication in seismotectonics*, Tectonophysics **248**, 219-234.
- Baisch, S., and H.-P. Harjes, 2003, *A model for fluid-injection-induced seismicity at the KTB, Germany*, Geophys. J. Int. **152**, 160-170.
- Domański, B., and S.J. Gibowicz, 2003, *The accuracy of source parameters estimated from the source time function of seismic events at Rudna copper mine in Poland*, Acta Geophys. Pol. **51**, 347-367.
- Felzer, K.R., R.E. Abercrombie and G. Ekström, 2004, *A common origin of aftershocks, foreshocks, and multiplets*, Bull. Seism. Soc. Am. **94**, 88-98.
- Gibowicz, S.J., and S. Lasocki, 2005, *Earthquake doublets and multiplets in the Fiji-Tonga-Kermadec region*, Acta Geophys. Pol. **53**, 239-274.
- Gomberg, J., M.L. Blanpied and N.M. Beeler, 1997, *Transient triggering of near and distant earthquakes*, Bull. Seism. Soc. Am. **87**, 294-309.
- Hanks, T.C., and H. Kanamori, 1979, *A moment magnitude scale*, J. Geophys. Res. **84**, 2348-2350.
- Horikawa, H., 2001, *Earthquake doublet in Kagoshima, Japan: Rupture of asperities in a stress shadow*, Bull. Seism. Soc. Am. **91**, 112-127.
- Kagan, Y.Y., 1991, *3-D rotation of double-couple earthquake sources*, Geophys. J. Int. **106**, 709-716.
- Kagan, Y.Y., 1992, *Correlations of earthquake focal mechanisms*, Geophys. J. Int. **110**, 305-320.

- Kagan, Y.Y., and D.D. Jackson, 1999, *Worldwide doublets of large shallow earthquakes*, Bull. Seism. Soc. Am. **89**, 1147-1155.
- King, G.C.P., and M. Cocco, 2001, *Fault interaction by elastic stress changes: New clues from earthquake sequences*, Adv. Geophys. **44**, 1-38.
- Lees, J.M., 1998, *Multiplet analysis at Coso geothermal*, Bull. Seism. Soc. Am. **88**, 1127-1143.
- Maisons, C., E. Fortier and M. Valette, 1997, *Induced microseismicity and procedure for closure of brine production caverns*, Pure Appl. Geophys. **150**, 585-603.
- Moriya, H., K. Nakazato, H. Niitsuma and R. Baria, 2002, *Detailed fracture system of the Soultz-sous-Forêts HDR field evaluated using microseismic multiplet analysis*, Pure Appl. Geophys. **159**, 517-541.
- Poupinet, G., W.L. Ellsworth and J. Frechet, 1984, *Monitoring velocity variations in the crust using earthquake doublets: An application to the Calaveras Fault, California*, J. Geophys. Res. **89**, 5719-5731.
- Ruff, L., 1992, *Asperity distributions and large earthquake occurrence in subduction zones*, Tectonophysics **211**, 61-83.
- Stein, R.S., 1999, *The role of stress transfer in earthquake occurrence*, Nature **402**, 605-609.
- Wiejacz, P., 1992, *Calculation of seismic moment tensor for mine tremors from the Legnica-Głogów Copper Basin*, Acta Geophys. Pol. **40**, 103-122.

Accepted 10 April 2006

## SEJSMICZNE DUBLETY I MULTIPLETY W POLSKICH KOPALNIACH MIEDZI

### Streszczenie

Sejsmicznym dubletem nazywamy parę wstrząsów o tej samej wielkości, występujących w pobliżu siebie w krótkim odstępie czasu. Nie powinny to zatem być zdarzenia przypadkowe. Przyjęliśmy następujące kryteria definiujące dublety: różnica magnitud (opartych na momencie sejsmicznym) obu wstrząsów nie większa niż 0.15, odległość między ich ogniskami nie większa niż 200 m oraz interwał czasowy między nimi nie większy niż 20 dni. Badaliśmy wstrząsy z kopalni „Polkowice” z lat 1994-1996 oraz z kopalni „Rudna” z lat 1994-2003, dla których mieliśmy obliczone parametry spektralne ogniska, mechanizm ogniska oraz dla niektórych przypadków czasową funkcję źródła. W sumie znaleźliśmy w obu kopalniach około 100 dubletów oraz szereg trypletów i kwadrupletów. Rozkład przestrzenny dubletów w poszczególnych oddziałach górniczych wykazuje istnienie charakterystycznych struktur liniowych o określonych trendach, często zbieżnych z kierunkiem płaszczyzn nodalnych określonych przez mechanizm ogniska jednego lub obu wstrząsów tworzących dublet oraz z kierunkiem rozrywów unilateralnych w ogniskach badanych zjawisk sejsmicznych. Takie korelacje świadczą o wspólnej genezie sejsmicznych dubletów, związanych z dominującym systemem uskoków i spękań w poszczególnych oddziałach kopalń.

## **Energy Distribution of Induced Seismic Events Occurring in Wesola Coalmine, Poland**

Łukasz RUDZIŃSKI and Adam Filip IDZIAK

University of Silesia, Faculty of Earth Sciences  
ul. Będzińska 60, 41-200 Sosnowiec, Poland

### **A b s t r a c t**

The paper presents a study on energy distribution of seismic events from the Wesola coalmine (Mysłowice, Poland). The seismic catalogue comprising 14,514 tremors occurring between January 2000 and March 2004 was analysed. Empirical cumulative distribution functions of energy (CDF) were calculated and estimated using Gumbel's asymptotic distributions. It was stated that the experimental CDFs of low energy events can be estimated by Gumbel's theoretical distributions of type II.

### **1. Introduction**

The energy of most of the seismic events observed in underground mines is in a wide range, between  $10^1$  and  $10^{10}$  J, which corresponds to local magnitude  $M_L$  range from 0.5 to 4.5 (Gibowicz and Kijko 1994). The largest mine tremor with local magnitude  $M_L = 5.6$  was observed in the south German potash mining district on March 13, 1989 (Knoll 1990).

The study on mining induced seismicity showed that seismic events occurring in mining areas can be divided into two general categories: type I — weak events occurring near excavations, induced by mining activity, and type II — with relatively higher magnitudes and epicentres located in a wider area around a mine, loosely relevant to mining activity (Johnston 1992). This feature was observed in underground coalmines of Upper Silesian Coal Basin (USCB). Two hypotheses about mechanisms of the two event sets were considered (Kijko et al. 1987):

- they result from homogeneity and discontinuity of rock mass structure (e.g. layered structure);

- low-energy events come from mining-induced stress release, whereas the high-energy events are associated with an interaction between the induced and tectonic stresses.

Since the mid-1980s it has been postulated that the occurrence of events with higher local magnitude could be affected by the local geological and tectonic conditions and the strong events had to be considered as a result of mutual interactions among mining, lithostatic and tectonic stresses (Teper et al. 1992, Sagan et al. 1996). The mining-induced stress field may interfere with the tectonic stress field causing the instability of shallow fault zones generating strong events of magnitude larger than 2.0. However, it is not clear yet whether the tectonic stress is a residuum of stress field existing during the Alpine orogenesis or a result of recent tectonic activity.

Gibowicz and Kijko (1994) described three possible models explaining bimodal energy distribution of seismic events occurring in mining areas. It seems that for the USCB the model assuming two different weakly interacting seismic processes might be applied. According to the model, stress in the rock mass increases linearly within time in the absence of a seismic event generated by the first mechanism and drops to a certain value when the event occurs. The probability of occurrence of event generated by the second mechanism does not depend on the amount of stress in the rock as long as the stress does not exceed some critical value.

The existence of different mechanisms generating mining events in the USCB is confirmed by bimodal event energy distribution with one mode suitable for low-energy components of the event catalogue and the second one appropriate to the high-energy components (Kijko et al. 1982, Dessokey 1984, Drzęźła et al. 1986, Kijko et al. 1987, Idziak et al. 1991). It is possible to construct theoretical distributions for low-energy events and stronger events separately but there is no way to approximate the obtained data by unimodal distribution in the whole energy range.

According to the model of two weakly interacting seismic processes, the events of tectonic origin should have the energy higher than minimum energy characteristic for given structural unit. Previous study of the USCB events energy distribution (Idziak et al. 1991) showed the threshold of high-energy mode to be approximately between  $10^6$  J and  $10^7$  J. The results can be now verified on the basis of new seismic data of better quality obtained since that time.

The aim of the present work was a detailed study of energy distribution of seismic events occurring in main anticline area which is the most active structural subunit of the USCB. Analysis was done for tremors occurred in Wesola coalmine (Mysłowice, Poland) situated in the eastern part of the mine anticline.

## 2. Seismic Data

The seismic catalogue containing 14,514 events with the energy not less than 100 J recorded by the mine seismological network during the period January 2000–March 2004 was used to study the energy distribution of shocks. The largest event had the energy equal to  $6 \cdot 10^6$  J.

Table 1

Numbers of tremors that occurred in Wesoła coalmine during the analysed time periods

Time period	Number of events				
	$< 10^3\text{J}$	$10^3\text{J} - 10^4\text{J}$	$10^4\text{J} - 10^5\text{J}$	$10^5\text{J} - 10^6\text{J}$	$\geq 10^6\text{J}$
01.01.00 – 30.06.00	137	230	23	2	0
01.07.00 – 31.12.00	105	229	50	4	0
01.01.01 – 30.06.01	150	438	58	6	1
01.07.01 – 31.12.01	681	1074	492	42	2
01.01.02 – 30.06.02	1651	1095	531	45	5
01.07.02 – 31.12.02	1435	773	131	6	2
01.01.03 – 30.06.03	1257	826	135	10	1
01.07.03 – 31.12.03	1214	867	245	45	6
01.01.04 – 04.03.04	218	235	46	11	0
Total	6848	5767	1711	171	17

Analysis was carried out for the whole mining area and particularly for the vicinity of long-walls sc37 and sc45 where more than half of tremors had been recorded (6430 records and 2106 records, respectively). Taking into consideration the exponential notation of event energy in seismic catalogues completed by the mine seismological survey, energy intervals in logarithmic scale were established. The cumulative number of events was calculated for consecutive interval boundaries  $E_i$  and interpolated inside the intervals.

Initially, empirical cumulative distribution functions (CDF) were calculated using the formula:

$$F(E_i) = P(E \leq E_i) = \frac{n_i}{N+1} \quad (1)$$

where  $n_i$  is the number of events with energy equal to or less than  $E_i$ , and  $N$  is the total number of events in the catalogue.

The CDF obtained using eq. (1) showed abnormal increments at every boundary of the order of magnitude (i.e.,  $E = 1 \cdot 10^n \text{J}$ , where  $n = 3, 4, 5, 6$ ). We suppose that it resulted from a lowering of event energy. All recorded events from the energy intervals  $1.0 \cdot 10^n \text{J} - 1.9 \cdot 10^n \text{J}$  were probably marked as events of energy  $1 \cdot 10^n \text{J}$ . In effect, data reported by mine are a little bit biased. To eliminate those increments and to smooth the empirical CDF, the modified equation was used:

$$F(E_i) = P(E < E_i) = \frac{n'_i}{N+1} \quad (2)$$

where  $n'_i$  are the numbers of events with energy less than  $E_i$ , and  $N$  is the total number of events in analysed time period.

The empirical cumulative energy distribution functions computed according to definition (2) for tremors from Wesoła coalmine are shown in Fig. 1.

### 3. Analysis of energy distribution

The theory of extreme values can be applied to seismic event catalogues, which are often incomplete, especially at the lowest energy range. Because the stronger events are better recognized, an analysis of these events is more useful than methods relying on complete data sets. According to Gumbel (1962) there are only three distributions asymptotically convergent to the exact distribution of extremes. The general equation of Gumbel's distribution has the form:

$$F(y(E)) = e^{-e^{-y}}. \quad (3)$$

The dependence of variable  $y$  on energy  $E$  defines the type of Gumbel's distribution.

The domain of Gumbel's distribution I is the whole energy range and:

$$y' = k_1(E - \nu) \quad (4)$$

where  $\nu$  and  $k_1 > 0$  are parameters.

The second asymptotic distribution (Gumbel's type II) assumes the lower limit of event energy. Variable  $y$  is defined as:

$$y'' = k_2 \ln \left( \frac{E - \varepsilon}{\nu - \varepsilon} \right) \quad (5)$$

where  $\varepsilon$  is the lower limit of event energy ( $0 < \varepsilon \leq \omega$ ) and  $k_2 > 0$ .

The third asymptotic distribution (Gumbel's type III) is defined under the assumption that the event energy cannot exceed some peak value  $\omega$ :

$$y''' = -k_3 \ln \left( \frac{\omega - E}{\omega - \nu} \right) \quad (6)$$

where  $k_3 > 0$  and  $0 < E \leq \omega$ .

A simple procedure named Jenkinson's method (Gumbel 1958), which allows to inspect Gumbel's distribution, should be used to fit the empirical energy distribution. Assuming  $y$  as an independent variable, one can establish energy as the function of  $y$ :  $E = f(y)$ . The function is linear for Gumbel's distribution I. For Gumbel's distributions II and III the energy  $E(y)$  is concave or convex exponential function, respectively. Values of  $y$  are calculated from the empirical cumulative energy distribution:

$$y = -\ln(-\ln(F(E))) \quad (7)$$

and then the graph of  $E$  versus  $y$  is plotted. The shape of plotted curve points to the type of Gumbel's distribution.

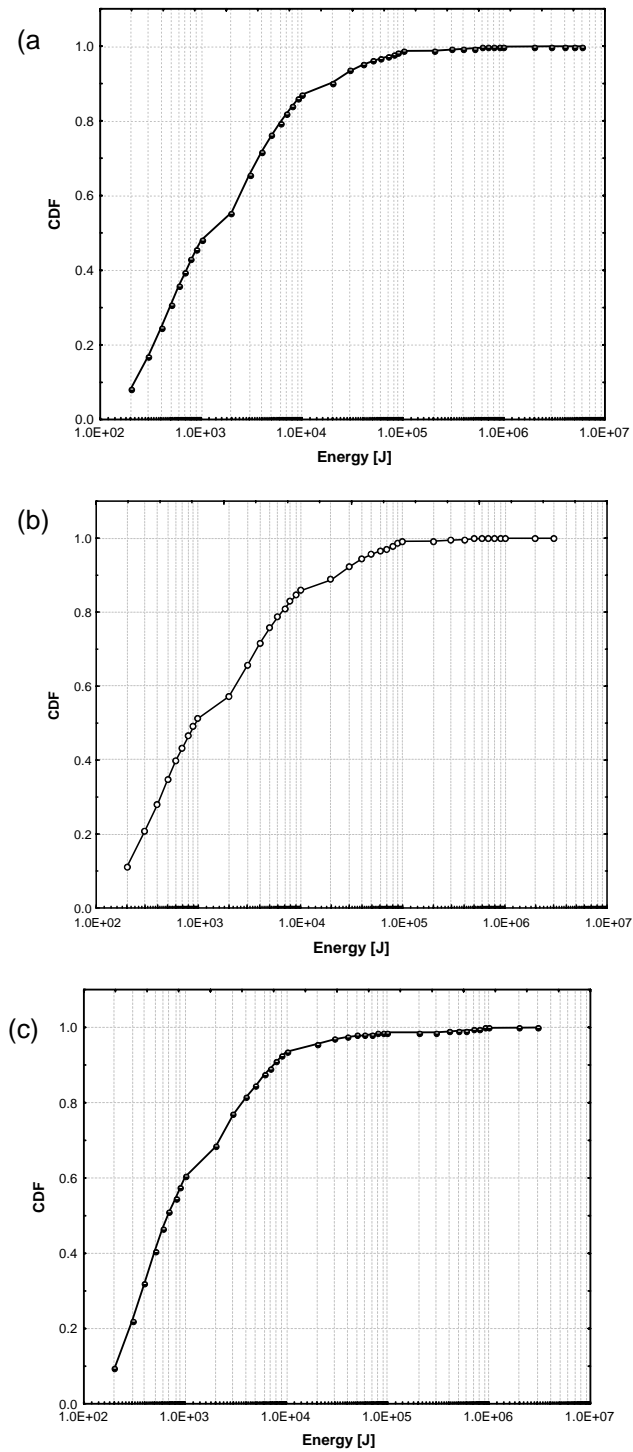


Fig. 1. Empirical CDFs for analysed seismic catalogue from Wesola coalmine (a) whole mine, (b) long-wall sc37, (c) long-wall sc45.

An analysis of the presented data showed that Jenkinson's method did not give an explicit answer about the type of empirical CDF. The plotted curve  $E(y)$  had a flex point for  $y \approx 4.2$  (Fig. 2a). The dependence  $E(y)$  for weak events was represented by concave curve (Fig. 2b) which changed to convex curve for higher energy. The same effect was established for events occurring nearby the long-walls.

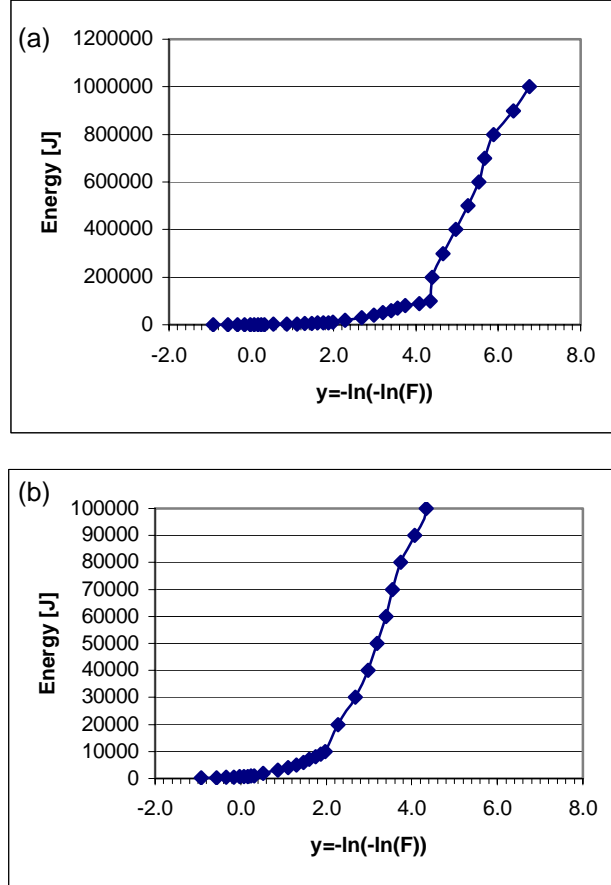


Fig. 2. Event energy versus double logarithm of empirical CDF for Wesola coalmine (a) the whole catalogue, (b) the fragment of  $E(y)$  curve for weak events.

Events of energy exceeding 100 kJ are only a small part of analysed catalogue. That is why we decided to estimate the empirical CDFs by asymptotic distribution of Gumbel's type II:

$$F(E) = e^{-e^{-k_2 \ln\left(\frac{E-\varepsilon}{\nu-\varepsilon}\right)}} = e^{-\left(\frac{E-\varepsilon}{\nu-\varepsilon}\right)^{-k_2}} \quad (8)$$

The non-linear estimation module of STATISTICA computer program was employed to estimate unknown parameters  $k_2$ ,  $\varepsilon$ ,  $\nu$ . The combined Rosenbrock-quasi-Newton method was used to minimize the sum of squared differences between the

empirical and theoretical data. The applied algorithm did not allow us to evaluate the uncertainty of parameter estimators. Quality of estimation could be evaluated by the distribution of errors and its standard deviation and the squared non-linear correlation coefficient (determination coefficient) showing proportion of the data variability explained by the model. The results of estimation are shown in Fig. 3. Gumbel's distributions are related to the Weibull probability density functions; thus, the Weibull probability scale was adopted for vertical axes of the right-hand graphs to highlight the estimation results in high-energy interval.

For the whole mine area and long-wall sc37, theoretical distributions of Gumbel's type II fit the empirical CDFs for event energy less than 40 kJ. For higher energy, empirical CDFs increase more quickly than the theoretical distributions. This could be the result of another seismic process generating additional strong events. The estimated parameters are similar for both areas of investigation mentioned above ( $\varepsilon \approx 75$  J,  $\nu \approx 600$  J,  $k_2 \approx 0,6$ ).

The Gumbel's distribution II obtained for the long-wall sc45 events fits experimental CDF in the whole analysed range of energy. That points to the lack of strong events caused by different mechanism in the vicinity of the long-wall sc45. The parameters of the theoretical function slightly differ from those calculated for the whole mine and sc37 areas ( $\varepsilon \approx 95$  J,  $\nu \approx 450$  J,  $k_2 \approx 0,7$ ). The estimated model is in good agreement with observational data. The distribution of errors is normal with a standard deviation equal to 0.001. The determination coefficient is 0.996, which means that only 0.4% of the data variability is not explained by the model.

#### 4. Conclusions

The obtained results point to bimodal character of energy distribution of seismic events occurring in the Wesola coalmine. This suggests the existence of two mechanisms generating mine tremors in different scales of energy. For 96% of investigated shocks, seismic energy is less than 50 kJ. The empirical CDF of these tremors can be approximated by Gumbel's II asymptotic distribution. Differences between the empirical distribution and the best fitted theoretical function are visible for energy higher than 40 kJ. This could be explained assuming the presence of a process generating additional strong shocks. Above a certain energy threshold the second mechanism increases the probability of seismic event. The previous research of seismic events occurring in the USCB done using less numerous catalogues showed the threshold energy to be approximately between  $10^6$  and  $10^7$  J (Kijko et al. 1986, Kijko et al. 1987, Idziak et al. 1991). The present study suggests that the threshold value for the Wesola coalmine is less than  $10^5$  J (about 50,000 J). Different results obtained for long-walls sc37 and sc45 indicate that shocks generated by the second mechanism do not occur on the whole mining area and they are not directly connected to mine excavations.

The study shows that most of events are generated by the mechanism directly connected to mining activity. The nature of their energy distributions doesn't depend on area of tremors occurrence but the CDFs may have slightly different parameters

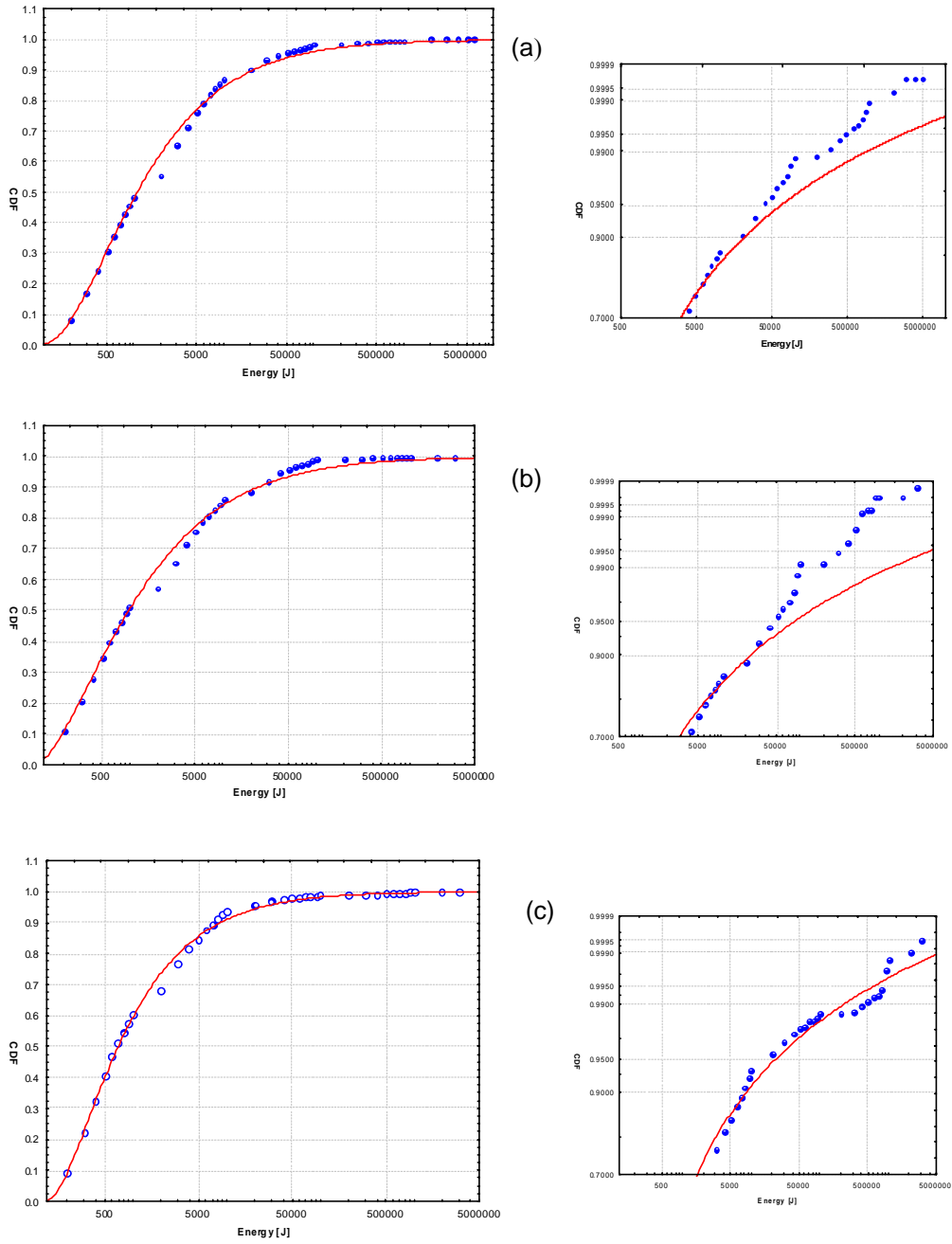


Fig. 3. Empirical energy distributions (dots) and theoretical Gumbel's distributions II (lines) of seismic events from the Wesola coalmine (left) and their high-energy fraction (right): (a) whole mine, (b) long-wall sc37, (c) long-wall sc 45. The Weibull probability scale was used for vertical axes of the right-hand graphs.

due to local geological conditions within rock mass. The approximation of low energy mode by the distribution of Gumbel's type II may be justified by a physical model which connects seismic phenomena with local rock stiffness and distribution of crack size. According to the model, event energy is a function of critical rupture size characterized by the Gumbel's second asymptotic distribution (Zuberek 1986). We tried to estimate the empirical energy distributions by the other Gumbel's distributions but the results were not satisfying. Determination coefficients of the best fitted functions were less than 0.5 and the distributions of errors were not normal.

The obtained results are related to the events occurring in the Wesola coalmine during the chosen time period. The estimated parameters could vary for data sets from different coal mines or time intervals but the type of energy distribution should be generally the same for events caused by the first type mechanism. This assumption is supported by the research of Idziak et al. (1991). The authors stated that the energy distributions of weak events occurring in different structural subunits of the USCB are close to Gumbel's distribution II.

**Acknowledgements.** The study was made according to the order placed by the Committee of Scientific Research of Poland (PBZ-KBN-104/T12/2003).

#### References

- Dessokey, M.M., 1984, *Statistical models of the seismic hazard analysis for mining tremors and natural earthquakes*, Publ. Inst. Geophys. Pol. Acad. Sci. **A-15(174)**, 1-82.
- Drzęźła, B., A. Garus and A. Kijko, 1986, *Energy distribution of largest mining tremors and their connection with geologic structure of rock mass*. **In:** A. Kidybiński and M. Kwaśniewski (eds.), "Mining Systems Adjusted to High Rock Pressure Conditions", Balkema, Rotterdam, 257-261.
- Gibowicz, S.J., and A. Kijko, 1994, *An Introduction to mining seismology*, Academic Press, Int. Geoph. Series. **55**, San Diego, New York.
- Gumbel, E.J., 1962, *Statistic of extremes*, Columbia Univ. Press, New York.
- Idziak, A., G. Sagan, and W.M. Zuberek, 1991, *An analysis of frequency distribution of shocks from the Upper Silesian Coal Basin*, Publ. Inst. Geophys. Pol. Acad. Sci. **M-15(235)**, 163-182.
- Johnston, J.C., 1992, *Rockbursts from a global perspective*. **In:** P. Knoll (ed.), "Induced seismicity". Rotterdam-Brookfield, Balkema, p. 63-78.
- Kijko, A., M.M. Dessokey, E. Głowacka and M. Kazimierczyk, 1982, *Periodicity of strong mining tremors in the Lubin copper mine*. Acta Geophys. Pol. **30**, 221-230.
- Kijko, A., B. Drzęźła and A. Mendecki, 1986, *Bimodalny charakter ekstremalnych rozkładów zjawisk sejsmicznych w kopalniach*. Publs. Inst. Geophys. Pol. Acad. Sci. **M-8(191)**, 91-102.
- Kijko, A., B. Drzęźła and T. Stankiewicz, 1987, *Bimodal charakter of the distribution of extreme seismic events in Polish mines*, Acta Geophys. Pol. **35**, 157-166.

- Knoll, P., 1990, *The fluid-induced tectonic rockburst of March 13, 1989 in the "Werra" potash mining district of the GDR (first results)*. Beitr. Geophys **99**, 239-245.
- Sagan, G., L. Teper and W.M. Zuberek, 1996, *Tectonic analysis of mine tremor mechanisms from the Upper Silesian Coal Basin*, Pure Appl. Geophys. **147(2)**, 217-238.
- Teper, L., A. Idziak, G. Sagan and W. Zuberek, 1992, *New approach to the studies of the relations between tectonics and mining tremor occurrence on example of the Upper Silesian Coal Basin (Poland)*, Acta Montana, Ser. A, 2 (88), 161-177.
- Zuberek, W.M., 1986, *Możliwość wykorzystania asymptotycznych rozkładów wartości ekstremalnych do oceny prawdopodobieństwa występowania wstrząsów indukowanych eksploatacją górniczą*. Zesz. Nauk. Polit. Śl. Ser. Górnictwo, Gliwice 243 – 253.

*Accepted October 16, 2006*

## **Concordance of Tremor Occurrence with Poisson Distribution in the Jas-Mos Coal Mine**

Krzysztof BANK and Waław M. ZUBEREK

Faculty of Earth Sciences, Department of Applied Geology  
University of Silesia  
ul. Będzińska 60, 41-200 Sosnowiec, Poland

### **A b s t r a c t**

About 70 000 mining tremors recorded from 1989 to 2004 at the Jas-Mos coal mine have been analysed. The tremors had seismic energy in the range from  $1 \cdot 10^3$  J to above  $1 \cdot 10^6$  J.

Statistical analysis of the concordance of empirical frequency of tremor occurrence distributions with Poisson distribution has been carried out, gradually decreasing the seismic energy discrimination level. Then the distributions of interevent time intervals have been determined verifying if they approached the exponential distribution.

It is concluded that in all cases one might determine the energy discrimination levels above which the tremor occurrence approaches the Poisson process. This means that the occurrence of tremors is random, and the consequences concerning their prediction are briefly discussed.

### **1. Introduction**

In Polish coal mines, mining seismology can be considered as a most common geophysical method. It is expected that on the basis of results of seismological observations one can evaluate rockburst hazard and would be able to predict stronger mine tremors. Therefore, the relations between induced seismicity and geological conditions as well as recent mining operations (their intensity and method) are relatively well known.

Recently one can meet concepts on the application of the Poisson process to the description of the stronger mine tremor occurrence in the areas of intense underground coal extraction. According to Gnedenko (1969) the Poisson process describing the occurrence of events in time interval from 0 to  $t$  has been derived under the following assumptions:

1. The process is stationary. This means that the occurrence probability of events depends only on the numbers and time interval duration and is not changed by a time shift in all time intervals;

2. There is an absence of aftereffects. This means that the probability of occurrence of  $k$  events during time interval  $(t, t+\Delta t)$  does not depend on how many times the events occurred previously or how they occurred. This signifies mutual independence of occurrence of any number of events during non-overlapping time intervals;

3. The process is orderly, sometimes referred to as orderly in a Khinchin sense. This means that the events do not occur simultaneously and it is impossible for two or several events to occur during appropriately small time interval.

Then the probability of occurrence of exactly  $n$  events in time interval of length  $t'$ ,  $p(n, \lambda t')$ , is determined (Gnedenko 1969, Fisz 1969) as:

$$p(n; \lambda t') = \frac{e^{-\lambda t'} (\lambda t')^n}{n!}, \quad (1)$$

$n = 0, 1, 2, \dots$   $\lambda t' = \frac{N}{T}$  is the parameter representing the expected value of event occurrence in time interval  $t'$ , and  $N$  is the total number of events in  $T$  time intervals of length  $t'$ .

If the event generation process is Poissonian, then it would be purely random, memoryless and stationary (Gnedenko 1969).

The aim of the paper is an analysis of the seismic activity distribution induced by mining operation to ascertain if one can approximate it by Poisson process. It has been assumed that the conformability will be checked for the sequence of tremors from the Jas-Mos coal mine, lowering successively their discrimination seismic energy level.

## 2. Description of the Research Area

The Jas-Mos coal mine is located in the south-west part of the Upper Silesian Coal Basin, where the westerly oriented compression is observed in the sedimentary cover with appropriate modification induced there by movements of the basement blocks (Kotas 1985, Pierwoła 1998). From the morphological point of view, there are several erosional depressions and uplifts (in the Quaternary series) with relative heights up to 30 m.

In this area, the Carboniferous deposits are strongly disturbed by tectonics as a result of the orogenic movements of the Carboniferous age with further interaction in the post-Triassic and post-Cretaceous periods.

In the tectonics of the area one may distinguish the generally dominant direction which has NNE-SSW orientation (direction of pressure). Besides this main direction, one can distinguish further two general zones dissimilar in their tectonic structure – eastern and western. The border between them is approximately along the Orłowa disturbance. The roof of the Carboniferous deposits (created by long lasting erosion

and tectonic process) is covered by impervious clay strata. The morphology of the roof is very diversified. Central and western parts of the deposit where the roof of the Carboniferous strata is  $0.0 \pm 190.0$  m above sea level, are the most elevated. The Earth surface consisting of irregular ridges cut by relatively deep erosional valleys creates the heights with slopes inclined to the north, east and south.

Due to complicated geological structure, the Jas-Mos coal deposit belongs to the folded-faulted type zone. Taking into account the fault dimensions in the deposit, the dominant system of their strikes is meridional while the latitudinal system is created by younger dislocations.

From January 1, 1989, at the Jastrzębie coal mine (presently it is part of the Jas-Mos coal mine) the seismological observations have been started using 6-channel Górnik 1 equipment (Jakubów 2001). Since 2003 the seismological equipment has been gradually modified; it contains now:

- 6-channel Górnik 1 equipment
- 24-channel ARES seismoacoustic system
- 24-channel TSS-SO equipment
- modernised seismological recorder AS-1 (up to 32 channels)
- seismological system ARAMIS (16 channels).

### 3. Data Base

The data base consisted of approx. 70 000 tremors recorded from 1989 to 2004. The tremors had seismic energies above the  $1 \cdot 10^3$  J level, the largest being above  $1 \cdot 10^6$  J. We have analysed more than 50% of them ( $\sim 40$  000 tremors) from the whole sequence of mine tremors, dividing them into 3 periods of seismic activity (Fig. 1):

- low seismicity (from 1 December 2000 to 1 September 2002); a total of 5617 tremors; 255.3 tremors per month, on the average,
- mean seismicity (from 1 May 1992 to 1 January 1994); a total of 9322 tremors; 443.9 tremors per month, on the average,
- high seismicity (from 1 November 1997 to 1 August 2000); a total of 26 370 tremors; 775.6 tremors per month, on the average.

For the selected seismic energy levels, the analysis of the concordance of tremor occurrence with Poisson distribution has been made in two ways:

1. by a statistical analysis of the consistence of tremor occurrence frequency with theoretical Poisson distribution,
2. by an analysis of the distribution of time duration intervals between two consecutive tremors and its consistence with exponential distribution.

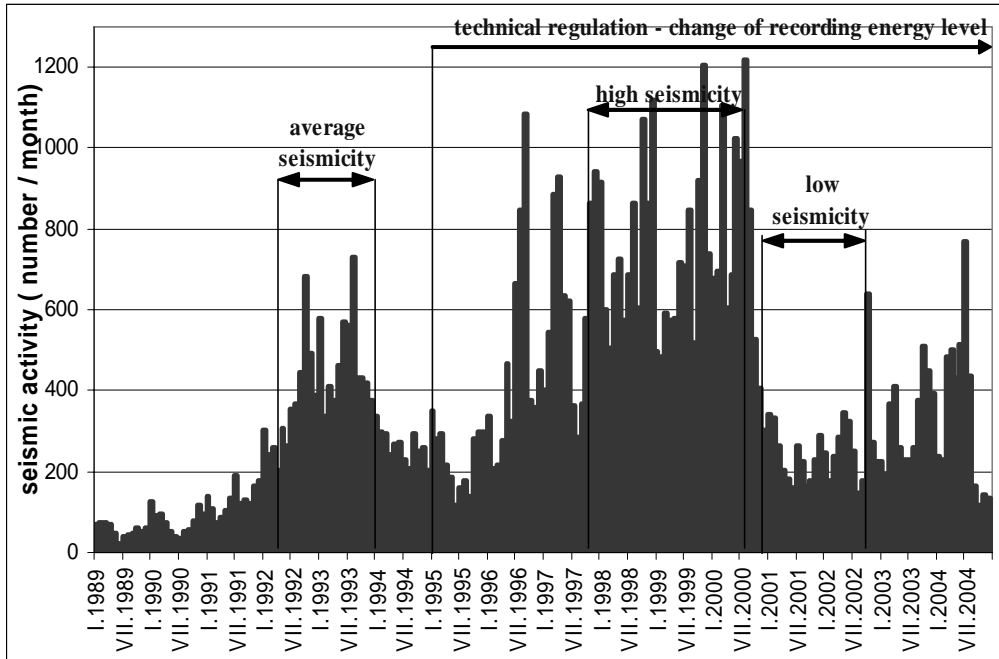


Fig. 1. Mining tremor activity in monthly intervals from the Jas-Mos coal mine in 1989-2004 (seismic energy  $E > 1 \cdot 10^3$  J).

#### 4. Analysis of Results

##### 4.1 Statistical analysis of the occurrence frequency with Poisson distribution

The observed frequencies of tremor occurrence in selected time intervals have been compared with frequencies expected from Poisson distribution determined from Eq. 1. Then the differences between empirical and theoretical distributions have been tested with  $\chi^2$  test (Fish 1969, Jasiulewicz and Kordecki 2001). In all the cases, the  $\chi^2$  statistics had 2 degrees of freedom ( $df = 2$ ) calculated from:

$$df = (k - 1 - c), \quad (2)$$

where  $k$  is the number of classes of tremor occurrence, and  $c$  is the number of estimated distribution parameters. At the confidence level  $\alpha = 0.05$  one can read  $\chi_a^2 = 0.59915$ . Therefore, the critical area is  $Q = [5.9915; \infty]$ . Thus, we have proceeded as follows:

1. when  $\chi_{obs}^2 \geq \chi_a^2$ , the hypothesis of distribution concordance was rejected,
2. when  $\chi_{obs}^2 < \chi_a^2$ , the hypothesis was accepted, that means, we had no statistical reasons to reject the hypothesis of concordance of both distributions (it is true in 90% confidence interval).

An example of statistical analysis is presented in Fig. 2.

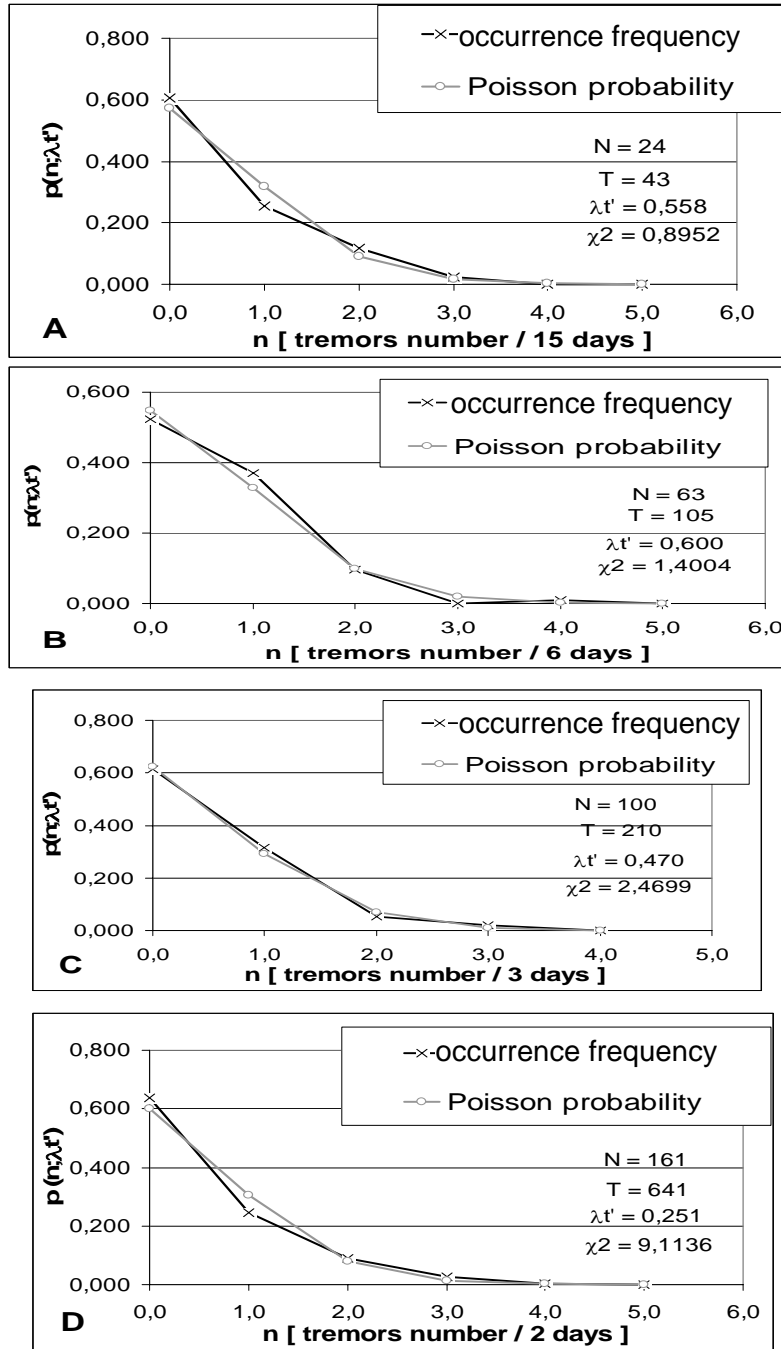


Fig. 2. Example of statistical analysis of the empirical frequency distribution concordance with Poisson distribution for the interval of average seismicity for discrimination levels of seismic energy  $E$ : A)  $E > 3 \cdot 10^5$  J, B)  $E > 1 \cdot 10^5$  J, C)  $E > 8 \cdot 10^4$  J, D)  $E > 5 \cdot 10^4$  J.  $N$  = number of tremors;  $T$  = number of time intervals of length  $t$ ;  $\lambda t'$  – occurrence of activity in period  $t'$ .

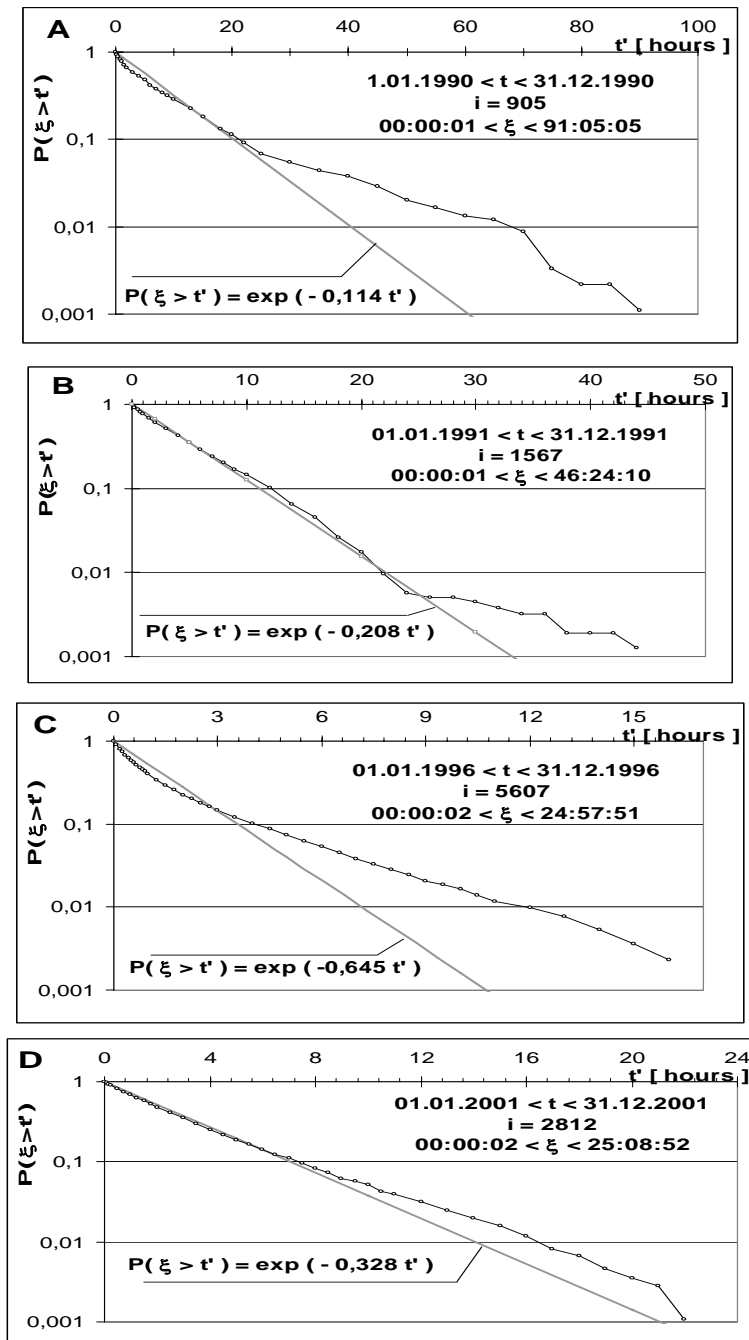


Fig. 3. Examples of the annual cumulated interevent time intervals distributions  $P(\xi > t')$  for the selected years of mining tremor sequences: A – 1990 and C – 1996 (the Kolmogorov test suggests to reject the concordance with exponential distribution); B – 1991 and D – 2001 (from the results of Kolmogorov tests there are no reasons to reject the hypothesis).

#### 4.2 Analysis of the interevent time from mine tremor sequence

The distributions of interevent time intervals have been analysed for successive years of mining (Fig. 3) as well as for the whole tremor sequence (Fig. 4). The concordance has been verified for both methods, that is:

- the distribution of interevent time intervals, and
- the comparison of the tremor occurrence frequency with the Poisson distribution.

The cumulative probability distributions  $P(\xi > t')$  representing the probability that expectation time  $\xi$  for tremor occurrence would be larger than  $t'$  are presented in semi-logarithmic scale. The  $P(\xi > t')$  values are obtained from

$$P(\xi > t') = \frac{i > t'}{i},$$

where  $i > t'$  is the number of interevent time intervals with  $\xi > t'$ , and  $i = n - 1$  is the total number of time intervals between two consecutive events.

In the figures the observed probability  $P(\xi > t')$  values are denoted by lines with triangles while the straight lines (in semi-log scale) denote the exponential distribution

$$P(\xi > t') = e^{-\lambda t'} \quad (3)$$

for the  $\lambda$  value determined from the tremor's statistics.

From the observed distributions of time intervals in successive years one can see that in some years (e.g., 1991, 2001) the empirical distribution  $P(\xi > t')$  fits the exponential distribution relatively well but in other periods (e.g., 1990, 1996) the deviation is large.

Figure 4 presents the observed distribution of  $P(\xi > t')$  for the whole mining tremor sequence of 1989-2004 for the Jas-Mos coal mine. Applying the Kolmogorov test we can confirm the concordance with exponential distribution at confidence level  $\alpha = 0.05$  ( $\lambda = [1.4652 \pm 0.091] < 1.36$ ).

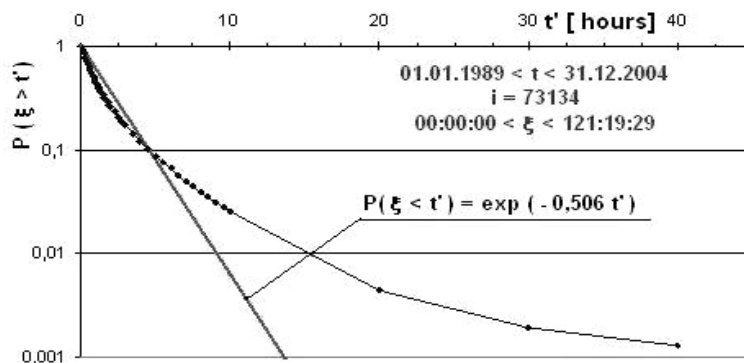


Fig. 4. Cumulative probability of interevent time distribution  $P(\xi > t')$  for 1989-2004 for the whole tremor sequence.

Then we made an analysis for the selected three periods of seismicity. The results are presented in Fig. 5: left panels show the frequency of occurrence distributions and the right panels the corresponding distributions of interevent time intervals  $P(\xi > t')$ . The  $\chi^2$  test indicates that when decreasing the seismic energy discrimination level, the value of  $\chi^2$  is increasing. This means that the concordance with Poisson distribution is decreasing. The same result can be observed on the time interval distributions – the increasing deviations from the exponential distribution, which is clearly seen from the Kolmogorov test (cf. Tables 1 and 2).

From the presented figures and results it can be concluded that the empirical tremor sequence can be considered as a Poisson distribution. This means that the tremor sequence is random. The randomness of tremor sequence indicates that basing on the information contained in that sequence only, the prediction of tremor occurrence is not possible. It is also seen that decreasing seismic energy discrimination level, the concordance with Poisson distribution is getting worse. Therefore, we may expect that below some specified seismic energy level we can look for some correlations (hidden relations) between tremor occurrence.

## 5. Discussion

Seismicity in underground mines is under the dominant influence of mining (Gibowicz and Kijko 1994). Large mining tremors may include non-reversible destructions in underground openings as well as in some cases may have unprofitable influence on structures located on the earth surface. Therefore, their prediction appears very important. In the deterministic sense the tremor prediction should include the determination of place (focal area), time of occurrence and tremor size. To be applicable, these data should be obtained quickly (Marcak and Zuberek 1994).

The reliability of statistical estimation of the probability of tremor occurrence depends on the amount and accuracy of a priori information used in prediction scheme and on the quality of data on which the prognosis is based.

Poissonian or non-Poissonian character of mining tremors sequence is a fundamental question in the problem of short-term or long-term prediction (Lasocki 1990, Marcak and Zuberek 1994, Gibowicz and Lasocki 2001).

Lasocki (1992) testing the Poissonian distribution of mine tremor generation has found that the Poissonian character of seismicity is observed in short time sequences and should be rejected for long complete series. It was also found that the series consisting only of large events tended to be Poissonian suggesting that the prediction of large events should be based on information carried by small events (Gibowicz and Lasocki 2001). Our results from the Jas-Mos coal mine support this hypothesis and indicate that above some seismic energy level the time distribution of mining tremors is approaching the Poisson process. From the assumptions of the Poissonian character of the process, one can conclude that the tremor occurrence is purely random. Therefore, using this tremor sequence we are not able to predict their occurrence. Increasing the detection range of seismic network and decreasing the seismic energy discrimination level we can look for some relations allowing the prediction in

the way similar to Kornowski's (2002) formulation. Further development of such models may help to find the best way to the proper formulation of the dilemma of the tremor prediction.

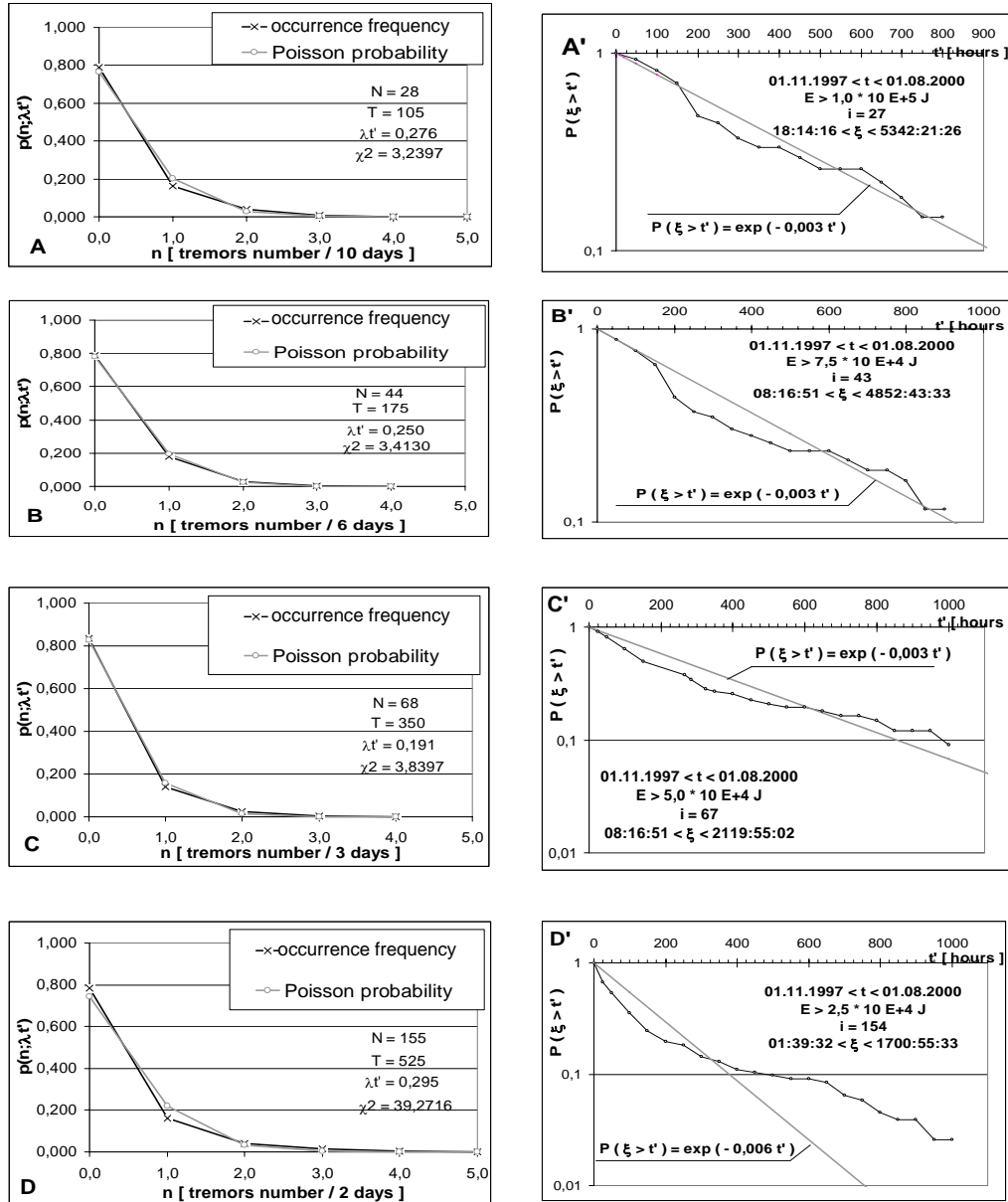


Fig. 5. Comparison of the frequency of occurrence distributions  $p(n; \lambda t')$  and cumulated distributions of the interevent time intervals  $P(\xi > t')$  for decreasing levels of seismic energy distribution  $E$  (high seismicity period): A)  $E > 1 \cdot 10^5$  J, B)  $E > 7,5 \cdot 10^4$  J, C)  $E > 5 \cdot 10^4$  J, D)  $E > 2,5 \cdot 10^4$  J.

Table 1

Statistical analysis of the empirical occurrence frequency distribution of tremors with Poisson distribution using  $\chi^2$  test at confidence level  $\alpha = 0.05$  (in all cases  $df = 2$ ),  
 $N$  – number of tremors,  $T$  – number of time intervals of length  $t$

Whole sequence				
Energy $E$ [J]	$\chi^2$	$\lambda t' = N/T$	$N$	$T$
$8.6 \times 10^5$	1.0642	0.810	13	16
$7.3 \times 10^5$	3.7646	0.343	22	64
$4.5 \times 10^5$	<b>11.7752</b>	0.097	56	576
Low seismicity				
$1.0 \times 10^5$	0.1092	0.730	16	22
$7.0 \times 10^4$	0.8803	0.510	34	66
$4.5 \times 10^4$	0.9522	0.424	56	132
$3.0 \times 10^4$	1.8599	0.377	83	220
$1.5 \times 10^4$	<b>9.2800</b>	0.257	172	669
Average seismicity				
$3.0 \times 10^5$	0.8952	0.558	24	43
$1.0 \times 10^5$	1.4004	0.600	63	105
$8.0 \times 10^4$	2.4699	0.470	100	210
$5.0 \times 10^4$	<b>9.1136</b>	0.251	161	641
High seismicity				
$1.0 \times 10^5$	3.2397	0.276	28	105
$7.5 \times 10^4$	3.4130	0.250	44	175
$5.0 \times 10^4$	3.8397	0.191	68	350
$2.5 \times 10^4$	<b>39.2716</b>	0.295	155	525

## 6. Conclusions

1. On the basis of statistical analysis of mining tremor occurrence at the Jas-Mos coal mine we are able to determine discrimination levels of seismic energy  $E$  for three selected periods of seismicity:

- low seismicity  $E > 3.0 \cdot 10^4$  J (6.9 tremors per month)
- average seismicity  $E > 7.0 \cdot 10^4$  J (13.4 tremors per month)
- high seismicity  $E > 5.0 \cdot 10^4$  J (5.7 tremors per month)

Above these levels, the tremor frequency occurrence approaches the Poisson process.

2. From conclusion (1) it follows that in these periods, above the specified energy discrimination levels, one cannot determine any correlations enabling unique description of tremors generation. Therefore, the tremor prediction on the basis of

Table 2

Results of Kolmogorov tests for cumulated interevent time intervals distributions for selected three periods of seismicity at confidence level  $\alpha = 0.05$  ( $F_i(x)$  – empirical distribuant;  $F_0(x)$  – hypothetic distribuant;  $\Delta\lambda$  – measurement fault  $\lambda$ )

$\sup  F_i(x) - F_0(x)  = D$	$N$	$A = D\sqrt{N}$	$\Delta\lambda$	Critical level for $\alpha = 0.05$ is $\lambda_\alpha = 1.36$
Whole sequence				
0.1312	12	0.4548	0.1003	$H_0$ – accepted
0.2963	21	1.3579	0.1296	$H_0$ – accepted
0.2986	55	2.2142	0.1235	$H_0$ – rejected
Low seismicity				
0.1488	15	0.5763	0.080	$H_0$ – accepted
0.1206	33	0.6929	0.043	$H_0$ – accepted
0.0831	55	0.6159	0.039	$H_0$ – accepted
0.1004	82	0.9094	0.043	$H_0$ – accepted
0.1009	171	1.3193	0.043	$H_0$ – rejected
Average seismicity				
0.0796	23	0.3818	0.035	$H_0$ – accepted
0.0553	62	0.4354	0.036	$H_0$ – accepted
0.0340	99	0.3427	0.015	$H_0$ – accepted
0.1115	160	0.1410	0.041	$H_0$ – rejected
High seismicity				
0.1250	27	0.6498	0.053	$H_0$ – accepted
0.1646	43	1.0789	0.064	$H_0$ – accepted
0.1744	67	1.4178	0.067	$H_0$ – accepted
0.1982	154	2.4591	0.089	$H_0$ – rejected

tremor sequence observations only cannot be achieved because of their random occurrence.

3. Below these seismic energy discrimination levels (this means, increasing the detectability of seismic network) one may look for some hidden rules (correlations) influencing the tremor occurrence and possibly their prediction.

4. In the tested tremor sequences the concordance of the frequency of tremor occurrence distribution with the Poisson distribution is well confirmed by the distributions of interevent time intervals. In case of their randomness, these distributions are approaching the exponential distribution.

## References

- Fisz, M., 1969, *Rachunek prawdopodobieństwa i statystyka matematyczna*, Warszawa, PWN.
- Gibowicz, S.J., and A. Kijko, 1994, *An Introduction to Mining Seismology*, Academic Press, San Diego, New York.
- Gibowicz, S.J., and S. Lasocki, 2001, *Seismicity induced by mining – 10 years later*. Adv. in Geophysics **44**, Academic Press, San Diego, New York.
- Gnedenko, B., 1969, *The theory of probability*, Mir Publishers, Moscow.
- Jakubów, A., 2001, *Badania geofizyczne w kopalniach ROW*, Badania geofizyczne w kopalniach, Wyd. IGSMiP PAN Kraków, 501-515.
- Jasiulewicz, H., i W. Kordecki, 2001, *Rachunek prawdopodobieństwa i statystyka matematyczna*, Oficyna Wydawnicza GiS, Wrocław.
- Kornowski, J., 2002, *Podstawy sejsmoakustycznej oceny i prognozy zagrożenia sejsmicznego w górnictwie*, Główny Instytut Górnictwa, Katowice.
- Kotas, A., 1985, *Uwagi o ewolucji strukturalnej GZW*. W: Mat. Konf. „Tektonika GZW”, Wyd. Uniw. Śląskiego Sosnowiec, 17-46.
- Lasocki, S., 1990, *Prognoza silnych wstrząsów górniczych*, Zeszyty Naukowe AGH, seria Geofizyka stosowana 7, Kraków.
- Lasocki, S., 1992, *Non-Poissonian structure of mining induced seismicity*, Acta Montana **84**, 51-58.
- Marcak, H., i W.M. Zuberek, 1994, *Geofizyka górnicza*, Śląskie Wydawnictwo Tech. Katowice, 127-165.
- Pierwoła, J., 1998, *Geologiczne uwarunkowania rozkładów energetycznych wstrząsów indukowanych działalnością górnictwem na Górnym Śląsku*. Uniw. Śl. Wydział Nauk o Ziemi Sosnowiec – Praca doktorska (niepublikowana).
- Zuberek, W.M., 1973, *Sejsmoakustyczna charakterystyka pęknięcia kalizny węglowej pod wpływem strzelań wstrząsowych* – Praca GIG, Komunikat nr 595, Katowice.

Accepted 13 June 2006

## **Focal Mechanisms of Mining Induced Seismic Events: Reliability of the Solutions**

Ryszard DUBIEL and Agnieszka GÓRKA

University of Silesia, Faculty of Earth Sciences  
Department of Applied Geology  
ul. Będzińska 60, 41-200 Sosnowiec, Poland

### **A b s t r a c t**

Focal mechanisms of 168 mining induced seismic events that occurred in the Halemba coal mine area (Upper Silesian Coal Basin, Poland) were determined using the seismic moment inversion method. 38 seismic events were studied in detail. For 12 tremors, non-double couple components were dominant in seismic moment tensor. Focal mechanisms of 38 tremors were repeatedly recalculated for gradually changing vertical Z coordinate values to obtain the maximum double couple seismic moment tensor component. The high value of non-shearing components in seismic moment tensor is probably a result of inaccurate localization. The non-double couple mining induced seismic events are not so common in the USCB as previous studies suggested.

### **1. Introduction**

Focal mechanisms of underground mining induced seismic events are mostly related to shearing process and double-couple (DC) seismic moment tensor component. However, there are many publications reporting that other focal mechanisms are possible (Feignier and Young 1992, Stickey and Sprende 1993). They are related to cavity collapse, pillar burst or tensial fault (Hasegawa et al. 1989) and their common feature is the high value of isotropic (I) or compensated linear vector dipole (CLVD) components.

The high value of non-double couple components can also be a result of improper distribution of seismic network. If seismometers are not distributed around the focal source (poor coverage of focal sphere), it is possible that not all of the components of force acting in the source are recognized (Dubiel 1996).

Furthermore, inaccurate localization of the source may influence the quality of focal mechanism estimation. This concerns particularly the vertical coordinate  $Z$  of seismic source (Dubiel 2003).

For seismicity observed in Upper Silesian Coal Basin (USCB) the number of seismic events with non-double couple focal mechanisms exceeds 30% (Sagan and Dubiel 1996). Considering the longwall opening exploitation system applied in the USCB mines, so large number of non-shearing seismic events seems to be difficult to explain.

The goal of the present study was to determine the reliability of focal mechanisms solutions and to estimate the relation between the value of vertical coordinate  $Z$  and the percentage share of DC component of seismic moment tensor.

## 2. The results

The series of 168 seismic events induced in the Halemba coal mine (USCB) was studied. The energy range of the events was 1÷700 kJ. All the events were recorded by local, underground seismic network consisting of 16 vertical seismometers. The localizations of the seismic events were determined by mine seismological staff with standard procedure.

Focal mechanisms of all the seismic events were calculated using the seismic moment tensor inversion method. The inversion was executed for P-wave first motion, in time domain, according to linear L1 and square L2 norms.

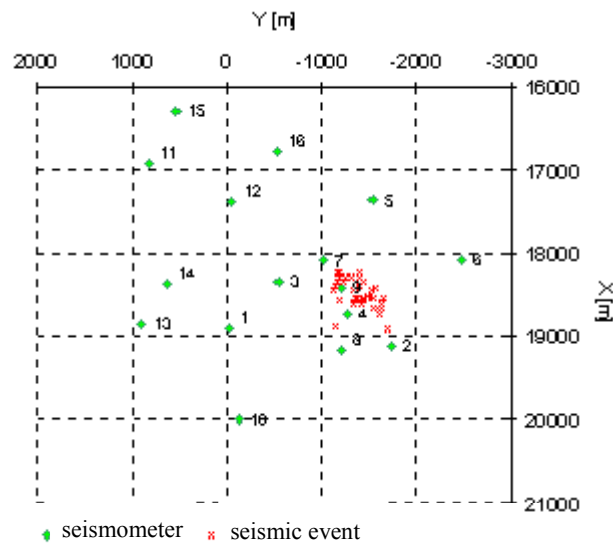


Fig. 1. Spatial distribution of 38 studied seismic events in relation to seismic network.

To obtain the most reliable focal mechanism solutions, the following seismic events were excluded:

- events with the low-quality records,
- events which differed in focal mechanism solutions according to L1 and L2 norms,
- events whose sources were localised outside the seismic network area.

The consequence of the selection was the rejection of 130 tremors. For 26 of the remaining 38 tremors, the dominant double couple component was observed. The average share of DC component was 55%. The spatial distribution of 38 studied seismic events in relation to seismic network is presented in Fig. 1.

Next, the focal mechanisms of all 38 seismic events were recalculated repeatedly for various Z-coordinate values. The value of vertical coordinate Z had been increased and decreased by 5 m in consecutive calculations until the maximum value of double couple component was achieved. The total number of calculations was 833. The example of recalculations for one seismic event is presented in Table 1. The table shows that the initial value of the percentage share of DC component increased from 32.2 to 97.7%

Table 1

An example of seismic moment tensor recalculations for one seismic event

Z coordinate [m]	Isotropic component [%]	CLVD component [%]	DC component [%]
<b>-498</b>	<b>13.4</b>	<b>54.4</b>	<b>32.2</b>
-508	11.08	50.2	38.1
-533	12.9	48.4	38.8
-558	5.1	26.4	68.5
-583	2.6	3.6	93.8
-593	0.6	2.6	96.8
<b>-598</b>	<b>0.3</b>	<b>2.1</b>	<b>97.7</b>
-603	1.6	0.8	97.5

For all 38 studied seismic events, the value of DC component significantly increased and exceeded 50%. Its average value was 79%. For most seismic events the maximum percentage share of DC component was achieved in the range  $\pm 100$  m but the maximum change of Z coordinate value was 300 m.

The spatial orientations of nodal planes for optimized focal mechanisms are presented in the Fig. 2. The orientations are closely related to N-S, NE-SW and NW-SE fracture orientations previously observed and measured in the rock mass.

The study revealed that the mining seismic events are induced in various and instantaneously changing stress conditions. Variation of state of stress manifests itself

by inducing the tremors related to various faulting processes. 21 studied seismic events were relevant to normal, 15 to reverse and 2 to strike-slip faulting (Fig. 3). The seismic events of various focal mechanisms were induced close each other in time and space alike.

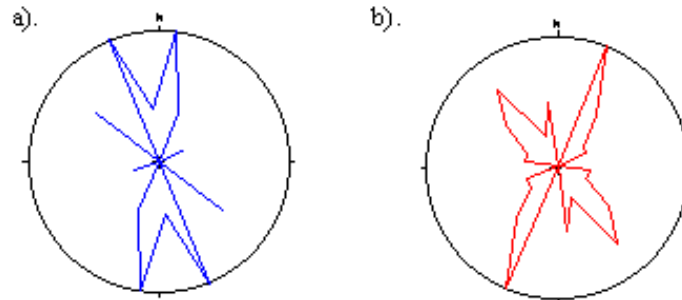


Fig. 2. Spatial orientations of nodal planes for optimized focal mechanisms solutions: (a) A-nodal plane, (b) B-nodal plane.

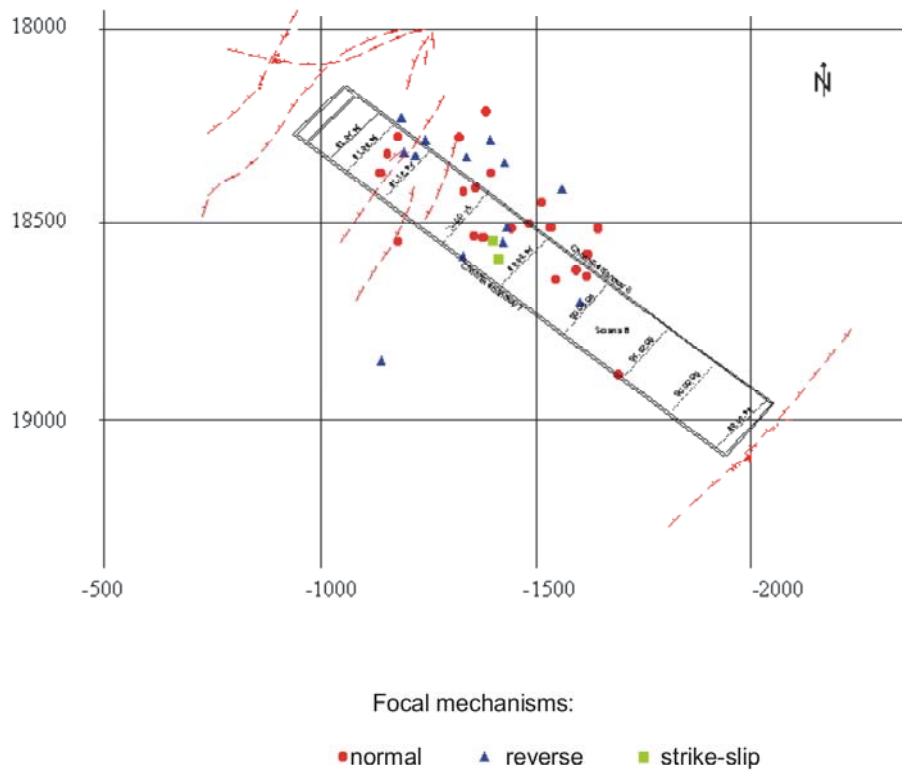


Fig. 3. Focal mechanisms of studied seismic events in relation to mining and geological conditions.

### 3. Conclusions

1. The non-double couple mining induced seismic events are not so common in the USCB as previous studies suggested.
2. The high value of non-shearing components in seismic moment tensor is probably a result of inaccurate localization, especially of the vertical coordinate  $Z$ .
3. The seismic events related to normal, reverse and strike slip faults were observed. These seismic events occur close to each other.
4. The spatial orientation of nodal planes is closely related to spatial orientation of fractures in the rock mass.
5. Assuming that the shearing process is the most reliable focal mechanism for seismicity in the USCB, the percentage share of non-double couple components can be applied for estimation of the accuracy of vertical localization of seismic events foci. Thus, the high value of non-double couple component may indicate inaccuracy of vertical localization.

### References

- Dubiel, R., 1996, *The influence of the seismic mine network distribution on the solutions of focal mechanisms*, Tectonophysics of Mining Areas, University of Silesia, Katowice, 189-195.
- Dubiel, R., 2003, *Non-double couple induced seismic events*, Sbornik vedeckich praci, Technical University Ostrava **2**, 61-66.
- Feignier, B., and R.P. Young, 1992, *Moment tensor inversion of induced microseismic events: Evidence of non-shear failures in the  $-4 < M < -2$  moment magnitude range*, Geophys. Res. Lett. **19**, 1503-1506.
- Hasegawa, H.S., R.J. Wetmiller and D.J. Gendzwill, 1989, *Induced seismicity in mines in Canada – an overview*, Seismicity in Mines, Pure and Appl. Geophys. **129**, 423-453.
- Sagan, G., and R. Dubiel, 1996, *Mining tremors mechanisms in the western zone of Klodnica fault*, Acta Montana, ser. A, No 10 (102), 25-30.
- Stickney, M.C., and K.F. Sprenke, 1993, *Seismic events with implosional focal mechanisms in the Coeur d'Alene mining district, Northern Idaho*, J. Geophys. Res. **98**, 6523-6528.

*Accepted October 16, 2006*



## Short-Term Prediction of Approximate Probability of Rockburst

Jerzy KORNOWSKI

Central Mining Institute  
Department of Geology and Geophysics  
Plac Gwarków 1, 40-166 Katowice, Poland  
e-mail: bhxjk@gig.katowice.pl

### Abstract

A new, approximate but formal predictor of rockburst probability has been presented. Given the predicted values of the mean and variance of the total (AE + tremors) energy that will be emitted from a well-defined time ( $t, t+\Delta t$ ) and space (S) region – which are obtainable with the known linear prediction algorithm – it allows to predict the rockburst probability in the same (time and space) region. The region S has to be observed with the seismic and seismoacoustic sensors, cumulated (AE + tremors) energies during the consecutive  $\Delta t$  periods have to be estimated, and the time series of  $E^c(t) = E^{AE}(t) + E^{trem}(t)$  then formed allow the prediction of  $E^c(t+1)$  mean and variance. With these values calculated, simple integration (eq. 4.2) allows us to predict the total probability of rockburst. The quality of prediction depends mainly on the quality of the AE and tremors observation.

### 1. Introduction and notation

A few years ago, a team from the Seismoacoustic Laboratory of the Central Mining Institute – with geophysicists from a few coal mines – has implemented the sequential (i.e. issued at the consecutive time intervals  $t_i = t_0 + iT$ ,  $i = 1, 2, \dots$ ;  $T = \text{const.}$ , e.g.  $T = 1$  hour) prediction method. The method probabilistically predicts – given the AE and tremors observations – the cumulated (logarithmic) total seismic energy {denoted, equivalently, as  $E(t) \equiv E_{T,S} \equiv \log E^C[(t, t+T), S]$ } which will be emitted from the (observed with AE and seismic sensors) space segment S (e.g., a long-wall) during a time period  $T = (t_i, t_i + T)$  – see Kornowski (2003a,b), Kurzeja (2004), Kornowski and Kurzeja (2005), Surma and Kornowski (2002), where the prediction algorithm and examples can be found.

**The total energy ( $E^C$ )** is estimated as a sum of AE ( $E^{AE}$ ) and tremors ( $E^W$ ) energies

$$E^C(t) = E^{AE}(t) + E^W(t). \quad (1.1)$$

By **probabilistic prediction** we mean the prediction of the mean value,  $\bar{E}(t+1)$ , and variance  $\sigma_E^2(t+1)$  of the  $E^C(t+1)$ , with  $T$  considered as the time unit ( $T = 1$ ).

It should be noted that the total  $E_{T,S}(t+1)$  energy prediction is a serious departure from the so desired by miners prediction of the “time, space and energy of the approaching strong tremors” but, as Lomnitz (1994, p. 3) noted “earthquake prediction (in the sense of forecasting the date, location and magnitude) is not feasible today”, and the same concerns mining tremors, while the total energy prediction in the predetermined time period and space segment is possible and not very difficult.

It is obviously not the same thing to predict the time, space and energy of the event and to predict the total emission energy in the known ( $T, S$ ) period of time and region of space, but note that as  $T \rightarrow 0$  they – asymptotically – become identical, so that optimizing the “sampling interval”  $T$  can bring them closer. In practice, unfortunately,  $T$  cannot be too short because the estimation variance grows up with decreasing  $T$ . This is the known “resolution versus variance” problem (see also the discussion in Section 3). Anyway, in the author’s opinion, the departure from the futile (time, space and energy) prediction attempts is the price to be paid for any useful seismic hazard prediction.

As many examples suggest (e.g. Kurzeja 2004), the predicted logarithmic total energy  $E(t)$  can be usefully – but not very closely – approximated with the time varying normal density  $N(\bar{E}(t+1), \sigma_E^2(t+1))$  and its error – with the density  $N(0, \sigma_E^2(t+1))$ . Parenthetically, this means also that the original (before taking logarithm) total energy can be approximated with the lognormal density (which is leptokurtic and “fat-tailed” but of finite variance). Approximating the prediction errors (on the logarithmic energy scale) with the normal distribution of known (predicted) mean value  $\bar{E}(t+1)$  and variance  $\sigma_E^2(t+1)$  is equivalent to prediction of the time-varying probability density  $p_E(t)$

$$p_E(t) = \left[ \sigma_E(t) \sqrt{2\pi} \right]^{-1} \exp[-(E(t) - \bar{E})^2 / 2\sigma^2(t)] \quad (1.2)$$

and allows us to (approximately) predict all the useful statistical information, for example, the limits of ( $\alpha\%$ ) confidence intervals for the predicted energy and/or the exceedance probability for the predetermined “safety threshold”  $E_g$  (e.g.  $E_g = 1 \cdot 10^5$  J), which can depend on local conditions (Dubínski and Konopko 2000, Table 5.4 therein). This exceedance probability is called the seismic hazard  $Z^S$ :

$$0 \leq Z_{T,S}^S(t+1) = P[E_{T,S}(t+1) > E_g] \leq 1 \quad (1.3)$$

where  $P[\bullet]$  is the probability of the event  $[\bullet]$ .

If the “space” ( $0 \div 1$ ) of possible seismic hazard is divided into a few “sub-spaces”, as, for example, ( $0-10^{-5}$ ,  $-10^{-4}$ ,  $-10^{-3}$ ,  $-1$ ) that are denoted (a, b, c, d), respectively, and called “the states of seismic hazard” – with connected preventive action – the users need not speculate “what should I do with this probability”. At the same time, the states of seismic hazard obtain a strict physical meaning, becoming – despite approximations – useful in practice and in the theory. It would be even more useful if one could – with comparable effort – predict the probability  $P_{T,S}^{T!}(t+1)$  of rockburst (T!) in the  $[(t, t+T), S]$  “space-time” region. A method which allows this prediction is described below.

In the sequel, “T!” symbolizes a rockburst, both  $P^{T!}$  and  $P(T!)$  mean the rockburst probability,  $P(T!|\bullet)$  is the conditional probability of rockburst, conditioned on the event “ $\bullet$ ”. Both the probability and the energy are always connected to the well defined time and space region (T, S), which must be observed with AE and seismic networks. It is also assumed that AE and tremors energies are additive (measured with identical physical units) and that normal approximation (of predicted energy) is considered useful.

Rockburst is defined here as the mining-induced tremor with results (catastrophic or fatal) recorded and refunded by an insurance company.

## 2. A Known Mathematical Theorem

Old and known mathematical theorem on “total probability” (e.g. Feller 1966, Chung 1974, Fisz 1969) should be shortly reminded here, as it is the most important instrument to derive the rockburst probability predictor. Chung (1974) states it in a concise manner: “Suppose that  $\Omega = \sum_n A_n$  is a partition of the sample space into dis-

joint sets. Then for any set B we have:  $P(B) = \sum_n P(A_n)P(B|A_n)$ ”. In our applications

“the sample space” is the logarithmic energy axis, from  $-\infty$  to  $+\infty$  (or, in practice, say, from 0 to 10, meaning energies from  $10^0$  J to  $10^{10}$  J). The “partition  $\Omega$ ” means the division of axis into unit segments (...0–1–2–...–9–10...). Putting into Chung’s equation T! instead of B and energy interval  $\varepsilon_j (=10^j \div 10^{j+1}$  J) instead  $A_n$ , for  $n=11$  we write

$$P(T!) = \sum_{j=0}^{10} P(\varepsilon_j)P(T!|\varepsilon_j). \quad (2.1)$$

For decreasing intervals  $\varepsilon_j$  it can be formally derived that

$$P(T!) = \int_{-\infty}^{\infty} p(E)P(T!|E)dE \quad (2.2)$$

and this form of total probability theorem can be found, e.g. in Fisz (1969 p. 62). Note that  $p(E)$  is the probability density (of, e.g., predicted energy if we are interested in prediction) and  $P(T!|E)$  is the conditional probability of rockburst if the E event occurred.

### 3. Conditional Probability of Rockburst

Conditional probability  $P(T!|E)$  of rockburst – provided the tremor  $E$  has occurred – can be approximated with the published statistics of rockbursts and tremors in the Polish mining industry (e.g. Konopko (ed.) 1998, ..., 2002, Barański 2003, Barański et al. 1999). Approximating further, we identify here the tremor energy  $E$  with the total energy emitted during the time interval  $T$ . Approximation is the better the shorter is  $T$  and the higher is  $E$ ; for  $h=1$  hour and  $E \approx 1 \cdot 10^4$  J the approximation is often rather poor, but such energies are of minor importance for rockburst probability estimation.

Given the  $N(\varepsilon_j)$ , the number of tremors in the  $\varepsilon_j=(10^j \div 10^{j+1})$  J energy interval and the  $N(T!, \varepsilon_j)$ , the number of fatal rockbursts accompanied by the tremor of energy  $\varepsilon_j$ , the conditional probability  $P(T! | \varepsilon_j)$  can be estimated with the known (e.g. Feller 1966) formula

$$P(T!|\varepsilon_j) = \frac{N(T!, \varepsilon_j)}{N(\varepsilon_j)} \quad (3.1)$$

The above mentioned statistics of rockbursts and tremors allows to calculate values of  $P(T! | \varepsilon_j)$  for various  $\varepsilon_j$ 's and to tabulate the results in the form of simple Table 1.

Table 1  
Conditional probabilities of rockburst

Energy $\varepsilon_j$	$10^4$ J	$10^5$ J	$10^6$ J	$10^7$ J	$10^8$ J	$10^9$ J
$P(T!   \varepsilon_j)$	$\sim 10^{-4}$	$3 \cdot 10^{-3}$	0.017	0.086	–	1

( $\varepsilon_j^- = 1 \cdot 10^j$  J, the lower limit of the  $\varepsilon_j$  energy interval).

Some remarks should be added here:

1. Both the lowest and the highest probabilities are uncertain.
2. Statistics used to estimate probabilities involve eleven years (1992–2002) and the whole Polish mining industry. They are quickly becoming outdated.
3. If the probabilities are to be used in formula (2.2) to sequentially (every hour) predict rockburst probability, they may be considered constant for an extended period of time (e.g. for a year).

The data in Table 1 are not sufficient to put forth a functional relationship – connecting energy  $E$  and conditional rockburst probability – that is needed in (2.2), but it is known both from the theory and from practice, that

$$P(T!|E) \rightarrow 0 \quad \text{as } E \rightarrow 0 \quad (3.2a)$$

$$P(T!|E) \rightarrow 1 \quad \text{as } E \rightarrow \infty \quad (3.2b)$$

so that the functional relationship has two horizontal asymptotes and, by necessity, the smooth, sigmoidal shape. Even this is not enough, but we can reasonably approximate the  $P(T! | E)$  relation with the known “logistic” curve in parametric form

$$P(T!|E) = \{1 + \exp[-\alpha(\log E - \beta)]\}^{-1} \quad (3.3a)$$

and with the data of Table 1 roughly estimate the  $(\alpha, \beta)$  parameters, obtaining  $\alpha \approx 2,3$ ,  $\beta \approx 8$  and the (very approximate only) relation

$$P(T!|E) = \{1 + \exp[-2,3(\log E - 8)]\}^{-1} \quad (3.3b)$$

odd on the logarithmic energy scale and with the reflection point at  $\beta$  (where  $P = 0,5$ ).

This relation can be updated when the new data are available, and fitted to any local conditions (i.e., for a given coal mine) if there are sufficient data. It is not clear at this moment what are the optimal time ( $W_t$ ) and space ( $W_s$ ) data windows to estimate „current and locally-fitted” probabilities  $P(T! | E)$ ; in this paper, just the whole available information is used, but no doubt it is partly obsolete and highly averaged/smoothed in space. On the other hand, it is known (e.g., Claerbout 1976, p. 70-75) that decreasing the window span decreases the number of observations and increases the variance  $\sigma_e^2$  (or error) of estimation: if we estimate a parameter (e.g., local mean value) of a space-and-time varying process (e.g. seismic emission), the form of “uncertainty principle” applies

$$\sigma_e^2 \geq \text{const} \cdot (W_t W_s)^{-1} \quad (3.4)$$

excluding the ideal estimation of space, time and the mean value of the process magnitude simultaneously. This also means that locally optimal parameters of  $W_t W_s$  can and should be looked for, both in the problem of  $P(T! | E)$  estimation and in the problem of estimation and prediction time resolution mentioned in Section 1.

#### 4. Rockburst Probability

As has been stated, the linear prediction algorithm sequentially (e.g., every hour) predicts the values  $\bar{E}(t+1)$  and  $\sigma_E^2(t+1)$  for the observed region  $S$  and time period  $T$  and it is possible to approximate the predicted energy (and prediction error) with the normal density (1.2) on the logarithmic energy scale – so that we are given explicit formula for  $p(E)$  in eq. (2.2). Inserting then (1.2) and (3.3b) into (2.2) with explicit time dependence, the approximate **predictor of rockburst probability** can be written as

$$P^{T!}(t+1) = \left[ \sigma_E(t+1) \sqrt{2\pi} \right]^{-1} \int_{-\infty}^{\infty} \frac{\exp[-(E - \bar{E}(t+1))^2 / (2\sigma_E^2(t+1))]}{1 + \exp[-2,3(E - 8)]} dE \quad (4.1)$$

where  $E \equiv \log E^c[(t_i, t_{i+1}), S]$  is the cumulated in  $(T, S)$  total logarithmic energy (of the far-field seismic waves). At the moment  $t_i$ , all the necessary data are available and the approximate probability of rockburst can be predicted. The quadrature (i.e. numerical integration) in (4.1) is, in fact, very easily calculable with the Romberg algorithm or even – due to very smooth shape of (4.1) – with the (much cheaper) simple 7-term Gaussian formula.

As the rockburst probability obeys the inequalities

$$0 \leq P^{T^i}(t) \leq 1 \quad (4.2)$$

exactly as in the case of seismic hazard mentioned earlier, the notion of **rockburst hazard**  $P^{T^i}$  can now be defined as the probability of rockburst in  $(T, S)$ . The “hazard space”  $(0,1)$ , can be divided into subspaces called “states” and denoted, for example,  $(A, B, C, D)$  with some preventive action connected to any state. Likewise in the case of seismic hazard, the states of rockburst hazard have now the well defined physical meaning and allow immediate decision taking.

Note that for probability  $P(t)$  constant in the time interval  $(t_i, t_i+T)$ , the conditional probability “on condition that nothing happened so far” – usually called “the hazard function” – is not more informative than  $P(t)$ .

It is the author’s duty to remind that many approximations have been applied while deriving the predictor (4.1). It is a crude and simple predictor, but any approximation creates both an error and opportunity for improvement. Especially the mining geophysicist should always be aware that no energy prediction (crucial in formula (4.1)) can be better – more exact – than the energy observations are. Probably, the most important point is that (4.1) is just a statistical formula and is useful only in a statistical sense: it guarantees nothing on any single case. But – in the author’s opinion – is much better than nothing.

## 5. Conclusions

1. In this paper a new, approximate and simple (statistical) predictor of rockburst probability (4.1) has been derived.
2. The predictor can be used – for given, observed region  $S$  (e.g., a longwall) – sequentially, every time unit  $T$  (e.g.,  $T = 1$  hour) issuing the new predicted probability of rockburst.
3. The rockburst probability can be identified as the rockburst hazard. The space  $(0 - 1)$  of possible hazard values can be divided into subspaces (e.g.,  $0 - 10^{-5} - 10^{-4} - 10^{-3} - 1$ ) called „the states of rockburst hazard” and denoted  $A, B, C, D$  states. This way, the states obtain a clear physical meaning, at the same time being operational.
4. The prediction is possible if the region  $S$  (e.g., a longwall) is observed with seismoacoustic and seismic networks, both AE and tremors energies are estimated during the time unit  $T$  and are additive, and the method (computer program) of linear prediction works, predicting the  $\bar{E}(t+1)$  and  $\sigma_E^2(t+1)$  values.
5. Predictions are based on previous observations. Mean (squared) energy prediction error cannot be smaller than the mean (squared) energy observation error.

## Reference

- Barański, A., 2003, *Analiza zmian stanu zagrożenia tąpnięciami w latach 1994 – 2003 w kopalniach tworzących obecnie Kompanię Węglową S.A. Tąpnięcia '2003*, GIG, Katowice.
- Barański, A., A. Barańska and W. Etryk, 1999, *Kształtowanie się zagrożenia tąpnięciami w polskich kopalniach węgla kamiennego w latach 1994 – 1998. Tąpnięcia '1999*, GIG, Katowice.
- Claerboat, J., 1976, *Fundamentals of Geophysical Data Processing*, Mc Graw-Hill, New York.
- Chung, K.L., 1974, *Elementary probability theory*, Springer – Verlag, New York.
- Dubiński, J., and W. Konopko, 2000, *Tąpnięcia – ocena, prognoza, zwalczanie*, GIG, Katowice
- Feller, W., 1966, *Wstęp do rachunku prawdopodobieństwa*, WNT, Warszawa.
- Fisz, M., 1969, *Rachunek prawdopodobieństwa i statystyka matematyczna*, PWN, Warszawa.
- Konopko, W. (red.), 1998, ..., 2002, *Raport roczny o stanie podstawowych zagrożeń naturalnych i technicznych w górnictwie węgla kamiennego*, GIG, Katowice.
- Kornowski, J., 2003a, *Linear Prediction of Hourly Aggregated AE and Tremors Energy Emitted from a Longwall and its Performance in Practice*, Arch. Min. Sci. **48**, 3, 315-337.
- Kornowski, J., 2003b, *Linear prediction of aggregated seismic and seismoacoustic energy emitted from a mining longwall*, Acta Montana, seria A, No. 22 (129), 5-14.
- Kornowski, J., and J. Kurzeja, 2005, *Krótkookresowa prognoza indukowanego zagrożenia sejsmicznego w górnictwie*, Prace Naukowe GIG – Górnictwo i Środowisko, Nr 1.
- Kurzeja, J., 2004, *Sekwencyjna prognoza emisji sejsmicznej generowanej eksploatacją pokładu węgla*, praca doktorska (niepubl.), GIG, Katowice.
- Lomnitz, C., 1994, *Fundamentals of Earthquake Prediction*. J. Wiley, New York.
- Surma, A., and J. Kornowski, 2002, *Liniowa prognoza zagrożenia sejsmicznego – na podstawie obserwacji w rejonie ściany 37 w pokł. 501 kopalni "Wesola"*. WUG – Bezpieczeństwo pracy i ochrona środowiska w górnictwie, Nr 12, 28-31

Accepted October 16, 2006

## KRÓTKOTERMINOWA PROGNOZA PRAWDOPODOBIEŃSTWA TĄPNIĘCIA

### Streszczenie

W artykule przedstawiono nowy, przybliżony lecz formalny predyktor prawdopodobieństwa tąpnięcia. Prognoza może być powtarzana sekwencyjnie co  $\Delta t$  (np. co godzinę) i dotyczy zawsze okresu  $(t, t+\Delta t)$  oraz obszaru  $S$  – np. ściany – który objęty musi być obserwacją sejsmoakustyczną i sejsmologiczną. Zakłada się że w chwili  $t$  znana jest całkowita energia  $E^c$  (będąca sumą energii AE i wstrząsów) z okresu  $(t-\Delta t, t)$  i okresów wcześniejszych, co umożliwia konstrukcję odpowiednich szeregów

czasowych energii i że znany algorytm prognozy liniowej umożliwia – na podstawie tego szeregu czasowego „obserwacji” – prognozę wartości średniej i wariancji energii  $E^c$  która wyemitowana będzie z obszaru  $S$  w okresie  $(t, t+\Delta t)$ . Dane te wystarczają, by – znając prawdopodobieństwo warunkowe  $P(T|E)$  – za pomocą operacji całkowania (4.2) po „przestrzeni” możliwych energii obliczyć całkowite prawdopodobieństwo tąpnięcia w okresie  $(t, t+\Delta t)$  w obszarze  $S$ . Jakość prognozy zależy przede wszystkim od jakości obserwacji i estymacji energii AE i wstrząsów.

## **Resampling Methods for Improving the Accuracy of Probabilistic Seismic Hazard Analysis**

Beata ORLECKA-SIKORA

Department of Geophysics,  
Faculty of Geology, Geophysics and Environmental Protection,  
AGH University of Science and Technology,  
al. Mickiewicza 30, 30-059 Kraków, Poland  
e-mail: orlecka@geol.agh.edu.pl

### **A b s t r a c t**

The cumulative distribution function (cdf) of the magnitude or energy of seismic events is one of the most important probabilistic characteristics in the Probabilistic Seismic Hazard Analysis. The probability distribution function (pdf) of the seismic events magnitude can be estimated through the parametric approach where the magnitude distribution model comes from the Gutenberg–Richter relation or the nonparametric approach using the kernel density estimators. In the nonparametric case, the pdf of the magnitude density estimator is unknown so the confidence intervals of the magnitude cdf are unable to be calculated using the classical methods of mathematical statistics. The evaluation of the magnitude cdf amounts to the point estimate. The same concerns the seismic hazard parameters.

To assess and reduce errors in the seismic events magnitude or energy estimation, and thereby in the seismic hazard parameters evaluation in nonparametric approach, we propose using resampling methods: the bootstrap and jackknife. These two resampling techniques applied to a one data set provide many replicas of this sample, which preserve its probabilistic properties.

In this paper we present an example of the use of the developed nonparametric interval estimation algorithm based on the bias corrected and accelerated method (BC<sub>a</sub> method), with iterated and smooth bootstrap for characterizing the seismicity from an underground copper mine in the Legnica–Głogów Copper District in Poland.

### **1. Introduction**

Probabilistic Seismic Hazard Analysis (PSHA) is the standard method used to assess the seismic risk over the areas of both natural seismicity and that induced by

human activity. The seismic hazard is evaluated on the basis of the information about the expected maximum level of the ground motion intensity. This information is closely related to the evaluation of the expected maximum seismic source size. Because the seismic event size is usually parameterised by magnitude or sometimes, in the case of Polish and Czech mine seismology, by the seismic energy, to assess the seismic source size the knowledge of the magnitude or energy probability distribution on the studied area is necessary. For the sake of the linear correlation between the magnitude and logarithm of the seismic energy, they both have the same probability distribution. In practice, this probability distribution is not known, it can only be estimated on the basis of seismic data catalogue.

The classical way of determining the probability distribution is to estimate the parameters of a given a priori statistical model on the basis of the data. Currently, the models of magnitude probability distribution, most commonly used in seismology, come from the classical Gutenberg–Richter relation (Gutenberg and Richter 1944) which assumes a linear drop of the logarithm of seismic events number with increasing magnitude. But analyses of the seismic data have indicated that for both natural and mining induced seismicity, the magnitude probability distribution can exhibit a more complex, non-linear structure (e.g. Kijko *et al.* 1987, Urbancic *et al.* 1992, Lasocki 2001, 2002). Since the presently known magnitude distribution models do not follow credible complex distributions, Lasocki *et al.* (2000, 2002) and Kijko *et al.* (2001a, b) proposed the use of a kernel non-parametric density estimator as an alternative approach to magnitude distribution modelling. The nonparametric density estimator with an adaptive kernel for the  $m \in [m_{\min}, m_{\max}]$  is defined according to the formula:

$$\hat{f}_m^a(m) = \begin{cases} 0 & \text{for } m < m_{\min} \\ \frac{1}{\sqrt{2\pi}} \sum_{i=1}^n \frac{1}{\omega_i h} \exp \left[ -0.5 \left( \frac{m - m_i}{\omega_i h} \right)^2 \right] & \text{for } m_{\min} \leq m \leq m_{\max} \\ \frac{\sum_{i=1}^n \left[ \Phi \left( \frac{m_{\max} - m_i}{\omega_i h} \right) - \Phi \left( \frac{m_{\min} - m_i}{\omega_i h} \right) \right]}{\sum_{i=1}^n \left[ \Phi \left( \frac{m_{\max} - m_i}{\omega_i h} \right) - \Phi \left( \frac{m_{\min} - m_i}{\omega_i h} \right) \right]} & \text{for } m > m_{\max} \end{cases}, \quad (1.1)$$

and the corresponding cumulative distribution estimator is:

$$\hat{F}_m^a(m) = \begin{cases} 0 & \text{for } m < m_{\min} \\ \frac{\sum_{i=1}^n \left[ \Phi \left( \frac{m - m_i}{\omega_i h} \right) - \Phi \left( \frac{m_{\min} - m_i}{\omega_i h} \right) \right]}{\sum_{i=1}^n \left[ \Phi \left( \frac{m_{\max} - m_i}{\omega_i h} \right) - \Phi \left( \frac{m_{\min} - m_i}{\omega_i h} \right) \right]} & \text{for } m_{\min} \leq m \leq m_{\max} \\ \frac{\sum_{i=1}^n \left[ \Phi \left( \frac{m_{\max} - m_i}{\omega_i h} \right) - \Phi \left( \frac{m_{\min} - m_i}{\omega_i h} \right) \right]}{\sum_{i=1}^n \left[ \Phi \left( \frac{m_{\max} - m_i}{\omega_i h} \right) - \Phi \left( \frac{m_{\min} - m_i}{\omega_i h} \right) \right]} & \text{for } m > m_{\max} \end{cases}, \quad (1.2)$$

where  $n$  is the number of events greater than or equal to  $m_{\min}$ ,  $m_i$  are the sizes of these events,  $\Phi(\bullet)$  denotes the standard Gaussian cumulative distribution,  $h$  is the smoothing factor, and  $\omega_i$ , where  $i = 1, \dots, n$ , are the local bandwidth factors. The smoothing factor is automatically selected upon the data by means of the least-squares cross-validation technique (e.g. Bowman *et al.* 1984), which in the case of estimator (1.1) means solving the equation

$$\sum_{i,j} \left\{ 2^{-0.5} \left[ \frac{(m_i - m_j)^2}{2h^2} - 1 \right] \exp \left[ -\frac{(m_i - m_j)^2}{4h^2} \right] - 2 \left[ \frac{(m_i - m_j)^2}{h^2} - 1 \right] \exp \left[ -\frac{(m_i - m_j)^2}{2h^2} \right] \right\} - 2n = 0. \quad (1.3)$$

The local bandwidth factors,  $\omega_i$ , can be, for instance:

$$\omega_i = \left[ \frac{\tilde{f}(m_i)}{g} \right]^{-0.5}, \quad (1.4)$$

where  $\tilde{f}(\bullet)$  is the pilot, constant kernel estimator in the unbounded magnitude range:

$$\tilde{f}(m) = \frac{1}{\sqrt{2\pi}} \cdot \frac{1}{nh} \sum_{i=1}^n \exp \left[ -0.5 \left( \frac{m - m_i}{h} \right)^2 \right], \quad (1.5)$$

and  $g = \left[ \prod_{i=1}^n \tilde{f}(m_i) \right]^{\frac{1}{n}}$  is the geometric mean of all constant kernel estimates (Silverman 1986). The studies showed that the nonparametric estimates, in their mean values, provide significantly better results than the parametric estimates when the magnitude distribution is complex (Kijko *et al.* 2001a).

In practical studies of the PSHA, the seismic catalogue is treated as a one data sample on the basis of which the statistical inference is carried out. If the probability distribution of the estimator is not known, as in the case of the magnitude cdf nonparametric estimator, the standard statistical analysis of the one data sample can provide only point estimates, that is only the singular values approximating an unknown magnitude cdf. However, the accuracy of this approximation is unknown. The results of the PSHA got in this way can sometimes differ significantly from their actual values.

In connection with discussed problems with the estimation of the seismic source size distribution in nonparametric approach to evaluate and reduce errors of the magnitude distribution estimation and seismic hazard parameters evaluation, we propose using the resampling methods: the bootstrap and the jackknife. The resampling methods enable to approximate the probability distribution of the estimator of random variable probability density on the basis of the one data sample, thanks to which they enable the evaluation of the probabilistic variability of this estimator. The tests made

with data simulated by the Monte Carlo technique allowed us to choose the optimal procedure from all of the tested procedures in the construction of the confidence intervals of the magnitude cdf and seismic hazard parameters (Orlecka-Sikora 2003, 2004a, b, 2005). On the basis of the bias corrected and accelerated method (BC<sub>a</sub> method, Efron 1987), we have developed an algorithm for the estimation of the confidence intervals of the magnitude cdf and the nonparametric seismic hazard parameters using iterated and smooth bootstrap.

In this paper we present the use of the resampling methods in the PSHA in non-parametric approach based on the example of the seismicity from an underground copper mine in the Legnica–Głogów Copper District in Poland.

## 2. Interval Estimation of the Cumulative Distribution Function of Magnitude

The bootstrap and jackknife resampling techniques replicate an original data sample in two different ways, preserving its statistical properties. The bootstrap method uses the Monte Carlo technique for random sampling with replacement from the original data points as many times as the data points are in the original data sample (Efron and Tibshirani 1998). If the original data set consists of  $n$  points, a bootstrap sample is defined to be a sample obtained by randomly sampling  $n$  times with replacement from the original data points. The bootstrap technique can provide as many data samples as required in the analysis. On the basis of each bootstrap sample, a bootstrap repetition of unknown parameter is obtained in the same way as in the original sample case. The bootstrap samples can make up the basis for generating the bootstrap samples of second level and then for estimating the unknown parameter of interest according to the same formula as in case of the original data set (Hall 1992). This procedure is named the iterated bootstrap and the number of levels can be greater than two.

The  $i$ -th jackknife sample is defined to be the original sample with the  $i$ -th data point removed (Efron and Tibshirani 1998). The jackknife method supplies the number of jackknife samples equal to the number of points in the original data set. The  $i$ -th jackknife replication of unknown parameter is calculated as in the case of the initial sample.

The algorithm for the magnitude cdf confidence interval estimation is based on the so-called *bias corrected and accelerated method* (Efron 1987). According to the BC<sub>a</sub> method, for any magnitude value,  $m$ , the interval of intended coverage  $1-2\alpha$  of the non-parametric magnitude cdf is given by:

$$\left( \hat{F}_{m,\alpha_1}^{a*}, \hat{F}_{m,\alpha_2}^{a*} \right), \quad (2.1)$$

where  $\hat{F}_{m,\alpha_1}^{a*}$  and  $\hat{F}_{m,\alpha_2}^{a*}$  are bootstrap estimated percentiles of the distribution of non-parametric magnitude cdf estimator,  $\hat{F}_m^a$ . The orders of percentiles,  $\alpha_1$  and  $\alpha_2$ , are calculated from the equations:

$$\alpha 1 = \Phi \left( \hat{z}_0 + \frac{\hat{z}_0 + z_\alpha}{1 - \hat{a}(\hat{z}_0 + z_\alpha)} \right), \quad (2.2)$$

$$\alpha 2 = \Phi \left( \hat{z}_0 + \frac{\hat{z}_0 + z_{1-\alpha}}{1 - \hat{a}(\hat{z}_0 + z_{1-\alpha})} \right), \quad (2.3)$$

where  $\Phi(\bullet)$  is the standard Gaussian cumulative distribution,  $z_\alpha$  and  $z_{1-\alpha}$  are percentiles of the standard Gaussian distribution,  $\hat{z}_0$  is the estimate of bias-correction, and  $\hat{a}$  is the estimate of acceleration constant. The bias-correction estimate,  $\hat{z}_0$ , is obtained from the proportion of bootstrap cdf estimates,  $\hat{F}_{m,i}^a$ , less than the magnitude cdf estimate obtained from the original data sample (Efron and Tibshirani 1998):

$$\hat{z}_0 = \Phi^{-1} \left( \frac{\text{number of } \hat{F}_{m,i}^a < \hat{F}_m^a}{k} \right), \quad (2.4)$$

where  $\Phi^{-1}(\bullet)$  indicates the inverse function of the standard Gaussian cdf. The acceleration constant can be evaluated in various ways, for instance, from the equation (Efron and Tibshirani 1998):

$$\hat{a} = \frac{\sum_{i=1}^n \left( \hat{F}_{m,(\bullet)}^a - \hat{F}_{m,(jack)}^a \right)^3}{6 \left\{ \sum_{i=1}^n \left( \hat{F}_{m,(\bullet)}^a - \hat{F}_{m,(jack)}^a \right)^2 \right\}^{3/2}}, \quad (2.5)$$

where  $\hat{F}_{m,(jack)}^a$  denotes the  $i$ -th jackknife nonparametric estimate of magnitude cdf, and  $\hat{F}_{m,(\bullet)}^a$  is the arithmetic mean of all jackknife estimates.

The bootstrap samples are generated here by sampling  $n$ -times with replacement from the original data set. Thus, each bootstrap sample contains the repetitions of the original data points. The existence of repetitions in the dataset can lead to spurious effects in the nonparametric probability distribution estimate. To avoid such a situation in nonparametric estimation, Silverman (1986) proposed using the smoothed bootstrap, according to which the bootstrap sample is generated in the following way:

$$y = x_i + h \cdot \omega_i \cdot \varepsilon, \quad (2.6)$$

where  $i = 1, 2, \dots, n$ ,  $x_i$  are the results of resampling with replacement from the original data points,  $h$  is the smooth parameter estimated on the basis of the original data sample according to (1.3),  $\omega_i$  are the local bandwidth factors calculated on the basis of the original data sample according to (1.4) for  $x_i$  values, and  $\varepsilon$  is the standard normal random variable.

In order to improve the accuracy of results of the magnitude cdf confidence interval estimation we have proposed additionally to modify the  $BC_a$  method and to use

an iterated bootstrap for estimating the bias-correction parameter,  $z_0$ . It means that from every bootstrap sample a set (say  $j$ ) of second order bootstrap samples is drawn and used to estimate the magnitude cdf,  $\{\hat{F}_m^a(m)_i^{**}, i = 1, 2, \dots, j\}$ , and then to estimate the parameter  $z_0$ :

$$\hat{z}_0^* = \Phi^{-1} \left( \frac{\text{number of II order bootstrap estimates } \hat{F}_m^a(m)_i^{**} < \hat{F}_m^a(m)_b^*}{j} \right), \quad (2.7)$$

where  $\hat{F}_m^a(m)_b^*$  is the bootstrap estimate of the magnitude cdf calculated on the basis of the  $b$ -th bootstrap sample and  $b = 1, 2, \dots, k$ . In this way one obtains  $k$  estimates of  $z_0$  where  $k$  is the number of the first order bootstrap samples. Finally, the mean value of these estimates,  $\bar{\hat{z}}_0$ , is calculated and used to evaluate  $\alpha 1$  and  $\alpha 2$ . We named this procedure *the iterated BC<sub>a</sub> method*. Algorithmic details of the iterated BC<sub>a</sub> method are presented in Orlecka-Sikora (2005). Monte Carlo simulation studies indicated that the iterated BC<sub>a</sub> method, applied for nonparametric interval estimation of magnitude cdf and related parameters of seismic hazard, can significantly improve the results of estimation (Orlecka-Sikora 2004a, b, 2005).

The bootstrap method, as every estimation technique, provides only the approximate values of unknown parameters. The error associated with the bootstrap approximation to the distribution of an unknown parameter, is the sum of two independent errors: the statistical and the simulation error. The statistical error is unavoidable and independent of the number of bootstrap samples,  $k$ , but the second type of error arises because the number of bootstrap samples is finite and the value of this error depends on  $k$  (Wehrens *et al.* 2000). From this standpoint,  $k$  should be chosen so that the simulation error is smaller than the statistical error. In the nonparametric magnitude cdf interval estimation, the proper number of bootstrap samples is calculated using the three-step method (Andrews and Buchinsky 2002). The assumption of this method is to achieve a desired level of accuracy that means the closeness of the BC<sub>a</sub> confidence interval based on  $k$  replications to the ideal bootstrap BC<sub>a</sub> confidence interval for which  $k = \infty$ . The Monte Carlo simulation experiments indicated that this method provides good results in the nonparametric magnitude cdf interval estimation (Orlecka-Sikora 2005).

### 3. Interval Estimation of the Seismic Hazard Parameters

On the basis of the probabilistic functions characterizing the seismic sources, other parameters of PSHA can be estimated, viz.:

– the probability that the specified value of a seismic event size, in this case the logarithm of energy  $\log E_p$ , will be exceeded in  $D$  time units:

$$R(\log E_p, D) = 1 - \exp\{-\lambda D[1 - F(\log E_p)]\} \quad (3.1)$$

– the mean return period of events of size  $\log E_p$ , defined by:

$$T(\log E_p) = \left\{ \lambda [1 - F(\log E_p)] \right\}^{-1}. \quad (3.2)$$

Thus, the  $\log E$  cdf confidence intervals can be used to find the confidence intervals of these parameters. Both,  $R(\log E_p, D)$  and  $T(\log E_p)$  functions are monotonic with  $F(\bullet)$ , then the confidence intervals of  $\log E$  cdf can be readily converted into the confidence intervals of  $R$  and  $T$ . The confidence interval of exceedance probability is:

$$\left( \hat{R}(\log E, D)_{\alpha_1}^*; \hat{R}(\log E, D)_{\alpha_2}^* \right) \quad (3.3)$$

where

$$\hat{R}(\log E, D)_{\alpha_1}^* = 1 - \exp \left\{ -\lambda D \left[ 1 - \hat{F}(\log E)_{\alpha_2}^* \right] \right\}, \quad (3.4)$$

$$\hat{R}(\log E, D)_{\alpha_2}^* = 1 - \exp \left\{ -\lambda D \left[ 1 - \hat{F}(\log E)_{\alpha_1}^* \right] \right\}. \quad (3.5)$$

and the confidence interval of the mean return period is:

$$\left( \hat{T}(\log E)_{\alpha_1}^*; \hat{T}(\log E)_{\alpha_2}^* \right) \quad (3.6)$$

where

$$\hat{T}(\log E)_{\alpha_1}^* = \left\{ \lambda \left[ 1 - \hat{F}(\log E)_{\alpha_1}^* \right] \right\}^{-1}, \quad (3.7)$$

$$\hat{T}(\log E)_{\alpha_2}^* = \left\{ \lambda \left[ 1 - \hat{F}(\log E)_{\alpha_2}^* \right] \right\}^{-1}. \quad (3.8)$$

#### 4. A Practical Example

The application of the iterated  $BC_a$  algorithm for characterizing mining induced seismicity can be illustrated on the example of the data from underground copper mines in the Legnica-Głogów Copper District (LGOM) in Poland. Detailed analysis of the seismicity occurred in the LGOM area has indicated its clustered structure. The seismic events have a tendency to form distinct time-space active zones, usually associated with the place and time of the mining works (Lasocki and Team 2000a, b, 2001, Gibowicz and Lasocki 2001, Orlecka-Sikora and Lasocki 2002, Lasocki and Orlecka-Sikora 2002a, b). Studying mining seismic catalogues from the last 20 years, Lasocki *et al.* (2003) identified 99 such seismic zones. All of these seismic zones exhibit a non-linear structure of the probability distribution of the seismic source size, thus the cdf of the logarithm of energy should be estimated in a nonparametric way. To demonstrate the proposed procedure for nonparametric confidence interval estimation of logarithm of energy cdf, we chose two of the identified zones of seismicity, Z6 located in the Polkowice-Sierszowice mine and Z36b located in the Lubin mine (Fig. 1). Parameters characterizing these zones are in Table 1.

The empirical recurrence relations shown in Fig. 2 distinctly suggest a complex event size distribution.

Table 1

Parameters characterizing the analysed seismic zones identified in the LGOM area

Zone	Time of activity	Number of events	Range of $\log E$
Z6	22.09.00–22.07.04	95	[3.5, 7.2]
Z36b	17.11.98–10.08.01	276	[3.5, 7.9]

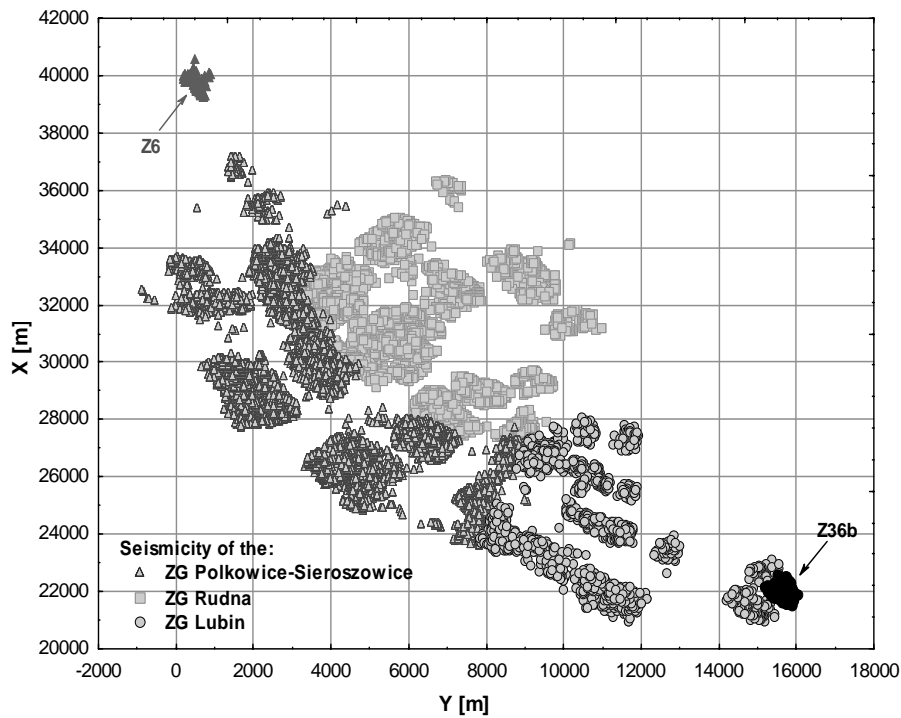


Fig. 1. Seismic activity in LGOM. Z6 and Z36b are the analysed seismic zones.

To estimate the confidence intervals of the seismic event size cdf for the analysed zones, the appropriate number of bootstrap samples, calculated by the 3-step method (Andrews and Buchinsky 2002), was drawn from 95 data points in the case of zone Z6, and from 276 data points in the case of zone Z36b, according to the smooth bootstrap method. On the basis of each bootstrap sample, the cdf of  $\log E$  was estimated according to equation (1.2). Each of the bootstrap samples was the source of a set of 200 second-order bootstrap samples. These were used to estimate the bias-correction parameter,  $z_0$ . Finally, the confidence intervals were calculated with a confidence level equal to 95 percent. The results of the analysis are shown in Figs. 3 and 4, respectively.

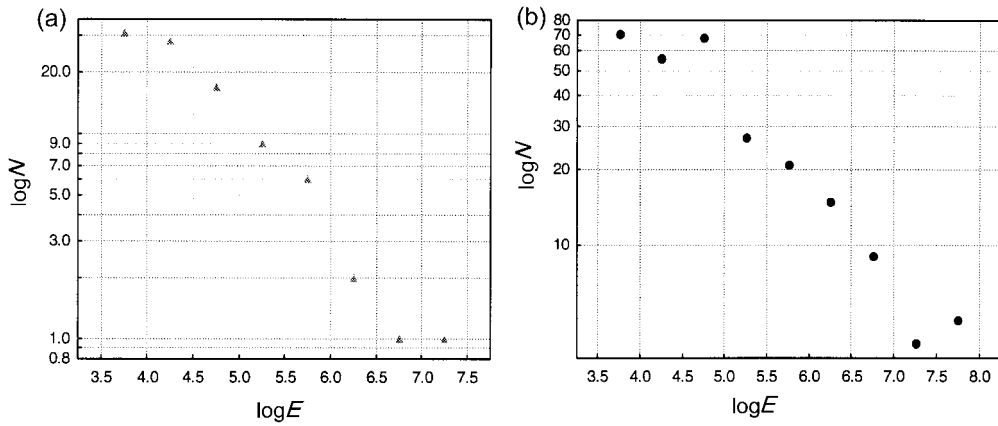


Fig. 2. The empirical cumulative recurrence relations for the studied dataset of zones: (a) Z6 and (b) Z36b.

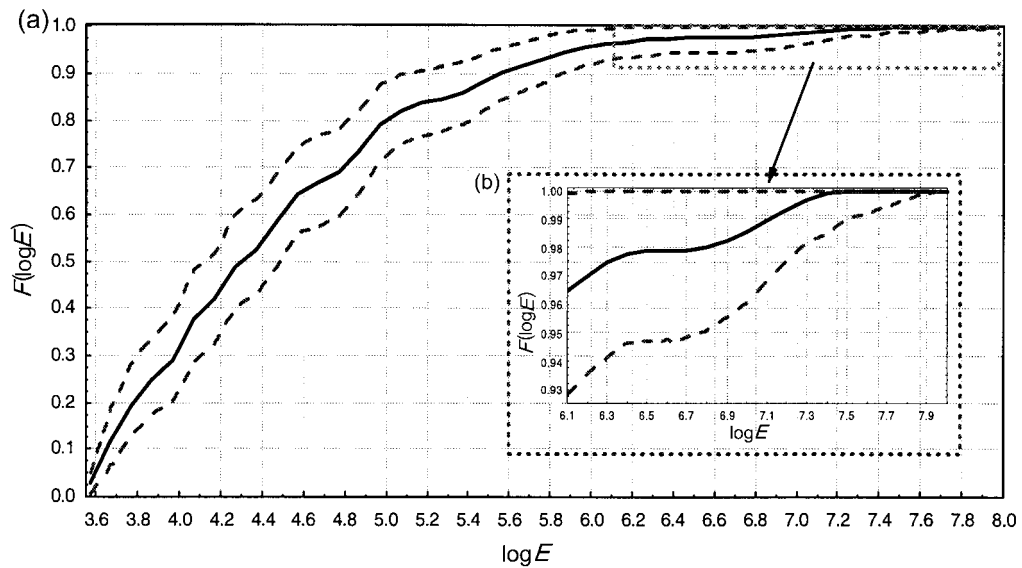


Fig. 3. (a) Nonparametric estimate of  $\log E$  cdf for the studied dataset from zone Z6. The solid line represents the point estimate while the 95 percent iterated  $BC_a$  confidence intervals are represented by dashed lines; (b) the magnification of the graph in the vital high  $\log E$  range.

Figures 5 and 6 present the confidence intervals of the exceedance probability for  $\log E = 7$  calculated according to (3.3), and of the mean return period, (3.6), estimated on the basis of dataset from the seismic zone Z6, respectively. The confidence intervals of the exceedance probability for  $\log E = 7$  and of the mean return period for the seismic zone Z36b are shown in the Figs. 7 and 8, respectively.

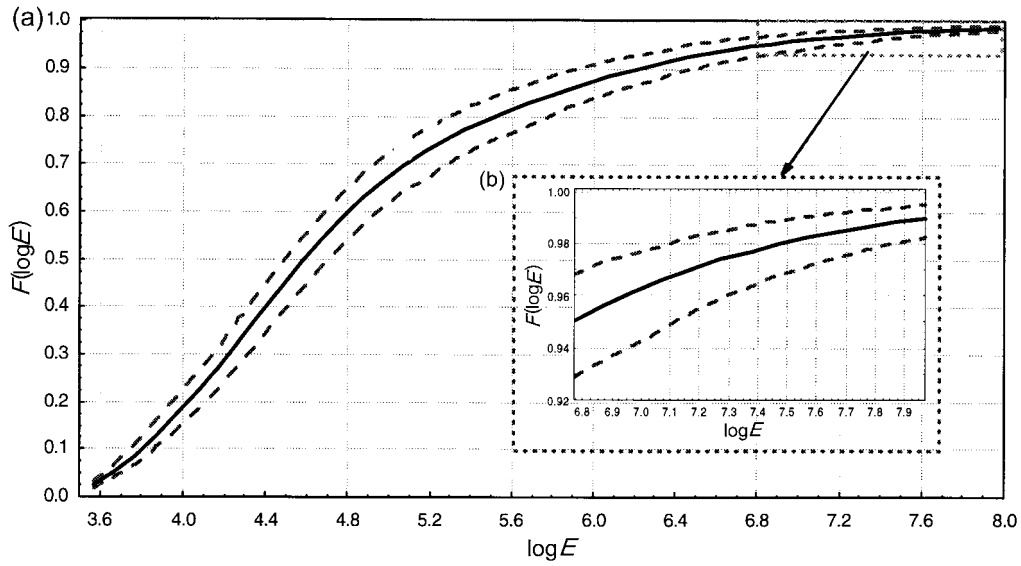


Fig. 4. (a) Nonparametric estimate of  $\log E$  cdf for the studied dataset from zone Z36b. The solid line represents the point estimate while the 95 percent iterated  $BC_a$  confidence intervals are represented by dashed lines; (b) the magnification of the graph in the vital high  $\log E$  range.

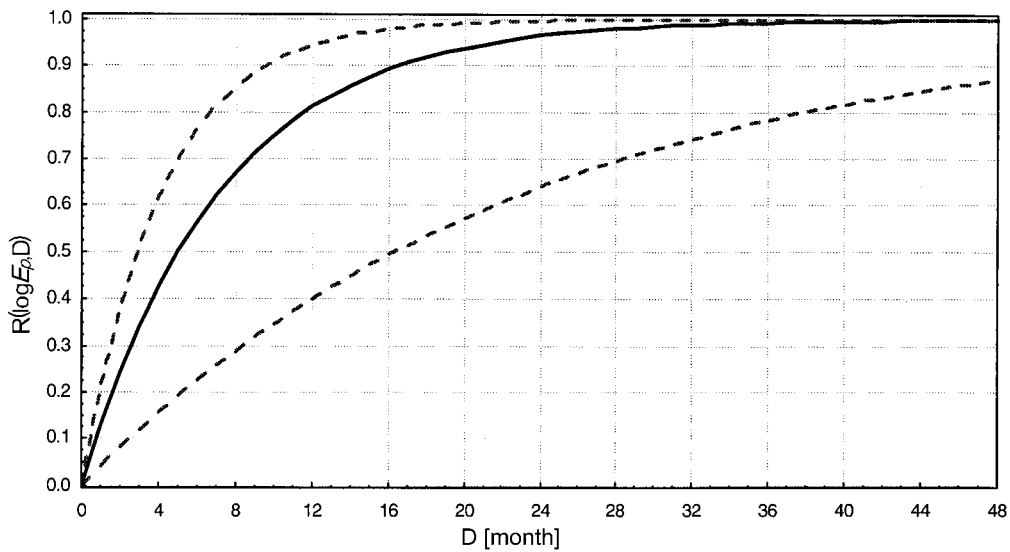


Fig. 5. Nonparametric estimate of the exceedance probability of  $\log E_p = 5.8$  for the studied dataset from zone Z6. The solid line represents the point estimate while the 95 percent iterated  $BC_a$  confidence intervals are represented by dashed lines. The mean activity rate is  $\lambda = 2.07$  1/month.

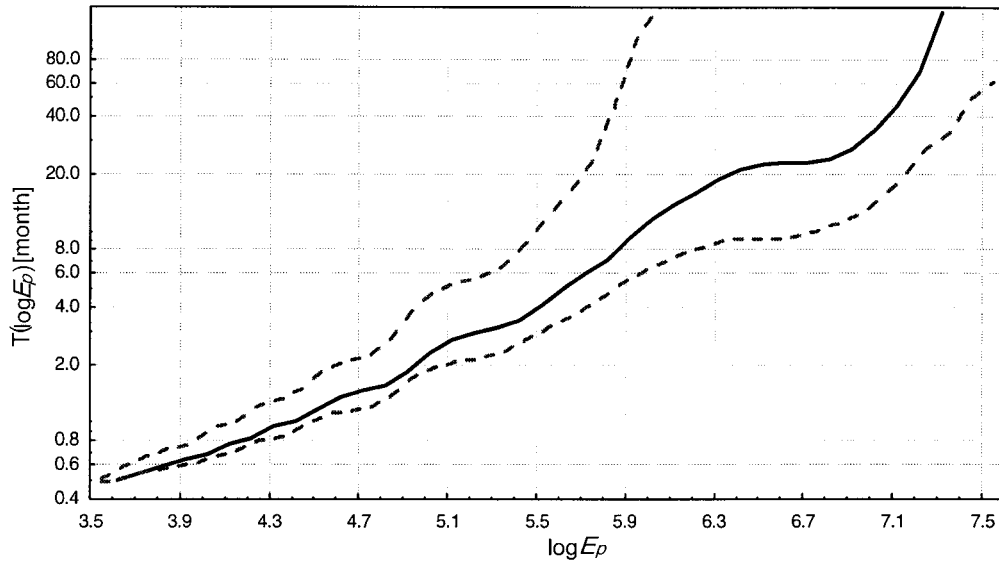


Fig. 6. Nonparametric estimate of the mean return period for the studied dataset from zone Z6. The solid line represents the point estimate while the 95 per-cent iterated  $BC_a$  confidence intervals are represented by dashed lines. The mean activity rate is  $\lambda = 2.07$  1/month.

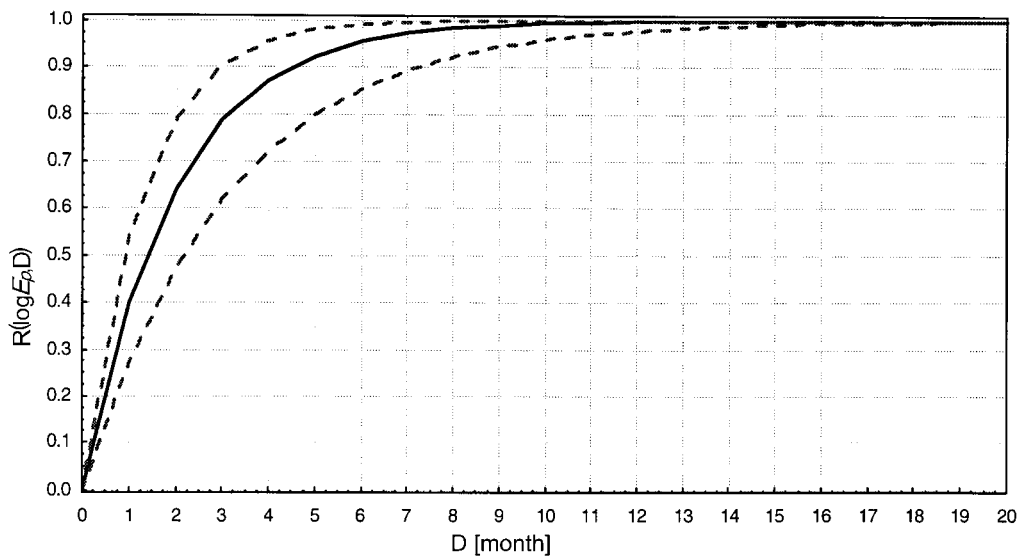


Fig. 7. Nonparametric estimate of exceedance probability of  $\log E_p = 7$  for the studied dataset from zone Z36b. The solid line represents the point estimate while the 95 per-cent iterated  $BC_a$  confidence intervals are represented by dashed lines. The mean activity rate is  $\lambda = 13.4$  1/month.

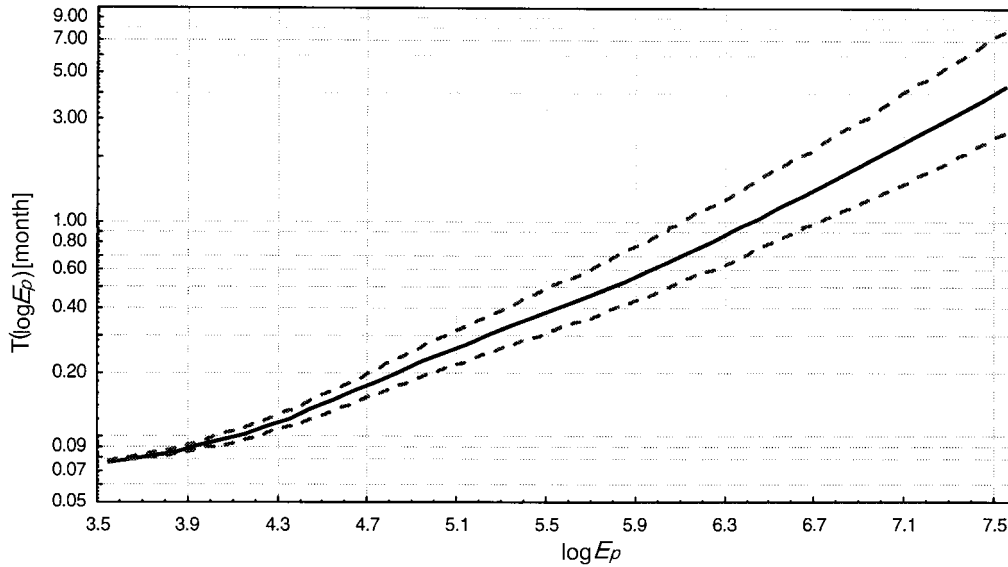


Fig. 8. Nonparametric estimate of the mean return period for the studied dataset from zone Z36b. The solid line represents the point estimate while the 95 percent iterated  $BC_a$  confidence intervals are represented by dashed lines. The mean activity rate is  $\lambda = 13.4$  1/month.

## 5. Conclusions

In seismic hazard analysis the magnitude cdf estimation is carried out from only one dataset, i.e. a seismic catalogue. The uncertainty of one-sample magnitude cdf and seismic hazard parameters estimation is not always possible to evaluate. In order to improve the seismic event size cdf and other seismic hazard descriptors estimation, the point estimate should be completed with an interval estimate. In the case of nonparametric kernel estimator of magnitude cdf, this is only possible through the use of resampling methods. Resampling methods enable to estimate the confidence intervals of the unknown parameter on the basis of only one data sample, even in such a situation where the probability distribution of the estimator of this parameter is unknown.

The Monte Carlo simulation studies showed that the iterated bias corrected and accelerated algorithm is an effective technique in the nonparametric interval estimation of seismic event size cdf. It provides satisfactory results regardless of the actual shape of the magnitude distribution and even if the data comprises a small number of elements. The confidence intervals of magnitude cdf can be transformed into the intervals of changeability for the sake of the magnitude cdf for the exceedance probability of event size and mean return period.

The presented practical examples illustrated how the iterated  $BC_a$  method, applied to real datasets, can provide useful information on dispersion of seismic source size cdf and hazard parameters estimates.

**A c k n o w l e d g m e n t s.** This work was financed by the Polish State Committee for Scientific Research under contract No. 5 T12A 046 25 during the period 2003-2005.

#### References

- Andrews, D.W.K., and M. Buchinsky, 2002, *On the number of bootstrap repetitions for  $BC_a$  confidence intervals*, *Econometric Theory* **18**, 962-984.
- Bowman, A.W., P. Hall and D.M. Titterton, 1984, *Cross-validation in nonparametric estimation of probabilities and probability densities*, *Biometrika* **71**, 341-351.
- Efron, B., 1987, *Better bootstrap confidence intervals*, *Journal of the American Statistical Association* **82**, 397, 171-200.
- Efron, B., and R.J. Tibshirani, 1998, *An Introduction to the Bootstrap*, Chapman and Hall, New York.
- Gibowicz, S.J., and S. Lasocki, 2001, *Seismicity induced by mining: Ten years later*, *Advances in Geophysics* **44**, 39-181.
- Gutenberg, B., and C.F. Richter, 1944, *Frequency of earthquakes in California*, *Bull. Seismol. Soc. Am.* **57**, 747-760.
- Hall, P., 1992, *The Bootstrap and Edgeworth Expansion*, Springer-Verlag, New York.
- Kijko, A., B. Drzeźła and T. Stankiewicz, 1987, *Bimodal character of extreme seismic events in Polish mines*, *Acta Geophys. Pol.* **35**, 157-166.
- Kijko, A., S. Lasocki and G. Graham, 2001a, *Nonparametric seismic hazard analysis in mines*, *Pure Appl. Geophys.* **158**, 1655-1676.
- Kijko, A., S. Lasocki, G. Graham and S.J.P. Retief, 2001b, *Non-parametric seismic hazard analysis in mines*, In 5<sup>th</sup> Int. Symp. Rockbursts and Seismicity in Mines "Dynamic rock mass response to mining", Magalisberg, 17-20 September 2001 (eds.: G. van Aswegen, R.J. Durrheim and W.D. Ortlepp) SAIMM S27, Johannesburg, South Africa, 493-500.
- Lasocki, S., 2001, *Quantitative evidences of complexity of magnitude distribution in mining-induced seismicity: Implications for hazard evaluation*, The Fifth International Symposium on Rockbursts and Seismicity in Mines "Dynamic rock mass response to mining" (eds.: G. van Aswegen, R.J. Durrheim and W.D. Ortlepp) SAIMM S27, Johannesburg, 543-550.
- Lasocki, S., 2002, *Testing complexity of magnitude distribution*, XXVIII General Assembly European Seismological Commission (ESC), University of Genoa, Genoa, Italy, Book of Abstracts, 232-233.
- Lasocki, S., and B. Orlecka-Sikora, 2002a, *Probabilistic seismic hazard analysis for time-varying seismicity: an example for Legnica-Głogów seismically active mining area*, XXVIII General Assembly of the European Seismological Commission, Genoa, Italy, Book of Abstracts, 259.
- Lasocki, S., and B. Orlecka-Sikora, 2002b, *Prognoza drgań gruntu na terenie miasta Polkowice dla okresu 2001-2013*, *Mat. XXV Zimowej Szkoły Mech. Górotw. „Geotechnika i Budownictwo Specjalne 2002”* (red. D. Flisiak), Wyd. Katedry Geomechaniki, Budownictwa i Geotechniki AGH, Kraków, 369-384.

- Lasocki, S., A. Kijko and G. Graham, 2000, *Model-free seismic hazard estimation*, Proc. Int. Conf. Earthquake Hazard and Risk in the Mediterranean Region, EHRMR'99 (ed. H. Gokcekus), Educational Foundation of Near East University, Lefkosa, T.R.N. Cyprus, 503-508.
- Lasocki, S., A. Kijko and G. Graham, 2002, *Model-free seismic hazard analysis, Seismogenic Process Monitoring*, (eds.: H. Ogasawara, T. Yanagidani and M. Ando), Balkema, Lisse, 327-339.
- Lasocki, S., Z. Kłeczek, J. Mirek, D. Olszewska, B. Orlecka-Sikora and S.J. Gibowicz, 2003, *Prediction of Seismic Impact on „Żelazny Most” Repository With a Use of Acceleration Ground Motion Data*. KGHM „Polska Miedź” S.A., Hydrotechnical Division – The Final Report, not published.
- Lasocki, S., and Team, 2000a, *Opracowanie prognozy aktywności sejsmicznej do końca działalności górniczej KGHM „Polska Miedź” S.A. w Lubinie pod kątem bezpieczeństwa stawu osadowego Żelazny Most i jego rozbudowy*, Zarząd Gminy Polkowice, not published.
- Lasocki, S., and Team, 2000b, *Opracowanie prognozy drgań gruntu w rejonie stawu osadowego Żelazny Most od aktywności sejsmicznej indukowanej działalnością górniczą KGHM „Polska Miedź” S.A. w Lubinie w kontekście rozbudowy stawu osadowego Żelazny Most do rzędnej +180 m n.p.m. i 200 m n.p.m.*, Zarząd Gminy Polkowice, not published.
- Orlecka-Sikora, B., 2003, *Bootstrap and jackknife resampling for improving in the nonparametric seismic hazard estimation*, The IUGG 2003 Proceedings Volume “Earthquake Hazard, Risk, and Strong Ground Motion” (Edited by Y.T. Chen, G.F. Panza and Z.L. Wu), 81-92.
- Orlecka-Sikora, B., 2004a, *Resampling methods in nonparametric seismic hazard estimation*, Acta Geophys. Pol. **52**, 1, 15 – 27.
- Orlecka-Sikora, B., 2004b, *A bootstrap technique for estimating the confidence intervals of source characteristics*, The European Seismological Commission (ESC) XXIX General Assembly, University and GFZ Potsdam, Potsdam, Niemcy, September 12-17, 2004, Book of Abstracts, 192.
- Orlecka-Sikora, B., 2005, *Resampling methods for improving accuracy of the probabilistic seismic hazard analysis*, PhD dissertation, Library of AGH University of Science and Technology, Krakow, not published.
- Orlecka-Sikora, B., and S. Lasocki, 2002, *Strefowa struktura sejsmiczności Legnicko-Głogowskiego Okręgu Miedziowego*, Publs. Inst. Geophys. Pol. Acad Sci. **M-27**, 340, 105-119.
- Silverman, B.W., 1986, *Density Estimation for Statistics and Data Analysis*, Chapman and Hall, London.
- Urbancic, T.I., C.-I. Trifu and R.P. Young, 1992, *Space-time correlations of b values with stress release*, Pure Appl. Geophys. **139**, 449-462.
- Wehrens, R., H. Putter, and L.M.C. Buydens, 2000, *The bootstrap: a tutorial*, Chemometrics and Intelligent Laboratory Systems **54**, 35-52.

Accepted 10 April 2006

## **Mining Tremors Registered at Ojców and Książ Observatories: Rotational Field Components**

Krzysztof P. TEISSEYRE

Institute of Geophysics, Polish Academy of Sciences  
ul. Księcia Janusza 64, 01-452 Warszawa, Poland  
e-mail: kt@igf.edu.pl

### **A b s t r a c t**

Analysis of rotational components of the seismic field is a new method in research of the processes in a seismic source. This work presents exemplary results obtained by the differential seismologic method. The chosen seismic events, mainly of mining origin, were registered at the observatories in Książ and Ojców. Two-fold analysis was performed: (i) after filtration of the original data with the pass-band of 0.3-3 Hz, and (ii) after filtration of the same data with the pass-band of 2.6-43 Hz; the obtained pictures of the shocks differ.

An attempt was made to find what fraction of the seismic energy of a shock was emitted as rotational waves. Various indexes, those known from previous works and also the new ones, were used. The index which informs on the share, in registered seismograms, of the differential components (connected with the rotational ones), was calculated, both for the whole shock and for consecutive short time-intervals; usually it varies in a characteristic way. With the same method, chosen parts of seismograms, bearing apparently only noise, were analysed too. The results obtained in this study had common features with those obtained while analysing seismic events in the Central Appennines and the Pasterze glacier, Austrian High Alps.

**Key words:** seismic rotation waves, Książ Observatory, Ojców Observatory.

### **1. Introduction**

Seismic waves contain, besides basic body and surface components, also the rotational ones. There are two main rotational components: the rotation or *spin*, and the *bend-twist*, or shortly *twist*, which is related to shear-strain oscillations. The amplitudes of rotation motions are so small that their registration and analysis meet many problems, also in the technical aspect.

Rotational components propagate as rotational waves, which travel through a rock medium which may be grainy or continuous with microstructure or defects (Teisseyre R. 2002). For a continuum with stress moments or for asymmetric continuum, such waves can also propagate even without an internal structure (Teisseyre R. 2005 and Teisseyre R. et al. 2005).

Opinions differ, whether all these waves travel jointly with the “classic” seismic waves, or some of them run with a different speed.

These vibrations are poorly known from experiments, but they are already in the scope of interest of many scientists, being a new source of information on processes in the focal zone. Theories and hypotheses concerning generation, propagation and dumping of rotational oscillations have constantly been developed in the recent years. The following sources of rotational vibrations and waves may be discerned:

- in a seismic source, when rock fracture and slip processes take place, there occur torsional deformations of rock grains or the fractions of rock volume containing internal defects; these movements may start rotational waves;
- under the influence of the seismic body or surface waves, secondary micro-morphic rotational waves can be formed;
- direct rotational components of the displacement field due to the seismic wave, which may be greatly enlarged in an inhomogeneous medium, or in a medium containing an internal structure.

In all these cases two main components of rotation are discerned: spin  $\gamma$  and twist  $\mathcal{G}$  motions. In these components, the proper spin  $\gamma^0$  and the proper twist  $\mathcal{G}^0$  are incorporated together with the respective influence of displacement motions:

$$\gamma = \omega + \gamma^0, \quad \mathcal{G} = E + \mathcal{G}^0 \quad (1)$$

where  $\omega$  and  $E$  are the displacement-related rotation and strain,

$$\omega_{ik} = \frac{1}{2} \left( \frac{\partial u_k}{\partial x_i} - \frac{\partial u_i}{\partial x_k} \right), \quad E_{ik} = \frac{1}{2} \left( \frac{\partial u_k}{\partial x_i} + \frac{\partial u_i}{\partial x_k} \right).$$

To register the rotational components, two groups of methods are usually used. One group gathers methods which directly measure the spin component only. Here the Sagnac interferometers are used, of various construction (fiber-coil and other), and rotational electrochemical seismometers. Methods of the second group are based on differential seismological measurements – differential signals are computed from seismometer pairs; such instruments are called the rotation seismographs.

The three-component fiber-coil interferometer was constructed by M. Takeo (Tokyo University, Japan), while the three-component rotation seismograph system has been introduced by T. Moriya (at Hokkaido University, Japan).

Rotational waves, sometimes called the proper spin and proper twist, are hard to separate from rotational effects in the displacement field – see: Teisseyre R. et al. (2003a). Our studies were based on the differential method – with the use of the sets of four simultaneous records from two rotational seismographs. Mainly the near-field

shocks were studied; therefore, the obtained information is treated as originating in the source, although distorted by the medium between the source and the measuring site.

We have partly followed the methods presented by Teisseyre R. et al. (2003a, b and c). The displacement velocities were measured with two rotation seismometers; four channels were used:  $V_1-V_4$ . First two of them are the velocities of oscillations in one direction, with the opposite (antiparallel) orientation of sensors in relation to the axis;  $2l_0$  is the doubled reduced length of pendulum, or the reduced distance between the first two sensors. The second rotation seismometer, oriented in perpendicular and close to the first, produced the channels  $V_3$  and  $V_4$ . The spin was computed with formula:

$$\gamma = \left( \frac{V_1 - V_2}{2l_0} + \frac{V_3 - V_4}{2l_0} \right), \quad (2)$$

and the twist with the following formula:

$$\vartheta = \left( \frac{V_1 - V_2}{2l_0} - \frac{V_3 - V_4}{2l_0} \right). \quad (3)$$

These expressions correspond to formulae (1), but the signs „-” and „+” come from the coordinates system (spin is the mean rotary movement in the plane, and twist is a measure of the anisotropy of this movement). Problems of signal normalisation have been discussed by: Teisseyre R. et al. (2003a)

The measuring station was placed near our fixed sites of classic seismograph systems; in the case of Ojców – in cave Koziarnia, and at Książ – in corridors below the castle. The sampling rate was 100 Hz. To some records from Książ, a noise reduction technique was applied, based on removal of the noise in the frequency domain; it helped only a little.

As in previous studies (e.g., Teisseyre R. et al. 2003c, Górski and Teisseyre K.P. 2006, Teisseyre K.P. and Suchcicki 2006), the ratio of energy emitted as rotational components to the whole emission was estimated. This was done by comparing the sum of squared amplitudes of rotational signal to the adequate squared sum of the mean displacement velocities. Thus, analyses of materials from various sites comprise calculation of such an index for the energy emitted as spin:

$$R_r = \frac{\Sigma \gamma^2}{\Sigma \bar{U}^2}, \quad (4)$$

and as twist:

$$R_t = \frac{\Sigma \vartheta^2}{\Sigma \bar{U}^2}, \quad (5)$$

where

$$\bar{U} = \frac{|V_1| + |V_2| + |V_3| + |V_4|}{4}. \quad (6)$$

Another index was also calculated, in which the mean absolute values of reduced differences within a seismometers pair were summed in place of spin or twist:

$$R_m = \frac{\Sigma T^2}{\Sigma U^2} \quad (7)$$

where

$$T = \left( \frac{|V_1 - V_2|}{2l_0} + \frac{|V_3 - V_4|}{2l_0} \right) / 2.$$

In the previous work, a similar analysis of twenty-four seismic events in central Italy, in vicinity of observatory in l'Aquila (Teisseyre K.P. and Suchcicki 2006), permitted to find certain common features, including a time-variable relation between differential components and seismic energy as whole; in other words, time-variations of the  $R_m$  index. It was noticed that usually at beginning of the event, the share of rotational, or differential components was large. In sixteen cases, the  $R_m$  indexes for consecutive stages at the beginning and near the end of tremor were much bigger than those for middle stages.

In a similar way, seismic events on the Pasterze glacier (in the Alps) were studied (Teisseyre K.P. et al. 2004, Górski and Teisseyre K.P. 2006); for many cases a distinct difference between ordinary and differential seismograms was found. This difference was especially large for records with small maximal amplitude and in the cases when the analysis was made in the low frequency range (the pass-band in the filtration was 0.3-3 Hz or 0-3 Hz, instead of 3-15 Hz). Also in this research, a changing proportion of rotational components to the whole emitted seismic energy was found.

Because the surface of glacier is unstable, horizontal seismometers become soon blocked there. Therefore, on the Pasterze glacier the vertical seismometers were used. Hence, the components of rotation around vertical axis were not measured there; instead, rotations around two other, horizontal axes were measured. These movements include rotational vibrations and may contain episodes of tilt change. Methodological differences are probably not important in assessing the rotational components of the field.

Quite often, an event may be found in ordinary seismograms, while in the derived, rotational ones it is not visible; apparently only the noise and disturbances are there. Such cases were not taken into consideration either in this work, or in the previous one.

## 2. The Results

To show the results of our study, eight cases were chosen, among which six occurred in mines or their vicinity, one in the Wałbrzych region, registered in the nearby Książ Observatory, and one was local tremor near the Ojców Observatory.

Two-fold analysis was performed: after filtration with the pass-band of 0.3-3 Hz, and independently, after filtration of the same original data with the pass-band

2.6-43 Hz. In the study of each case, index  $R_m$  was calculated for many consecutive, short time-intervals of shock, together with a period just before the shock started, and one index for whole main part of the shock, thus excluding the beginning and end – this index has been called  $R_{mc}$ .

For indexes  $R_r$ ,  $R_t$  and  $R_{mc}$  we have used the same periods. The same parameters were put for low- and middle- frequencies analysis; this applies also to calculations of  $R_m$ -index sequences. In all cases except one, each  $R_m$ -index has been calculated from 50 samples (0.5 s). Only one seismic event was analysed more precisely – with 20 samples for each  $R_m$ -index.

Diagrams show the results of two typical case studies: one from Książ (Figs. 1-4) and one from Ojców (Figs. 5-8). Additionally, part of results of other shock analysis is given. This was a shock of low magnitude, registered in Ojców (Figs. 9 and 10). The indexes  $R_{mc}$  and ratios  $R_{mc}/\langle R_m(\text{noise}) \rangle$  (related to mean value of  $R_m$  for noise) are shown in the Fig. 11 and after rearrangement – in the Fig. 12.

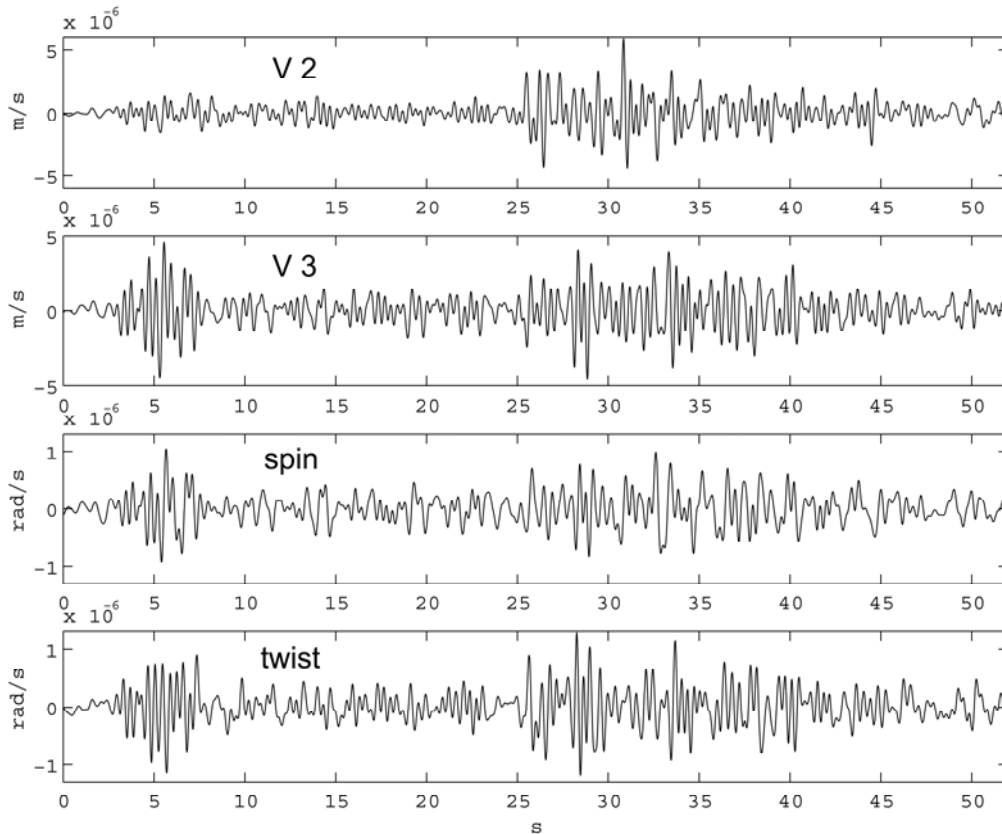


Fig. 1. Recorded at Książ, 6 February 2002, Silesia, 01:31:25.5. Low frequencies, the pass band 0.3-3 Hz. From the top: channel 2, channel 3, spin, twist.

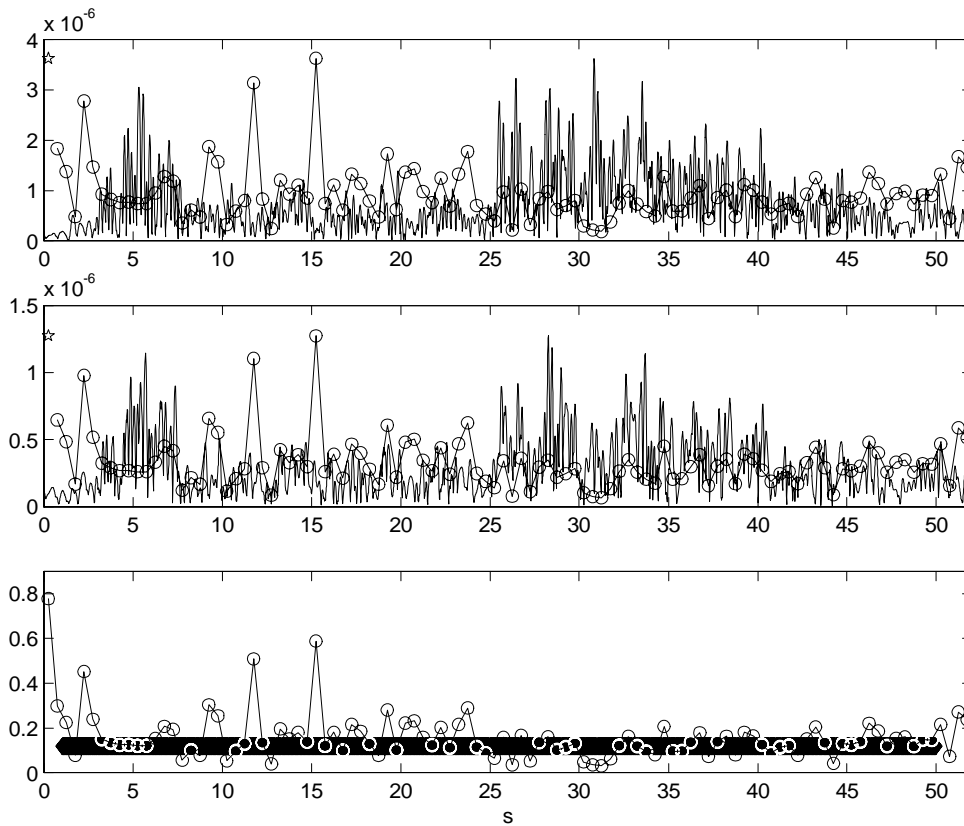


Fig. 2. Recorded at Książ, 6 February 2002, Silesia, 01:31:25.5. Low frequencies, the pass band 0.3-3 Hz. Top panel: Comparison of mean displacement velocity and  $R_m$  indexes (circles), given in different scales (*star indicates that first  $R_m$  index is the biggest one and may not fit to the scale*); Middle: Comparison of mean absolute, reduced differences within a pair and  $R_m$  indexes (circles), given in different scales; Bottom:  $R_m$  indexes in the real scale, black bar denotes central part of the shock record, for which  $R_{mc}$  was calculated, its vertical position denotes the  $R_{mc}$  value. For the time period 1 to 50 s:  $R_r = 0.067$ ,  $R_t = 0.085$ ,  $R_{mc} = 0.12$ .

Plots of rotational components differ from the ordinary seismograms, but less than it was noticed for the glacial seismic events and those in the Central Apennines (registered in l'Aquila). The greatest discrepancy between basic and rotational records appears at the start of seismic event – usually, differential and rotational components are at this time unproportionally high. Only in two cases, the tremor in Wałbrzych region and in the vicinity of Ojców, both analysed in low-frequency mode, this increase is mild. Usually this increase is followed by abrupt decrease of the  $R_m$  index and then by short-time stabilisation of  $R_m$  on low level, during the summit of the  $P$  waves. In further stages, when oscillations decrease in ordinary seismograms, transient increases were found. These phenomena are clearly visible on diagrams showing the  $R_m$  indexes for consecutive, equally short stages – see Figs. 2, 4, 6 and 8-10 (circles).

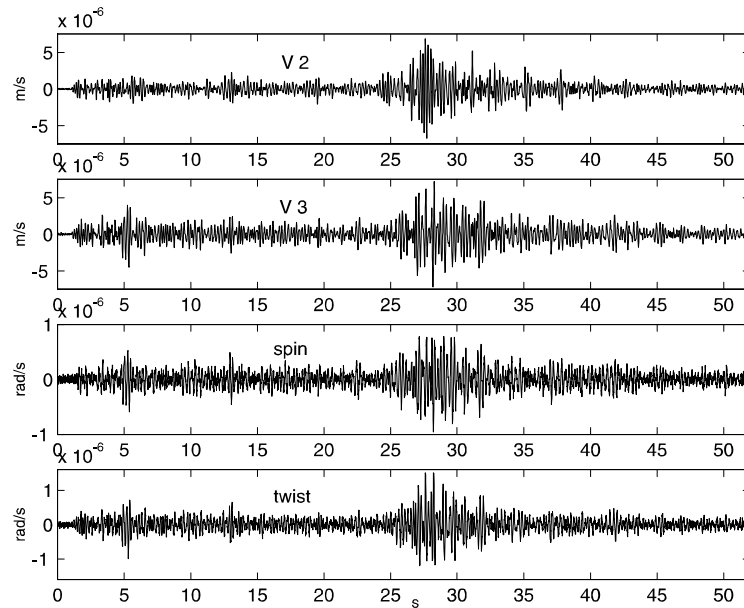


Fig. 3. Recorded at Książ, 6 February 2002, Silesia, 01:31:25.5. Middle frequencies, the pass band 2.6-43 Hz. From the top: channel 2, channel 3, spin, twist.

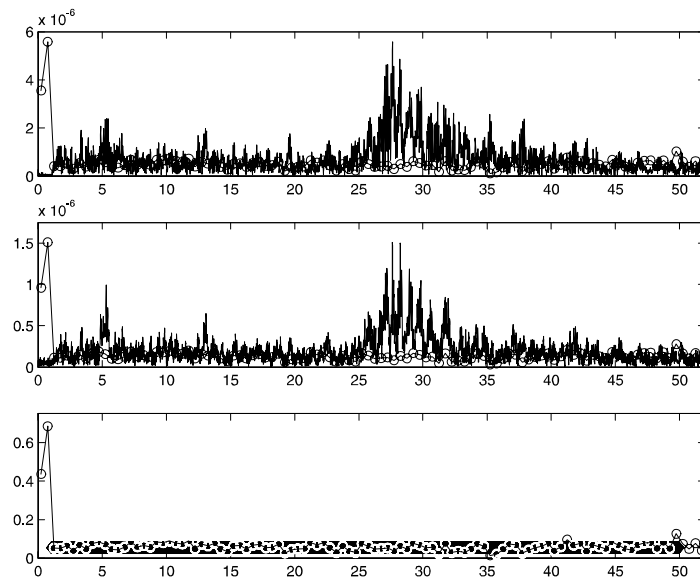


Fig. 4. Recorded at Książ, 6 February 2002, Silesia, 01:31:25.5. Middle frequencies, the pass band 2.6-43 Hz. Top panel: Comparison of mean displacement velocity and  $R_m$  indexes (circles), given in different scales; Middle: Comparison of mean absolute, reduced differences within a pair and  $R_m$  indexes (circles), given in different scales; Bottom:  $R_m$  indexes in the real scale, black bar denotes central part of the shock record, for which  $R_{mc}$  index was calculated, its vertical position denotes the  $R_{mc}$  value. For the time period 1 to 50 s:  $R_r = 0.023$ ,  $R_t = 0.044$ ,  $R_{mc} = 0.054$ .

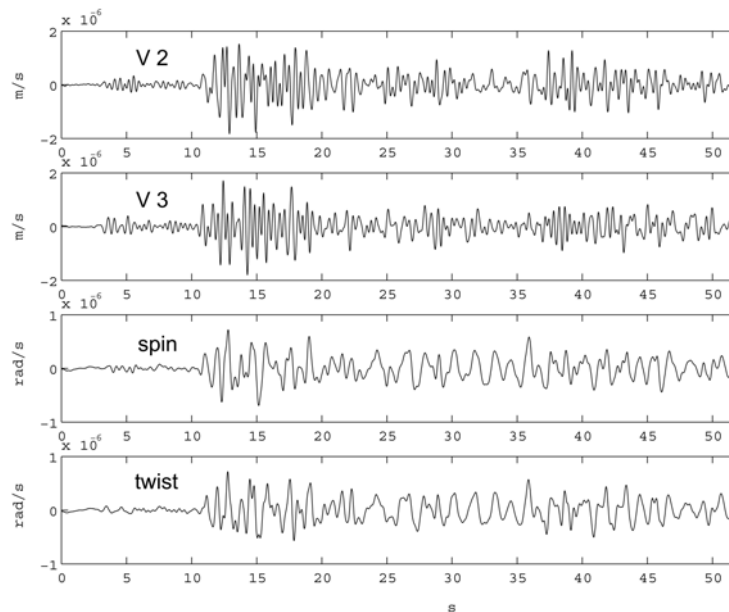


Fig. 5. Recorded at Ojców, 20 March 2004, Silesia, 03:12:42.8. Low frequencies, the pass band 0.3-3 Hz. From the top: channel 2, channel 3, spin, twist.

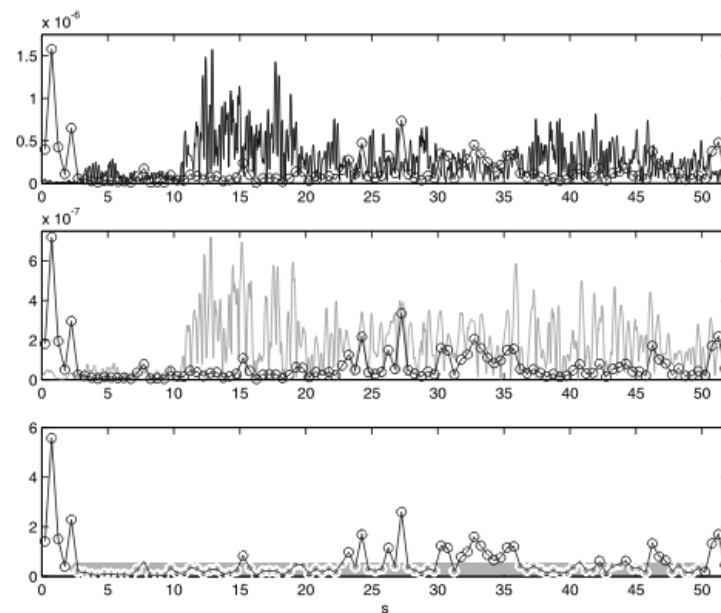


Fig. 6. Recorded at Ojców, 20 March 2004, Silesia, 03:12:42.8. Low frequencies, the pass band 0.3-3 Hz. Top panel: Comparison of mean displacement velocity and  $R_m$  indexes (circles), given different scales; Middle: Comparison of mean absolute, reduced differences within a pair and  $R_m$  indexes (circles), given different scales; Bottom:  $R_m$  indexes in the real scale, black bar denotes central part of the shock record, for which  $R_{mc}$  index was calculated, its vertical position denotes the  $R_{mc}$  value. For the time-period 2.5-50 s:  $R_r = 0.24$ ,  $R_l = 0.24$ ,  $R_{mc} = 0.31$ .

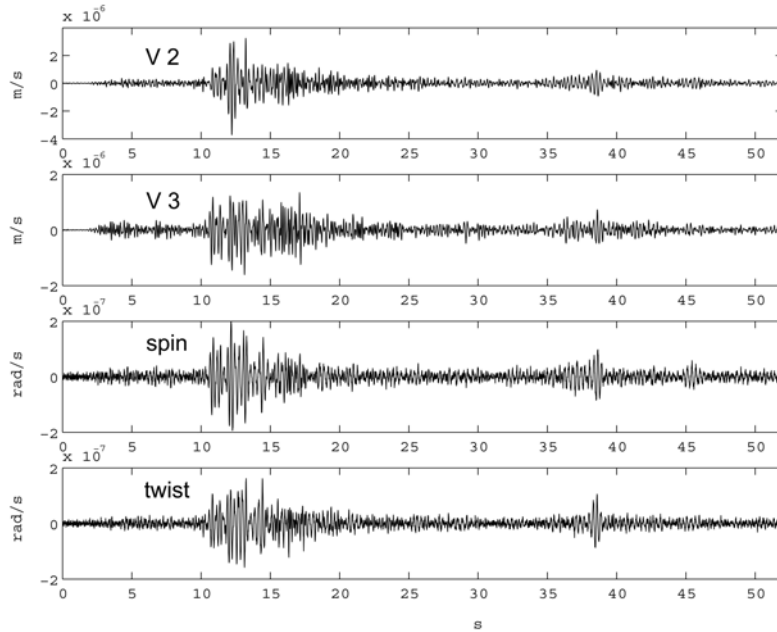


Fig. 7. Recorded at Ojców, 20 March 2004, Silesia, 03:12:42.8. Middle frequencies, the pass band 2.6-43 Hz. From the top: channel 2, channel 3, spin, twist.

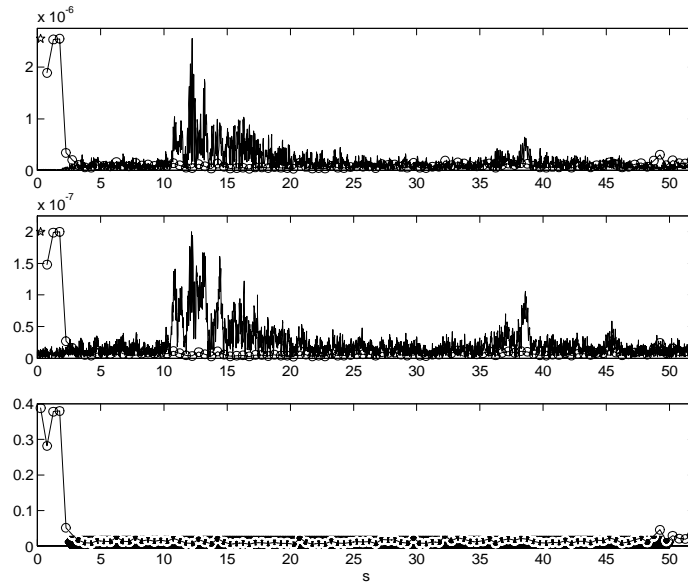


Fig. 8. Recorded at Ojców, 20 March 2004, Silesia, 03:12:42.8. Middle frequencies, the pass band 2.6-43 Hz. Top panel: Comparison of mean displacement velocity and  $R_m$  indexes (circles), given different scales; Middle: Comparison of mean absolute, reduced differences within a pair and  $R_m$  indexes (circles), given different scales; Bottom:  $R_m$  indexes in the real scale, black bar denotes central part of the shock record, for which  $R_{mc}$  index was calculated, its vertical position denotes the  $R_{mc}$  value. For the time-period 2.5-50 s:  $R_r = 0.0076$ ,  $R_l = 0.0057$ ,  $R_{mc} = 0.011$ .

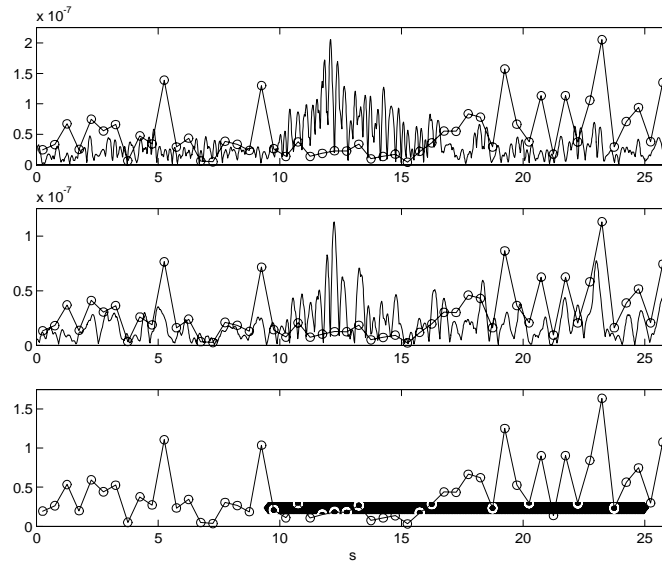


Fig. 9. Recorded at Ojców, 22 March 2004, Silesia, 10:22:24.5. Low frequencies, the pass band 0.3-3 Hz. Top panel: Comparison of mean displacement velocity and  $R_m$  indexes (circles), given different scales; Middle: Comparison of mean absolute, reduced differences within a pair and  $R_m$  indexes (circles), given different scales; Bottom:  $R_m$  indexes in the real scale, black bar denotes central part of the shock record, for which  $R_{mc}$  index was calculated, its vertical position denotes the  $R_{mc}$  value. For the time period 9.5 to 25 s:  $R_r = 0.16$ ,  $R_t = 0.195$ ,  $R_{mc} = 0.24$ .

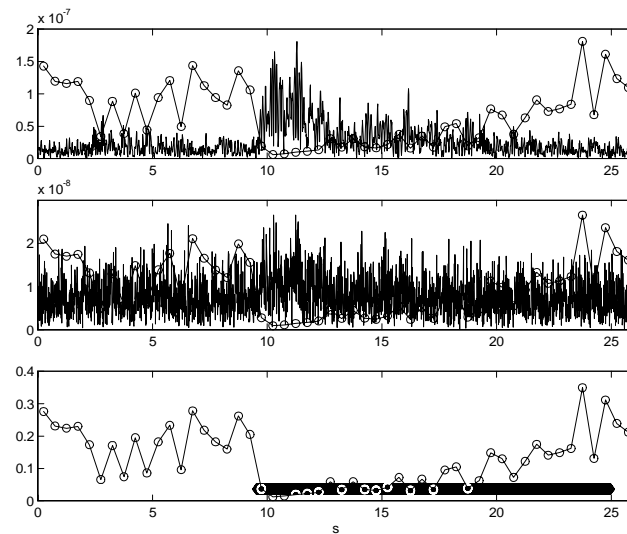


Fig. 10. Recorded at Ojców, 22 March 2004, Silesia, 10:22:24.5. Middle frequencies, the pass band 2.6-43 Hz. Top panel: Comparison of mean displacement velocity and  $R_m$  indexes (circles), given different scales; Middle: Comparison of mean absolute, reduced differences within a pair and  $R_m$  indexes (circles), given different scales; Bottom:  $R_m$  indexes in the real scale, black bar denotes central part of the shock record, for which  $R_{mc}$  index was calculated, its vertical position denotes the  $R_{mc}$  value. For the time period 9.5 to 25 s:  $R_r = 0.024$ ,  $R_t = 0.02$ ,  $R_{mc} = 0.036$ .

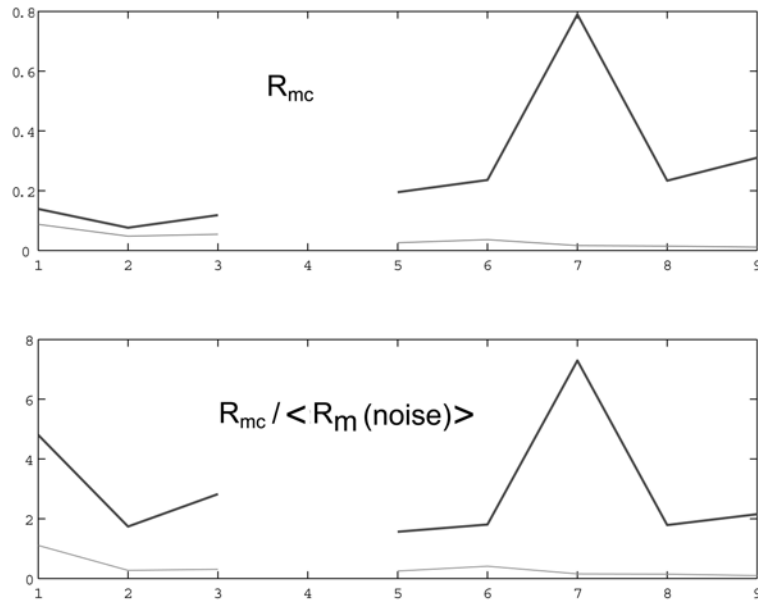


Fig. 11. Upper panel: indices  $R_{mc}$  for the analysed shocks. Lower the  $R_{mc} / \langle R_m(\text{noise}) \rangle$  quotients. The results from Książ on the left, from Ojców on the right. Thick line – analysis in low frequencies, thin line – the middle frequencies. The seismic events are arranged in accord with increasing distance to the recording station.

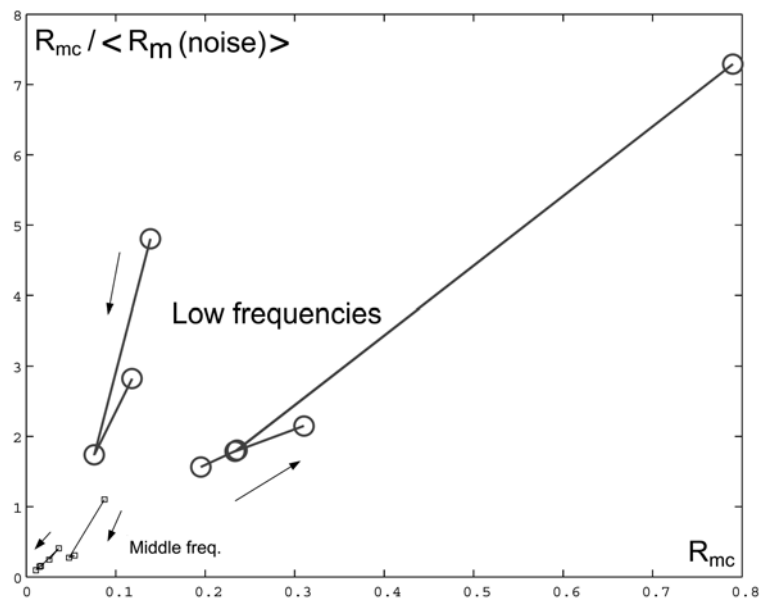


Fig. 12. The  $R_{mc} / \langle R_m(\text{noise}) \rangle$  quotients versus indices  $R_{mc}$  for all analysed cases. Circles – results of analysis in low frequencies, squares – for middle frequencies. Arrows show the direction in the sequence in which the distance between focal zone and the station increases. Sequences of three events are from Książ, while sequences of five events from Ojców.

For each case the following data are given: date and region, the distance from the recording station (if known), time (UTC) of the  $P$ -wave arrival, magnitude  $M_m$  (if known), the  $\Delta_{PS}$  delay and – for both frequency ranges – maximum velocity of displacement in the ordinary signal (after filtration and normalisation), indexes  $R_r$ ,  $R_t$  and  $R_{mc}$ , and also the ratio of  $R_{mc}$  to mean of two  $R_m$ -indexes calculated for two quiet periods of noise (far before the shock, two stages of equal length, 2 or 8 seconds). Also the period is given, for which indexes  $R_r$ ,  $R_t$  and  $R_{mc}$  were counted, in relation to the beginning of diagram.

### **Results from Książ, 2002**

#### 13 February, region of Wałbrzych

10:53:13.6,  $\Delta_{PS} = 2.4$  s

Low frequencies

Max.  $v$  of displacement =  $1.8 * 10^{-6}$

$R_r = 0.11$ ,  $R_t = 0.057$ ,  $R_{mc} = 0.14$

for 4-15 s

$R_{mc}/\langle R_m(\text{noise}) \rangle = 4.8$

Middle frequencies, noise reduction

Max.  $v$  of displacement =  $2.14 * 10^{-6}$

$R_r = 0.042$ ,  $R_t = 0.065$ ,  $R_{mc} = 0.087$

for 4-15 s

$R_{mc}/\langle R_m(\text{noise}) \rangle = 1.1$

#### 17 February, region of Lubin

08:54:09.9,  $M_m = 2.4$ ,  $\Delta_{PS} = 8.7$  s

Low frequencies, noise reduction

Max.  $v$  of displacement =  $1.9 * 10^{-6}$

$R_r = 0.061$ ,  $R_t = 0.031$ ,  $R_{mc} = 0.076$

for 5-42 s

$R_{mc}/\langle R_m(\text{noise}) \rangle = 1.74$

Middle frequencies, noise reduction

Max.  $v$  of displacement =  $4.3 * 10^{-6}$

$R_r = 0.018$ ,  $R_t = 0.04$ ,  $R_{mc} = 0.048$

for 5-42 s

$R_{mc}/\langle R_m(\text{noise}) \rangle = 0.274$

#### 6 February, Silesia

01:31:25.5,  $M_m = 3.2$ ,  $\Delta_{PS} = 23.4$  s

Low frequencies

See – Figs. 1 and 2

Max.  $v$  of displacement =  $6.1 * 10^{-6}$

$R_r = 0.067$ ,  $R_t = 0.085$ ,  $R_{mc} = 0.12$

for 1-50 s

$R_{mc}/\langle R_m(\text{noise}) \rangle = 2.82$

Middle frequencies

See – Figs. 3 and 4

Max.  $v$  of displacement =  $7.1 * 10^{-6}$

$R_r = 0.023$ ,  $R_t = 0.044$ ,  $R_{mc} = 0.054$

for 1-50 s

$R_{mc}/\langle R_m(\text{noise}) \rangle = 0.306$

### **Results from Ojców, 2004**

22 March, local. For each  $R_m$ , 20 samples were taken, not 50.

23:48:56,  $\Delta_{PS} \sim 2$  s

Low frequencies

Max.  $v$  of displacement =  $4.5 * 10^{-7}$

$R_r = 0.17, R_t = 0.12, R_{mc} = 0.2$

for 2-16 s

$R_{mc}/\langle R_m(\text{noise}) \rangle = 1.57$

Middle frequencies

Max.  $v$  of displacement =  $5 * 10^{-7}$

$R_r = 0.017, R_t = 0.015, R_{mc} = 0.026$

for 2-16 s

$R_{mc}/\langle R_m(\text{noise}) \rangle = 0.247$

22 March, Silesia,  $d = 57$  km

10:22:24.5,  $Mm = 2.0, \Delta_{PS} = 7.5$  s

Low frequencies

See – Fig. 9

Max.  $v$  of displacement =  $3.25 * 10^{-7}$

$R_r = 0.16, R_t = 0.195, R_{mc} = 0.24$

for 9.5-25 s

$R_{mc}/\langle R_m(\text{noise}) \rangle = 1.81$

Middle frequencies

See – Fig. 10

Max.  $v$  of displacement =  $2 * 10^{-7}$

$R_r = 0.024, R_t = 0.02, R_{mc} = 0.036$

for 9.5-25 s

$R_{mc}/\langle R_m(\text{noise}) \rangle = 0.41$

22 March, Silesia,  $d = 61$  km

10:26:21.5,  $Mm = 2.5, \Delta_{PS} = 8.2$  s

Low frequencies

Max.  $v$  of displacement =  $1.3 * 10^{-6}$

$R_r = 0.7, R_t = 0.59, R_{mc} = 0.79$

for 2.5-50 s

$R_{mc}/\langle R_m(\text{noise}) \rangle = 7.29$

Middle frequencies

Max.  $v$  of displacement =  $9 * 10^{-7}$

$R_r = 0.011, R_t = 0.0087, R_{mc} = 0.016$

for 2.5-50 s

$R_{mc}/\langle R_m(\text{noise}) \rangle = 0.156$

22 March, Silesia,  $d = 62$  km

18:58:14,  $Mm = 2.5, \Delta_{PS} = 8.3$  s

Low frequencies

Max.  $v$  of displacement =  $1.4 * 10^{-6}$

$R_r = 0.18, R_t = 0.17, R_{mc} = 0.23$

for 5-35 s

$R_{mc}/\langle R_m(\text{noise}) \rangle = 1.79$

Middle frequencies

Max.  $v$  of displacement =  $8.6 * 10^{-7}$

$R_r = 0.01, R_t = 0.008, R_{mc} = 0.015$

for 5-35 s

$R_{mc}/\langle R_m(\text{noise}) \rangle = 0.146$

20 March, Silesia,  $d = 66$  km

03:12:42.8,  $Mm = 2.1, \Delta_{PS} = 8.5$  s

Low frequencies

See – Figs. 5 and 6

Middle frequencies

See – Figs. 7 and 8

Max.  $v$  of displacement =  $1.8 * 10^{-6}$

$R_r = 0.24, R_t = 0.24, R_{mc} = 0.31$

for 2.5-50 s

$R_{mc}/\langle R_m(\text{noise}) \rangle = 2.15$

Max.  $v$  of displacement =  $3.5 * 10^{-6}$

$R_r = 0.0076, R_t = 0.0057, R_{mc} = 0.011$

for 2.5-50 s

$R_{mc}/\langle R_m(\text{noise}) \rangle = 0.095$

Results of low- and middle-frequency analysis of the same case are compared. In three cases from Książ, the maximum displacement velocity was bigger in middle frequencies, in two cases from Ojców it was roughly the same in both frequency ranges, and for two other cases it was smaller than in the low frequencies.

In all the cases analysed in this work, index  $R_{mc}$  is smaller for middle frequencies; in registrations from Ojców the difference is about one order of magnitude. Also the ratio  $R_{mc}/\langle R_m(\text{noise}) \rangle$  is smaller in middle frequencies, and almost always  $< 1$  (this means that in the noise preceding these events the rotational components had greater share than in the events, excluding their starting and ending part). The  $R_r$  and  $R_t$ -indexes were in almost every case smaller for middle frequencies, with the exception of seismic event from Wałbrzych region, 2002.02.06, where the  $R_t$ -index, in the middle frequencies, was found to be slightly bigger.

### 3. Discussion and Cumulative Results

The time-varying proportion of the seismic energy arriving to the station in rotational vibrations reflects the processes in the source. The great share of this part of seismic energy at the start of tremor is especially characteristic. Such results, quite similar to those obtained in other regions, will be more easy to interpret when simultaneous records from many stations will be accessible.

In cases of weak shocks, in the records of rotational or differential signals, it is hard to find the beginning of tremor. But a sharp decrease of  $R_m$ -index, in middle-frequencies analysis, helps to find arrivals of  $P$ -waves in these plots.

These results should be tested by further studies, especially related to possible relation between maximal amplitude of ordinary signal and the rotational components share in seismic energy released in the shock. We shall note that such a relation was found for seismic events near l'Aquila (Teisseyre K.P. and Suchcicki 2006) and on Pasterze glacier (Górski and Teisseyre K.P. 2006).

An interesting observation was made while analyzing the tremors recorded at Pasterze Glacier: quite often a transient increase of rotational components occurred **before** the registered arrival of basic seismic waves, and also after the main part of the shock there appeared relatively strong rotational oscillations. Some explanations of this finding are given in Górski and Teisseyre K.P. (2006); it is possible that in the focal zones some rotational movements occur already before the tremor, in preparatory stage and also after the shock. Existence of such motions in the focal zone has been postulated by Teisseyre R. et al. (2006). A search for pre- and post-shock rotary undulations has been conducted also in the present study; results, however, appear ambiguous.

Hypotheses of pre- and post-event rotational vibrations and existence of relatively long periods of coda waves, also bearing rotational components, may lead to looking at the seismic noise as fertile field of hidden, but very interesting data. This may also lead to conclusion that rotational components “behave” chaotically. Search for order in this domain has only begun. In this work, the content of rotation movements in the central part of the analysed events was compared with rotation content in the noise, by calculation of the quotients  $R_{mc}/\langle R_m(\text{noise}) \rangle$ . For low-frequency analysis these quotients appeared higher than 1 and for middle frequencies – usually lower (as it was mentioned, see Fig. 11); this means that in the seismic event, rotation movements emanate as low frequency waves (here: results for 0.3-3 Hz band), while the basic seismic motions – as oscillations in higher frequencies.

It appears that the  $R_{mc}$ -index (recall that it is, a measure of relative share of rotation motions in the seismic energy emitted in the shock’s main part) is positively correlated with the ratio  $R_{mc}/\langle R_m(\text{noise}) \rangle$ ; a greater share of rotational motions in the seismic event corresponds with proportion  $R_{mc}/\langle R_m(\text{noise}) \rangle$  biased toward the shock, not toward the noise. This is true also for middle frequencies results, despite general prevalence of the noise in rotational competition in this frequency band (see Fig. 12, lower left corner). Too small number of seismic events analysed in this work does not allow to compute any distance effects.

For distant shocks, the rotational components often are masked by noise. Removing the noise contribution by signal processing methods, spectral methods including, helps to some extent. Alas, it was found that if the seismic event is not visible in the rotational signal, the attempt to remove the noise by the spectral method fails. What is interesting, some very remote but strong earthquakes are visible in the rotational signals, for example, on Crete – 2002.01.22, 04:57'45 (registration in Książ), and near Sumatra – 2004.12.26, 00:58 (registration in Ojców).

## References

- Górski, M., and K.P. Teisseyre, 2006, *Glacier Motion: Seismic Events and Rotation/Tilt Phenomena*. **In:** R. Teisseyre, M. Takeo and E. Majewski (eds.) “Earthquake Source Asymmetry, Structural Media and Rotation Effects”, Springer, Berlin, Heidelberg, New York.
- Teisseyre, K.P., and J. Suchcicki, 2006, *Rotation Motions: Recording and Analysis*. **In:** R. Teisseyre, M. Takeo and E. Majewski (eds.) “Earthquake Source Asymmetry Structural Media and Rotation Effects”, Springer, Berlin, Heidelberg, New York.
- Teisseyre, K.P., M. Górski and J. Suchcicki, 2004, *Seismic events and rotation waves in the Hans Glacier, Spitsbergen, and the Pasterze Glacier, Austria*, Acta Geophys. Pol. **52**, 4, 465-476.
- Teisseyre, R., 2005, *Asymmetric continuum mechanics: deviations from elasticity and symmetry*, Acta Geophys. Pol. **53**, 2, 115-126.

- Teisseyre, R., M. Białecki and M. Górski, 2005, *Degenerated mechanics in a homogeneous continuum: potentials for spin and twist*, Acta Geophys. Pol. **53**, 3, 219-230.
- Teisseyre, R., J. Suchcicki and K.P. Teisseyre, 2003a, *Recording the seismic rotation waves: reliability analysis*, Acta Geophys. Pol. **51**, 1, 37-50.
- Teisseyre, R., J. Suchcicki, K.P. Teisseyre, J. Wiszniowski and P. Palangio, 2003b, *Seismic rotation waves: basic elements of theory and recording*, Annals of Geophysics **46**, 4, 671-685.
- Teisseyre, R., K.P. Teisseyre, T. Moriya and P. Palangio, 2003c, *Seismic rotation waves related to volcanic, mining and seismic events: near-field and micromorphic motions*, Acta Geophys. Pol. **51**, 4, 409-431.
- Teisseyre, R., M. Górski and K.P. Teisseyre, 2006, *Fracture-Band Geometry and Rotation Energy Release*. In: R. Teisseyre, M. Takeo and E. Majewski (eds.) "Earthquake Source Asymmetry, Structural Media and Rotation Effects", Springer, Berlin, Heidelberg, New York.

*Accepted October 16, 2006*

## Tomography Imaging Through the Monte Carlo Sampling

Wojciech DEBSKI

Institute of Geophysics, Polish Academy of Sciences  
ul. Księcia Janusza 64, 01-452 Warszawa, Poland  
debski@igf.edu.pl

### A b s t r a c t

This paper illustrates advantages of the Bayesian approach to seismic tomography imaging enhanced by the Monte Carlo sampling technique. The theoretical considerations are illustrated by an analysis of seismic data from Rudna (Poland) copper mine. Contrary to the classical *LSQR* techniques, the Bayesian approach allows to construct not only the “best fitting” model of the sought velocity distribution but also other estimators like, for example, the average model which is often expected to be a more robust estimator than the maximum likelihood solution. We demonstrate that using the Markov Chain Monte Carlo sampling technique within the Bayesian approach opens a possibility of an analysis of tomography imaging uncertainties with a minimal additional computational effort compared to the robust optimization approach.

### 1. Introduction

Seismic velocity tomography is the inversion technique aimed at imaging spatial distribution of velocity heterogeneities in global, regional, local or even laboratory scale problems. It relies on the high frequency approximation according to which seismic energy may be assumed to propagate along a thin “tube” between a source and a receiver, called the ray path. Thus, the energy travel time between two points provides information on the average seismic velocity along the ray path. If the travel time data are available for a number of ray paths probing different parts of the studied area, it becomes possible to obtain a spatial map of the local heterogeneities of the velocity distribution – the velocity image called also a tomogram.

The basic tomography forward problem formula relates the observable travel time data  $d^{obs}$  with the slowness distribution  $s(\mathbf{r})$  and reads (Aki and Richards 1985)

$$\mathbf{d}^{th}(\mathbf{s}) = \int_{ray[\mathbf{s}]} \mathbf{s}(\mathbf{r}) dl \quad (1)$$

where  $\mathbf{s}(\mathbf{r})$  denotes slowness (inverse of velocity),  $\mathbf{d}^{th}$  is the predicted travel time, and the integral is taken along a seismic ray path. The ray path depends on the slowness distribution; consequently, the above relation between  $\mathbf{d}^{th}$  and  $\mathbf{s}$  is highly nonlinear what manifests itself in a bending of the ray path. However, this effect may often be neglected in case of local seismic tomography if the slowness distribution does not have large gradients (Cardarelli and Cerrito 2002). Such a simplification makes the tomography problem easier to solve at the cost of a slight loss of sharpness of tomograms (Maxwell and Young 1993). We follow this assumption through the analysis presented here.

Having a set of travel times data  $\mathbf{d} = (t_1, t_2, \dots, t_N)$  recorded for different source-receiver pairs and having the discretized slowness distribution (for example, assuming that the images may be described as a set of homogeneous cells) the linearized tomography forward problem turns to a set of linear equations (Nolet 1987)

$$d_i^{th} = \sum_j^M G^{ij} s_j \quad i = 1 \dots N \quad (2)$$

where  $\mathbf{s} = (s_1, s_2, \dots, s_M)$  is the vector of discretized slowness field and  $\mathbf{G}$  is a matrix whose elements  $G^{ij}$  are equal fractions of  $i$ -th ray path in a  $j$ -th cell.

An estimation of the slowness parameters  $\mathbf{s}$  can be carried out in various ways, among which a version of the direct algebraic solution and the optimization approach are the most often used (Iyer and Hirahara 1993). Another, Bayesian approach based on the sampling of the *a posteriori* probability density is the method which, following the pioneer work of Tarantola and Vallet (1982) (see also Sambridge and Mosegaard (2002) for a review of the history of application of the Monte Carlo technique in geophysics) is recently gaining greater and greater popularity (Curtis and Lomax 2001, Bosch *et al.* 2000, Mosegaard and Tarantola 2002, Dębski 2004). Both approaches are shortly described below.

## 2. Tomography Imaging – Theory

### 2.1 Classical approach

If the forward modeling formula given by Eq. 1 can be linearized, the relation between the data  $\mathbf{d}$  and model parameters  $\mathbf{s}$  (slowness) takes the form of a set of linear equations

$$\mathbf{d} = \mathbf{G} \cdot \mathbf{s}, \quad (3)$$

and the problem of estimation of  $\mathbf{s}$  from  $\mathbf{d}^{obs}$  can be viewed as the task of solving the set of linear equations after the substitution  $\mathbf{d} = \mathbf{d}^{obs}$ . This task can be accomplished within a simple algebraic approach (Menke 1989, Tarantola 1987, Parker 1994) by matrix manipulation, as follows.

In the first step, the so-called normal equation is formed by multiplying both sides of Eq. 3 by the transposed  $\mathbf{G}^T$  operator(matrix)

$$\mathbf{G}^T \mathbf{d}^{obs} = (\mathbf{G}^T \cdot \mathbf{G}) \mathbf{s}. \quad (4)$$

The matrix  $\mathbf{G}^T \mathbf{G}$  is a square matrix which usually cannot be inverted yet because of possible singularity. To fix this problem, the  $\mathbf{G}^T \mathbf{G}$  matrix is regularized which, in the simplest case, is achieved by adding a small diagonal term:

$$\mathbf{G}^T \cdot \mathbf{G} \longrightarrow \mathbf{G}^T \cdot \mathbf{G} + \gamma \mathbf{I} \quad (5)$$

where  $\mathbf{I}$  is a diagonal matrix. Finally, the analytical formula for the model  $\mathbf{s}^{lsqr}$  regarded as the solution can be cast into the form with the explicitly introduced initial (*a priori*) model  $\mathbf{s}^{apr}$  (Menke 1989, Tarantola 1987)

$$\mathbf{s}^{lsqr} = \mathbf{s}^{apr} + (\mathbf{G}^T \cdot \mathbf{G} + \gamma \mathbf{I})^{-1} \mathbf{G}^T (\mathbf{d}^{obs} - \mathbf{G} \mathbf{s}^{apr}) + O(\gamma^2). \quad (6)$$

This form is particularly convenient when  $\mathbf{s}^{lsqr}$  is estimated iteratively (Tarantola 1987) and is *de facto* the starting point of various linear inversion techniques (Parker 1994, Limes and Treitel 1983).

The above formula for  $\mathbf{s}^{lsqr}$  in fact coincides with the solution obtained by the optimization approach, when the least squares difference between observed and modeled travel times is minimized, subject to an additional “smoothness” condition. For this reason, this method is often called the *LSQR* (Damped Least Squares) solution (Parker 1994, Menke 1989).

## 2.2 Bayesian point of view

The method shortly described above is very popular and most often used in everyday practice (Zhao 2001, Iyer and Hirahara 1993, Nolet 1987). The drawback of this approach is the lack of a reliable estimation of the quality of the image found, because the solution is just a single (optimum) model. The method provides no information on how large is a region in the model space around the best solution such the models (slowness distribution) taken from it lead to similar predictions as the optimum model.

The above drawbacks of the classical method are conveniently overcome when the Bayesian inverse theory is applied to the tomography problem in hand (Bosch 1999, Dębski 2004).

The solution of the tomography inverse problem according to the Bayesian inverse theory consists in building the *a posteriori* probability distribution  $\sigma(\mathbf{s})$  over the model space which describes the probability of a given model (slowness distribution  $\mathbf{s}$ ) being the true one (Tarantola 1987, Dębski 2004). It has been shown by Tarantola and Vallete (1982), Tarantola (1987), Jackson and Matsu'ura (1985) that  $\sigma(\mathbf{s})$  is the product of the distribution  $f(\mathbf{s})$  describing *a priori* information by the *likelihood function*  $L(\mathbf{s})$  which measures to what extent theoretical predictions fit the observed data:

$$\sigma(\mathbf{s}) = \text{const.} f(\mathbf{s}) L(\mathbf{s}) \quad (7)$$

where the constant represents normalization of the probability density and the *likelihood function*  $L(\mathbf{s})$  reads (see, for instance, Tarantola 1987, Duijndam 1988, Jackson and Matsu'ura 1985)

$$L(\mathbf{s}) = \exp \left\{ -\|\mathbf{d}^{obs} - \mathbf{d}^{th}(\mathbf{s})\| \right\} \quad (8)$$

and the symbol  $\|\cdot\|$  stands for a norm used to measure the “distance” between two vectors.

Knowledge of the  $\sigma(\mathbf{s})$  distribution allows not only to find the most likelihood model  $\mathbf{s}^{ml}$  for which  $\sigma(\mathbf{s}^{ml}) = \max$  but also other characteristics like, for example, the average model

$$\mathbf{s}^{avr} = \int_{\mathcal{M}} \mathbf{s} \sigma(\mathbf{s}) d\mathbf{s}, \quad (9)$$

and the covariance matrix

$$\mathbf{C}_{ij}^p = \int_{\mathcal{M}} (\mathbf{s}_i - \mathbf{s}_i^{avr})(\mathbf{s}_j - \mathbf{s}_j^{avr}) \sigma(\mathbf{s}) d\mathbf{s}. \quad (10)$$

These two basic characteristics of the *a posteriori* distribution  $\sigma(\mathbf{s})$  are indeed very important. The importance of the average model  $\mathbf{s}^{avr}$  comes from the fact that it provides not only information on the best fitting model but also includes information about other plausible models from the neighborhood of the “best” model  $\mathbf{s}^{ml}$ . If sub-optimum models defined as those for which  $\sigma(\mathbf{s}) \sim \sigma(\mathbf{s}^{ml})$  are similar to  $\mathbf{s}^{ml}$ , then  $\mathbf{s}^{avr} \sim \mathbf{s}^{ml}$ . The diagonal elements of the *a posteriori* covariance matrix  $\mathbf{C}^p$  are convenient estimators of the inversion uncertainties for each component of  $\mathbf{s}$  while the non-diagonal elements measure the degree of correlation between pairs of parameters

(Menke 1989, Jeffreys 1983). In fact,  $\mathbf{C}^p$  given by Eq. 10 is a generalization of the *LSQR* covariance matrix to the case of an arbitrary statistics  $\sigma(\mathbf{s})$  including possibly nonlinear forward problems. As in the case of the average model, the posterior covariance matrix is meaningful only if the  $\sigma(\mathbf{s})$  distribution is unimodal. In cases of multi-modality, the existence of non-resolved directions in the model space, or other “pathologies”, a more exhaustive error analysis is necessary by a full inspection of the *a posteriori* distribution (Tarantola 1987, Wiejacz and Dębski 2001). This can be achieved, for example, by calculating the higher-order moments of the *a posteriori* distribution (Jeffreys 1983).

### 2.3 Sampling a posteriori PDF

To calculate the point estimators like the average model and the covariance matrix, we face the problem of sampling of  $\sigma(\mathbf{s})$ , usually in the context of calculation of multidimensional integrals as in Eqs. 9, 10.

More generally, we may need to calculate the average integrals represented in a general form as

$$\langle F \rangle = \int_{\mathcal{M}} F(\mathbf{s})\sigma(\mathbf{s})d\mathbf{s} \quad (11)$$

where  $F(\mathbf{s})$  is an arbitrary function of  $\mathbf{s}$ .

If the number of parameters is very small (smaller than, say, 10), the integral in Eq. 11 can be calculated by sampling of  $\sigma(\mathbf{s})$  over a predefined regular grid like, for example, in the case of the seismic source location problem (Wiejacz and Dębski 2001, Lomax *et al.* 2000, Sambridge and Kennett 2001). Otherwise, the stochastic Monte Carlo technique (*MC*) is to be used (Mosegaard and Tarantola 1995, Bosch *et al.* 2000, Dębski 2004).

Generally speaking, the *MC* technique allows to generate an ensemble of models which can be regarded as a set of samples drawn from the  $\sigma(\mathbf{s})$  distribution. Then, the integral  $\langle F \rangle$  can be approximated by (Robert and Casella 1999)

$$\langle F \rangle \approx \frac{1}{N} \sum_{\mathbf{s}^\alpha} F(\mathbf{s}^\alpha) \quad (12)$$

where the sum is taken over an ensemble of all  $N$  generated models  $\mathbf{s}^\alpha$ .

One of the greatest advantages of the possibility of calculating the statistical averages from the ensemble of the *MC* generated models is that inversion errors can be easily estimated with no additional cost. If they can be approximated by variance of the *a posteriori PDF* then the choice

$$F = (\mathbf{s} - \mathbf{s}^{avr})^2 \quad (13)$$

leads to the extremely simple, easy to calculate estimator of the *a posteriori* errors

$$\epsilon_a^2 = \frac{1}{N} \sum_{\mathbf{s}^\alpha} (\mathbf{s}^\alpha - \mathbf{s}^{avr})^2. \quad (14)$$

The choice of a sampling scheme of  $\sigma(\mathbf{s})$  (generating samples drawn from the  $\sigma(\mathbf{s})$ ) is by no means a trivial task especially when the number of estimated parameters is large (Mosegaard and Tarantola 2002, Bosch *et al.* 2000) like in the case of seismic tomography. This is caused by the fact that with an increasing number of parameters, the model space becomes extremely large but only its very small part contributes to the *a posteriori* distribution (Curtis and Lomax 2001). In cases like seismic tomography, only the Monte Carlo technique can be applied to solve practical problems. Among various *MC* algorithms, the most flexible and the most efficient for tomography problems seems to be the class of the Markov Chain Monte Carlo algorithms (*MCMC*).

These algorithms originally simulate Markovian stochastic processes (Gillespie 1992, Robert and Casella 1999) which “samples” a given stationary *PDF* (Tierney 1994, Mosegaard and Tarantola 2002, Robert and Casella 1999). The simplest form of such an algorithm, the Metropolis algorithm, is shown in Fig. 1.

- Initialize  $\mathbf{s}^0$
- Repeat
  - generate uniform random number  $u \sim U(0, 1)$
  - generate new test sample  $\mathbf{s}^\beta = \mathbf{s}^\alpha + \delta\mathbf{s}$   
where  $\delta\mathbf{s}$  is a small perturbation to the current sample
  - if  $u < P(\mathbf{s}^\beta, \mathbf{s}^\alpha) = \min \left[ 1, \frac{\sigma(\mathbf{s}^\beta)}{\sigma(\mathbf{s}^\alpha)} \right]$   
 $\mathbf{s}^{\alpha+1} = \mathbf{s}^\beta$   
 otherwise  
 $\mathbf{s}^{\alpha+1} = \mathbf{s}^\alpha$
- Continue until sufficient number of samples  $\{\mathbf{s}^\alpha\}$  is generated

Fig. 1: The Metropolis algorithm for sampling *a posteriori PDF*  $\sigma(\mathbf{s})$ .

### 3. Rudna Copper Mine Case

#### 3.1 Data, parametrization and inversion setup

The Bayesian algorithm was used to image the velocity distribution in a part of the Rudna copper mine in south-western Poland. The data set was collected during July, August and September 2004. The Rudna mine runs a digital seismic network composed of 32 vertical sensors located underground at depths from 550 m to 1150 m. Willmore seismometers MK-II and MK-III are used. The seismic signals are transmitted to a central site at the surface where they are digitized by a 14-bit converter. The frequency band of digitized data is from 0.5 to 150 Hz, and the final dynamics is about 70 dB. The sampling frequency which determines the absolute accuracy of travel time onset reading is  $F_s = 500$  Hz ( $C_d = 2$  ms). The uncertainty of event location is better than 100 m, typically around 50 m.

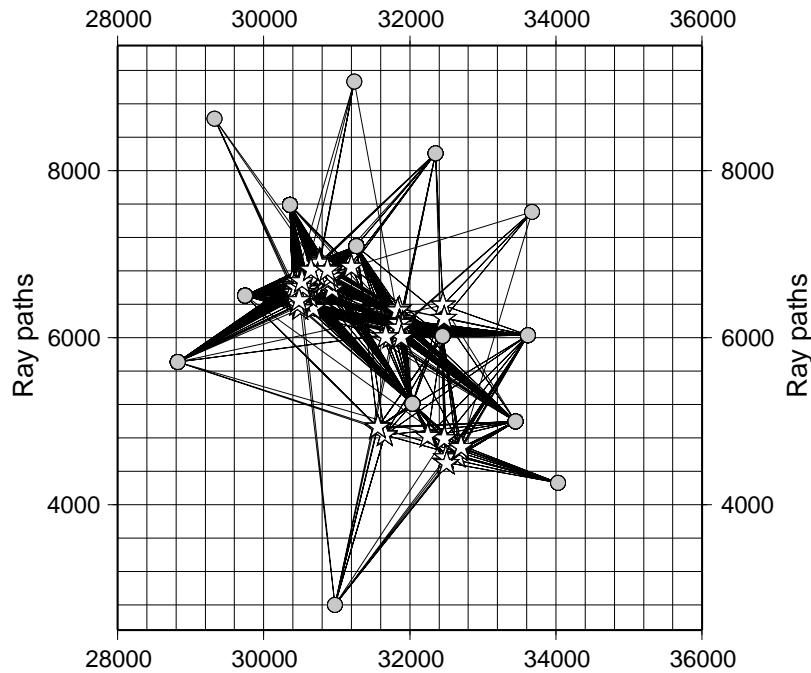


Fig. 2: Ray paths coverage of the studied region. Seismometer positions are marked by circles and the locations of seismic sources used in the current study are depicted by stars.

For the current study I selected a set of 36 events which occurred in the Rudna mine and were recorded by at least 4 out of the 8 nearby stations located almost at the same depth as the estimated hypocenters. This gave a total of 177 travel times used for P-wave velocity inversion. The distribution of selected events, employed stations and considered ray paths are shown in Fig. 2. The events were located assuming a constant background velocity,  $V_a = 5800$  m/s. This value was also taken as the initial *a priori* velocity model for the tomography inversion.

The studied area of around  $8 \times 8$  km was parameterized by division into 400 m by 400 m square cells, which meant 400 parameters to be estimated. However, most of these cells were probed by no ray, as shown in Fig. 2. In fact, only 107 cells were touched by at least one ray path. Only such cells were effectively considered during the inversion, and the *a priori* velocity  $V_a = 5800$  m/s was assigned to the remaining, untouched cells.

The Gaussian distributions with constant diagonal covariance matrices  $\mathbf{C}^{apr} = C_s \mathbf{I}$  and  $\mathbf{C}^p = C_d \mathbf{I}$  were used to model the *a priori*  $f(\mathbf{s})$  and the likelihood  $L(\mathbf{s})$  functions. The corresponding values of  $C_s$  and  $C_d$  were estimated in the following way. Firstly, I assumed *ad hoc* but on the basis of mining practice that velocity changes cannot exceed 10% of background velocity with a 95% confidence level. This *a priori* assumption corresponds approximately to the choice  $C_s^{-1} = 200$  m/s. The value of  $C_d$  is limited by the sampling period (2 ms) on the one hand and by the location errors on the other. Location errors of about 100 m lead to travel time inaccuracies of about 17 ms. I choose the intermediate value  $C_d = 10$  ms.

### 3.2 Results

The main results of the tomography imaging are shown in Figs. 3 and 4. Figure 3 shows the average velocity image obtained on the base of 500,000 models generated by the Metropolis algorithm sampling the *a posteriori* PDF. Spatial distribution of the imaging errors estimated by the diagonal elements of *a posteriori* covariance matrix according to Eq. 14 is shown in Fig. 4. In addition, Fig. 5 shows the travel time residua calculated for the *a posteriori* average model.

The very first step in evaluating tomography results relies on inspecting the residua for the model found. Figure 5 shows that *a posteriori* residua are well bounded within the *a priori* assumed value of data errors of 10 ms. In fact, the root mean square value of the residua is about 5.5 ms. Only for a few ray paths the differences between observed and modeled travel times are larger than  $2C_d$  amounting to 20 ms. It means that the *a posteriori* velocity model explains the travel time data quite well.

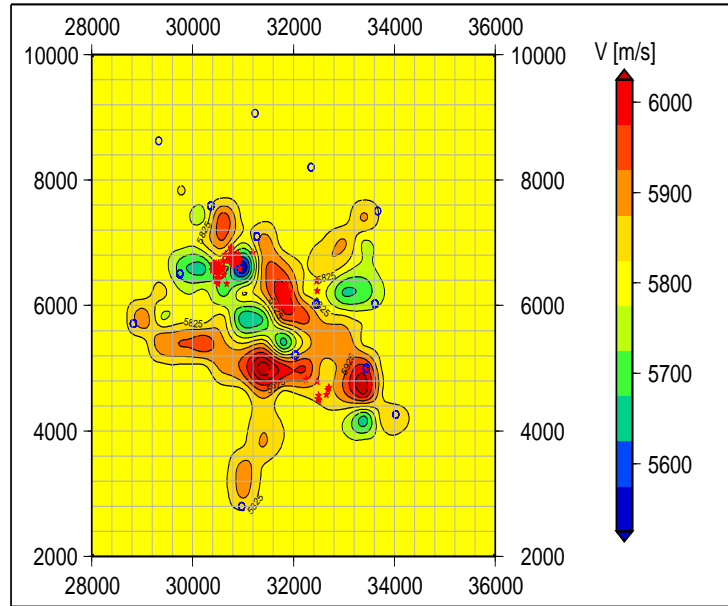


Fig. 3: Average velocity image obtained by the Monte Carlo sampling technique. The seismometers and epicenters of used seismic events are depicted by squares and white stars, respectively.

A more comprehensive insight into the imaging accuracy is obtained by an inspection of the *a posteriori* covariance matrix which is shown in Fig. 4.

Note that the *a priori* value  $C_s = 200$  m/s is attached to cells probed by no rays. The obtained distribution shows that within the applied velocity parameterization (cell size) the imaging errors were diminished with respect to  $C_s$  in the area well covered by ray paths. In the central part of this area, the *a posteriori* errors get values lower than 150 m/s. Let us note, however, that outside of it the imaging errors were generally larger than  $C_s$  which means that the velocity distribution in this part is poorly resolved by tomography. Finally, let us note the irregular shape of the area where the *a posteriori* errors are smaller than  $C_s$ .

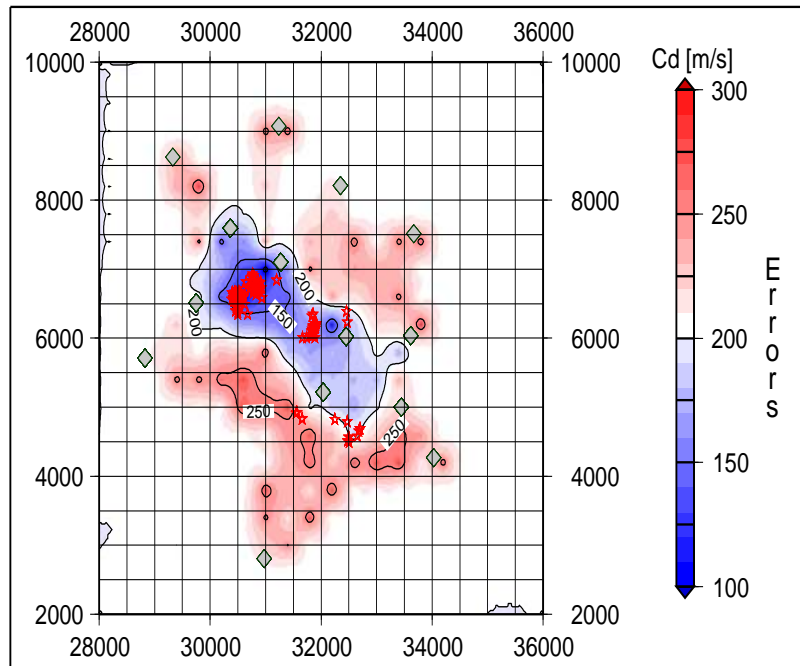


Fig. 4: Spatial distribution of imaging errors. The seismometers and epicenters of used seismic events are depicted by squares and stars, respectively. Notice a decrease of the *a posteriori* errors with respect to the *a priori* value  $C_s = 200$  m/s in the central, well resolved part of the imaging area, and their increase outside of it.

#### 4. Discussion

Two types of conclusions can be drawn on the basis of the studied case. The first one concerns the performance of the Bayesian approach enhanced by the *MCMC* sampling technique. Secondly, a very preliminary and quantitative physical interpretation of the obtained image can be attempted.

As follows from the presented case study, the *MCMC* sampling technique seems to be able to provide a quite robust estimation of the velocity distribution by an efficient generation of an ensemble of velocity models which follows the *a posteriori PDF*.

Following these comments, one can state that the Monte Carlo sampling for the solution of tomography imaging is a very promising technique which is able to provide

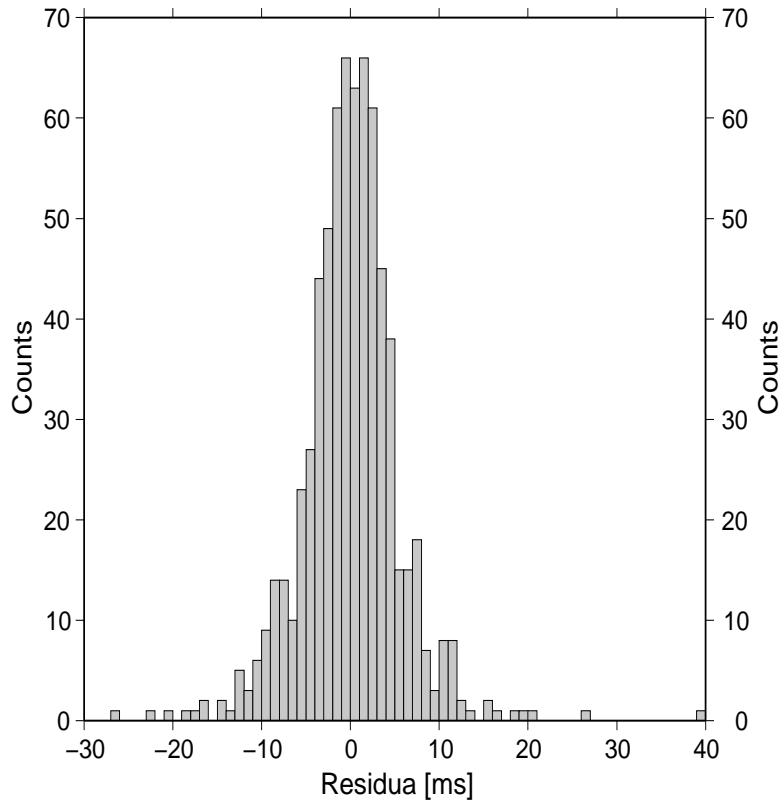


Fig. 5: Residua for the *a posteriori* average velocity model.

robust and more reliable images than any other currently used techniques. Its application is only limited by the size of the problem in hand. In the studied case, the simple Metropolis sampling algorithm was efficient enough to sample the *a posteriori PDF* due to the very small scale of the problem. In the case of larger-scale problems, when significantly more parameters have to be estimated (sampled), more complicated sampling techniques like, for example, the multi-step Metropolis algorithm, have to be employed (Robert and Casella 1999, Mosegaard and Tarantola 2002).

Finally, having obtained velocity distribution images, it is natural to attempt to try to infer information on the correlation of the velocity field with the observed seismicity. Although the current investigation was carried out to check numerical algorithms only, the obtained results seem to be robust enough to make some preliminary comments.

Firstly, note that the events used in the current studies formed a few spatial clusters, three of which are located in the well resolved region as shown in Fig. 4. For those

clusters, the tomography method has a sufficient resolution to map the velocity heterogeneities with the sufficient precision. The obtained tomogram suggests that two clusters located around  $x = 30500 - 31000$ ,  $y = 6500 - 7000$  occurred in the area where the velocity was smaller than background but high spatial velocity gradients are mapped. On the other hand, the cluster located at around  $x = 31800$ ,  $y = 6200$  appeared in the area where the velocity was higher than background but the mapped spatial velocity gradient is smaller than in the case of the previous clusters. No much can be said about other events, as they are located in regions poorly resolved by tomography.

Can the occurrence of the seismic clusters in the areas of the different velocity and velocity gradient characteristics suggest different mechanisms of induced seismicity? Unfortunately, it is impossible to answer this question within the current study. The limited spatial resolution due to the small number of seismic events, the non-homogeneous ray path coverage, and the finite accuracy of forward modeling prevents any more detailed attempt at a physical interpretation of the obtained results and prompts for the further, more detailed studies.

### References

- Aki, K., and P.G. Richards, 1985, *Quantitative Seismology*, San Francisco: Freeman and Co.
- Bosch, M. (1999). Lithologic tomography: From plural geophysical data to lithology estimation. *J. Geophys. Res.* 104(B1), 749–766.
- Bosch, M., C. Barnes and K. Mosegaard, 2000, *Multi-step samplers for improving efficiency in probabilistic geophysical inference*. In: P.C. Hansen, B.H. Jacobsen and K. Mosegaard (eds.), "Methods and Application of Inversion", vol. 92 of Lecture Notes in Earth Sciences, 50–68, Berlin: Springer.
- Cardarelli, E., and A. Cerrito, 2002, *Ray tracing in elliptical anisotropic media using the linear traveltimes interpolation (LTI) method applied to traveltimes seismic tomography*, *Geophys. Prosp.* **50** 55–72.
- Curtis, A., and A. Lomax, 2001, *Prior information, sampling distributions and the course of dimensionality*, *Geophysics* **66** (2), 372–378.
- Dębski, W., 2004, *Application of Monte Carlo techniques for solving selected seismological inverse problems*, *Publ. Inst. Geophys. Pol. Acad. Sc.* **B-34**(367), 1–207.

- Duijndam, A. (1988). Bayesian estimation in seismic inversion. part I: Principles. *Geophys. Prosp.* 36, 878–898.
- Gillespie, D. T. (1992). *Markov Processes - An Introduction for Physical Scientists*. San Diego: Academic Press, Inc.
- Iyer, H., and K. Hirahara, 1993, *Seismic Tomography, Theory and Practice*, London: Chapman and Hall.
- Jackson, D. D. and M. Matsu'ura (1985, January). A Bayesian approach to nonlinear inversion. *J. Geophys. Res.* 90(B1), 581–591.
- Jeffreys, H., 1983, *Theory of Probability*, Oxford: Clarendon Press.
- Limes, L. R. and S. Treitel (1983). Tutorial, a review of least-squares inversion and its application to geophysical problems. *Geophys. Prospect.* 32, 159–186.
- Lomax, A., J. Virieux, P. Volant and C. Berge, 2000, *Probabilistic earthquake location in 3D and layered models: Introduction of a Metropolis-Gibbs method and comparison with linear location*. In: C. Thurber, E. Kissling and N. Rabinovitz (eds.), "Advances in Seismic Event Location", Amsterdam: Kluwer.
- Maxwell, S.C., and R.P. Young, 1993, *A comparison between controlled source and passive source seismic velocity images*, Bull. Seismol. Soc. Am. **83** (6), 1813–1834.
- Menke, W., 1989, *Geophysical Data Analysis: Discrete Inverse Theory*, International Geophysics Series. San Diego: Academic Press.
- Mosegaard, K. and A. Tarantola (1995). Monte Carlo sampling of solutions to inverse problems. *J. Geophys. Res.* 100(B7), 12431–1247.
- Mosegaard, K., and A. Tarantola, 2002, *International Handbook of Earthquake Engineering Seismology*, Chapter Probabilistic Approach to Inverse Problems, pp. 237–265, Academic Press.
- Nolet, G. (1987). *Seismic Tomography*. Dordrecht: D. Reidel Publishing Company.
- Parker, R.L., 1994, *Geophysical Inverse Theory*, New Jersey: Princeton University Press.
- Robert, C.P., and G. Casella, 1999, *Monte Carlo Statistical Methods*, Springer Verlag.
- Sambridge, M., and K. Mosegaard, 2002, *Monte Carlo methods in geophysical inverse problems*, Rev. Geophys. **40**(3), 3.1–3.29.

- Sambridge, M. S. and B. L. N. Kennett (2001). Seismic event location: Nonlinear inversion using a Neighbourhood Algorithm. *Pure Appl. Geophys.* **158**, 241–257.
- Tarantola, A., 1987, *Inverse Problem Theory: Methods for Data Fitting and Model Parameter Estimation*, Amsterdam: Elsevier.
- Tarantola, A., and B. Vallete, 1982, *Inverse Problems = Quest for Information*, *J. Geophys.* **50**, 159–170.
- Tierney, L. (1994). Markov chains for exploring posterior distributions. *Ann. of Stat.* **22**(4), 1701–1762.
- Wiejacz, P., and W. Dębski, 2001, *New observation of Gulf of Gdansk Seismic Events*, *Phys. Earth Planet. Int.* **123**(2-4), 233–245.
- Zhao, D., 2001, *New advances of seismic tomography and its applications to subduction zones and earthquake fault zones: A review*, *The Island Arc* **10**, 68–84.

*Accepted 13 June 2006*

## **Tidal and Non-Tidal Frequencies Found in the Seismicity of California**

Pavel KALENDA<sup>1</sup>, Jiří MÁLEK<sup>1</sup> and Lumír SKALSKÝ<sup>2</sup>

<sup>1</sup> Institute of Rock Structure and Mechanics AS CR  
V Holešovičkách 41, 182 09 Praha 8, Czech Republic  
e-mails: pkalenda@volny.cz; malek@irsm.cas.cz

<sup>2</sup> Geophysical Institute, Academy of Sciences of the Czech Republic  
Boční II/1401, 14131 Praha 4, Czech Republic

### **A b s t r a c t**

The seismicity of California (ANCC catalogue) was tested for the possible tidal and/or non-tidal frequencies. The local maxima of tidal potential were computed as a comparative base using global elastic tidal model of Earth by Wahr-Dehant-Zschau. The imperfect elasticity of the Earth mantle was used. Tidal cycles were defined by the analysis of quasi-periods of tidal potential maxima with comparable lengths. We found semi-diurnal, diurnal, fortnightly, monthly, semi-annual, annual, 4.425-years up to 18.6-years long tidal cycles. Ocean tides were not considered.

Results of the comparison of tidal cycles and seismicity show that tidal cycles with periods equal or longer than semi-diurnal were found in the catalogue and/or in the sub-catalogues.

Besides the tidal diurnal cycle, the daily (24:00 hours) period was found. This wave has stronger influence on the seismicity than the tidal diurnal cycle. Its origin is connected probably with temperature cycles on the Earth's surface. The combination of tidal diurnal cycle and daily (24:00 hours) wave leads to the superimposed wave.

The 7-days and 3-months long periods were also found in the seismicity. They correspond to the half-size of tidal periods. In this case, maxima of seismicity or other seismic parameters coincide both with maxima and minima of tidal potential.

## 1. Introduction

For a long time it has been assumed that near the critical state the Earth tides shape the seismicity (Knopoff 1964, Heaton 1982, Hartzel and Heaton 1989). But these studies did not show any significant results. Small influence was found in the case of mid-ocean ridges (Wilcock 2001) or at the seaside regions due to ocean tides (McNutt and Beavan 1981, Rydelek *et al.* 1988, Shirley 1988, Tsuruoka *et al.* 1995, Voight *et al.* 1998). At the Pyrenees, the ocean tides influence was observed for a long distance from the sea (Souriau *et al.* 1982).

Lockner and Beeler (1999) showed on rock samples that tides could trigger seismic events. They showed that the variations of stress which are 5-times bigger than the amplitudes of the tides had significant influence on seismicity in a laboratory. On the other hand, they denied in their next paper (Beeler and Lockner 2003) a possible influence due to the nucleation time of large earthquakes, which is much longer than tidal periods, which destroys this relationship. Sobolev and Ponomarev (1996) showed that tidal oscillations could decrease the peak force (and friction coefficient) and to postpone the main shock. The seismic events have the prevailing periods corresponding to the vibration periods.

Recent tests on rock samples (Yin *et al.* 2004) show high LURR (Load-Unload Response Ratio) anomalies before the main shock.

Tanaka *et al.* (2002a) showed that dividing of seismic events according to their focal mechanism, the subgroups had statistically significant distribution in the tidal cycle although the original mixed group showed no dependence. The strongest dependence showed shallow reverse or normal fault types. In the next papers Tanaka *et al.* (2002b) showed that it is possible to predict the main event on the basis of correlation between tides and seismicity or to recognise earthquake-prone areas (Tanaka *et al.* 2004).

The most recent paper by Cochran *et al.* (2004) proves the relationship between seismicity and ocean tides for the whole California.

In this paper we analyzed the seismicity in California without considering its focal mechanisms. We preferred analysis of long-term and medium-term (beat) cycles of tidal potential (18.6-year, 4.425-year, annual, semi-annual, monthly and fortnightly), because such periods are not influenced by the time shift depending on their focal mechanisms. Such a time shift should be less than 6 hours (Tanaka *et al.* 2002a), but during long-term tidal cycle, the Coulomb criterion varies around tidal potential maximum and its beat-cycles have the same length as the tidal potential maximum. We analyzed also the short-term tidal cycle (diurnal and semi-diurnal) assuming the single prevailing focal mechanism of seismic events which will dominate (if any) in the distribution of seismic events in the tidal cycle. (Lack of domination of some prevailing phase shift in the tidal cycle does not mean that there is no dependence between tides and seismicity – this could be hidden as in the case of mixture of all types of world seismic events (Tanaka *et al.* 2002a)).

We accepted the hypothesis of dependence of nucleation phase on the magnitude (Beeler and Lockner 2003) and so we analyzed as small seismic events as possible which have short nucleation phase.

## 2. Data and Analysis

The theoretical course of tidal potential was computed for the Parkfield area by own program (Skalský 1991) using Tamura's development of tidal potential of 1200 tidal waves (Tamura 1987) and Wahr-Dehant-Zschau model of the Earth (Wahr 1981, Dehant 1987, Zschau and Wang 1987) including imperfect elasticity of the Earth's mantle.

ANSS Composite Catalogue (<http://quake.geo.berkeley.edu/anss/catalog-search.html>) for the period 1980-2004 was used. This catalogue is complete approximately from the magnitude 2.

The Palm Springs area sub-catalogue (37.2 to 37.9N; -118.2 to -119.2E) and events with  $m \geq 2$  were used for the detailed analyses (see Fig. 1). The sub-catalogue contains 18,228 seismic events.

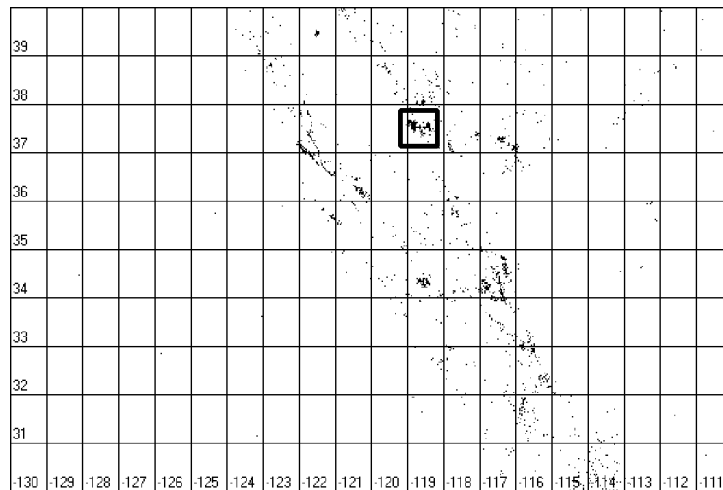


Fig. 1. The area under study (Palm Springs) and whole California seismicity ( $m > 4$ ).

The Palm Springs area is supposed to be almost independent of other areas in the surrounding. So, we can make the distribution of inter-event times for various magnitude ranges to divide the catalogue to non-random and random parts following the method of Bak *et al.* (2002). The cut-off limit of linear part of distribution of inter-event times was 1 day for magnitude range 2-3. That means that all events which were registered sooner than 1 day after the previous event were regarded as time-dependent (or non-random) while all the events which were registered later than 1 day after previous event are time-independent (or random) (see Fig. 2). We did not divide the time-dependent (or non-random) events to foreshocks and aftershocks.

The number of random events varies according to the number of non-random events, because during huge aftershock sequence it is not possible to find random events among aftershocks (see Fig. 3).

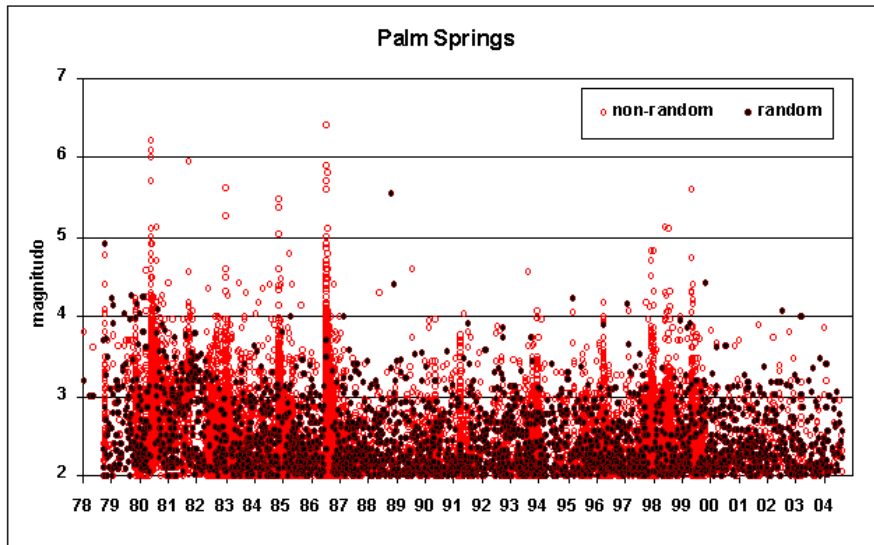


Fig. 2. Random and non-random events registered in the Palm Spring area.

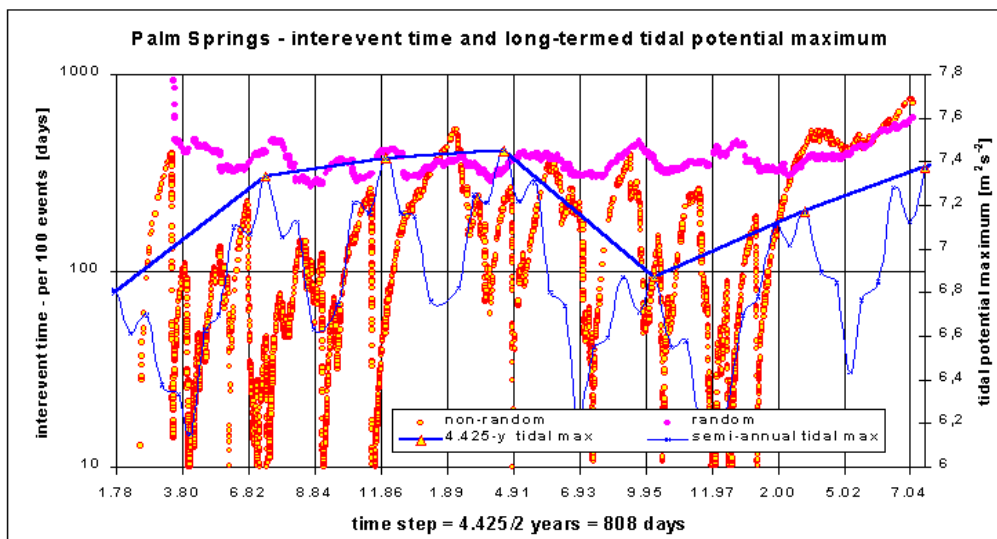


Fig. 3. Inter-event time and long-term tidal potential maximum.

It has been widely shown from Fig. 3 that during the years 1980-1986 and 1991-1997 the starting parts of main aftershock sequences correspond to maxima or minima of 4.425-years long tidal cycle (for example 3/80, 6/82, 9/84, 10/86, 4/91, 6-7/93, 9/95, 11/97).

Several parameters were chosen for analysis of seismicity on tidal period: number of events, parameters  $a$  and  $b$  of Guttenberg-Richter magnitude-frequency distribution evaluated from linear part of distribution in magnitude range 2-4. The last pa-

parameter was the expected maximum magnitude  $m_{\max}$  which was evaluated simply as  $m_{\max} = a/b$ .

We started our analysis for beat tidal cycles from the Moon nodal period i.e. 18.6 years. This period was recognized in the global NEIC catalogue (Kalenda *et al.* 2005). The maximum number of events occurs before 1/2 of tidal cycle (0.4) and before maximum (0.81). Because the data cover only 1 period, the result is not statistically valid, but it is in agreement with our previous study of global seismicity (Kalenda *et al.* 2005).

Analysis of 4.425-years long beat cycle of tidal potential showed typical maximum of number of non-random seismic events before 1/2 of tidal cycle and before maximum of tidal potential (i.e. starting point of cycle) (see Figs. 3 and 4). Parameter  $b$  of Guttenberg-Richter (G-R) distribution shows its minimum (and maximum of seismic risk) before 1/2 of tidal cycle (0.45) and before maximum of tidal potential (0.8) (see Fig. 4b). Random seismic events were contaminated by aftershocks; parameter  $b$  shows its minimum before half of tidal cycle (0.3) and before the maximum of tidal potential (0.8).

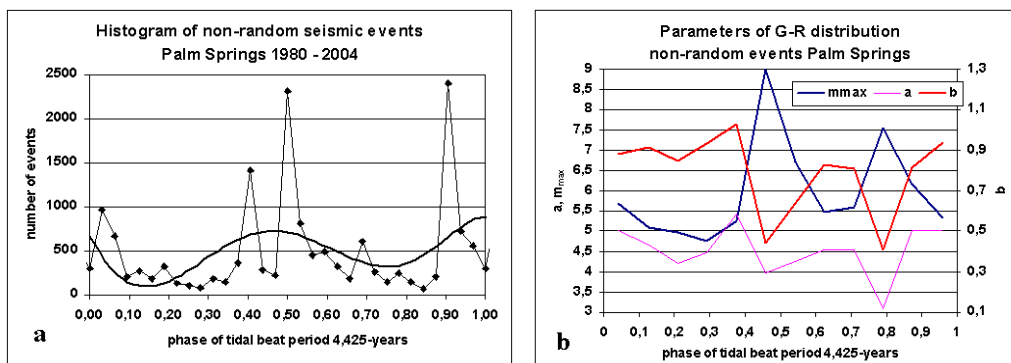


Fig. 4. Dependence of the number of events and parameters of G-R distribution on 4.425-years tidal cycle.

Analysis of 6-months long tidal cycle shows the main maximum of the number of non-random events round tidal potential maximum (0.8-1.2) and secondary maximum number of events round half of tidal cycle (see Fig. 5a). Parameter  $b$  of Guttenberg-Richter (G-R) distribution shows its minimum round half of tidal cycle (0.5) and before the maximum of tidal potential (0.8) (see Fig. 5b). Distribution of the number of random events is complementary with the distribution of number of non-random events due to their contamination (see Fig. 5c). Distributions of G-R parameters of random events show maximum of seismic risk before the tidal potential maximum (0.9), but they are statistically nearly independent of tidal cycle (see Fig. 5d).

The fortnightly tidal cycle shows the main maximum of the number of non-random events after the tidal potential maximum (0.95-1.1) and the secondary maximum number of events after 1/2 of tidal cycle (0.55-0.7) (see Fig. 6a). Parameter  $b$  of Guttenberg-Richter (G-R) distribution shows its minimum before maximum of tidal

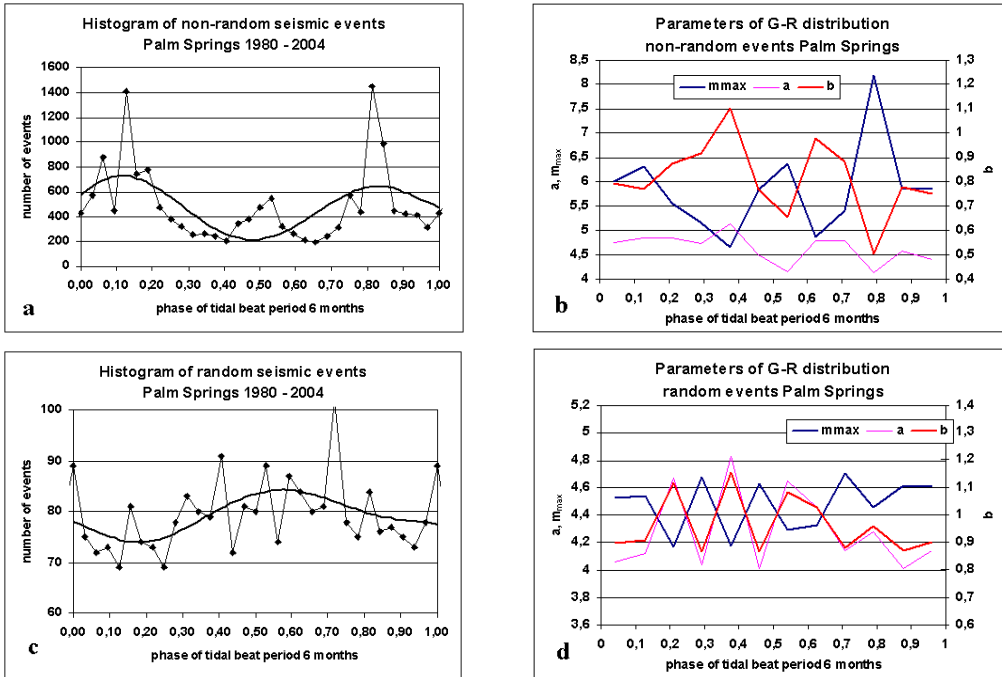


Fig. 5. Dependence of number of events and parameters of G-R distribution on semi-annual tidal beat cycle.

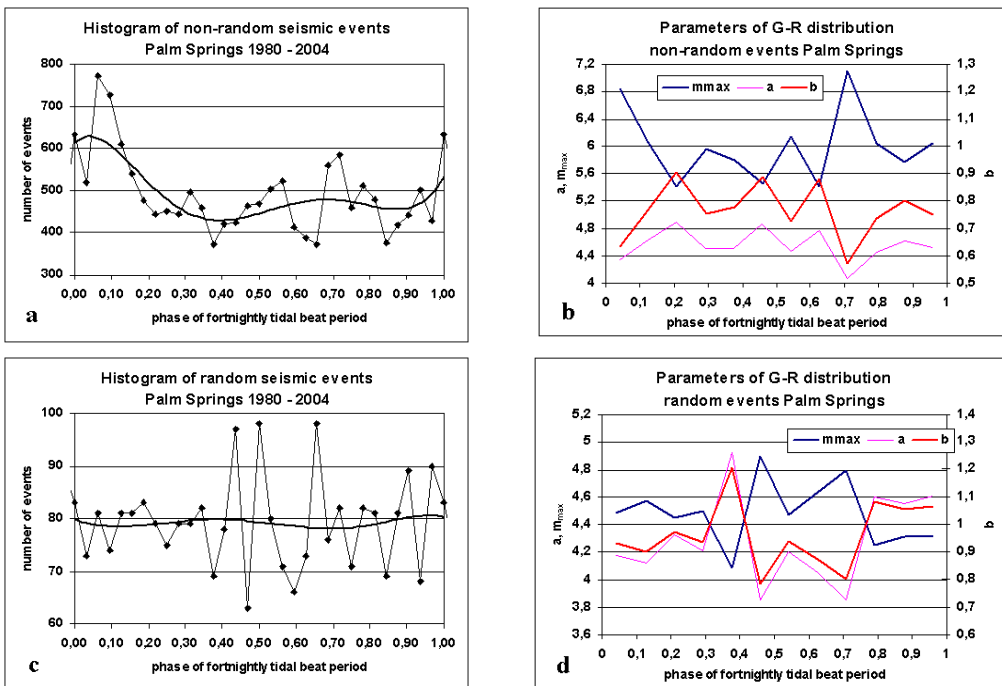


Fig. 6. Dependence of the number of events and parameters of G-R distribution on fortnightly tidal cycle.

potential (0.7-1.1) (see Fig. 6b). Distribution of number of random events is nearly independent of tidal cycle (see Fig. 6c). Distributions of G-R parameters of random events show maximum of seismic risk between phases 0.5 and 0.7 (see Fig. 6d).

The diurnal tidal cycle shows the main maximum of the number of non-random events after tidal potential maximum (0.95-1.1) and the secondary maximum after 1/2 of the tidal cycle (0.55-0.65) (see Fig. 7a). Parameter **b** of Guttenberg-Richter (G-R) distribution shows its minimum before the maximum of tidal potential (0.9-1.05) (see Fig. 7b). Second maximum of seismic risk is before 1/2 of tidal cycle (0.3-0.45). Distribution of the number of random events is nearly independent of tidal cycle (see Fig. 7c). Distributions of G-R parameters of random events show maximum of seismic risk between phases 0.55 and 1.05 (see Fig. 7d).

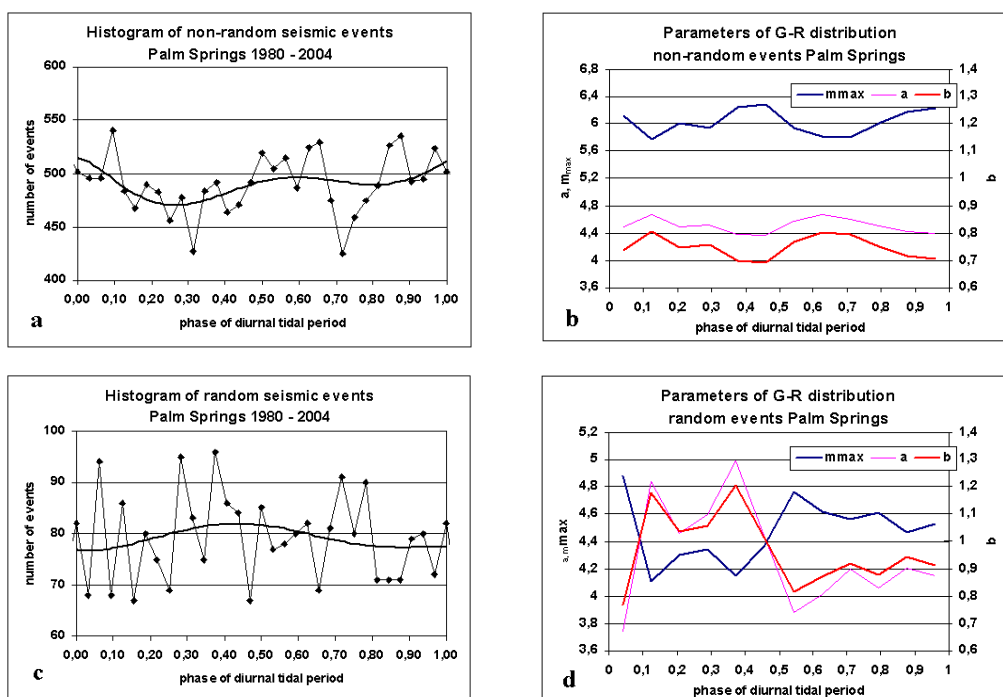


Fig. 7. Dependence of the number of events and parameters of G-R distribution on diurnal tidal cycle.

Besides of tidal beat cycles (18.6-years, 4.425-years, annual, semi-annual, monthly, fortnightly) and short-term tidal cycles (diurnal and semi-diurnal) we found 24:00 hours long non-tidal period which contaminates the fortnightly beat period too. The distribution of the number of non-random events shows two maxima that are bigger than in the case of tidal diurnal cycle (compare Figs. 7a and 8a). Maximum of seismic risk is before both maxima of the number of events (see Figs. 8a and 8b). The number of random seismic events is nearly independent of the daily cycle (see Fig. 8c), but the maximum of risk is after the beginning of daily cycle (see Fig. 8d).

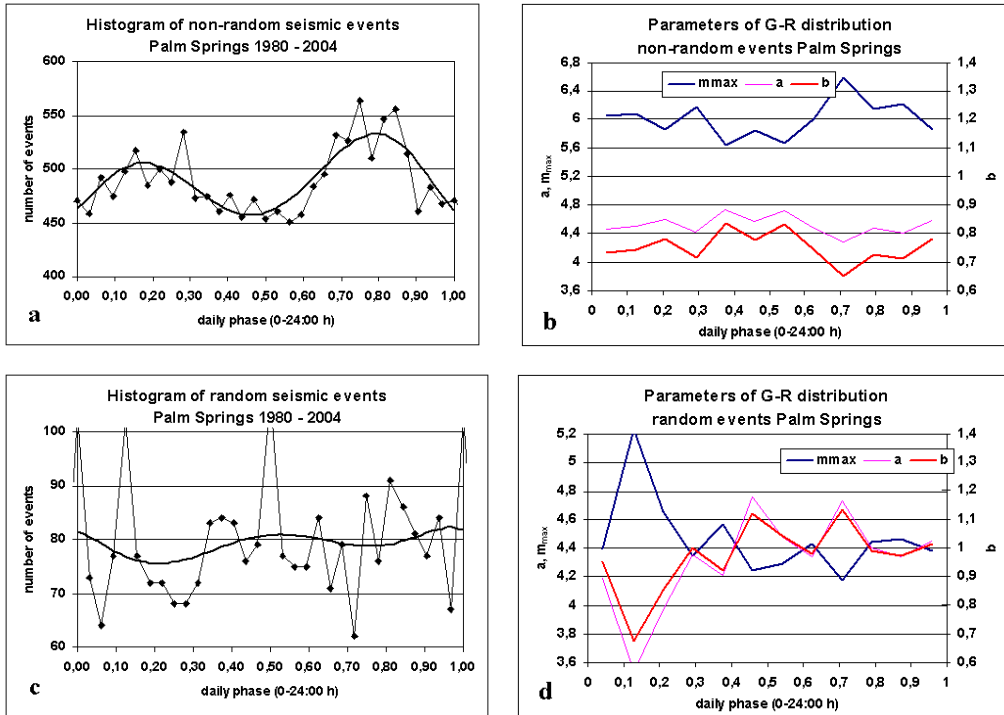


Fig. 8. Dependence of the number of events and parameters of G-R distribution on daily non-tidal cycle.

### 3. Results and Discussion

The number of random events shows no dependence on tidal cycle or this dependence is complementary with non-random events, which is probably due to impossibility of extraction of random events from aftershock sequence. The contamination of random events in aftershock sequence is less than 5% which makes results of non-random distribution statistically significant. Random events are probably independent of tidal or non-tidal cycles.

The distribution of the number of non-random events in the tidal cycles is in agreement with previous analysis – the dependence of distribution of events on tidal cycle drops from long-period cycle down to semi-diurnal cycle. The ratio between maximal and minimal number of events in the case of 4.425-years cycle is about 10, in the case of annual cycle it is about 5, in the case of semi-annual cycle it is about 2-4, in the case of fortnightly cycle it is about 1.5 and in the case of diurnal cycle it is about 1.1.

The Schuster test for distribution of seismic events in semi-annual tidal cycle shows that probability that such distribution is random in time is very low, about  $6E-289$ . In this distribution there are 18228 events in 52 tidal cycles. Even if we reduce (resample) the data set to only 100 events choosing each 180-th event, the prob-

ability of random distribution would be only 0.014 by Schuster test, i.e. the probability that seismicity is dependent on semi-annual tides is more than 95%.

The distribution of the number of non-random events in the daily – non-tidal – cycle has about twice greater amplitudes than in the case of diurnal tidal cycle. From this point of view, this cause (probably temperature daily changes) has greater influence than tides. The maximum number of events is observed round noon – i.e. at the time of the highest temperature. The secondary maximum of the distribution is in the night (midnight) and consists mostly of the smallest events which are unobservable during daily period with higher seismic noise (from 6 a.m. to 6 p.m.). If we analyze only higher seismic events ( $m > 4$ ), such peak of events disappears. On the other hand, when analyzing only events with magnitude smaller than 1, only one peak round midnight is observed.

Our analysis of number of events as well as parameters of G-R distribution and their dependence of all tidal cycles shows that instead of one maximum peak we obtained two maxima – one main and one secondary. The best result is obtained for 4.425-years tidal cycle (see Fig. 4). Amplitude of the secondary maximum drops with shorter cycle (except daily period, which is not of the same origin). The main maximum is around tidal potential maximum and the secondary maximum is around tidal potential minimum (except for diurnal cycle). The tidal phase of the main peak of the number of seismic events is after the tidal potential maximum for short-term tidal cycles with tendency to precede maximum for long-term tidal cycles (see Fig. 9). The secondary maximum of the number of seismic events is after the minimum of tidal potential (tidal phase = 0.5) with the tendency to fall down.

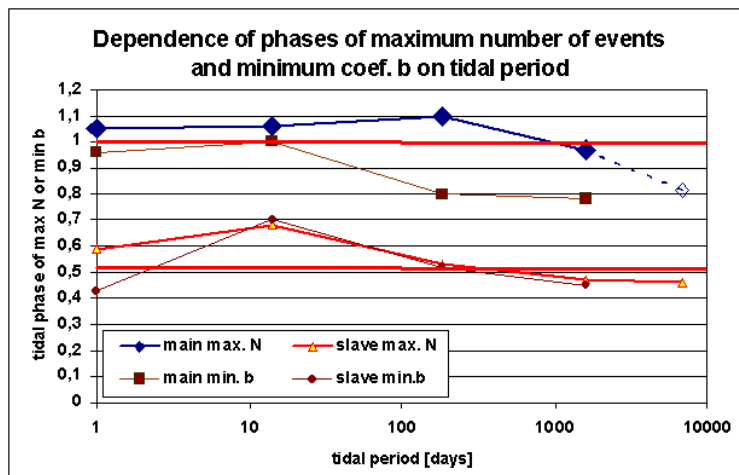


Fig. 9. Dependence of phases of maximum number of events and minimum coefficient  $b$  on tidal cycle.

The phase of main minimum of coefficient  $b$  of G-R distribution shows the same tendency as the phase of maximum of number of seismic events, but this phase

is in front of phase of number of seismic events. In all cases it is in the increasing period of tidal potential before its maximum. The phase of secondary minimum of coefficient  $b$  is nearly the same as the phase of maximum number of seismic events.

The combination of tidal diurnal cycle and daily cycle (24:00 hours) leads to the superimposed wave with the period same as the tidal wave K1 (approx. 1.03 days), which resulted in the same position of this wave once a year.

The analysis showed that coefficients  $b$  and  $m_{\max}$  varied in a wide range. From these parameters we can obtain seismic risk which varies in the range 0.8 to 2.5 compared with the average seismic risk. The seismic risk is time dependent and it has tidal and non-tidal cycles: semi-diurnal, diurnal, daily (24:00), fortnightly, monthly, semi-annual, annual, 2.212-years, 4.425-years, 9.3-years and 18.6-years and longer, which were not analyzed.

All tidal cycles are dependent on each other and so this analysis of seismicity on tides should be made in many-dimensional space and not only in 1-D space as was shown in this paper. Such an analysis can show that the dependence between tides and seismicity is much stronger than it was shown from 1-D analysis.

#### 4. Conclusions

1. We recognised all tidal cycles in the seismicity of California from semi-diurnal to 4.425 years.
2. All beat periods are doubled (diurnal, fortnightly, semi-annual, 4.425-years, 18.6-years?).
3. The daily (24:00) – non-tidal cycle – has great influence on the seismicity with its maximum around noon.
4. The number of events is the highest after tidal potential maximum in the case of short-period tidal cycles. In the case of medium-period ones the highest number of events is around tidal potential maximum and in the case of long-period ones the highest number is before tidal potential maximum.
5. The high seismic risk (and low coefficient  $b$  of G-R) is before tidal potential maximum. Seismic risk is time-dependent!
6. The pattern of the seismic risk is similar in the whole spectrum of beat periods.
7. The time shift in the semi-diurnal tidal cycle according various focal mechanisms of seismic events was not recognised.
8. The strong dependence between tides and seismicity was recognised only in the case of non-random events.

## References

- ANSS Composite Catalogue (<http://quake.geo.berkeley.edu/anss/catalog-search.html>).
- Bak, P., *et al.*, 2002, *Unified scaling law for earthquakes*, Phys. Rev. Letts. **88**, 17, 178501-1-4.
- Beeler, N.M., and D.A. Lockner, 2003, *Why earthquakes correlate weakly with the solid Earth tides: Effects of periodic stress on the rate and probability of earthquake occurrence*, J. Geophys. Res. **108**, B8, 8-17.
- Cochran, E.S., J.E. Vidale and S. Tanaka, 2004, *Earth tides can trigger shallow thrust fault earthquakes*, Science, Oct. 21, 2004, 10.1126. pp. 1-3.
- Dehant, V., 1987, *Tidal parameters for an inelastic Earth*, Phys. Earth Planet. Inter. **49**, 97-116.
- Hartzel, S., and T. Heaton, 1989, *The fortnightly tide and the tidal triggering of earthquakes*, BSSA **79**, 4, 1282-1286.
- Heaton, T.H., 1982, *Tidal triggering of earthquakes*, BSSA **72**, 6, 2181-2200.
- Kalenda, P., J. Málek and L. Skalský, 2005, *Influence of tides on global seismicity*, Chinese J. Geophys. (submitted).
- Knopoff, L., 1964, *Earth tides as a triggering mechanism for earthquakes*, BSSA **54**, 1865-1870.
- Lockner, D.A., and N.M. Beeler, 1999, *Premonitory slip and tidal triggering of earthquakes*, J. Geophys. Res. **104**, B9, 20133-20151.
- McNutt, S.R., and R.J. Beavan, 1981, *Correlation of the solid Earth tide with volcanic earthquakes at Pavlof volcano, Alaska*. Nature **294**, 5842, 615-618.
- Rydelek, P.A., *et al.*, 1988, *Tidal triggering of earthquake swarms at Kilauea Volcano, Hawaii*, J. Geophys. Res. **93**, B5, 4401-4411.
- Shirley, J.H., 1988, *Lunar and solar periodicities of large earthquakes: Southern California and the Alaska-Aleutian Islands seismic region*, Geophys. J. **92**, 403-420.
- Skalský, L., 1991, *Calculation of theoretical values of the tidal strain components with respect to their practical use*. In: Proceedings from seminary "Advances in Gravimetry", December 10-14, 1990, Smolenice, pp. 179-184. Geophysical Institute, Slovak Academy of Sciences, Bratislava.
- Sobolev, G.A., and A.V. Ponomarev, 1996, *The effect of harmonic oscillations on the deformation and acoustic regime of the fault zone model*, ESC XXV General Assembly, Sep. 9-14, 1996, 94-99.
- Souriau, M., *et al.*, 1982, *Modeling and detecting interactions between Earth tides and earthquakes with application to an aftershock sequence in the Pyrenees*, BSSA **72**, 165-180.
- Tamura, Y., 1987, *A Harmonic Development of the Tide-generating Potential*, Marées Terrestres Bulletin d'Informations **99**, 6813-6855.
- Tanaka, S., *et al.*, 2002a, *Evidence for tidal triggering of earthquakes as revealed from statistical analysis of global data*, J. Geophys. Res. **107**, B10, ESE 1-1-11.
- Tanaka, S., *et al.*, 2002b, *Spatio-temporal variation of the tidal triggering effect on earthquake occurrence associated with the 1982 South Tonga earthquake of Mw 7.5*, Geophys. Res. Letts. **29**, 16, 3-1-4.

- Tanaka, S., *et al.*, 2004, *Tidal triggering of earthquakes in Japan related to the regional tectonic stress*, *Earth Planets Space* **56**, 511-515.
- Tsuruoka, H.M., *et al.*, 1995, *Statistical test of the tidal triggering of earthquakes: Contribution of the ocean tide loading effect*. *Geophys. J. Int.* **122**, 183-194.
- Voight, B., *et al.*, 1998, *Remarkable cyclic ground deformation monitored in real-time on Monserrat, and its use in eruption forecasting*, *Geophys. Res. Letts.* **25**, 18, 3405-3408.
- Wahr, J.M., 1981, *Body tides on an elliptical, rotating, elastic and oceanless Earth*, *Geophys. J. Roy. Astr. Soc.* **64**, 677-703.
- Wenzel, H.-G., 1993, *ETERNA 3.0. Earth Tide Analysis Program System ETERNA*, Universität Karlsruhe.
- Wilcock, W.S.D., 2001, *Tidal triggering of microearthquakes on the Juan de Fuca Ridge*, *Geophys. Res. Letts.* **28**, 20, 3999-4002.
- Yin, X-Ch., *et al.*, 2004, *Load-Unload Response Ratio (LURR), Acceleration Moment/Energy Release (AM/ER) and state vector saltation as precursors to failure of rock specimens*, *Pageoph* **161**, 2405-2416.
- Zschau, J., and R. Wang, 1981, *Imperfect elasticity in the Earth's mantle. Implications for Earth tides and long period deformations*. **In:** J.T. Kuo (ed.), *Proceedings of the 9<sup>th</sup> International Symposium on Earth Tides*, New York 1981, Schweizerbartsche Verlagsbuchhandlung, Stuttgart, 605-629.

*Accepted 10 April 2006*

## **Analysis of Displacement Geometry: A Tool for Identifying Kinematic Type of Fault**

Lesław TEPER and Anna LISEK

University of Silesia, Department of Applied Geology  
ul. Będzińska 60, 41-200 Sosnowiec, Poland  
e-mail: teper@us.edu.pl

### **Abstract**

Tectonic motion along fault is the basic cause of mining induced tremors. Determining focal mechanism of tremor produced by slip on a fault is ineffective with regard to slip direction until rock volume is identified reliably. An orthogonal projection of fault onto the vertical plane containing strike of the fault surface seems to be the technique which can provide information appropriate to help with answering the question about the focal mechanism. The projection enables three-dimensional geometry of fault to be illustrated by constructing contour displacement diagrams and calculating displacement gradients over fault surface. This paper describes displacement distribution along selected well-identified faults from the central part of the Upper Silesian Coal Basin. Using contour displacement diagrams we have calculated displacement gradients, drawing attention to the existence of four distinct types of pattern. The different patterns are related to different orientations of principal axes that characterise the fault growth. Examining the gradient data patterns, one can determine direction and sense of actual slip on the fault surface. Information brought by displacement geometry analysis, supplemented with ellipticity study and shear moduli calculation, enables kinematic types of faults to be identified. Strike-slip faults, oblique-slip faults, and dip-slip faults can be recognised by means of the presented method. Similarly, left-handed faults can be distinguished from right-handed ones. The procedure presented enables measurements and observation of faults made by mine surveyors to be directly used in seismological interpretations for identifying fault plane responsible for mine tremor occurrence.

## 1. Introduction

Tectonic motion along natural planar structure in a rockmass is the basic cause of seismic event, playing also a major role in generation of mining induced tremors. Determining focal mechanism of tremor produced by slip on a fault is ineffective until the rock volume is identified reliably. Neither the classic Fault Plane Solution nor the seismic moment tensor inversion methods give unequivocal information on the orientation of the fault plane and the direction of slip. Additional details facilitating the diagnosis can be derived from kinematic characteristics of faults that occur in the rock volume surrounding the focus of seismic event. An orthogonal projection of fault onto the vertical plane containing strike of the fault surface seems to be the technique to provide data appropriate to help with answering the question about the focal mechanism. The projection illustrates some aspects of three-dimensional geometry of fault not apparent on conventional map and cross-section projections. Displacement values measured at points on a fault surface are projected onto the vertical plane parallel to the fault strike (Rippon 1985) and are contoured to allow a visual appreciation of the pattern of displacement variation over the fault surface. More detailed information about displacement distribution on the fault surface can be brought by measuring displacement gradients (Walsh and Watterson 1989). The presented projection helps to recognise geometrical features of individual faults, local fault systems and regional fault networks as well as properties of fractured rockmass (Rippon 1985, Watterson 1986, Barnett *et al.* 1987, Walsh and Watterson 1988, 1990, Teper 1996, 1998; Lisek and Teper 2004).

This paper describes displacement distribution along selected well-identified faults from the central part of the Upper Silesian Coal Basin. Using contour displacement diagrams we have calculated displacement gradients, drawing attention to the existence of four distinct types of pattern. Discussing the origin of the four patterns we attempt to find out how to determine kinematic type of fault directly from original large-scale plans produced by mine surveyors. The knowledge about kinematic features and coherence of the local fault network can be utilised by seismologists in the course of determining the fault planes responsible for the mining induced tremors.

## 2. Data and Method

The fault projections discussed here are derived from large-scale plans made for a single geological unit (the Orzesze beds) located within a single coalfield (Staszic colliery). Contour displacement diagrams were drawn for faults identified directly in roadways and face headings driven in the panel between seams 402 and 350. In the course of the study, only completely exposed faults that exhibited both ends of the traces and exist exclusively in the rock complex considered were taken into account. On such structures, displacement distribution could be traced over the entire

fault surface, from tip-line loop to maximum throw point. To construct, from available recorded data, a projection of the entire multi-seam fault (i.e. fault proved in at least two seams) the positions of the point of maximum throw and fault terminations were estimated by linear extrapolation and interpolation, exhibiting both lateral (in-seam) and vertical (between seams) variations in displacement.

Four representative cases (Fig. 1) were selected to demonstrate displacement geometry on the fault surfaces (Figs. 2, 3, 4 and 5). Faults one and four form conjugate structures while faults two and three are typical single ones (Fig. 1). Single faults were analysed according to Rippon (1985) and Barnett *et al.* (1987) instructions. For conjugate faults, Nicol *et al.* (1995) method was adopted. In each contour diagram, principal axes were scribed intersecting at the point of maximum throw (Fig. 2).

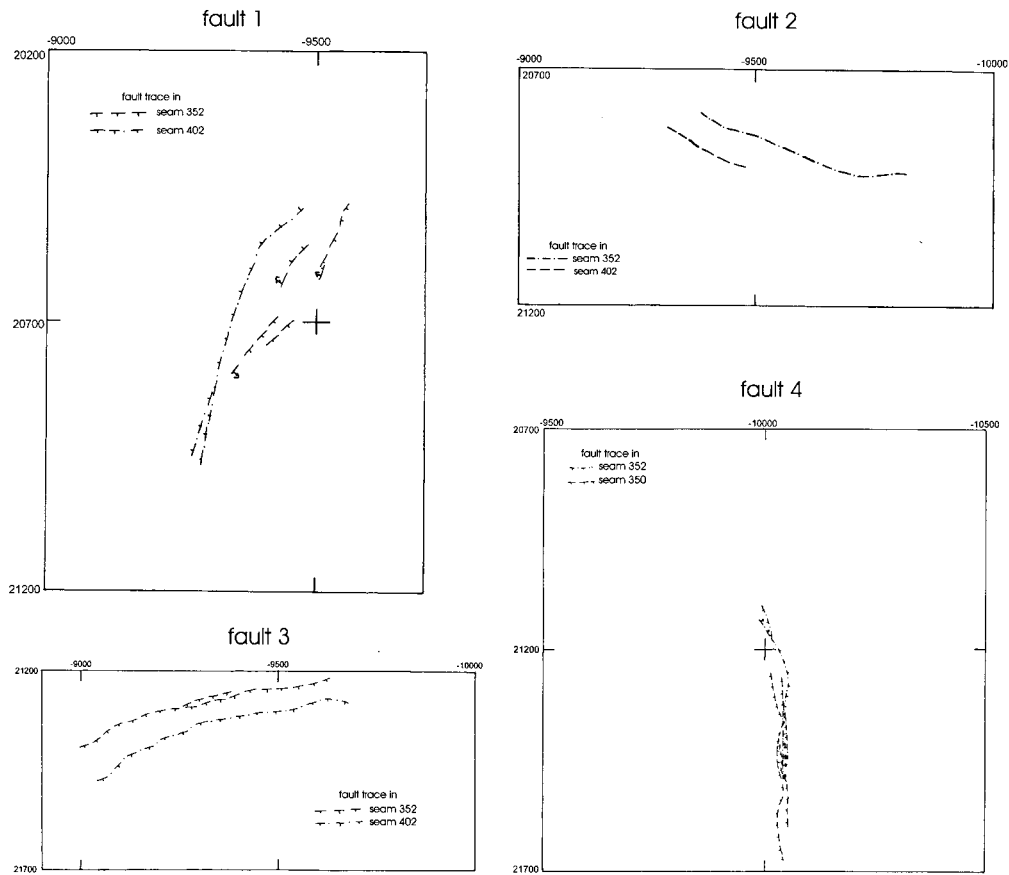


Fig. 1. Generalised plan views, showing traces of examined faults on various seams of the Orzesze beds within the Staszic coalfield. Available recorded throw data are shown along traces of fault three.

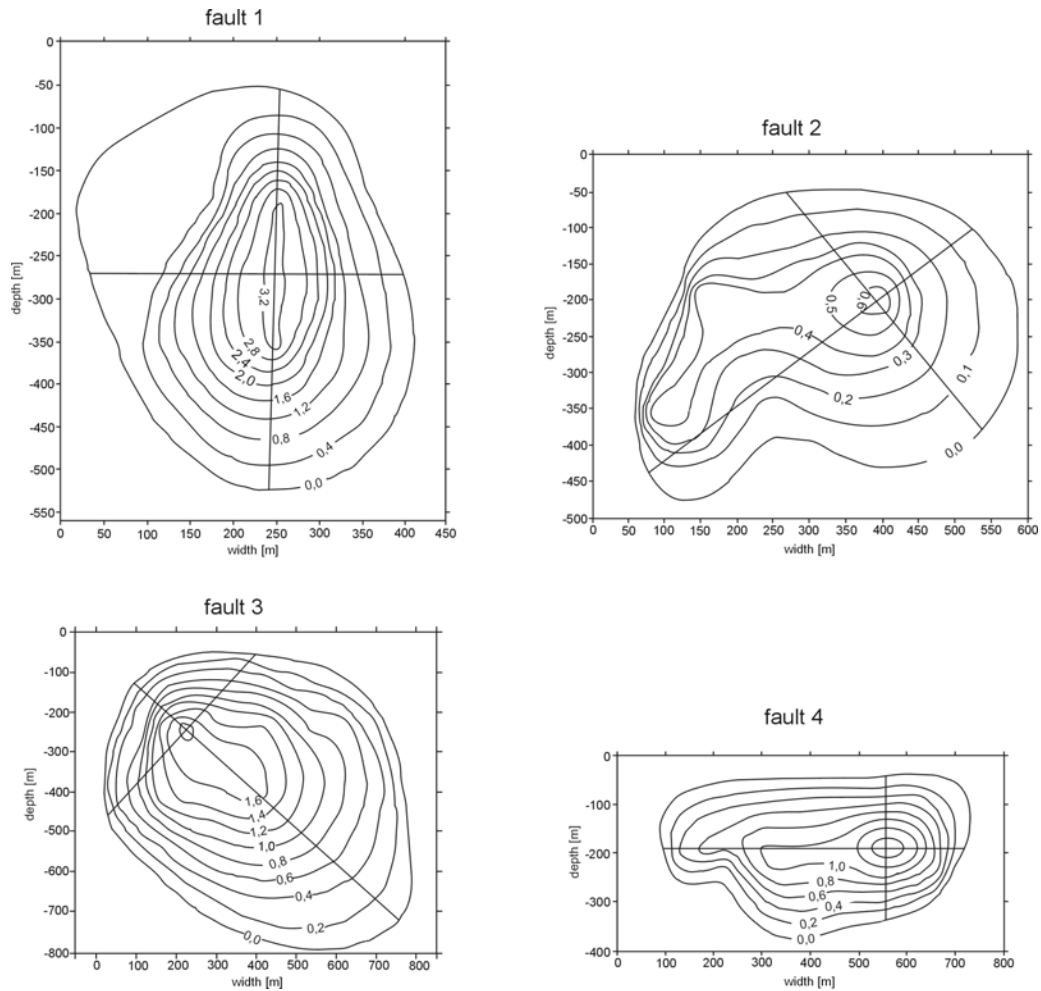


Fig. 2. Faults from the Orzesze beds within the Staszic coalfield. Contour displacement diagrams are shown using an orthogonal projection of fault onto the vertical plane containing strike of the fault surface. On the diagrams, principal axes are drawn and displacement values are placed where the fault throws were proved.

Contour diagrams have served for measuring displacement gradients. Gradients along the major principal axis (Fig. 3) and horizontal displacement gradients (Fig. 4) were calculated in accordance to Walsh and Watterson's (1989) instruction. The values plotted in Fig. 3 were obtained using a fixed measuring interval of 5% of the minor axis of the contour diagram (Teper and Lisek 2005). As fault traces on coal seam plans have low plunges (up to  $10^\circ$ ), the gradients calculated between adjacent points on these traces can be taken to be horizontal. The displacement halfway between ad-

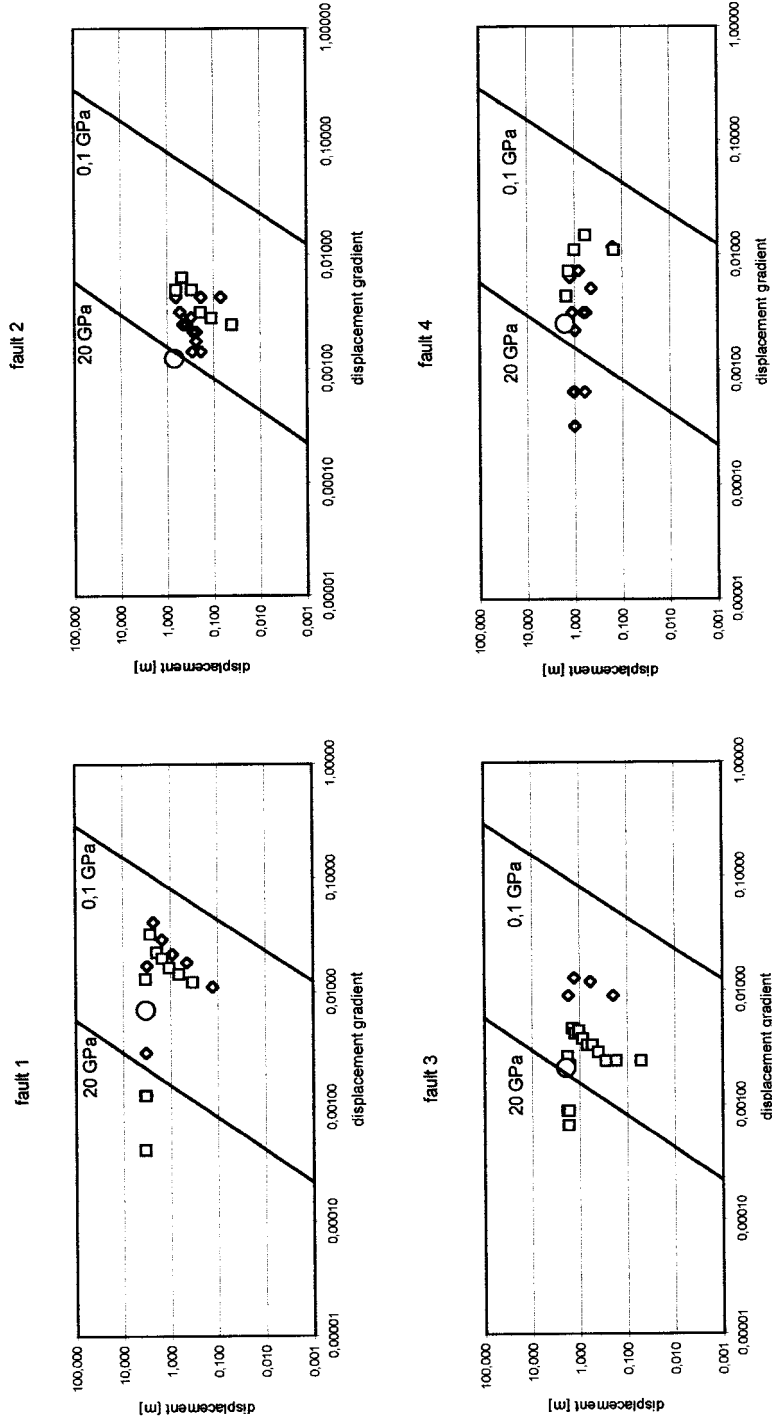


Fig. 3. Logarithmic plots of displacement gradient vs displacement for measurements derived from faults in the Staszic coalfield. Gradient was each time calculated along the major principal axis of adequate contour displacement diagram (cf. Fig. 2). Rhombuses are the gradients worked out in those parts of the diagrams which are situated left of the maximum throw. Squares mark the gradients calculated in the parts located right of the maximum throw. Large rhombus and large square represent mid-values of distinguished gradient sets. Circle stands for position of gross displacement gradient. Solid lines are 0.1 and 20 GPa shear modulus curves, which respectively denote lowest and highest shear moduli for rocks in the Staszic coalfield.

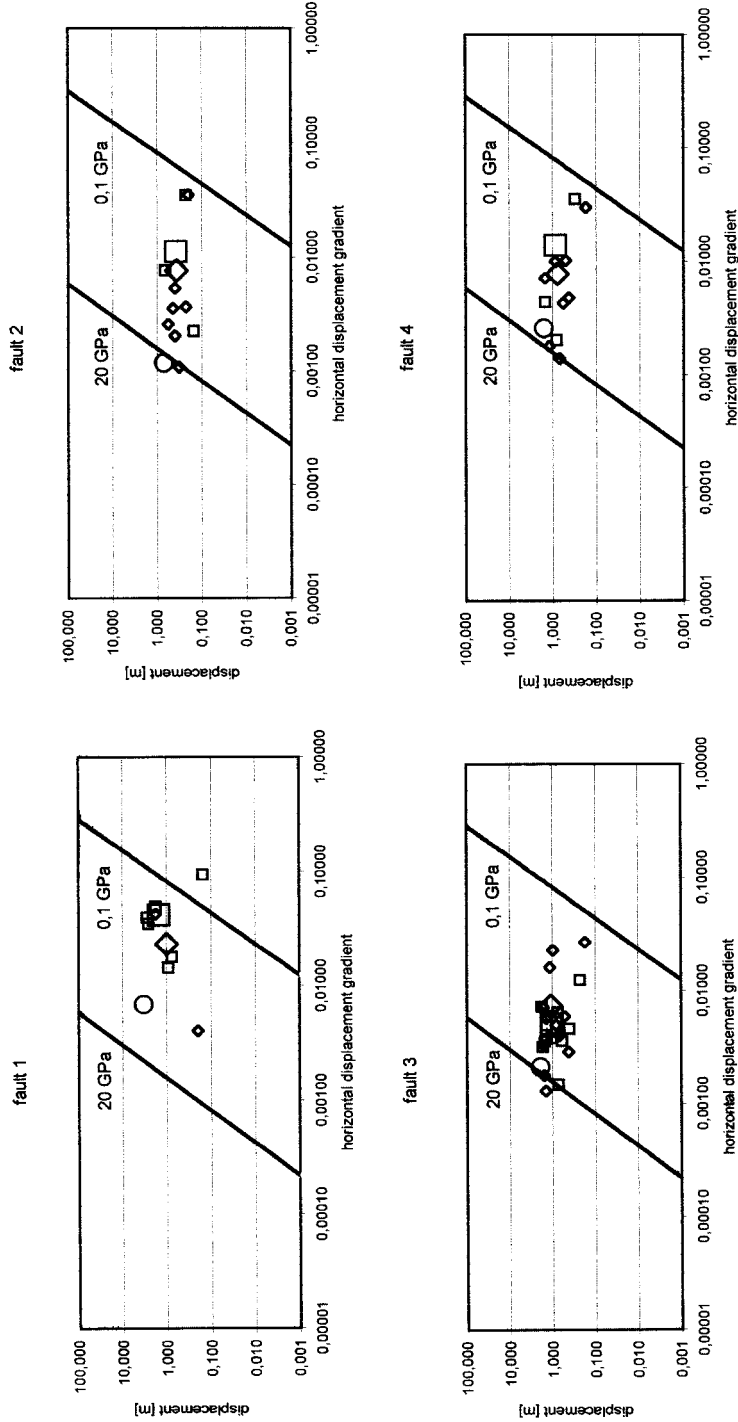


Fig. 4. Logarithmic plots of horizontal displacement gradient vs displacement derived from examined faults. Rhombuses correspond with the gradients calculated in the parts of the displacement diagrams (cf. Fig. 2) situated left of the maximum throw (cf. Fig. 3). Squares refer to the gradients calculated in the parts of diagrams located right of the maximum throw (cf. Fig. 3). Large rhombus and large square represent centres of distinguished gradient sets. Circle stands for position of gross displacement gradient. Solid lines symbolise boundary values of shear modulus for rocks in the Staszic coalfield.

adjacent recorded throw readings  $d_1$  and  $d_2$  is obtained by linear interpolation and horizontal gradient calculated from the two recorded readings is  $(d_1 - d_2)/MI$ , where the measuring interval, MI, is the distance between the points (Walsh and Watterson 1989).

All contour diagrams presented in Fig. 2 are asymmetric with respect to the minor principal axis. That is why two sets of gradients were distinguished in Figs. 3 and 4. Rhombuses in Fig. 3 symbolise the gradients measured in those parts of the diagrams which are situated on the left side of the maximum throw while squares represent the gradients calculated in the parts located on the right from the maximum throw. Sets illustrated in Fig. 4 were isolated similarly. Rhombuses represent points in which differential displacement is positive ( $d_1 - d_2 > 0$ ) and correspond with the gradients calculated in the parts of the displacement diagrams situated left of maximum throw (cf. Fig. 3). Squares, representing points in which differential displacement is negative ( $d_1 - d_2 < 0$ ), refer to the gradients calculated in the parts of diagrams located right of the maximum throw (cf. Fig. 3). Mid-value of each distinguished set was calculated and shown graphically as centre of point pattern by large rhombus and large square, respectively (Figs. 3 and 4).

According to Walsh and Watterson (1989) a plot incorporating both gradient and displacement can provide a useful indication of the width and maximum displacement of a fault. Therefore, Fig. 3 compiles logarithmic plots of displacement gradient calculated along major principal axis of adequate contour displacement diagram vs displacement, while Fig. 4 is putting together logarithmic plots of horizontal displacement gradient vs displacement for measurements derived from examined faults. The large circles in Figs. 3 and 4 represent the maximum displacement and the gross gradient of the fault. Gross gradient  $G_g$  was calculated as the mean displacement gradient over the complete fault radius (i.e. the maximum displacement  $D$  in relation to the length of major principal axis of contour diagram).

The gross gradient is related to mechanical properties of a rockmass  $P$  (Walsh and Watterson 1989):

$$G_g = kD^{0.5},$$

where  $k = 2P^{-0.5}$  can be expressed by shear modulus value.

For rocks that compose the Orzesze beds within the Staszic coalfield, shear moduli were calculated using Young's modulus and Poisson's ratio values. Lines appropriate to the values of 0.1 and 20 GPa, which denote lowest and highest shear moduli for rocks from the Staszic coalfield, are shown in Figs. 3 and 4.

Displacement gradients measured along major and minor principal axes over the examined faults (Fig. 5) are also plotted to demonstrate the ellipticity of fault surfaces. The ellipticity is represented by line of symmetry of the data point distribution (bold broken line). Thin broken lines show fault ellipticities calculated as a ratio of

major to minor axis lengths. Additionally, symmetry lines for fault ellipticities of 1:1 (circular fault surface) and 1:2 (elliptical fault surface) are drawn as solid lines.

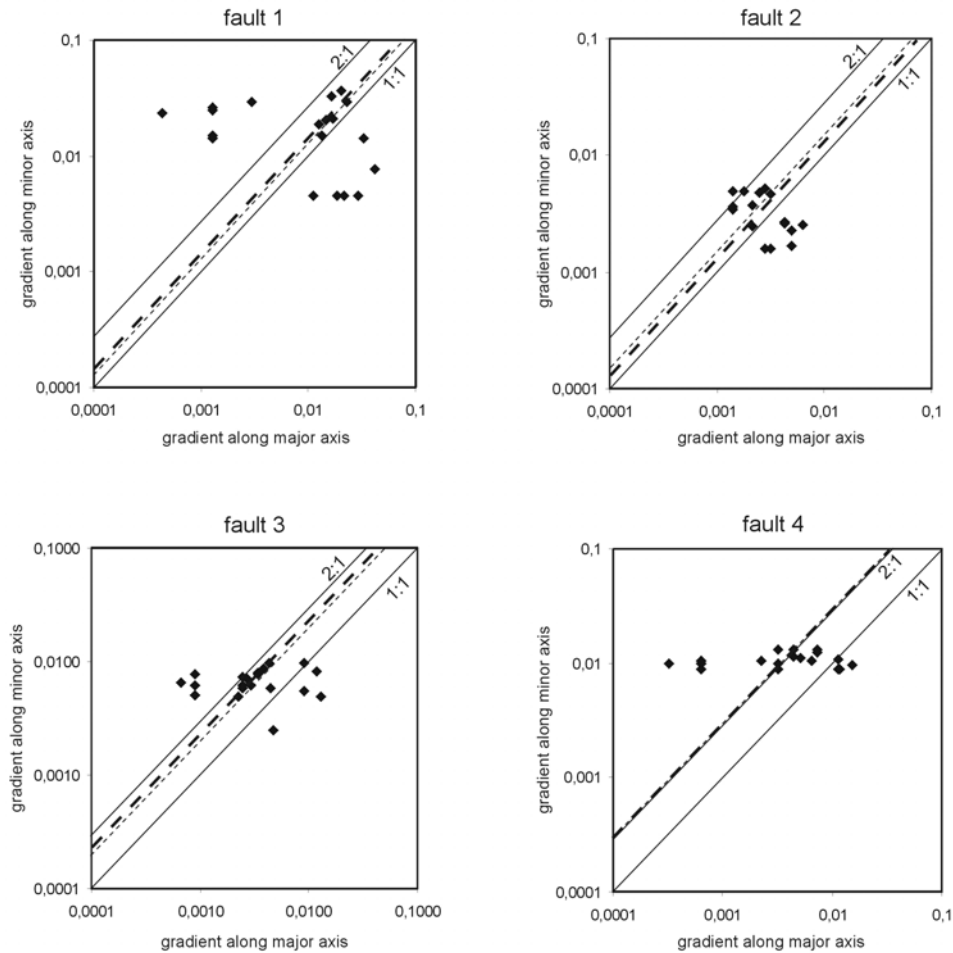


Fig. 5. Logarithmic plots of major axis displacement gradient vs minor axis displacement gradient for examined faults. Symmetry lines for fault ellipticities of 1 and 2 are shown as solid lines. Symmetry line determined geometrically for the data points is shown by bold broken line, while thin broken line denotes ellipticity value calculated for studied faults.

### 3. Results

After Watterson (1986), a fault is assumed to grow by radial extension of the tip line with no migration of the point of maximum displacement. Displacement and

dimensions are believed to be accumulated throughout the active life of fault and the accumulation is realised by successive slips occurring during single seismic events. It follows that a fault increases in width with time along major axis of contour displacement diagram. Thus, knowing spatial position of principal axes of fault surface one can determine direction and sense of real slip defined as actual displacement of fault sides measured in the plane of movement.

The contour diagrams presented in Fig. 2 differ fundamentally in orientation of major axis. The axis is vertical for fault one, diagonally inclined to opposing directions – for faults two and three, and horizontal – for fault four. According to the fault growth model mentioned above, the cases illustrated could be recognised as four distinct kinematic types of fault, which are strike-slip fault, sinistral oblique-slip fault, dextral oblique-slip fault, and normal dip-slip fault, respectively.

Logarithmic plots of displacement gradient calculated along major principal axis *vs* displacement (Fig. 3) reveal four different types of distribution. Differences relate to position of empirical points with reference to the lines which represent the lowest and highest shear moduli for the coalfield rocks. Distribution patterns obtained for gradients measured in either “left” or “right” part of the fault surfaces as well as position of the centre of each pattern are also significantly distinct. Analysis of gradient distribution made for examined fault surfaces (Teper and Lisek 2005) enables types of distribution from Fig. 3 to be correlated with geometries of contour diagrams distinguished. This result leads to the conclusion that kinematic type of fault can be identified using the plots of gradient along fault major axis against displacement (Fig. 3).

Plots presented in Fig. 3 provide accurate information about displacement geometry. In order to construct them, the introduced projection of fault has been needed and contour diagrams (Fig. 2) have to be analysed. The point is whether the procedure of identifying fault kinematics could be simplified to such an extent that actual throw readings available from mine plans would be used directly. Relation illustrated in Fig. 3 can be simplified and roughly estimated plotting horizontal gradient *vs* displacement (Fig. 4). That is just the case when displacement gradient calculations base on a throw data recorded in underground roadways.

At this point, a study comparing plots depicted in Fig. 4 with those gathered in Fig. 3 is of great importance. Results of the Kolmogorov-Smirnov Goodness-of-Fit Test ensure that there is no basis for rejecting the null hypothesis telling that the distribution of horizontal gradients fits the distribution of gradients calculated over major principal axis of fault surface. Similarity is apparent while we compare the arrangement of points with respect to lines representing boundary values of shear modulus. Resemblance is also visible in configuration of empirical points and mid-values of the sets derived from gradient calculations in the parts of the faults situated either on the left or on the right side of the maximum throw. Such a similarity of distributions tested (Fig. 3 *vs* Fig. 4) certifies that, for the examined cases, the use of horizontal

displacement gradients for identifying kinematic type of fault is both valid and sufficient.

Displacement on some parts of the fault surface may be partly or wholly accommodated by ductile deformation (Walsh and Watterson 1989). The proportion of discontinuous and continuous components of deformation influences the fault ellipticity. If the elliptical form of the fault surface is due to mechanical properties of the rock complex, then different complexes might be characterised by different ellipticities. Fig. 5 is of interest for the information it provides on the ellipticity of the coalfield faults studied.

#### 4. Concluding Remarks

The presented plots exhibit distinct patterns of values of gradient/displacement ratio. The different patterns are related to different orientations of principal axes that characterise fault growth. Thus, examining the gradient data patterns one can determine direction and sense of actual slip on the fault surface. Therefore, knowledge brought by displacement geometry analysis, supplemented with ellipticity study and shear moduli calculation, enables kinematic types of faults to be differentiated. Strike-slip faults, oblique-slip faults, and dip-slip faults can be recognised by means of the presented method. Similarly, left-handed faults can be distinguished from right-handed ones.

The procedure presented enables measurements and observation of faults made by mine surveyors to be directly used in seismological interpretations for identifying the fault plane responsible for mine tremor occurrence.

#### References

- Barnett, J.A.M., J. Mortimer, J.H. Rippon, J.J. Walsh and J. Watterson, 1987, *Displacement geometry in the volume containing a single normal fault*, Am. Assoc. Petrol. Geol. Bull. **71**, 925-937.
- Lisek, A., and L. Teper, 2004, *Fault dimensions in the "Staszic" coalfield (Upper Silesian Coal Basin): a key to recognition of a fault zone growth*. In: Proc. XXVII Symp. Geology of Coal-bearing Strata of Poland, AGH Univ. of Sci. and Techn., Cracow, 93-98 (in Polish, with English summary).
- Nicol, A., J.J. Walsh, J. Watterson and P.G. Bretan, 1995, *Three-dimensional geometry and growth of conjugate normal faults*, J. Struct. Geol. **17**, 847-862.
- Rippon, J.H., 1985, *Contoured patterns of the throw and hade of normal faults in the Coal Measures (Westphalian) of north-east Derbyshire*, Proc. Yorks. Geol. Soc. **45**, 147-161.

- Teper, L., 1996, *Fault dimensions and displacements in mining area: Northern part of the Upper Silesian Coal Basin*. **In:** Tectonophysics of Mining Areas, University of Silesia Press, Katowice, 41-56.
- Teper, L., 1998, *Seismotectonics in the Northern Part of the Upper Silesian Coal Basin: Deep-Seated Fractures-Controlled Pattern*, University of Silesia Press, Katowice (in Polish, with English summary).
- Teper, L., and A. Lisek, 2005, *Types of displacement distribution on fault surfaces from the central part of the Upper Silesian Coal Basin*. **In:** Proc. XXVIII Symp. Geology of Coal-Bearing Strata of Poland, AGH Univ. of Sci. and Techn., Cracow, 119-124 (in Polish, with English summary).
- Walsh, J.J., and J. Watterson, 1988, *Analysis of the relationship between displacements and dimension of faults*, J. Struct. Geol. **10**, 239-247.
- Walsh, J.J., and J. Watterson, 1989, *Displacement gradients on fault surfaces*, J. Struct. Geol. **11**, 307-316.
- Walsh, J.J., and J. Watterson, 1990, *New methods of fault projection for coalmine planning*, Proc. Yorks. Geol. Soc. **48**, 209-219.
- Watterson, J., 1986, *Fault dimensions, displacements and growth*, Pageoph **124**, 365-373.

*Accepted 10 April 2006*



## **SPS – Seismic Signal Processing System**

Janusz MIREK

AGH University of Science and Technology  
Faculty of Geology, Geophysics and Environmental Protection  
Department of Geophysics  
Al. Mickiewicza 30, 30-059 Cracow, Poland  
e-mail: [jmirek@geol.agh.edu.pl](mailto:jmirek@geol.agh.edu.pl)

### **A b s t r a c t**

A brief foredesign and status of development of a system to compute seismic signals (SPS) are presented. The system is designed to work in a client-server system architecture, controlled by the Unix operating system. Authorized SPS users can access resources of the system server via Internet browsers. The resources include gathered data, a set of numerical procedures, and a collection of presentation functions. Users can graphically program the to-be-accomplished tasks using the available software elements and to write their own data processing procedures. Implemented within the system are, among other things, spectral analysis and digital signal processing, in particular signal differentiating and integrating. The system may serve to process (e.g. filter) individual signals, as well as determine common attributes in a collection of signals and further analyze such collections (e.g. attenuation relations). SPS has been designed as an open and scalable software that will be offered free-of-charge under the GPL licence.

### **1. Introduction**

The Seismic Signal Processing System (SPS) has been designed to process three components of seismic signals originating in earthquakes, mining-related tremors, and other phenomena causing vibrations that may be registered on the Earth's surface and/or in structures. The system consists of data importation procedures, data processing procedures, and visualization procedures. Each procedure is implemented as a separate executable programme in the `c/c++` programming language. Such an approach enables the easy programming of individual procedures, and the programs are short and coherent. Adding new procedures to the system is also straightforward in that programs developed are written in a set procedure. The only requirement is that

the program realizes the in/out operations in cohesion with the data format within the system.

SPS runs under the Unix operating system. The user working with this system has at his/her disposal many user shells that are simultaneously programming languages. The combination of the SPS procedures with the capabilities of user shells and programs built into Unix produces a very flexible tool to process seismic data.

The graphical user interface of the SPS system, based on the HTTP protocol, has been programmed in PHP. The interface is available via an Internet browser.

## 2. Data Import

SPS operates on data written in its own internal format. Data in other formats must be imported prior to processing. Sets of tools to import data from the *SAC* format or from systems like *SEJS-NET*, *Wors*, *Mars*, or *Pas-Prosejs* have been designed. A program to import ASCII data is planned.

## 3. Internal Data Format

SPS operates on data written to text files in space-separated (or tab-separated) columns. Successive columns contain sampling time, amplitude values of horizontal components, and amplitude value of vertical amplitude.

Each file may begin with a text header separated from the data block with a single empty line. Each line of data in the header (a record) contains the record name, the “=” character, and a value. The record name may be composed of letters, digits and the underscore character only. Record value may be either a number or a text. Each record must end with the new line character. Sample file (header and data) is shown in Fig. 1.

```

date=2005-07-22
time=13:21:17
sampling_rate=0.001
data_unit=m/s^2
time_unit=s
type=raw
src_x=123
src_y=234
comment=artificial

0.000 -0.001335 0.000634 -0.000053
0.001 0.000997 0.000634 0.002269
0.002 -0.001334 0.000633 -0.000053
0.003 0.000997 0.000633 -0.000053
0.004 -0.001334 0.000633 -0.000053
...
7.400 -0.001335 0.000734 -0.000053
7.401 -0.000997 0.000334 0.002269

```

Fig. 1. Sample SPS file.

Text format was chosen for data files of the SPS system since it facilitates importing data from other systems and exporting data to other systems, as well as provides visual control of data existing in a file and/or during file generation. An alternative binary format is planned for the future to reduce data file size and to increase efficiency of in/out operations. Data files saved under the binary format are usually smaller and render block reading/writing possible, which may significantly speed up the operations.

#### 4. Basic Processing

Basic processing consists of applying a given command available in the system in order to process a single data file. A list of these commands may be easily extended to include new programs. Results of such processing are written to a file with new (processed) data, or a file with the results of the calculations performed on the input data, or a file with a chart. Depending on the produced results, each of the system procedures may be assigned to one of the following three groups: signal processing, parameter calculation, or visualization.

The signal processing group includes procedures to:

- Filter signal with the Butterworth filter (e.g. Izydorczyk)
- Filter with a programmable filter (any shape of the transmittance function)
- Find and subtract the signal average
- Find and subtract a linear trend
- Find Discrete Fourier Transform (DFT) (e.g. Mitra, Bellanger)
- Integrate
- Differentiate
- Apply median filter (e.g. Stranneby)
- Interpolate/decimate (e.g. Lyons)
- Cut out a fragment from the signal
- Add/subtract a constant
- Multiply/divide by a constant
- Add, subtract, multiply, divide two signals
- Convolute two signals (e.g. Szabatin, Zieliński)

The parameter calculation group includes procedures to:

- Find the peak values of individual displacement components
- Calculate response spectra
- Find the peak values in frequency bands
- Determine signal duration
- Cross-correlate or auto-correlate.

The visualization group includes procedures to:

- Chart displacement vs. time (seismogram)
- Chart acceleration vs. time (accelerogram)
- Chart frequency spectrum
- Chart the histogram.

## 5. Stream Processing

Stream processing – an Unix operating system feature – allows for a more efficient process of SPS signals. Stream processing means that output data of one process are not written to a file, but instead directly fed to another process as the input data of that latter process. More than two processes may be chained in a stream processing. An example of three subsequent processes run in a stream processing scheme is here shown:

```
sps_import_sacfname=event23.sac|sps_fbutter fmax=0.5|sps_plot1 fname=p23.jpg
```

Data stored in the **event23.sac** file are imported and converted to the internal SPS format by the **sps\_import\_sac** program, filtered in a low-pass Butterworth filter run by the **sps\_fbutter** program, and finally charted by the **sps\_plot1** program. The resulting chart will be written to the **p23.jpg** file.

## 6. Script Processing

The shell programming feature of Unix means that operating system commands may be grouped into scripts. Prepared scripts may be run as separate programs, be called with parameters, and also may appear as procedures in other scripts. Bourne shell (**sh**), c-shell (**cs**h), or some extensions of the latter (e.g. **bash**, **tcsh**) are the most often used Unix shells. These shells have different syntax but may be freely selected by users. Users experienced in **c/c++** programming languages most probably select the c-shell due to similarities of its syntax to the **c** language syntax. Users familiar with Unix administrative functions most probably select the **sh** shell, since most configuration/administration scripts are written in that shell.

SPS programming does not have to be restricted to shell programming. High level languages (like **c/c++** or **Pascal**), or languages dedicated to stream processing of texts (like **perl** or **awk**) may also be used. Unix itself has many built-in commands dedicated to stream processing of texts, which may be used to write scripts. The commands include: *sort* – sort the stream according to a specified column; *grep* – search for a specified keyword; *cut* – remove specified columns from the stream; *sed* – stream text editor; *bc* – calculator; *head* – cut out from the stream all data beyond a specified line; *tail* – cut out from the stream all data except a specified number of last lines; *tee* – store the stream to a specified file and turn it over to a specified next process.

The above list of programs that might be used in scripts is by no means complete. There are practically no system limits as far as cooperation with third-party software, necessary to adapt the system to some specific needs, is concerned. If a

complex mathematical treatment is necessary, even advanced software packages may be used; either commercially available ones like **matlab**, or freeware like **scilab** and/or **octave**.

## 7. Result Visualization

Visualization is necessary in every step of data processing, starting from input data quality control, through controlling individual processing steps, to presentation of the final results. Procedures supporting presentation of the final results are based on the **gnuplot** chart generator program. This freeware is included in most Linux distributions. In other Unix systems it must be installed separately if charts are to be generated.

Programs responsible within the SPS system for visualization generate scripts for the **gnuplot** program. In this way the user may avoid using rather complicated commands of the chart generator and can obtain a desired chart with a single command. The resulting images are written to graphical files in one of the following formats: PNG, JPG or GIF. The images may be browsed in an Internet browser, in any other graphical program, or displayed directly on the monitor screen in X-window based systems.

## 8. Graphical User Interface

The capabilities of the SPS system described above are available to a user operating from an Unix system terminal. However, an Internet-based graphical user interface has also been designed to make the system more easy and efficient to use. One of the browser applications within the system has already been mentioned: to display graphical files with charts. This is only one of the many possibilities of the user interface.

The basic task of the graphical interface is to administer system resources on the file level. Any Internet browser may be used to transmit input data to the system and to retrieve processing results. Data existing in a format different than the required internal SPS format may be imported and converted, or appropriately exported to that format. The user interface allows for the copying of files, renaming them, deleting unnecessary ones, etc. Scripts for batch processing may also be generated, edited, or deleted within the interface.

The principal advantage of a browser-based user interface is that it enables remote operation. Users are authorized by their logins and passwords. Authorized users have access to all SPS procedures and to the directory containing their data. Users have access exclusively to their own data.

## 9. Hardware Requirements and Availability of the System

The system has been implemented on a Intel-processor-based computer controlled by the Linux RedHat 9 operating system. The **gcc/g++** compiler is required for installation. If graphical user interface is to be operational, an HTTP server (e.g. **apache**) with a PHP module and the **gnuplot** program must be installed. SPS may run

on any hardware platform meeting the requirements of the operating system. Hardware may limit the amount of data that one will be able to process.

The first version of the SPS system is to be released at the turn of 2005/2006. Data importing and processing modules have been developed first. Next, data presentation modules and graphical user interface modules are to be implemented.

The SPS system will be free of charge for non-commercial applications. The system will be distributed as a collection of source codes. Depending on the demand, installation-ready versions for selected Unix versions are also foreseen.

More information on the current status of development of the system may be obtained on the [www.SPS.geol.agh.edu.pl](http://www.SPS.geol.agh.edu.pl) Website, or directly from the author.

**A c k n o w l e d g m e n t s:** This work was financed by the Polish State Committee for Scientific Research, AGH University of Science and Technology, Faculty of Geology, Geophysics and Environmental Protection, contract No. 10.10.140.192.

#### References

- Bellanger, M., 1988, *Digital Processing of Signals: Theory and Practice*, Wiley, Chichester, ISBN 0471921017
- Izydorczyk, J., and J. Konopacki, 2000, *Filtry analogowe i cyfrowe*, Wydawnictwo Pracowni Komputerowej Jacka Skalmierskiego, ISBN 8389105470
- Lyons, R.G., 1997, *Understanding Digital Signal Processing*, Reading, MA. Addison Wesley Pub., ISBN 0201634678
- Mitra, K., and J. Kaiser, 1993, *Handbook for Digital Signal Processing*, Wiley, New York, ISBN 0471619957
- Stranneby, D., 2001, *Digital Signal Processing: DSP and Application*, Newnes, Oxford, ISBN 0750648112
- Szabatin, J., 2003, *Podstawy teorii sygnałów*, Wydawnictwa Komunikacji i Łączności, ISBN 8320613310
- Zieliński, T.P., 2002, *Od teorii do cyfrowego przetwarzania sygnałów*, Akademia Górniczo-Hutnicza, ISBN 8388309552

*Accepted 10 April 2006*

## **Cultural Monument Jeroným Mine, Czech Republic – Contribution to the Geomechanical Stability Assessment**

Zdeněk KALÁB<sup>1,2</sup>, Jaromír KNEJZLÍK<sup>1</sup>, Robert KOŘÍNEK<sup>2</sup>, and Petr ŽŮREK<sup>2</sup>

<sup>1</sup>Institute of Geonics, Academy of Sciences of the Czech Republic  
Studentská str.1768, CZ-708 00 Ostrava, Czech Republic  
e-mail: kalab@ugn.cas.cz; knejzlik@ugn.cas.cz

<sup>2</sup>VSB – Technical University of Ostrava  
17. listopadu str. 15, CZ-708 33 Ostrava, Czech Republic  
e-mail: robert.korinek@vsb.cz; petr.zurek@vsb.cz

### **A b s t r a c t**

The geomechanical stability assessment of the cultural monument Jeroným Mine at Čistá near Mariánské Lázně, Czech Republic, deals with the issues of the evaluation of the geomechanical condition of the rock mass and the mine workings. This monument supplements the fund of European mining monuments, especially in the area of tin mining and treatment in the period of the second half of the 16<sup>th</sup> century by the part of old mine workings and in the period of more than 400 years by a part of abandoned mine workings.

Since the year 2001, measurements have been carried out to check the crack development in the mine working (mainly by means of plaster and glass targets – 10 measuring points), development in changes in convergence cross-sections of linear and spatial workings (21 measuring points) and fluctuations in the groundwater level (4 locations). Detailed surface geophysical survey was made in the same year by the method of apparent resistivity and radiometric measurement. In the year 2004, together with the reconstruction of the drainage adit, seismological monitoring of seismic load on the mine working was started by means of a station installed directly in the mine working. First results of these measurements are presented in this contribution.

**Key words:** geomechanical monitoring, seismological monitoring.

## 1. Introduction

From its very beginning, human society has required food, energy and raw materials for its existence; food was necessary for survival, energy for increasing the human strength and raw materials for ensuring the human's own existence and also for enhancing what is now called the standard of living. If we consider the initial impulse to the development of workmanship and industrial skill, we shall arrive at the conclusion that the mining industry must be one of fundamental sources. At first, our ancestors had collected raw materials from the Earth surface or watercourses; gradually they began searching for them at depths. They had to settle problems connected with soil and rock breaking, lighting, supporting and ventilation of underground spaces, and haulage of broken materials to the surface. Another effort was related to getting desired substances from minerals mined, i.e. to processing and metallurgical treating. Solving all these problems led to development of techniques such as the engineering thinking and subsequently the technical education.

If a set of favorable conditions led to the preservation of an engineering monument as a whole, it would be an unforgivable mistake to leave the monument derelict without trying to save, restore and open it to the public. The Jeroným Mine at Čistá is undoubtedly such an engineering monument. It offers a downright textbook example of medieval mining from the point of view of mining technologies (Fig. 1); it is possible that during remediation works, mining artefacts from several centuries may be found in the underground as happened in an already closed, relatively near-by Stannum Mine in Horní Slavkov.

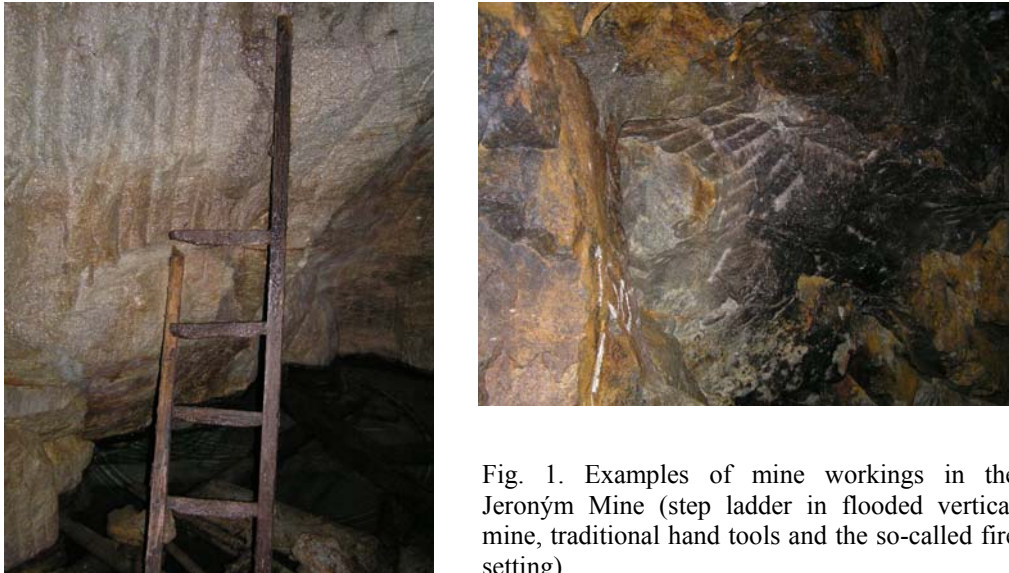


Fig. 1. Examples of mine workings in the Jeroným Mine (step ladder in flooded vertical mine, traditional hand tools and the so-called fire setting).

The first steps leading to the preservation of the set of mine workings in Jeroným, and the opening of the complex to the public have already been taken. For its uniqueness, the extent of the mine workings and a high degree of preservation of late medieval mine workings, the Ministry of Culture declared the Jeroným Mine to be a cultural monument on February 2, 1990. The geomechanical stability assessment of the cultural monument Jeroným Mine deals with the issues of the evaluation of the geomechanical condition of the rock mass and the mine workings of National Cultural Monument at Čistá. Mining operations themselves that will be performed in the locality in the future will have to be commenced, completed, or overlapped according to time schedules. Designs of such schedules were already presented in expert opinions and studies elaborated earlier (Majer 1995, Bernard and Suček 2000, Kořínek and Žůrek, 1999, Žůrek *et al.* 2001). The schedules designed earlier are not fully valid at present, because in the course of observations taken in the locality concerned, the opinion on the extent of some mining operations has changed (e.g. discovery of modern fissures of unknown development).

The history and geology of this monument was published, e.g., by Žůrek and Kořínek (2003). This article is focused primarily on seismological monitoring and geomechanical problems connected with the opening of this complex to the public.

## **2. Geological, Geomechanical and Hydrogeological Monitoring**

The assessment of the stability of historical structures is always a difficult matter because there is a lack of information available. In the case of the Jeroným Mine, the structure, layout and extent of mine spaces and exact time of their origin are not known (during the fire of the archives at Horní Slavkov, all mine documentation was destroyed). At the beginning of detailed analyses, local geological structure, hydrogeological situation (pathways of mine and surface waters) and petrophysical properties of rocks (with various degrees of weathering) are not known. The complicated structure of stopped-out spaces supplemented with pillars, blocks of rocks in the hanging wall, and others do not make it possible to assess, without measurement, the stress conditions and the stability of particular elements of the mass. The hydrogeological situation is a very significant factor that can change suddenly and thus can cause unexpected hazardous conditions.

Geological monitoring is based on implementation of detailed structural and tectonic measurements and observation of crack development in the mine working. About 10 measuring points were realized above all by means of plaster and glass targets. Methodology of measurements and interpretation in the frame of evaluation of disjunctive tectonics was presented in report in 2001 (Žůrek *et al.*). Geological observations reveal some changes (e.g. new fissures or broken targets) but we are able to say that we do not document significant changes in measuring points. The most important movements were documented in small spatial working on pillar with a diame-

ter of about 1 m that is situated on the bottom of bulk material (the so-called “stone bridge”).

Development of changes in convergence cross-sections of linear and spatial workings has been measured quarterly since 2001 in 21 measuring points. Convergence cross-sections of linear workings (16 points) are measured using convergence standard with spring-actuated mechanism and optical scale reading, in horizontal and vertical positions. Measured values are in range 75-125 cm. These measurements do not document significant values of convergence. Convergence cross-sections of spatial workings are determined by means of laser range finder; the measured values ranged from 3.5 up to 11 m. The graph of measured values is shown in Fig. 2. But the period under consideration is short, and therefore, it is not possible to make conclusion about the stability of mine workings. It will be also necessary to take into account other influences.

Four locations were chosen for measurement of fluctuations in the groundwater level that have been also carried out quarterly. Two locations are situated above the gallery level near the Jeroným shaft (V1 and V2), the other two are approximately at the level of the Jeroným adit (V3 and V4). The graph of relative levels of groundwater is shown in Fig. 3.

Fluctuations of groundwater level do not offer detailed logical explanation. It is evident that water gets to the mine solely by seeping the surface water due to gravity. The drainage of the mine is done via the Jeroným adit along the non-travelable way through the extensive caved area in the adit. A part of mine workings below the adit

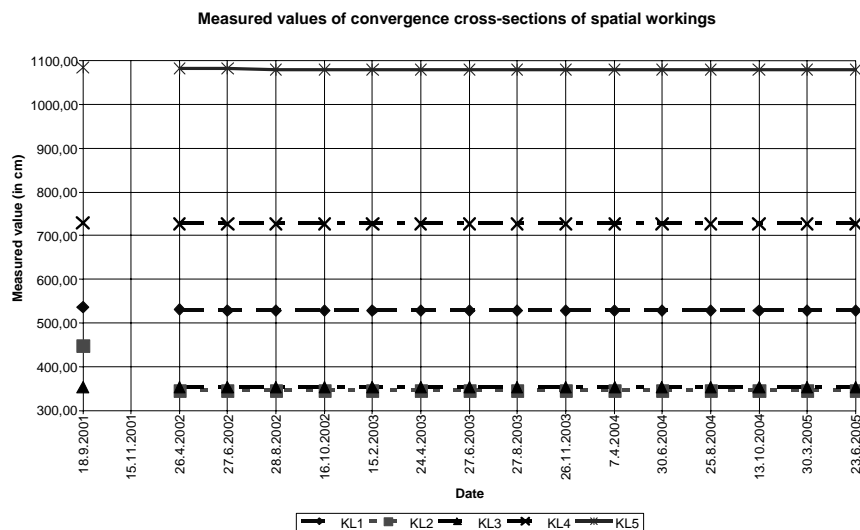


Fig. 2. Graph of measured values of convergence cross-sections of spatial workings.

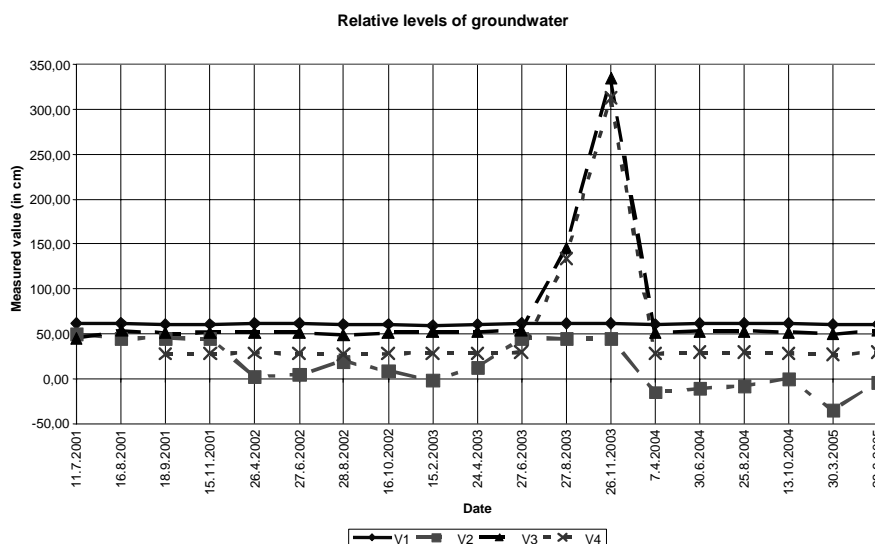


Fig. 3. Graph of relative levels of groundwater (positive numbers represent decrease of groundwater level).

level of the Jeroným Mine, as well as some mine workings above the adit level (drainless spaces) are permanently flooded with closed mine water. In addition to visible drainless spaces, other spaces may exist in the mass that could be closed by the caved areas already existing and this prevented any communication with mine water. Measurement on the V1, V3 and V4 locations, excluding measurement at autumn 2003, do not show significant changes. Significant fluctuation is detected on the V2 location that is situated at the bottom of bulk material in mine room named K1. The measured changes range up to 1 m (positive numbers in graph represent decrease of groundwater level). The evaluation of these factors according to the significance of adverse effects is difficult. In all cases, this concerns factors whose manifestations are, from the temporal point of view, long-term. In the authors' opinion, the most serious factor is water flow pressure and related suffosion. The factor of water flow pressure and suffosion are regarded as the causes of the existing caving of the Jeroným adit.

The initial state for observing the geomechanical stability of the mine workings in the course of stability securing operations is the present condition, and will be observed by a designed monitoring system in the future. The same system is valid for the evaluation of the character and the geomechanical condition of pillars and coal between rooms and for the evaluation of the origin and development of the so-called modern fissures that have been assessed only in virtue of visual observation so far. At any rate, an unfavorable factor that negatively affects the geomechanical stability of

the part of the Jeroným Mine is the uncompleted closure of the mine by partial backfilling the Jeroným shaft (in 1960s). The formed cone of unconsolidated rock backfilling material loads the bottom of the room K1 below the Jeroným shaft in the vertical direction and simultaneously compresses the adjacent rock pillars laterally (preliminarily the pressure of soils at rest).

It is necessary to add that in 2001 detailed surface geophysical measurements were made by the method of apparent resistivity measurement with the aim to delimit zones of low and high resistivity, and by radiometric measurements with the aim to document tectonic lines and weakened zones (Žůrek *et al.* 2001).

### 3. Seismological Monitoring

A significant factor is loading of the mine working due to natural and technical seismicity. The area of foci of natural earthquakes closest to the area observed is situated approximately 25 km to the west (Kraslice area). In this area, seismic swarms occur even at present (see *Studia Geoph. et Geod.* Nos. 2 and 4, Vol. 44, 2000). Technical seismicity is induced by traffic on the road above the mine working and, during the building operations, by vibrations generated by various work activities and blasting operations. Those are an integral part of construction technology for the treatment of mine spaces and the building of new structures (Kaláb 2003, Kaláb and Knejzlík 2004).

In the year 2004, together with the reconstruction of the adit Jeroným, seismological monitoring of seismic load on the mine working was started by means of a station installed directly in the mine working. Seismic recording apparatus PCM3-EPC (Knejzlík and Kaláb 2002) with special modification for environment with high air humidity and drip water (inner and outer housing IP55) is used. Therefore, signal cables (connection with DCF 77,5 kHz receiver, seismometer junction box and GSM modem) are pulled-on to additional silicon tube (Fig. 4). Seismometers SM3 with up-

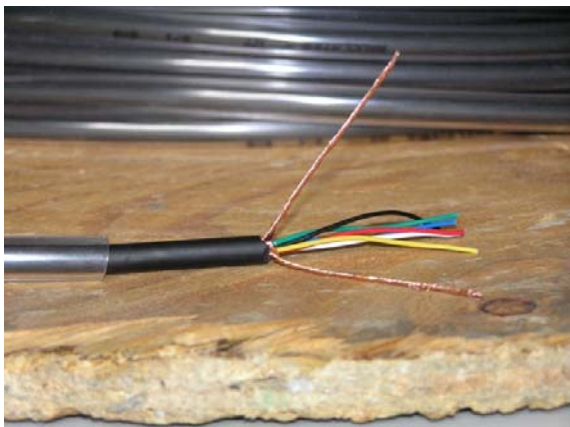


Fig. 4. Signal cable pulled-on to additional silicon tube.

per limit frequency 80 Hz are used because the main aim is detecting vibrations generated by blasts used as a part of technology during renovation of passage for drainage and ventilation. Three sensors in geographical organization are anchored on concrete pillar to have possibility to detect the highest frequencies of recorded vibrations. Amplified analogue signals are connected to the PCM3. This apparatus is telemetrically connected to the Institute of Geonics, which will enable the remote control of station operation, change in the setting of operating parameters and data transmission to the interpretation centre. Sketch of seismic system is shown in Fig. 5.

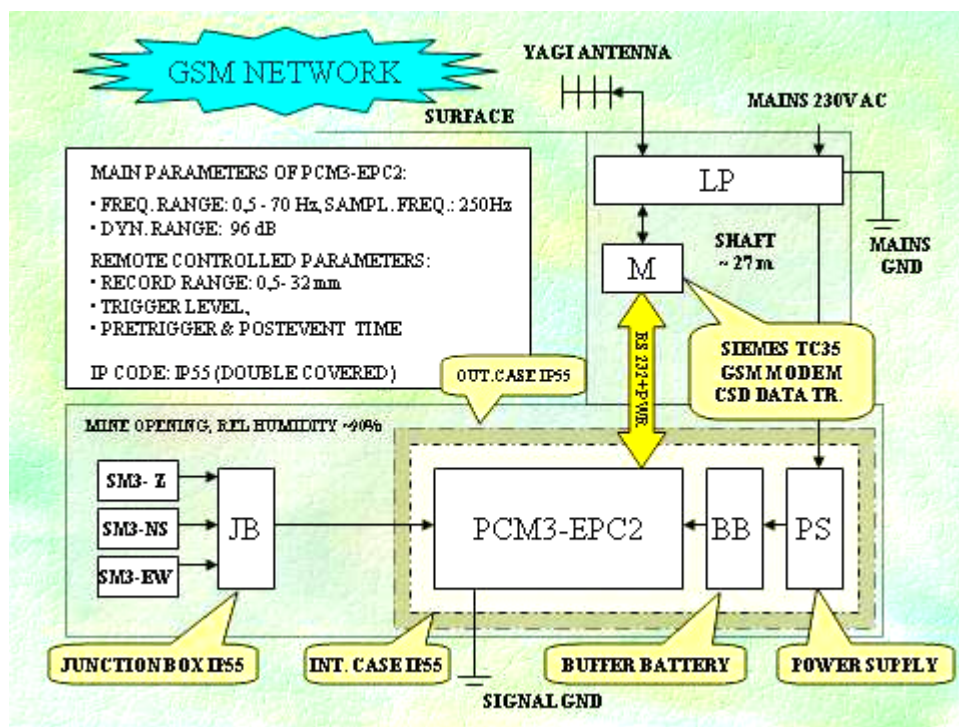


Fig. 5. Sketch of seismic system.

Results of seismological measurements are continuously presented in reports to the buyer. The main part of records is represented by blasts mentioned above. Further, seismic records of quarry blasts from Krásno (about 15 km), unidentified parts of teleseismic events and some vibrations generated by traffic are also recorded. Data are collected and interpreted in the Institute of Geonics. The described seismological monitoring has been performed without a break up to now. Altogether 223 records were interpreted in 1.1.2005 – 31.8.2005; most of them are effects of blasts in reconstructed adit (71.7%). Summary of maximum component velocity is shown in Fig. 6.

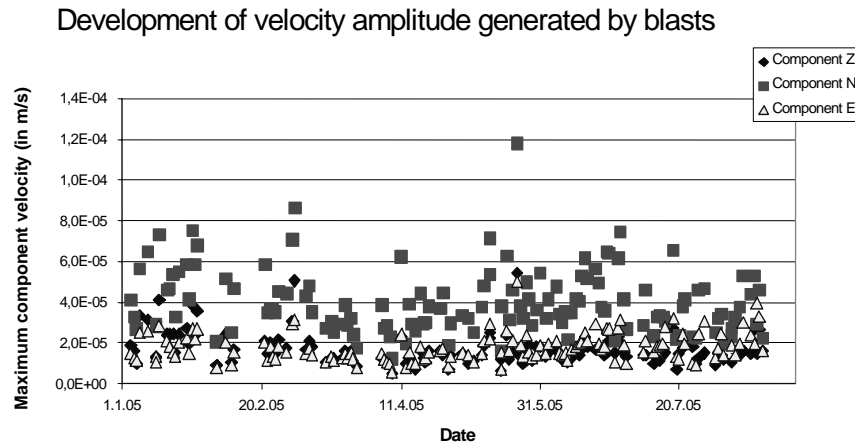


Fig. 6. Summary of maximum component velocity generated by blasts.

Approximately 300 m of the Jeroným adit was reconstructed up to the end of August 2005. The whole length is about 400 m and about 50 m is a prolongation of mine works. The highest values were measured on north-south component because of orientation of mine spaces and location of seismic pillar. The velocity of  $0.1 \text{ mm}\cdot\text{s}^{-1}$  was not exceeded, excluding the record from 23.5.2005 (Fig. 7). This value is very low and also under conventional critical value, but to take into account significant and present state of mine spaces (weathering and jointing firstly) it is necessary to admit higher seismic loadings.

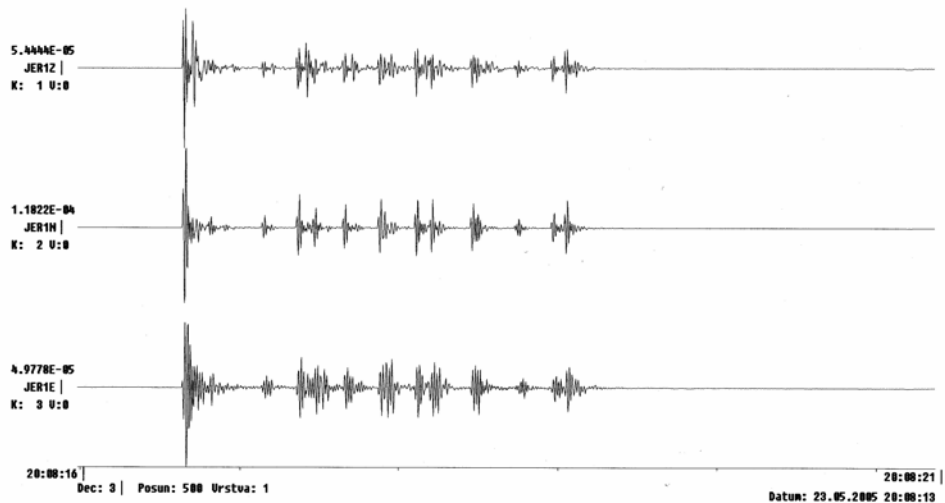


Fig. 7. Example of wave pattern of blast generated in the Jeroným adit.

#### 4. Conclusion

The current geomechanical and seismological monitoring is performed with the aim to prevent the monument from damaging. The main results are as follows:

- Medieval mine Jeroným is in preparation for public including construction works,
- Geomechanical stability measurements are performed periodically,
- Seismological monitoring began in June 2004; extended seismological monitoring must determine admissible parameters of seismicity for safe operation after making the mine accessible to the public; up to now more than 300 seismic events were recorded; the maximum velocity amplitude did not exceed value of  $0.1 \text{ mm}\cdot\text{s}^{-1}$ .

This research is partly sponsored by project of Czech Science Foundation No. 105/06/0068 and Research Programme of the Academy of Sciences of the CR, No. OZ30860518.

#### References

- Bernard, J., and P. Suček, 2000, *Study on Opening of the Historic Mine Working, Jeroným, to the public*, Manuscript, RD Příbram s.p., unpublished (in Czech).
- Kaláb, Z., 2003, *Evaluation of seismic load of the Medieval Mine Jeroným, Czech Republic*, Acta Montanistica Slovaca **8**, 1, 36-41 (in Czech).
- Kaláb, Z., 2004, *Observation of vibrations in the Medieval Mine Jeroným, Čistá, Czech Republic*, Geotechnics 2004, Proc. Conf. ORGWARE and BERG TU Košice, Slovakia, 477-482 (in Czech).
- Kaláb, Z., and J. Knejzlík, 2004, *Experimental measurement of seismic effect generated by blasts in Medieval Mine Jeroným*, Transaction of the VSB-TU, Civil Engin. Ser. **4**, 2, 159-166 (in Czech).
- Knejzlík, J., and Z. Kaláb, 2002, *Seismic recording apparatus PCM3-EPC*, Publs. Inst. Geophys. Pol. Acad. Sc. **M-24**, 340, 187-194.
- Kořínek, R., and P. Žůrek, 1999, *Expert opinion "Opening of the Engineering Cultural Monument, Former Jeroným Mine, at Čistá, Sokolov Region, to the public"*, Report, Technical University of Ostrava, unpublished (in Czech).
- Majer, J., 1995, *Expert Opinion on the Historic Mine Working, Jeroným at Čistá*, Manuscript, Prague, unpublished (in Czech).
- Žůrek, P., and R. Kořínek, 2003, *Opening of the Medieval Jeroným Mine in the Czech Republic to the Public*, Acta Montanistica Slovaca **8**, 2-3, 96-100 (in Czech).
- Žůrek, P., et al., 2001, *Geomechanical stability of the cultural monument, Jeroným Mine – Čistá, Sokolov Region*, Report, Technical University of Ostrava, unpublished (in Czech).

*Accepted 10 April 2006*



## **Historical Buildings in the Ostrava and Karviná Region and their Seismic Loads**

Markéta LEDNICKÁ

VŠB – Technical University of Ostrava, Faculty of Civil Engineering  
Ludvíka Podéště 1875, CZ-708 33 Ostrava-Poruba, Czech Republic  
and  
Institute of Geonics, Academy of Sciences of the Czech Republic  
Studentská 1768, CZ-708 00 Ostrava, Czech Republic  
e-mail: lednicka@ugn.cas.cz

### **A b s t r a c t**

This paper refers to the present state of historical buildings situated in the Karviná and Ostrava region and also to the problems of these buildings caused first of all by surface vibrations generated by mining-induced seismicity in the Karviná region and by technical seismicity caused by industrial activities and transportation in the Ostrava region. Designing of earthquake-resistant structures and analyses of structures affected by surface vibrations are governed by standards ČSN 73 0036 *Seismic loads of buildings*, ČSN EN 1998–1 *Design of structures for earthquake resistance* and ČSN 73 0040 *Loads of technical structures by technical seismicity*. In the second part of this paper, these three standards are described and compared. In the last part of the paper, the measured data from the last six years are shown and reviewed, specifically the maximum values of amplitudes of oscillation velocities. These data come from seismic monitoring using solitary stations of the Institute of Geonics, situated in surface structures in the Karviná region, and from experimental measurements of the influence of transport in Ostrava in 2004.

### **1. Introduction**

Building constructions must be designed, built and maintained well enough to meet the requested purpose for their whole expected lifetime at an adequate security level. Such a design benefits from the knowledge of multiple loads acting on the construction during its lifetime. One of the numerous loads is seismic load, which is classified as a dynamical load; as such, it causes significant acceleration of the construction or construction elements (Procházka and Krátký 1999).

This paper refers to problems connected with the occurrence of technical seismicity in the area around Karviná and Ostrava, especially to the significant effects of this load on historical buildings in this area. Such effects are commonly encountered here in spite of the present inhibition of mining and industry. It is therefore necessary for the technical seismicity load to be considered in the assessment of existing objects, of which the least resistant are, e.g., historical buildings.

When evaluating the effects of seismic load and the response of the assessed object, the object must be considered on an individual basis, respecting its construction and material specificities and the ambient conditions characterised by the type of foundation soil, location of the building, purpose of the object, kind of seismic load, etc. The present assessment of buildings subject to seismic load in the Czech Republic is governed by the following standards: ČSN 73 0036 *Seismic loads of buildings* and ČSN EN 1998-1 *Designing of structures for earthquake resistance* for natural seismicity; and ČSN 73 0040 *Loads of technical structures by technical seismicity* for technical seismicity. The problems related to seismic load-specific object assessment in compliance with the above standards are discussed in more detail, for instance in Lednická (2005).

The first part of this paper evaluates the present condition of historical buildings in the Ostrava and Karviná regions. The next part gives the results of measurements from 1999-2004 in the studied area and their comparison with the limit values specified in valid standards. The last part presents an example of mathematical modelling in the PLAXIS program system of a selected construction subject to seismic load.

## **2. Historical Buildings in the Ostrava and Karviná Regions**

Many historical cultural monuments located in the area of Ostrava and Karviná, together with a number of unique technical monuments, are the result of the industrial boom in the past centuries. Unfortunately, many of these objects are now in poor technical condition. These are mostly unused historical buildings, and particularly technical monuments such as former coalmines. The constructions tend to dilapidate, and their static conditions may be seriously impaired.

Historical objects are, due to their old age and vulnerability, highly sensitive to any new loading effects. One of the undesirable loads acting on these constructions is seismic load. Its effects were not considered at the time these buildings were designed and subsequently realised, because the technical seismicity loads appeared later, as a result of the starting coal mining and industrial development. Therefore, historical buildings are very sensitive to vibrations.

### ***A review of historical monuments in the area of Ostrava and Karviná***

*Central List of Cultural Monuments of the Czech Republic* (accessible on the Internet) was used to map historically and culturally valuable objects. Only building objects were processed. Due to the high number of these objects, only those now declared as cultural monuments were selected. The former county of Karviná represents a still operated mining area of the Karviná partial basin; the town of Ostrava covers a

larger part of the Ostrava partial basin, where mining activities have been discontinued.

**Abstract from the Central List of Cultural Monuments (for the former county of Karviná)**

*Immovable monuments*

(total number: 149, of these 99 building objects, of these 74 declared as cultural monuments)

Castles and chateaus	total	10 objects
	declared as cultural monuments	8 objects
Ecclesiastical objects (churches and chapels)	total	37 objects
	declared as cultural monuments	29 objects
Objects of urban architecture	total	29 objects
	declared as cultural monuments	23 objects
Objects of folk architecture	total	7 objects
	declared as cultural monuments	4 objects
Monuments of production science and technology	total	16 objects
	declared as cultural monuments	10 objects

**Abstract from the Central List of Cultural Monuments (for the former county of Ostrava)**

*Immovable monuments*

(total number: 366, of these 338 building objects, of these 244 declared as cultural monuments)

Castles and chateaus	total	5 objects
	declared as cultural monuments	4 objects
Ecclesiastical objects (churches and chapels)	total	16 objects
	declared as cultural monuments	15 objects
Objects of urban architecture	total	287 objects
	declared as cultural monuments	198 objects
Objects of folk architecture	total	1 object
	declared as a cultural monument	1 object
Monuments of production science and technology	total	29 objects
	declared as cultural monuments	26 objects

### *Constructional design of historical buildings*

Let us focus on particular historical buildings in the Ostrava and Karviná regions, especially those of more interesting construction. Timber buildings include timber churches, and masonry buildings include chateaus, churches and technical monuments. Steel-concrete and steel constructions are generally met among technical monuments: frame constructions combined with masonry.

Masonry objects, obviously the most numerous objects among historical buildings, belong to the constructions that are least resistant to dynamic load. These buildings are usually the oldest and most valuable ones in the study area. In addition, some of them are now in a very poor technical condition with serious static failures. Steel-concrete and steel constructions of the monuments are now in a relatively good technical condition, compared to the previously mentioned masonry objects. This category includes relatively new buildings ranked among technical monuments, from the early 20th century.

The map in Fig. 1 shows, due to limited space, only objects of more interesting construction among all cultural monuments of the Ostrava and Karviná regions.

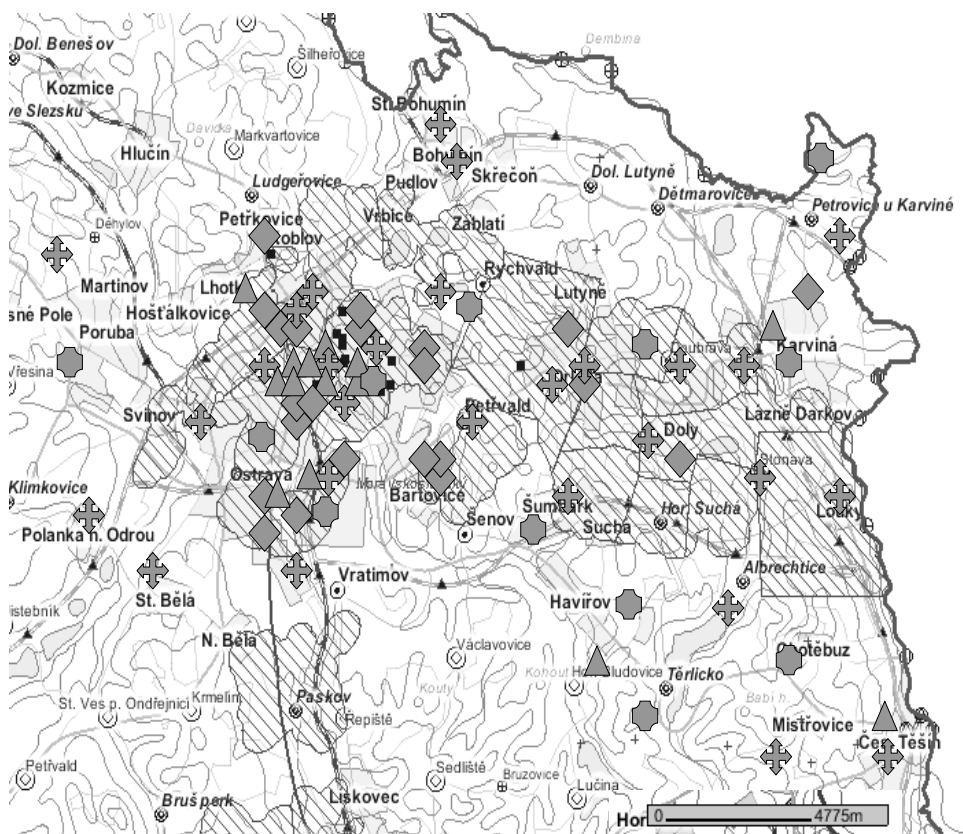


Fig. 1. A map of the study area with indicated cultural objects: ✚ – church, ◻ – chateau, ◊ – technical monument, ▲ – other object. The undermined areas are hatched.

### 3. Measurement of the Oscillation Velocity on the Surface

To assess the response of the existing buildings to technical seismicity load, it is necessary to take the appropriate measurements first (of the oscillation velocity at a reference point, according to ČSN).

The stations of mine network administered by the DPB-OKD are usually located in mine workings at present. The effects of mine-induced seismicity on the surface in the Karviná area are now monitored by solitary seismic stations of the Institute of Geonics, situated in selected objects on the surface (Holečko et al., 2005). This monitoring was started in the years 1999-2000, when four solitary seismic stations were established within the Program of Research and Development of the Czech Mining Bureau in the areas of Orlová (ORL1 and ORL2), Doubrava (DOU1) and Stonava (STO1). Since 2003, the measurement has been carried out with the support from the Grant Agency of the Czech Rep. (Project No. 105/03/0078). Two more stations were established: in the area of Darkov (DAR1) in 2003 and in the area of Karviná (KAR1) in 2004. The stations are situated at places of elevated incidence of mine-induced seismicity effects. Data from these stations are recorded in a trigger mode after exceeding the pre-set level of the oscillation velocity. Digital three-component instruments PCM3-PC and PCM3-EPC are used for the measurements (Knejzlík and Kaláb, 2001). The seismometers are oriented to geographic directions, the third component is vertical. A review of maximum measured values of the amplitudes of the oscillation velocity at particular stations in 1999-2004 is given in Table 1.

Table 1  
Maximum recorded amplitude of the oscillation velocity ( $\text{mm}\cdot\text{s}^{-1}$ )  
(according to Holečko et al. 2005)

	ORL1	ORL2	DOU1	STO1	DAR1	KAR1
1999-2002	> 8.00*	> 8.00*	> 9.00*	6.2		
2003	1.21	2.95	10.4	3.99	4.07	
2004	1.55	3.41	5.77	4.09	2.31	4.31

\* the adjusted maximum range of the device was exceeded

**a** maximum recorded component amplitude of the oscillation velocity in years 1999 – 2004 ( $\text{mm}\cdot\text{s}^{-1}$ )

In some strongest seismic effects, the values of the amplitude of oscillation velocity exceed the limit values of the maximum oscillation velocities stipulated by the appropriate standard for the respective object class, the type of the foundation soil and the degree of damage, as stated in Table 2 (ČSN 73 0040).

If the maximum values given above were measured in a historical building, Table 2 implies that the lower limits of the marked ranges of maximum oscillation velocity would be exceeded by the maximum measured value of oscillation velocity in the monitored period ( $10.4 \text{ mm}\cdot\text{s}^{-1}$ ). In such a case, these objects might reach the respec-

tive degree of damage, namely degree 1 (first signs of damage) for all types of foundation soil or degree 2 (mild deterioration with minor damage) for foundation soil with the least loading capacity.

Table 2

Maximum oscillation velocity for historical buildings (class A) depending on the degree of damage of the building and the type of the foundation soil (according to Table 14 in ČSN 73 0040)

Maximum oscillation velocity ( $\text{mm}\cdot\text{s}^{-1}$ ) for the field of disturbance frequency			Degree of damage	Resistance class of the object	Type of foundation soil
$f < 10\text{Hz}$	$10\text{ Hz} \leq f \leq 50\text{ Hz}$	$f > 50\text{ Hz}$			
below 3	6 to 3	6 to 15	0	A	a
3 to 6	6 to 12	12 to 20	0	A	b,c
6 to 10	10 to 20	15 to 30	1	A	a
8 to 15	15 to 30	20 to 40	1	A	b,c
10 to 20	20 to 30	30 to 50	2	A	a
15 to 25	25 to 40	40 to 70	2	A	b,c

The occurrence of mine-induced seismicity now concerns mainly the area of Karviná. The Ostrava region is dominated by technical seismicity caused by industrial activity and traffic. Dynamic response to technical seismicity should be assessed after the limit value of effective velocity (Table 8 in ČSN 73 0040) is exceeded by the value of effective velocity measured at a reference point. Experimental measurements of the effect of traffic taken in Ostrava in 2004 give us information about the key parameters of vibrations, i.e., the maximum amplitude of oscillation velocity for the sample file and frequency ranges for the categories of urban transportation – see Table 3 (Káláb et al. 2005). The measurements were taken in the immediate neighbourhood (within 50 cm from the closer wheel). This is why these particular measured values refer to buildings in the immediate proximity to the traffic.

Table 3

Frequency ranges and maximum amplitudes of oscillation velocity acquired from the measurements (according to Buričan, 2004)

	Frequency ranges (Hz)	Range of maximum amplitudes of oscillation velocity ( $\text{mm}\cdot\text{s}^{-1}$ )
Cars	5 – 13	within 0.1
Buses and trolleys	1 – 7	0.4 – 0.8
Trams	33 – 50	0.9 – 1.3

Table 4 shows limit values of effective oscillation velocity, specifically for historical buildings classified in resistance-class A, depending on the class of importance of the building (ČSN 73 00 40).

Table 4  
Limit values of effective velocity  $v_{ef}$  [m.s<sup>-1</sup>] for historical objects  
(according to Table 8 in ČSN 73 0040)

Resistance class of the object	$v_{ef}$			
	Class of importance of the object (according to ČSN 73 0031)			
	U	I	II	III
A	0.2	0.4	0.7	1.1

If such measurements were taken for historical buildings, the marked limit values of effective oscillation velocity would be exceeded by the measured value. In such cases, it would be necessary to assess the dynamic response according to Czech standards.

***Example of mathematical modelling in PLAXIS program system of a selected construction subject to seismic load***

The PLAXIS program system, developed for both static and dynamic analyses of stress–strain conditions in geotechnical tasks, is based on the principle of the Finite Elements Method (six- or fifteen-node triangular elements). Modelling of the behaviour of constructions subject to seismic load is enabled by an additional dynamic module of this program. This module allows to solve tasks related to the effects of both natural and technical seismicity. The tasks can be modelled using two basic approaches – the point source of vibrations (radial wave propagation) or application of dynamic loads along the lower boundary of the model (shear waves propagate from the lower boundary upwards). The applied dynamic load may either have the character of harmonic oscillation (amplitude and frequency of oscillation are defined) or can be loaded from the appropriate ASCII files in the format of time values for shifts, velocities or accelerations.

Construction of vault was chosen as the case study for the formulation of a model, because vault is a typical construction element in historical masonry buildings. Generally, a vault is an arch-like supporting structure, which transfers the entire acting load into the support beams only by pressure. This is due to the curvature of the central surface of the vault. The ordinates of the vault are proportional to moment of flexion from the load (Lipanská 1998). Such constructional arrangement permits to use materials with very low tensile strength, such as brick or stone masonry. Vault supports must be immovable and stiff enough. A very important element in vault assessment is the so-called line of pressure. It is generally a curve, more accurately, a connection line among pressure centres of all cross sections of the vault. The vault assessment consists of checking of three conditions of balance:

- line of pressure of the vault arch must not protrude from the cross-section core (this follows from the condition that only compressional normal stress may originate upon loading in any cross-section. If the line of pressure shifts beyond the inner,  $1/3 t$  wide zone,  $t$  being the vault thickness, a tensile normal stress is generated on the edges of the cross-sections),
- the angle between the resulting  $R$  at each point of the vault and a normal to the joint must be lower than the friction angle of the masonry,
- the compression force at any cross-section must not exceed the calculated loading capacity of this cross section under eccentric compression.

This model case study was designed as to determine the changes of normal stresses upon dynamic loading at chosen cross sections of the vault. Material characteristics of other constructions – walls and foundations – and the parameters of the rock environment were adjusted to fit the requirements of the model.

### ***Geometry of the model***

The calculation model consists of the rock environment and a simplified model of a historical building (Fig. 2). The model of the rock environment is 80 m long and 20 m high. A homogeneous rock environment is considered for simplicity. The simplified model of a historical building suggests a semicircular wagon-vault supported by walls based on continuous footing. The vault has a graded thickness in its cross section and a backing.

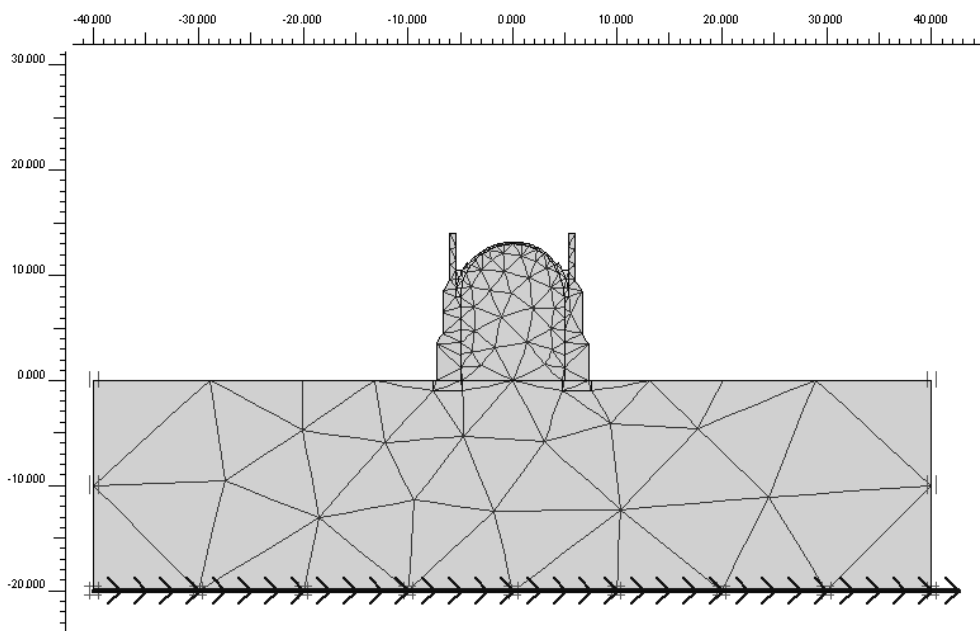


Fig. 2. Calculation model with indicated grid of finite elements and defined boundary conditions.

Geometrical parameters of the vault:

– clear span of the vault	10.0 m
– rise of the vault	5.0 m
– thickness at vault head	0.21 m

***Boundary conditions***

The boundary conditions of the model are defined by standard strain conditions (stiff basement) and conditions for earthquake modelling (the horizontal displacement, recalculated from input velocity record, is defined on the lower boundary). Vertical boundary conditions are defined by absorption.

***Characteristics of the finite elements grid***

Fifteen-nod triangular elements were chosen for the calculation. A loose grid was chosen for the model of rock environment, a detailed grid was chosen for the constructions of the building.

***Material properties***

Properties of the rock environment and the construction materials are given in Tables 5 and 6. The influence of groundwater is not considered in the model.

Table 5

Material characteristics of the rock environment

Parameter	Units	
Volume weight $\gamma$	kN/m <sup>3</sup>	23
Elasticity modulus E	kN/m <sup>2</sup>	100,000
Poisson number $\nu$	–	0.25
Cohesion c	kN/m <sup>2</sup>	80
Internal friction angle $\varphi$	°	30

Table 6

Material characteristics of the constructions

Parameter	Units	Vault	Walls	Foundations
Volume weight $\gamma$	kN/m <sup>3</sup>	18	20	20
Elasticity modulus E	kN/m <sup>2</sup>	2500,000	5000,000	5000,000

***Dynamic loads***

A record of a mine-induced seismic event taken at the Stonava station at 7:49 AM on 6 February 2005 was used for the model (Fig. 3). The maximum componential

amplitude of oscillation velocity on horizontal component E-W is 2.92 mm/s. Dynamic load is applied along the lower boundary of the model by uploading the relevant ASCII file, specifically modified for this purpose. The file contains time values and values of oscillation velocity of particular components.

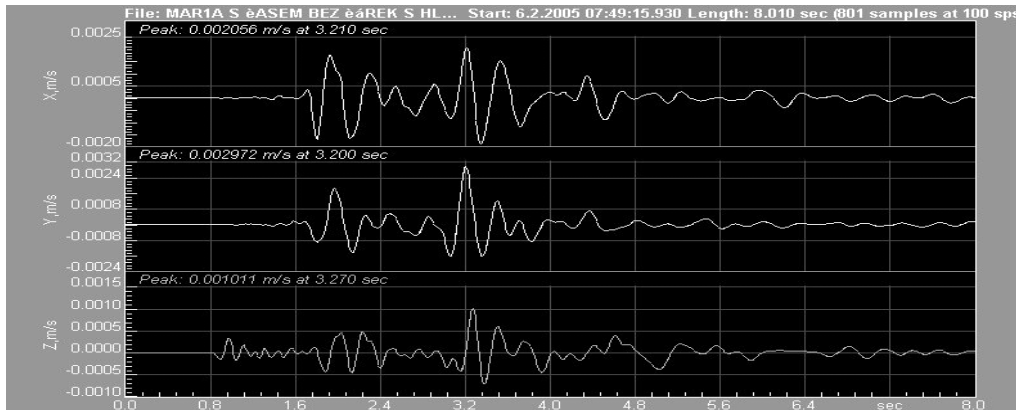


Fig. 3. Wave image of a mine-induced seismic event from the Stonava station of 7:49 AM, 6th Feb. 2005.

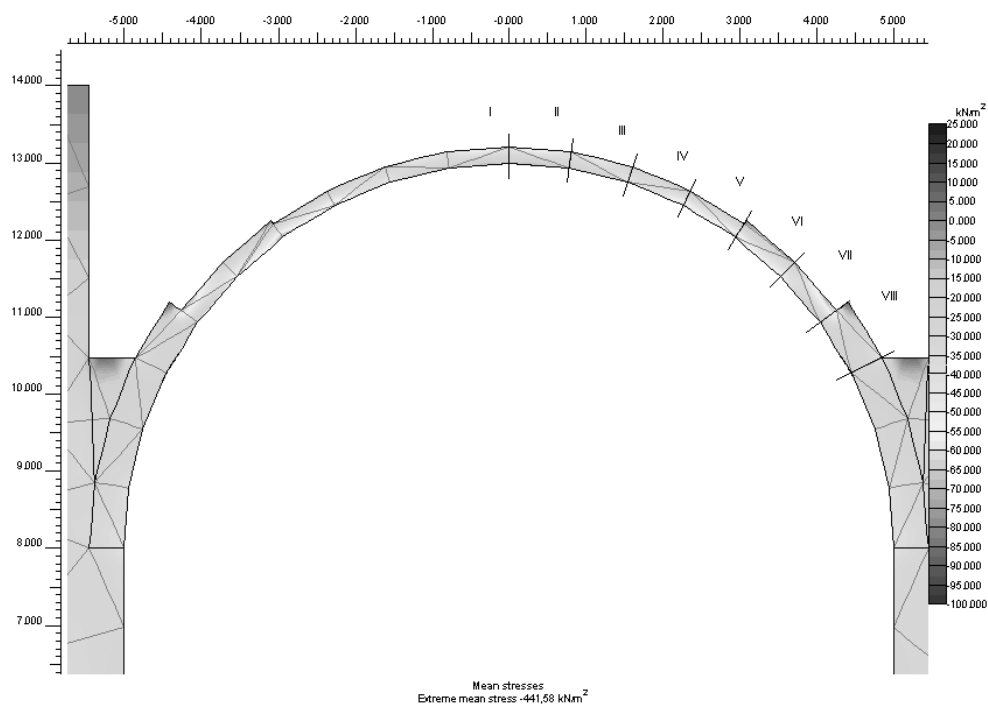


Fig. 4. Stress patterns for the vault construction at time  $t = 0$  s.

### Calculation

During the calculation, stress patterns at chosen cross sections were first determined under static load on the construction (at time  $t = 0$  s) (Fig. 4). Then, stress patterns at the same cross sections were determined under dynamic load at time  $t = 2.97$  s with vault oscillation to the right (Fig. 5), and at time  $t = 3.4$  s with vault oscillation to the left (Fig. 6).

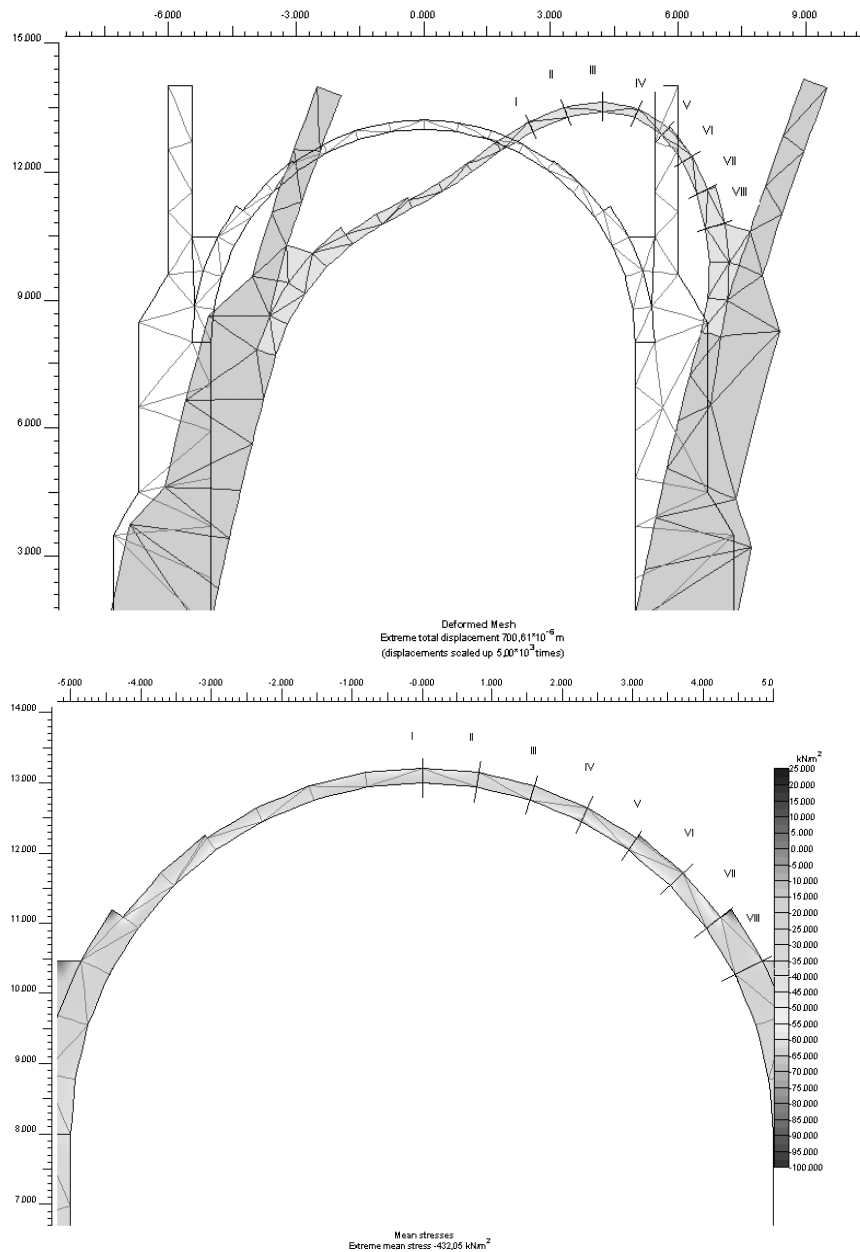


Fig. 5. Shape of the deformed grid and stress patterns for the vault construction at time  $t=2.97$ s.

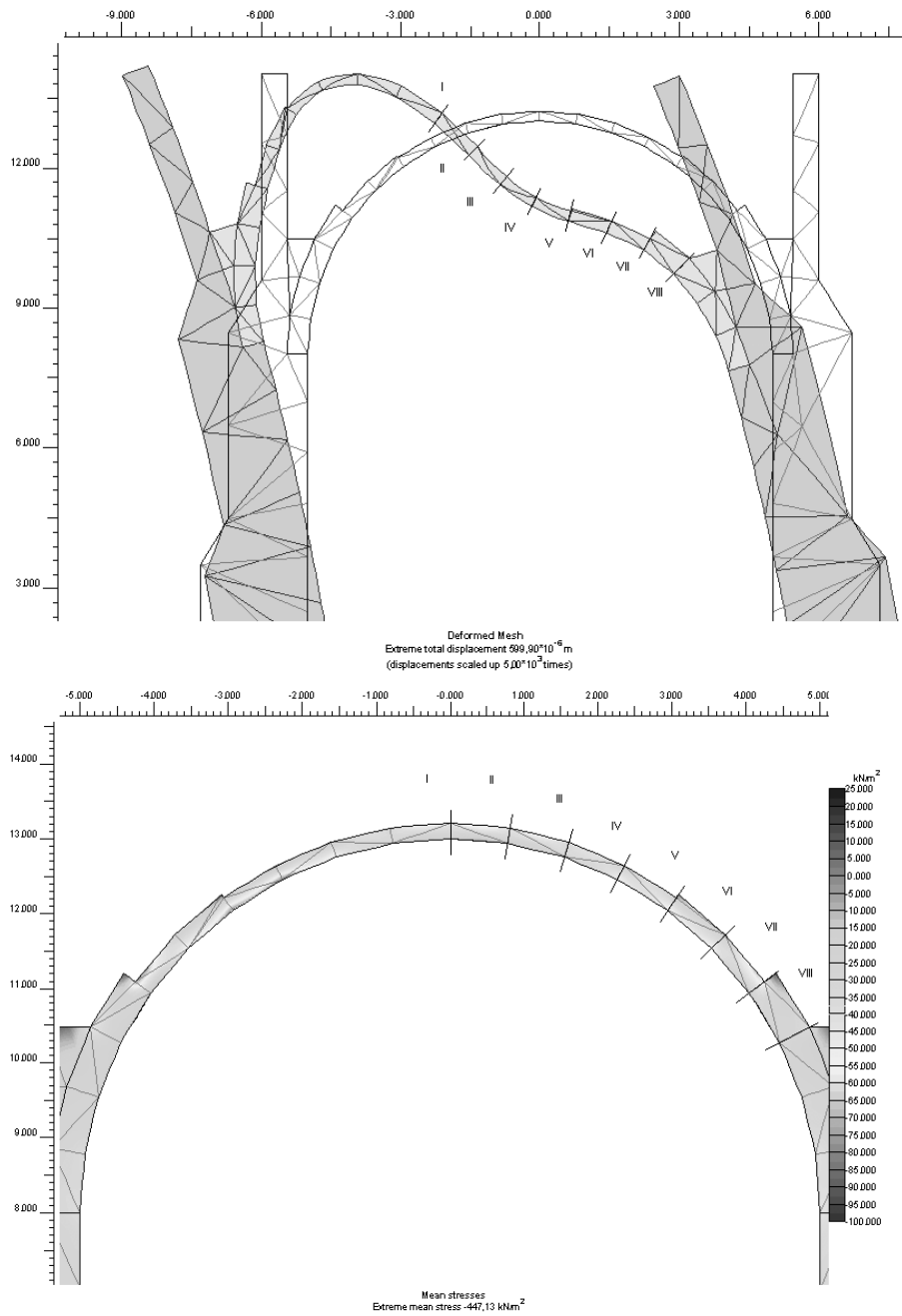


Fig. 6. Shape of the deformed grid and stress patterns for the vault construction at time  $t = 3.4$  s.

The aim of this model case study was to determine how normal stresses at chosen cross sections of the vault change and whether any tensile stress originates or not. In this model case study, no tensile stress originates but we can note some decrease of compression normal stress at cross-sections III, IV and V (Table 7).

Table 7

Magnitudes of normal stress at upper and lower boundaries at individual cross-sections of the vault for the defined times

	Normal stresses [kN/m <sup>2</sup> ]							
	Cross-section I	Cross-section II	Cross-section III	Cross-section IV	Cross-section V	Cross-section VI	Cross-section VII	Cross-section VIII
$t = 0 \text{ s}$	-117.156	-95.932	-61.238	-33.802	-41.16	-49.231	-197.662	-111.61
	-49.987	-68.522	-102.824	-160.481	-160.364	-135.667	-32.917	-55.861
$t = 2.97 \text{ s}$	-116.87	-88.853	-48.087	-21.429	-25.444	-42.727	-196.614	-115.908
	-49.608	-66.594	-116.5	-178.424	-176.717	-146.79	-34.534	-53.2
$t = 3.4 \text{ s}$	-117.303	-88.812	-86.021	-63.043	-62.977	-50.852	-179.94	-96.384
	-48.872	-66.593	-76.334	-129.965	-138.264	-134.243	-46.072	-67.834

The dynamic module of the PLAXIS program system enables us to obtain basic information about response of structures affected by the seismic load. For solving complex and difficult cases of modelling structures we usually use another program system, for example ANSYS (Kanický et al. 2005).

#### 4. Conclusion

This contribution aims at highlighting the urgency of technical seismicity-induced problems in the area of Ostrava and Karviná, particularly the effects of this load on historical buildings. Due to their historical and cultural values, these buildings should be now given the effort towards their conservation for the future in a functional state in the greatest possible number. Otherwise, their progressive dilapidation will finally necessitate their demolition. The hitherto obtained experimental measurements from the recent years and the subsequent interpretation of the maximum oscillation velocities suggest that in particular cases depending on the kind of building and ambient conditions, the oscillation velocities may exceed the permitted limit values of oscillation velocity stipulated by the relevant standards (Tables 8 and 14 in ČSN 73 0040). This leads (or should lead) to the necessity of setting provisions aimed at sufficient securing of the buildings to prevent their further possible damage.

**Acknowledgments.** This contribution was prepared with the support from the GAČR, project 105/04/1424.

#### References

- ČSN 73 00 36 Seismic loads of buildings.
- ČSN 73 00 40 Loads of technical structures by technical seismicity.
- ČSN EN 1998-1 Design of structures for earthquake resistance.

- Buričan, M., 2004, *Seismic effects of traffic in town (Seizmické projevy městské dopravy)*, MS manuscript of VŠB-TU Ostrava, FAST, Ostrava, unpublished.
- Holečko, J., Z. Kaláb, J. Knejzlík and J. Ptáček, 2005, *Oscillation velocity on the surface in the Karviná part of the Upper Silesian Coal Basin (Rychlost kmitání povrchu v Karvinské části hornoslezské pánve)*, Uhlí-Rudy-Geologický průzkum, Czech Republic, in print.
- Kaláb, Z., R. Kořínek and K. Kubečka, 2005, *Study of building response to seismic load caused by traffic (Studium odezvy stavebního objektu na zatížení dopravní seismicitou)*, Proceedings of the 3rd International Conference on Dynamics of Civil Engineering and Transport Structures and Wind Engineering (DYN-WIND 2005), University of Žilina, Slovak Republic, 86-89.
- Kanický, V., V. Salajka and P. Hradil, 2005, *Seismic response of a high residential building structure – a case study*, Proceedings VSU'2005, Sofia, Bulgaria.
- Knejzlík, J., and Z. Kaláb, 2002, *Seismic Recording Apparatus PCM3-EPC*, Publs. Inst. Geophys. Pol. Acad. Sc. **M-24(340)**, 187-194.
- Lednická, M., 2005, *Historical monuments in Ostrava and Karviná region (Historické a kulturně cenné objekty na Ostravsku a Karvinsku)*, MS Report, VŠB-TU Ostrava, FAST, Ostrava.
- Lipanská, E., 1998, *Historical vaults (Historické klenby)*, EL CONSULT, Praha.
- Procházka, J., and J. Krátký, 1999, *Design provisions for concrete structures by Eurocode 2 (Navrhování betonových konstrukcí podle Eurocode 2)*, PROCON, Praha.

*Accepted October 16, 2006*

## **Attenuation Relations of Ground Motion Acceleration Response Spectra for the Polkowice Region**

Dorota OLSZEWSKA

Department of Geophysics  
Faculty of Geology, Geophysics and Environmental Protection  
AGH University of Science and Technology  
Al. Mickiewicza 30, 30-059 Kraków, Poland  
e-mail: dolszewska@seismo.geol.agh.edu.pl

### **A b s t r a c t**

Attenuation relations of the transversal and radial components are presented for the absolute acceleration response spectra for 5% damping for 16 periods between 0.05 to 1 s. The equations were obtained using 387 data from three recording stations situated in Polkowice. All models have been tested statistically and for each of them a confidence interval for prediction has been estimated. These relations provide a possibility of predicting the response spectra over the range of epicenter distances less than 2000 m and a source energy logarithm between 5 and 8.

### **1. Introduction**

The attenuation relation illustrates the relationship between parameters of motions caused by seismic events and factors which determined those seismic effects on the ground (Douglas 2002). Parameters which characterize the signal are the following: peak ground acceleration (PGA), response spectra type, and duration time (Ambraseys and Douglas 2003). Parameters which determine the seismic effect are the distance between events and the recording station, source energy, and site condition. The attenuation relation provides for the possibility of predicting the value of a motion parameter, when put at the value of parameters which determined the seismic effect on the ground (e.g. epicentral distance, energy source).

The attenuation relations for PGA have often been studied (e.g. Joyner and Boore 1981, Lasocki 2002) even though they are only functional for the analysis of short period structures (Douglas 2002). We should obtain response spectra if we want to know the frequency-dependence of ground motion. This is why the estimation of

attenuation relation for response spectra is very popular (Ambraseys *et al.* 1996, Ambraseys and Simpson 1996, Boore *et al.* 1997).

The response of a single degree of freedom oscillator to an input accelerogram can be considered a simple example of the response of a structure. In order to obtain the response spectrum we have to consider a range of different oscillators, each of which has the same damping, e.g. 5%, and different natural period of oscillation. The acceleration response spectrum is the absolute acceleration response given as a function of the natural period of the oscillator. Attenuation relations of the acceleration response spectra are the relation between spectral acceleration amplitudes and epicentral distance and source energy, obtained using regression analysis. Such models provide an opportunity to estimate the spectral acceleration amplitude for any assumed epicentral distance and source energy.

In this paper the attenuation relations for acceleration response spectrum for 5% damping, in 16 natural periods of oscillator have been calculated. All ground models were tested statistically and for each of them a confidence interval for prediction has been determined.

## 2. Data and Method Used

### 2.1 Selection of records

Measurements of ground motion caused by mining seismic events are from three recording stations located in Polkowice. All recording stations have three-component accelerometers and the sensors are mounted in the ground. The location of the recording stations is presented in Fig. 1.

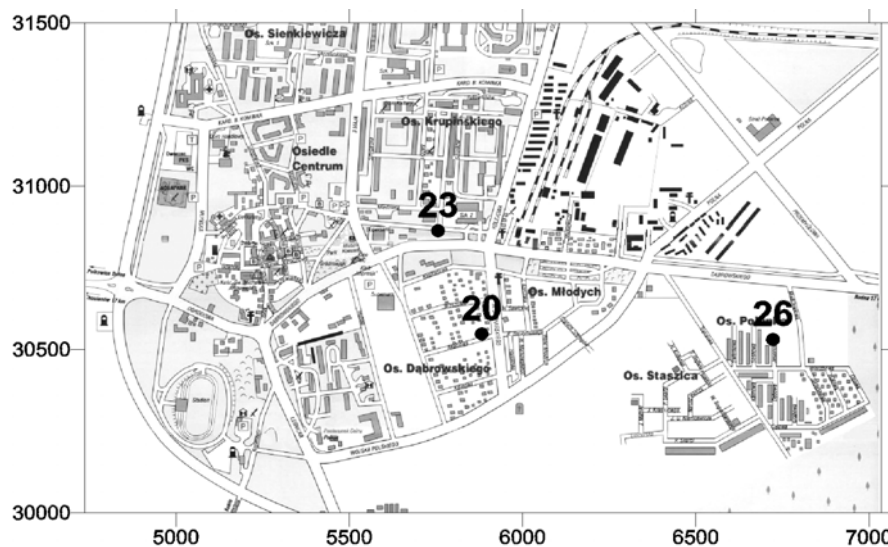


Fig. 1. Location of the recording stations in Polkowice. Coordinates are provided in the local (mining) system.

The peak ground accelerations of the horizontal component ranged from 0.01 to 1.734 m/s<sup>2</sup>. The signals were analyzed whose horizontal PGA was greater than 0.04 m/s<sup>2</sup>. In this manner, records with a considerable level of noise were not studied. Besides, the dominant frequency of every signal used was in the range from 4 to 16 Hz. Altogether 387 signals were selected for processing. The signals were rotated so that the x-axis of the sensor had the same direction as the direction between the station and epicenter of the event. In this way, the x- and y-components became the radial and transversal components of the signal, respectively. Table 1 presents summarized information concerning the processed data.

Table 1  
Data used in the analysis

Location of recording stations	Station ID number	Station coordinates		Recording period	Number of records
		x	y		
Polkowice, ul. Akacjowa 4	20	30548	5882	19 Feb 2000 19 Dec 2004	67
Polkowice, ul. 3-go Maja 8	22	31130	5546	22 Jan 2000 19 Dec 2004	107
Polkowice, ul. Sosnowa 14	26	30531	6722,5	8 Jan 2000 31 Dec 2004	214

The range of the epicenter distance was from 74 to 6174 m and the range of source energy was from  $1 \cdot 10^4$  to  $2.5 \cdot 10^9$  J. Histograms of epicenter distance and event energy are presented in Fig. 2.

## 2.2 Acceleration response spectra

The absolute acceleration response spectra for 5% damping for 16 periods between 0.05 and 1 s were computed for the radial and transversal component of all selected signals. The absolute acceleration response spectrum is the maximum of the absolute second derivative of relative displacement of a single-degree-of-freedom oscillator (Jennings 2003):

$$SA(T, D) = \max \left| \ddot{y}(t, T, D) + a(t) \right|, \quad (1)$$

where  $T$  is the natural period of oscillator,  $T = 1/\omega$ ,  $D$  is the damping ratio (in percent),  $a(t)$  is the accelerogram, and  $y(t, T, D)$  is Duhamel's integral

$$y(t, T, D) = -\frac{1}{\omega\sqrt{1-D^2}} \int_0^{t_{end}} a(\tau) \cdot e^{-\omega D(t-\tau)} \sin \left[ \omega\sqrt{1-D^2}(t-\tau) \right] d\tau \quad (2)$$

An example of the response spectrum is presented in Fig. 3.

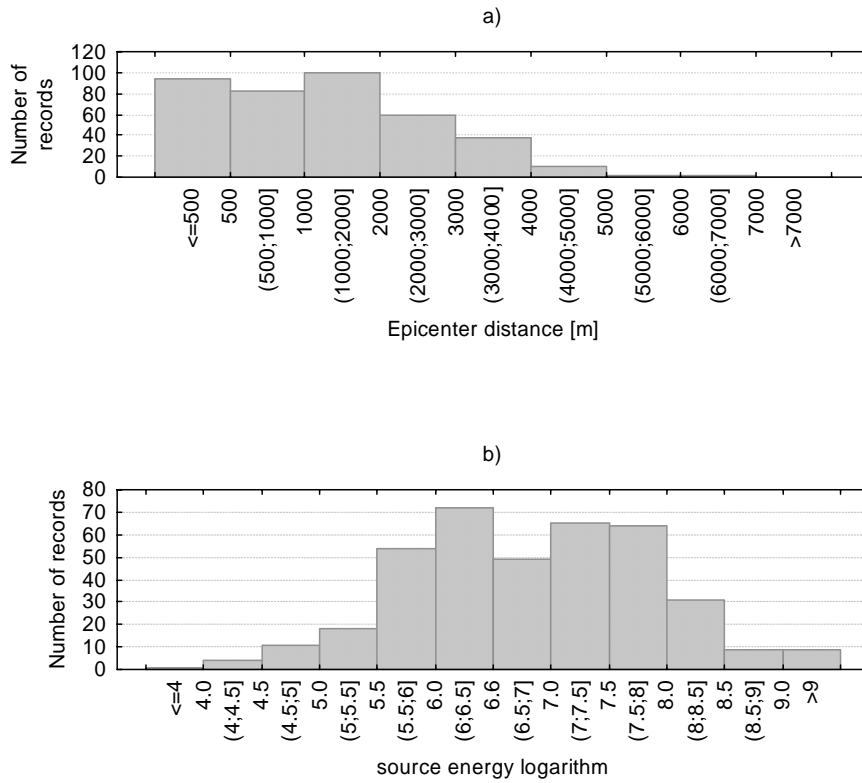


Fig. 2. Histograms of measurements used for the attenuation relation: (a) histogram of the epicenter distance and (b) histogram of events energy.

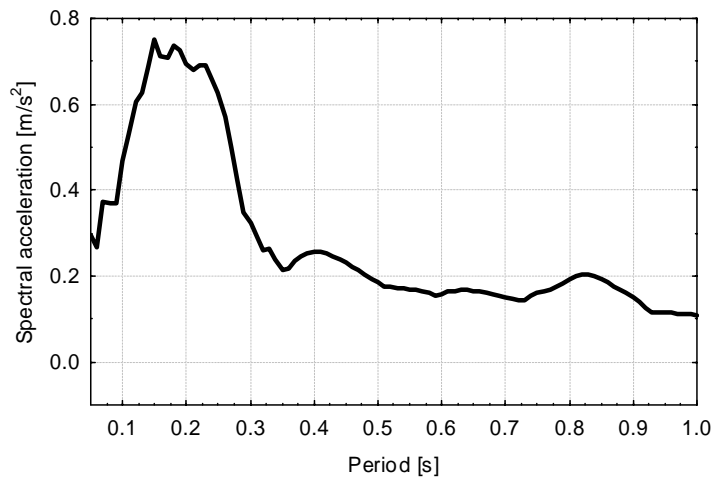


Fig. 3. Acceleration response spectra.

The parameters for absolute acceleration response spectra for 5% damping for radial and transversal component at 16 periods are presented in Table 2.

Table 2  
Parameters of absolute acceleration response spectra of radial and transversal components for 5% damping for 16 periods

$T$	Radial component			Transversal component		
	Band	Median	Average	Band	Median	Average
0.05	0.022-3.94	0.219	0.357	0.045-2.614	0.219	0.366
0.1	0.014-2.792	0.189	0.311	0.02-2.809	0.237	0.347
0.125	0.006-2.244	0.169	0.266	0.011-2.957	0.217	0.308
0.15	0.005-1.512	0.173	0.256	0.008-2.674	0.224	0.307
0.2	0.003-1.81	0.132	0.198	0.005-1.702	0.178	0.247
0.25	0.002-1.429	0.099	0.156	0.004-1.829	0.136	0.208
0.3	0.001-1.762	0.081	0.127	0.002-1.418	0.111	0.168
0.35	0.001-1.543	0.059	0.099	0.002-1.149	0.085	0.135
0.4	0.002-1.462	0.046	0.082	0.003-0.957	0.065	0.11
0.45	0.001-1.515	0.037	0.071	0.002-0.836	0.053	0.092
0.5	0.001-1.37	0.031	0.062	0.002-0.761	0.045	0.081
0.6	0.001-0.875	0.023	0.047	0.002-1.078	0.034	0.066
0.7	0.001-0.756	0.018	0.037	0.001-0.821	0.026	0.051
0.8	0.001-0.609	0.016	0.032	0.002-0.52	0.022	0.044
0.9	0.001-0.509	0.013	0.026	0.002-0.423	0.018	0.037
1	0.001-0.402	0.012	0.023	0.001-0.367	0.015	0.03

### 2.3 Model of ground motion

The ground motion model used has the form (Boore and Joyner 1982):

$$\log a_{\max} = \alpha + \beta \log E - \gamma \log \sqrt{r^2 + h^2} \quad (3)$$

where  $a_{\max}$  is the maximum absolute acceleration response spectra for 5% damping in a natural period,  $E$  is the event energy [J],  $r$  is the epicentral distance,  $h$  is a free parameter estimated so that the standard error of estimation is the least (it accounts for the non-linearity of the relation at small distances from the epicenter), and  $\alpha$ ,  $\beta$ ,  $\gamma$  are parameters determined from regression analysis.

The estimation of the attenuation relation parameters was made for the radial and transversal components in each of 16 periods in two steps: Firstly, parameter  $h$  was found, for which the standard error of estimation of the attenuation relation was the least. Secondly, parameters  $\alpha$ ,  $\beta$ ,  $\gamma$  were found using a classic regression method (least squares estimation). The attenuation relations for the radial and transversal com-

ponents were estimated separately for each of the 16 periods, so 32 regression models were prepared. Relation (3) is nonlinear so it can be used in the whole range of epicenter distance.

Relation (3) predicts the median of  $\log a_{\max}$  for the known epicentral distance ( $r$ ) and source energy ( $E$ ) so that it gives as 50% the chance that the real value of  $\log a_{\max}$  will be greater. The confidence intervals for prediction of regression (3) are given by (Lasocki 2002):

$$\log a_{\max} = \alpha + \beta \log E - \gamma \log \sqrt{r^2 + h^2} \pm t_p(n-v-1) \sqrt{X^T C_b X + SSE^2} \quad (4)$$

where  $n$  is the number of data used for estimation attenuation relation (3),  $v$  is the number of independent variables (here  $v = 2$ ),  $t_p(n-v-1)$  is the critical value from the  $t$ -distribution with  $n-v-1$  degrees of freedom,  $SSE$  is the standard error of estimation,

$C_b$  is the covariance matrix,  $X = \begin{bmatrix} 1 \\ \log E \\ \log \sqrt{r^2 + h^2} \end{bmatrix}$ , and  $X^T$  is the matrix transpose.

Given the values of independent variables, the confidence interval for prediction of the dependent variable ( $\log a_{\max}$ ) gives us a range in which values of the dependent variable can be expected.

The result of regression analyses are the parameters  $\alpha$ ,  $\beta$ ,  $\gamma$  and the probabilistic significance of the regression (3). We can also check the individual significances of each regression coefficient using an individual  $t$ -test. The coefficient of determination ( $R$ -square) informs us what percentage of the original variability of the dependent variable was explained by the model (3). The residual analysis enables one to check the quality of models. The standard error of estimation is computed and normality of the residual distribution is tested.

### 3. Results

The coefficients of the radial and transversal spectral acceleration equations for 5% damping in 16 periods are given in Tables 3 and 4. All relations were significant at a level less than  $10^{-6}$  and for all of them the square residual variance and standard error of estimation was computed (Tables 3 and 4). Relations were corrected by removing the outliers so the number of data used for estimating the model is different for separate relations. Residuals distributions of models were consistent with the normal distribution.

We have a possibility of predicting the acceleration response spectra using these models of ground motions. Figure 4 shows the response spectra predicted for  $\log E = 6$  at five epicentral distances. Figure 5 shows the response spectra predicted for the epicentral distance of 1500 m at five source energies.

The radial spectral accelerations are less than the transversal spectral accelerations (Figs. 4 and 5). The amplitude of the radial component should be less than the amplitude of the transversal component, because the transversal component includes S-wave and surface waves, which have greater amplitudes than the P-wave. The PGA

and the spectral acceleration for each period of radial component were less than those of the transversal one (Table 2). The hypothesis that the absolute acceleration response spectrum of the radial component is less than the transversal one separately for each period was tested using the *t*-test. This hypothesis was significant with a probability of less than 5%.

Table 3  
Coefficients of radial spectral acceleration relations

$T$	$\alpha$	$\beta$	$\gamma$	$h$	$R^2$	$SSE$	No of observations
0.05	5.726	0.231	-2.384	1546	0.44	0.29	384
0.1	1.717	0.308	-1.396	1009	0.46	0.28	387
0.125	0.396	0.326	-1.062	750	0.49	0.27	387
0.15	-0.286	0.344	-0.889	746	0.57	0.26	385
0.2	-0.969	0.385	-0.815	572	0.62	0.24	384
0.25	-0.532	0.414	-1.037	801	0.66	0.24	384
0.3	-0.152	0.426	-1.202	979	0.65	0.25	384
0.35	-0.089	0.434	-1.265	1078	0.64	0.26	384
0.4	-1.058	0.452	-1.053	854	0.65	0.27	385
0.45	-0.697	0.456	-1.191	981	0.65	0.27	386
0.5	-0.135	0.470	-1.403	1142	0.66	0.28	387
0.6	-0.887	0.461	-1.203	1012	0.68	0.26	385
0.7	-1.602	0.462	-1.029	829	0.69	0.26	386
0.8	-2.502	0.462	-0.784	540	0.69	0.26	385
0.9	-2.695	0.444	-0.711	377	0.66	0.26	387
1	-2.79	0.435	-0.684	297	0.65	0.26	387

The absolute acceleration response spectra are greater for a shorter epicenter distance (Fig. 4), and a bigger source energy (Fig. 5). Differences between curves for the same epicentral distance with another source energy are considerable over the whole range of periods (Fig. 5). The biggest differences are for source energy logarithms greater than 6. We can say that huge source energy has an enormous effect on spectral acceleration. There are also differences between curves for the same source energy and another epicentral distance, but the changes are fewer and only in the range of periods from 0.05 to 0.4 s (Fig. 4). The changes of epicentral distance especially strongly influence the short periods. The maximum of acceleration spectra are for the periods ranging from 0.05-0.2 s (5-20 Hz).

Table 4  
Coefficients of transversal spectral acceleration relations

$T$	$\alpha$	$\beta$	$\gamma$	$h$	$R^2$	$SSE$	No of observations
0.05	5.127	0.224	-2.165	1644	0.40	0.28	386
0.1	2.846	0.290	-1.626	1600	0.50	0.23	383
0.125	0.933	0.294	-1.104	1137	0.50	0.24	383
0.15	-0.589	0.334	-0.745	769	0.58	0.23	380
0.2	-0.887	0.389	-0.804	824	0.65	0.23	382
0.25	-0.378	0.431	-1.071	1037	0.66	0.24	380
0.3	-0.071	0.436	-1.197	1199	0.65	0.26	381
0.35	-0.158	0.449	-1.225	1281	0.65	0.27	381
0.4	-0.136	0.475	-1.317	1296	0.68	0.26	381
0.45	-0.339	0.478	-1.294	1253	0.68	0.27	382
0.5	-0.192	0.489	-1.374	1335	0.69	0.27	383
0.6	-0.452	0.506	-1.362	1329	0.73	0.25	382
0.7	-1.070	0.499	-1.196	1273	0.75	0.24	383
0.8	-2.486	0.483	-0.768	863	0.74	0.24	383
0.9	-3.366	0.463	-0.493	345	0.72	0.25	384
1	-3.508	0.445	-0.435	192	0.72	0.24	389

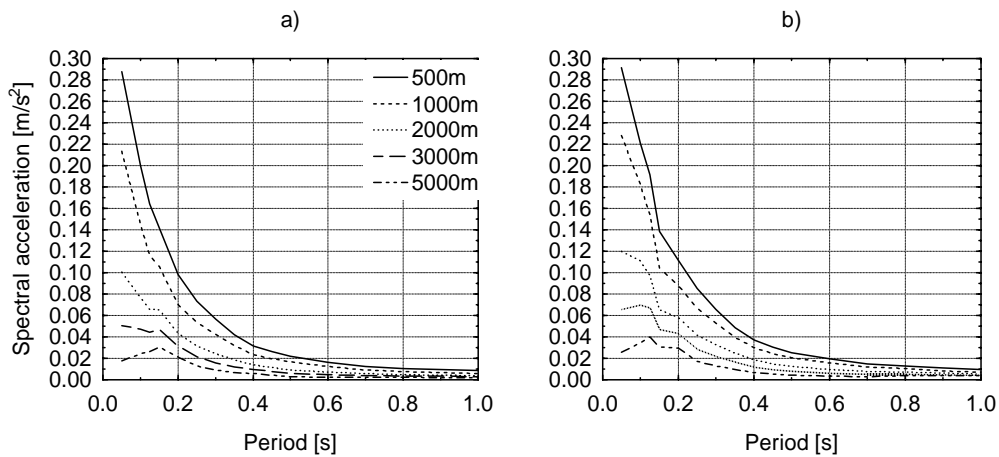


Fig. 4. Comparison of predicted response spectra for  $\log E = 6$ , for different epicenter distances: 500 m (solid line), 1000 m (dashed line), 2000 m (dotted line), 3000 m (long dashed line), 5000 m (dashed-dotted line) for both ordinates; (a) radial component; (b) transversal component.

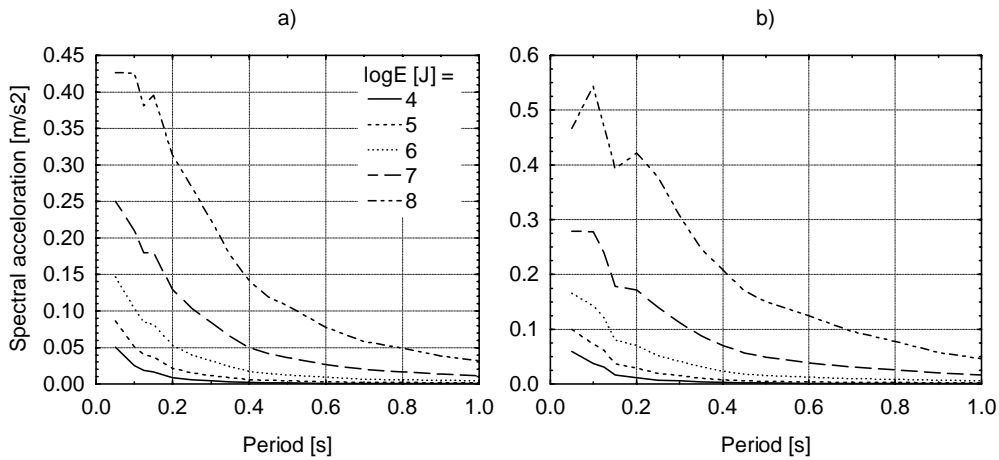


Fig. 5. Comparison of predicted response spectra for epicenter distance of 1500 m for different source energy logarithms: 4 (solid line), 5 (dashed line), 6 (dotted line), 7 (long dashed line), 8 (dashed-dotted line) for both ordinates; (a) radial component; (b) transversal component.

Relation (3) predicts the median of  $\log a_{\max}$  for the known epicentral distance ( $r$ ) and source energy ( $E$ ), so that it gives a 50% chance that the real value of  $\log a_{\max}$  will be greater. Estimation of the spectral acceleration with prediction interval (relation 4) gives us more specific information on the predicted spectral acceleration. We need a standard error of estimate and covariance matrix for each model to build the prediction interval (Tables 5 and 6).

Figure 6 shows the measured response spectra from an event at an epicentral distance of 1163 m and source energy  $\log E = 6.99$ , and the response spectrum estimate with a 90% confidence interval for prediction with the same epicenter distance and source energy as the measured one.

The measured response spectrum is located within the prediction interval. The estimated curve corresponds well with the observed one although the interval is wide, especially for the short period.

If the model is correct for the whole ranges of independent variables, the model residuals should be statistically the same for different ranges of epicentral distance and source energy. Also, the residuals connected with particular recording stations should be the same. In order to check this, the data was divided into 7 groups of different epicentral distance ranges:  $\leq 200$ , (200; 500], (500; 800], (800; 1000], (1000; 1500], (1500; 2000],  $> 2000$ . For each group, the means of the residuals of estimated models were computed. Figure 7 shows the comparisons between the residual means for these groups for both radial and transversal components. The differences are insignificant, which shows that the calculated regression models are applicable to the whole considered range of epicentral distance.

Table 5  
Covariance matrix of the radial component

$T$				$T$			
0.05	0.1499	0.0029	-0.0509	0.4	0.0445	0.0009	-0.0158
	0.0029	0.0003	-0.0016		0.0009	0.0003	-0.0009
	-0.0509	-0.0016	0.0185		-0.0158	-0.0009	0.0069
0.1	0.0614	0.0013	-0.0217	0.45	0.0545	0.0012	-0.0193
	0.0013	0.0003	-0.0011		0.0012	0.0003	-0.0010
	-0.0217	-0.0011	0.0090		-0.0193	-0.0010	0.0081
0.125	0.0367	0.0007	-0.0129	0.5	0.0760	0.0016	-0.0267
	0.0007	0.0003	-0.0009		0.0016	0.0003	-0.0012
	-0.0129	-0.0009	0.0059		-0.0267	-0.0012	0.0107
0.15	0.0339	0.0006	-0.0119	0.6	0.0533	0.0011	-0.0189
	0.0006	0.0003	-0.0008		0.0011	0.0003	-0.0009
	-0.0119	-0.0008	0.0054		-0.0189	-0.0009	0.0078
0.2	0.0213	0.0002	-0.0073	0.7	0.0391	0.0008	-0.0139
	0.0002	0.0002	-0.0006		0.0008	0.0003	-0.0008
	-0.0073	-0.0006	0.0036		-0.0139	-0.0008	0.0062
0.25	0.0321	0.0006	-0.0113	0.8	0.0420	0.0009	-0.0149
	0.0006	0.0002	-0.0007		0.0009	0.0003	-0.0009
	-0.0113	-0.0007	0.0051		-0.0149	-0.0009	0.0066
0.3	0.0472	0.0010	-0.0168	0.9	0.0175	-0.0001	-0.0055
	0.0010	0.0003	-0.0009		-0.0001	0.0003	-0.0006
	-0.0168	-0.0009	0.0071		-0.0055	-0.0006	0.0031
0.35	0.0601	0.0014	-0.0212	1	0.0153	-0.0002	-0.0045
	0.0014	0.0003	-0.0010		-0.0002	0.0003	-0.0005
	-0.0212	-0.0010	0.0087		-0.0045	-0.0005	0.0027

The same testing was performed for the source energy. Firstly, the data was divided into 7 groups of different logarithms of source energy ranges:  $\leq 5.5$ , (5.5; 6], (6; 6.5], (6.5; 7], (7; 7.5], (7.5; 8],  $> 8$ . Then, for each group of source energy, the mean value of the residuals of estimated models was computed. Figure 8 shows comparisons between the residual means for these groups. One can conclude from the figure that the attenuation relations are correct over the whole studied range of source energy.

Finally, the studied signals were divided into three groups of measurements from stations 20, 22 and 26. Then, for each of these groups the mean of model residuals was computed. The comparisons of residual means obtained for measurements from different stations are shown in Fig. 9. The figure shows that for both compo-

Table 6  
Covariance matrix of the transversal component

$T$				$T$			
0.05	0.1588	0.0030	-0.0534	0.4	0.0849	0.0019	-0.0296
	0.0030	0.0003	-0.0015		0.0019	0.0003	-0.0011
	-0.0534	-0.0015	0.0191		-0.0296	-0.0011	0.0114
0.1	0.1022	0.0020	-0.0346	0.45	0.0855	0.0019	-0.0299
	0.0020	0.0002	-0.0011		0.0019	0.0003	-0.0012
	-0.0346	-0.0011	0.0125		-0.0299	-0.0012	0.0117
0.125	0.0556	0.0012	-0.0195	0.5	0.0968	0.0021	-0.0337
	0.0012	0.0002	-0.0009		0.0021	0.0003	-0.0012
	-0.0195	-0.0009	0.0078		-0.0337	-0.0012	0.0128
0.15	0.0280	0.0005	-0.0098	0.6	0.0829	0.0018	-0.0289
	0.0005	0.0002	-0.0006		0.0018	0.0003	-0.0011
	-0.0098	-0.0006	0.0045		-0.0289	-0.0011	0.0111
0.2	0.0307	0.0006	-0.0109	0.7	0.0696	0.0015	-0.0243
	0.0006	0.0002	-0.0007		0.0015	0.0002	-0.0010
	-0.0109	-0.0007	0.0049		-0.0243	-0.0010	0.0094
0.25	0.0481	0.0011	-0.0170	0.8	0.0358	0.0007	-0.0127
	0.0011	0.0002	-0.0009		0.0007	0.0002	-0.0007
	-0.0170	-0.0009	0.0071		-0.0127	-0.0007	0.0056
0.3	0.0730	0.0016	-0.0256	0.9	0.0156	-0.0001	-0.0048
	0.0016	0.0003	-0.0011		-0.0001	0.0003	-0.0006
	-0.0256	-0.0011	0.0101		-0.0048	-0.0006	0.0028
0.35	0.0893	0.0019	-0.0311	1	0.0115	-0.0003	-0.0030
	0.0019	0.0003	-0.0012		-0.0003	0.0002	-0.0004
	-0.0311	-0.0012	0.0121		-0.0030	-0.0004	0.0020

nents, the differences between the mean residuals of different groups are significant. These differences apparently result from differences in local site conditions at the recording stations, which were not accounted for in the elaborated attenuation relations. It can therefore be expected that if information about site conditions were incorporated into the attenuation models, the explained portion of dependent variable variability would be largely increased.

#### 4. Conclusions

In this paper, the attenuation relation for acceleration response spectrum for 5% percent damping in 16 natural periods of the oscillator has been calculated. All of the

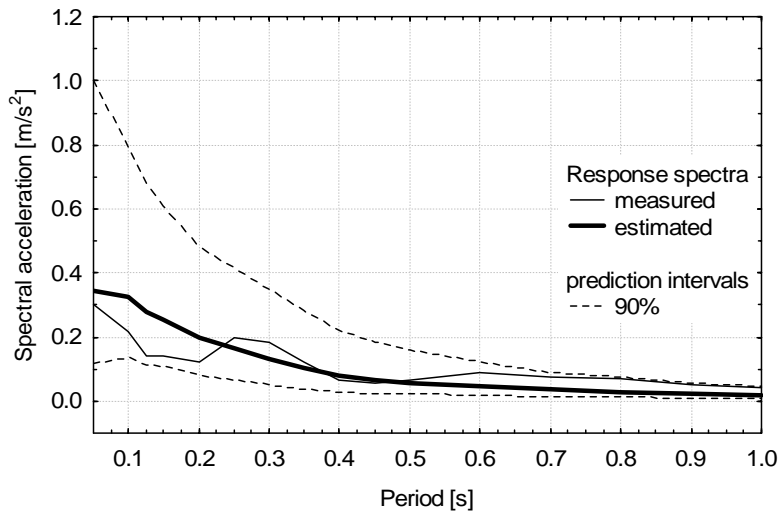


Fig. 6. Comparison of measured response spectrum ( $\log E = 6.99$ ,  $r = 1163$ ) (thin line) to the predicted response spectrum (solid line) and 90% confidence intervals for prediction (dashed line).

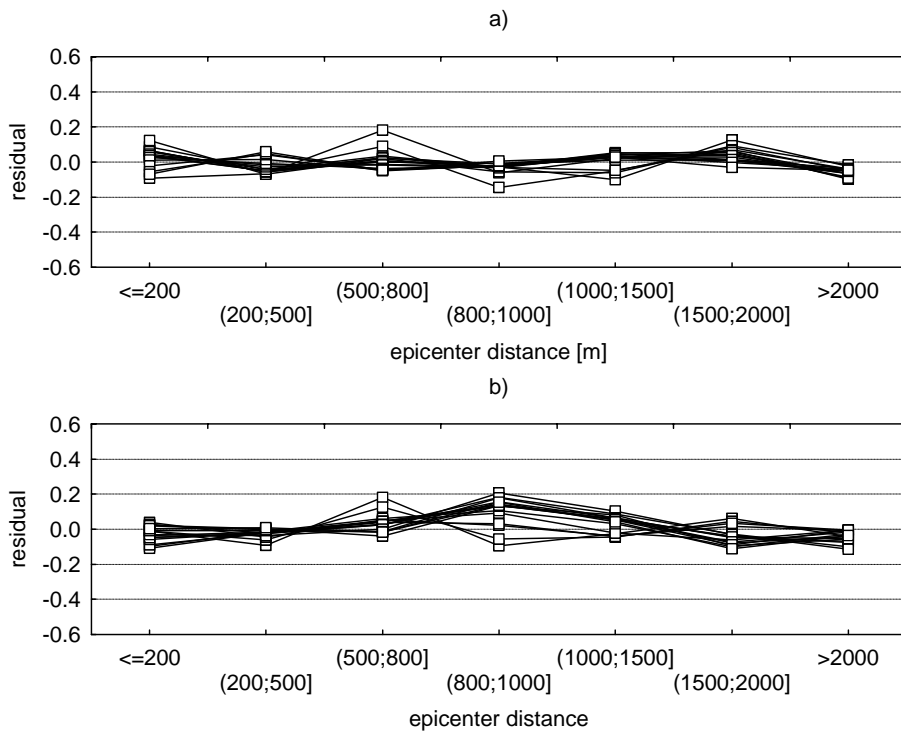


Fig. 7. Distribution residual mean of the estimated models spectral acceleration versus categorical epicentral distance for (a) radial component and (b) transversal component.

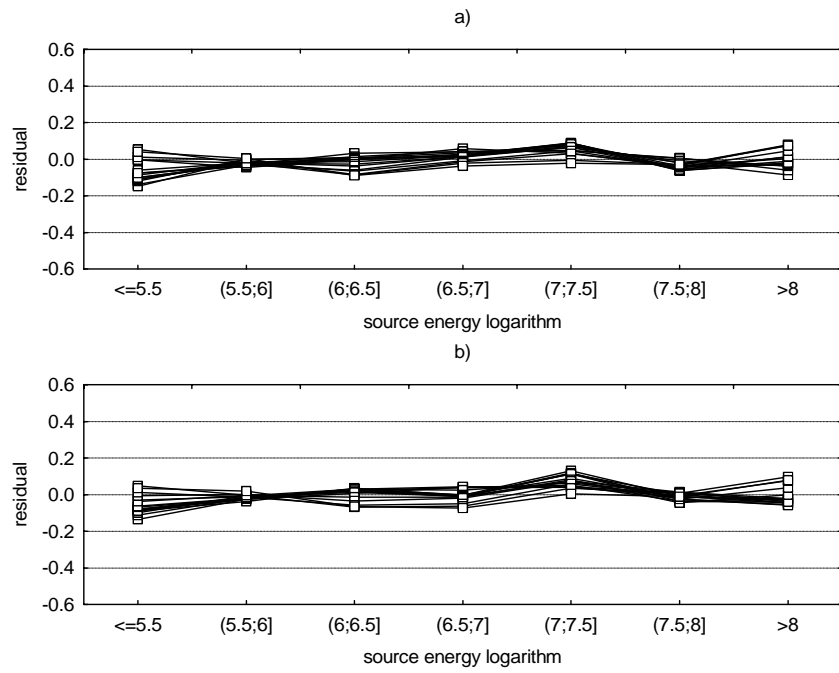


Fig. 8. Distribution residual mean of the estimated models spectral acceleration versus source energy logarithm for (a) radial component and (b) transversal component.

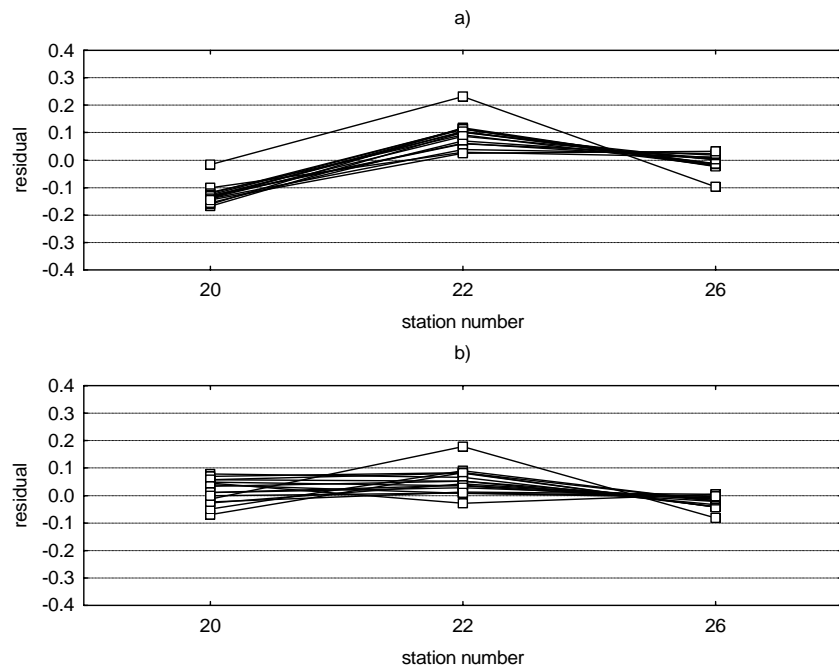


Fig. 9. Distribution residual mean of the estimated models spectral acceleration versus station number for (a) radial component and (b) transversal component.

introduced models were tested statistically and for each of them a confidence interval for prediction has been estimated. The models provide for the possibility of predicting the response spectrum for any assumed epicentral distance and source energy.

It has been shown that these models are correct over the whole range of epicenter distance and source energy. It has been also shown that the place of measurement can affect the distribution of the model residuals. Hence, it is concluded that also the local site conditions have significant influence on spectral amplitudes. The attenuation models for spectral amplitudes will improve when information about site conditions is included.

The relations were derived using data from only three recording stations. Further studies should include signals from a greater number of recording stations in the region.

#### References

- Jennings, P.C., 2003, *An Introduction to the Earthquake Response of Structures*. In: W.H.K. Lee, H. Kanamori, P.C. Jennings and C. Kisslinger (eds.), *International Handbook of Earthquake and Engineering Seismology*, Academic Press, London, Part B, Chapter 58, 1097.
- Ambraseys, N.N., and J. Douglas, 2003, *Near-field horizontal to vertical earthquake ground motions*, *Soil Dynamic and Earthquake Engineering* **23**, 1-18.
- Ambraseys, N.N., A. Simpson and J.J Bommer, 1996, *Prediction of horizontal response spectra in Europe*, *Earthq. Eng. Struct. Dynamics* **25**, 371-400.
- Ambraseys, N.N., and A. Simpson, 1996, *Prediction of vertical response spectra in Europe*, *Earthq. Eng. Struct. Dynamics* **25**, 401-412.
- Boore, D.M., and W.B. Joyner, 1982, *The empirical prediction of ground motion*, *Bull. Seismol. Soc. Am.* **72**, S43-S60 (part B).
- Boore, D.M., W.B. Joyner and T.E. Fumal, 1997, *Estimation of response spectra and peak acceleration from western North American earthquakes: A summary of recent work*, *Seismol. Res. Letts.* **68**, 128-153.
- Douglas, J., 2003, *Earthquake ground motion estimation using strong-motion records: a review of equations for the estimation of peak ground acceleration and response spectra*, *Earth-Science Rev.* **61**, 43-104.
- Joyner, W.B., and D.M. Boore, 1981, *Peak horizontal acceleration and velocity from strong-motion records including records from the 1979 Imperial Valley, California Earthquake*, *Bull. Seismol. Soc. Am.* **71**, 2011-2038.
- Lasocki, S., 2002, *Attenuation relation for horizontal component of peak ground acceleration below 10 Hz frequency for the Polkowice region*, *Publs. Inst. Geophys. Pol. Acad. Sc.*, **M-27** (352), 79-90 (in Polish with English abstract and figure captions).

Accepted 13 June 2006

## **Determination of Authentic Formulae for Seismic Acceleration Decay in the Bohemian Massif**

Vladimír RUDAJEV and Jiří BUBEN

Institute of Rock Structure and Mechanics  
Academy of Sciences of the Czech Republic  
V Holešovičkách 41, 182 00 Prague 8, Czech Republic  
e-mail: buben@irsm.cas.cz

### **A b s t r a c t**

Two seismic profiles were established for experimental determination of a decrease of the maximum ground motion acceleration amplitudes as a function of the distance and magnitude of seismic sources. Profile I (direction N-S) was equipped by four accelerometers in the period from 2003 July 1 till 2004 December 31. At present, five additional seismometers are dislocated along the Profile II (NW-SE). In this paper, only mining tremors from Legnica-Głogów rockbursts region recorded on Profile I were processed. The local seismic service of Lubin mine yielded data about geographic and time coordinates of foci, as well as local magnitude ML. Magnitude values ML were correlated with magnitude values MV given in the bulletins of near seismic events, recorded by the Czech regional seismic network. Preliminary acceleration attenuation relation was derived for Profile I in the Bohemian massif. Input magnitude ML data are in the interval 2.7-4.1 and epicentre distances are 100-250 km. The obtained relation was compared with two relations derived for data abroad.

**Key words.** Mining tremors, attenuation acceleration relation, seismic profile, local magnitude.

### **1. Introduction**

At present, there are two nuclear power plants (NPP), Dukovany and Temelín, on the territory of the Czech Republic, whose seismic hazard has to be re-evaluated based on international NPP standards (IAEA 50-SG-D15, 1992, IAEA – TECDOC-724, 1993) issued by the International Atomic Energy Agency (IAEA). Similar standards for evaluating seismic hazard also refer to places of future depositories of radioactive and/or toxic waste. Besides this, evaluation of seismic hazard is also required

for vulnerable technical and engineering facilities such as underground gas reservoirs, chemical plants and constructions subject to a high degree of risk.

From the point of view of seismic activity, the Bohemian Massif belongs to regions with moderate seismic activity. Natural seismic activity in the Bohemian Massif is concentrated primarily in the border areas of the state. Among the most active areas is the West Bohemian earthquake-swarm region, the Opava region and the region of the Hronov-Poříčí fault. The magnitude of the strongest earthquakes in these regions quite exceptionally attains the value of 4.5. Higher seismic activity is to be expected also in regions of mining induced activity (Ostrava, Pribram) and in the close vicinity of technical seismic sources (blasting of large extent).

As regards the seismic hazard to localities on the Czech territory, seismic activity has to be considered in several outer seismically active zones, which are located within 300 km of the locality in question. These earthquake source zones include, primarily, the Vienna Basin, Slovenia, Friuli–Villach, the Swabian Jurassic and the areas where induced seismic events occur (Lubin, Lower Silesian Coal Basin).

The determination of seismic hazard consists of several steps, which can be divided into the following groups:

- (a) Determination of seismic source zones, and their geographical and depth coordinates;
- (b) Determination of the seismic activity in the individual zones, i.e. mainly determining the magnitude-frequency distribution;
- (c) Determination of the attenuation of seismic waves along the path between the source and the locality in question;
- (d) Computation of the occurrence probability of severe events within a given time interval;
- (e) Estimation of the maximum seismic effects (maximum acceleration of ground motion oscillations, spectral content and spectral amplitude, duration of maximum amplitudes) at the locality.

The inaccuracy in determining the attenuation can cause an error of as much as an order of magnitude in estimating the acceleration of seismic oscillations for distant sources. Not only peak acceleration, but also the frequency content and duration of the seismic event is important for the stability of engineering and geologic structures. These parameters differ greatly for various sources of seismic hazard; therefore, monitoring and processing of the seismic data have to include all these parameters.

The attenuation of seismic waves is determined on the basis of instrumental data, i.e., seismograms. To avoid errors generated in the unconsolidated Quaternary surface layer, only the records of stations built on a solid rock foundation were considered.

For this purpose, two new profiles were established for the experimental determination of the maximum acceleration amplitudes decrease and the response spectra as a function of the distance and magnitude of seismic sources.

## 2. Seismic Profile I (NS)

Seismic Profile I was established on July 20, 2003. It links the zone of tectonic earthquakes (Vienna Basin) and the zone of strong mining induced events (the Lubin mine, Poland). Numerous seismic events, which contribute to the seismic hazard on Czech territory and are suitable for studying subsidence regularities, are generated in these two zones.

The profile consists of four seismic stations, the co-ordinates of which are given in Table 1.

Table 1  
Seismic stations along Profile I

Seismic station	Code	Latitude [°N]	Longitude [°E]
Broumov – Šonov	SON	50.614	16.396
Potštejn	POT	50.079	16.306
Skalka	SKA	49.445	16.277
Znojmo – Konice	KON	48.834	16.021

Seismic pillars were built at all stations; they were fed from electric mains, and the appropriate protection of instruments has been installed. Seismic noise has been measured at all sites and, with a view to its level, the sites for the seismic pillar were chosen. The maxima of seismic noise occur in the frequency range of 1-15 Hz. The maximum amplitudes of acceleration reach values of  $6.3 \mu\text{m}\cdot\text{s}^{-2}$  at stations KON and POT and at stations SON and SKA the level of permanent noise is  $15 \mu\text{m}\cdot\text{s}^{-2}$ . Since the seismic events to be analyzed and used in constructing the subsidence relation and in determining the response spectra display amplitudes at least 100 times larger, the level of noise is negligible.

All stations are located on a rock base, which enables the observed values to be compared without applying corrections of the transfer function of the sedimentary subsoil. Locating all the seismic stations on a rock outcrop minimizes the local seismic noise and the effect of sediments, stratification, etc., on the one hand, and corresponds to the present conditions for siting nuclear facilities (power plants, as well as future radioactive waste depositories) in granite rocks, on the other.

Three-component sensors of the oscillation velocity produced by the Swiss firm Syscom, model MR 2003, with an MR 2002 recording unit have been installed at all stations. The sensors are placed in an aluminum cover, 12 by 12 by 8 cm in size, which is equipped with levelling screws. Their total weight is 1.55 kg. The MR 2002 recording unit is protected by an aluminum cover, 20 by 23 by 11 cm in size, and its total weight is 7.2 kg. The cover is watertight (the device is able to operate at 100% humidity) and the permitted range of ambient temperature is  $-20^{\circ}\text{C}$  to  $+50^{\circ}\text{C}$ . The manufacturer increased the sensitivity of the apparatus 50 times as compared with

standard models, which makes it possible to record weaker seismic events. The device's dynamics is 16 bits, range  $\pm 114 \text{ mm.s}^{-1}$ , and sampling frequency 200 samples/s/channel. It can be fed from the mains (220 V, 50 Hz) or autonomously (12 V). The time data are derived from the system clock of the station's recording unit. In 2005 all the apparatuses along Profile I (NS) will be equipped with a record of the time system based on receiving DCF time signals. This unified time system will, moreover, enable the monitoring of long-term variations of the velocities of seismic waves in the Bohemian Massif. The apparatus is triggered once the signal amplitude exceeds the triggering level. The triggering level has been set with a view to the level of the local seismic noise. The data are stored on a disc and the RS-232 port realizes their transfer to the processing unit.

The records are processed in the Central Laboratory of the Institute of Rock Structure and Mechanics (IRSM) using the VIEW 2002 software, version 3.0 (of 22.5.2003). Seismic signals (velocities, displacements, acceleration of individual components and the total vector) are processed within the frequency range of 1-40 Hz. Fourier and power spectra and the particles motion in planes XY, XZ and YZ are determined of the whole record, as well as of selected parts.

### 3. Seismic Profile II (NW–SE)

Seismic Profile II was established along the line between the Voigtland region, where earthquake swarms occur, and the region where tectonic earthquakes occur in the Vienna Basin. This profile runs close to the localities of the nuclear power plant Temelín and close to the locality of the Příbram–Háje gas reservoir. A detailed check of the formula for the decrease of oscillation amplitudes is thus also of practical importance for obtaining a more accurate value of the seismic hazard of these structures, which is in accord with the recommendations of the IAEA.

There are seven seismic stations along Profile II, the names and co-ordinates of which are given in Table 2.

Table 2  
Seismic stations along Profile II

Seismic station	Code	Seismometers	Latitude [°N]	Longitude [°E]
Komorní hůrka	KOH	GURALP CMG – 40 T	50.600	12.336
Krásno	KRA	GURALP CMG – 40 T	50.111	12.783
Nečtiny	NEC	GURALP CMG – 40 T	49.977	13.170
Háje	HAJ	GURALP CMG – 40 T	49.675	14.049
Tábor	TBR	GURALP CMG – 40 T	49.413	14.648
Mrákotín	MRA	Syscom, MR 2003	49.187	15.379
Znojmo–Konice	KON	Syscom, MR 2003	48.834	16.021

All stations are located on rock base, which enables the results between both profiles to be compared without correction for a sedimentary base. The seismometers have been installed on seismic pillars, and the stations are connected to electrical mains.

The frequency of continual quasi-stationary seismic noise displays values within the range of 4-5 Hz, which is characteristic for the Bohemian Massif. Amplitudes of rare temporary disturbances of technical origin do not exceed the value of  $1 \mu\text{m}\cdot\text{s}^{-1}$ .

Broadband GURALP CMG – 40 T seismometers have been installed at stations KOH, KRA, NEC, HAJ and TBR. Electronic circuits with a frequency-dependent feedback set the natural frequency of these systems. The broadband frequency characteristic is practically constant within the frequency range of 0.03-30 Hz. The adjustable amplification is practically restricted only by the level of permanent noise. The sampling frequency of the digital recording device is 100 samples/s/channel. The dynamic range is at least 110 dB. The recording device operates in the triggering mode. The triggering criterion is the ratio LTA:STA. All stations receive the GPS time signal.

The recorded data are transferred to the processing centre by removable hard-disc memories. The data are collected and the operation of the apparatuses is checked at intervals of one month. Unexpected faults in the operation of the apparatuses are immediately identified telemetrically using USW links. The acceleration is determined by numerical differentiation of the velocity records with the appropriate low-pass and high-pass filtration of the fourth order with limiting frequencies of 0.3 and 30 Hz.

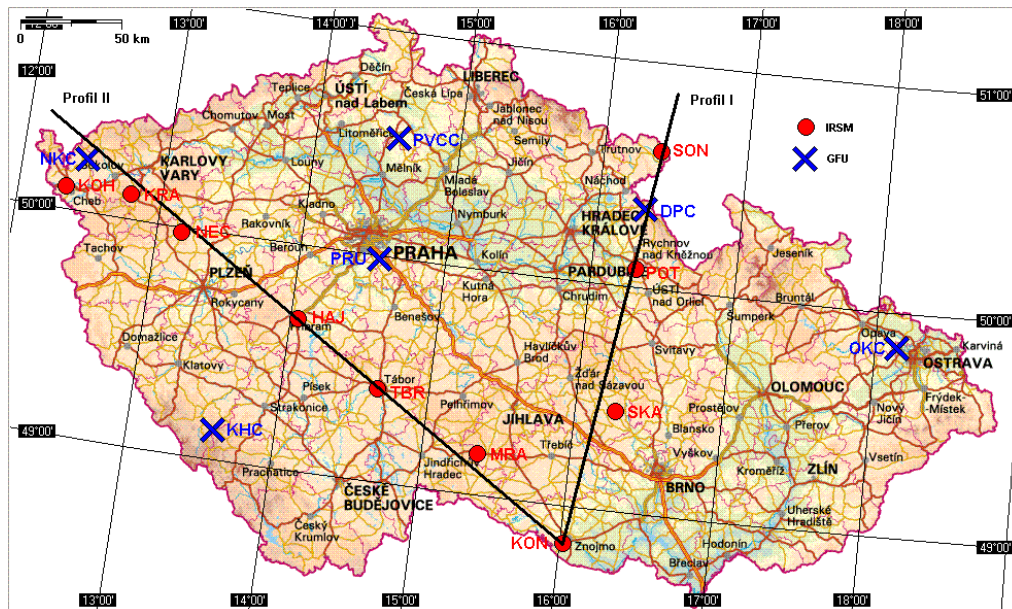


Fig. 1. Layout of seismic Profile I and Profile II and positions of source zones (Lubin, Vienna and Vogtland).

Stations MRA and KON are equipped with Syscom instruments, whose technical data are given above.

The two profiles described are depicted in Fig. 1.

#### 4. Attenuation Relation for the Bohemian Massif

The general function of acceleration attenuation is  $PGAH = f(M, D)$ ,

where PGAH is the peak ground motion acceleration – horizontal component [ $m/s^2$ ], M is the magnitude of seismic event and D is the focal distance [km]. This relation usually satisfies the equation:

$$\log PGAH = a + bM + c \log R + dR,$$

where a, b, c, and d are parameters being derived from accelerograms of seismic events with foci within the near region ( $50 \text{ km} \leq R \leq 300 \text{ km}$ ).

Due to insufficient number of authentic accelerograms recorded in the territory of the Bohemian Massif, the abroad formula of Sadigh et al. (1986) had to be used for assessment of the seismic hazard to nuclear facilities located in the Czech Republic (Rudajev and Buben 2002). This relation had been derived for rock subsoil in North America and for earthquakes foci with depth less than 20 km and magnitude less than 6.5.

$$\log(PGHA)[\text{cm} \cdot \text{s}^{-2}] = 2.39 + 0.4774M - 2.05 \log[R + 1.353 \exp(0.406M)],$$

where R[km] is focal distance. Recently, Smitt and Rüttener (1998) derived another acceleration attenuation formula for earthquakes in Switzerland

$$\log PGAH[\text{cm} \cdot \text{s}^{-2}] = -1.946 + 0.868M - \log R - 0.001059R[\text{km}].$$

The authentic decay relation could be assessed on the basis of mining tremors occurred in the Legnica–Głogów source zone. The distribution of foci is shown in Fig. 2. The seismic energy release was practically stationary, as illustrated in Fig. 3.

During the period July 2003 to December 2004, seventy mine tremors were recorded on two stations (R = 100 and 160 km) of Profile I. On the basis of smoothing of the recorded PGAH the following attenuation relation AB-ML was derived:

$$\log A[\text{cm} \cdot \text{s}^{-2}] = -2.5 + 0.545ML - 0.486 \log R[\text{km}],$$

where ML is the local magnitude determined by Lubin local seismic network.

The mining tremors from this region with  $ML > 2.7$  are recorded on almost all Czech seismic stations. The magnitudes MV determined from these stations are given in seismic bulletins.

The relation between ML and local magnitude MV, determined from seismic station Pruhonice (Czech seismic network) is:

$$MV = 1.06ML - 0.92$$

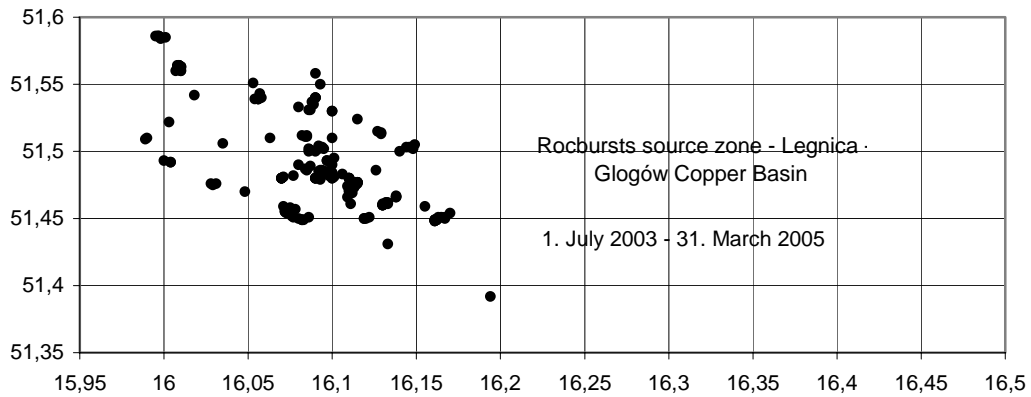


Fig. 2. Distribution of mining tremors epicentres in the Legnica-Głogów Copper Basin. Period: 2003, July 1 – 2005, March 31.

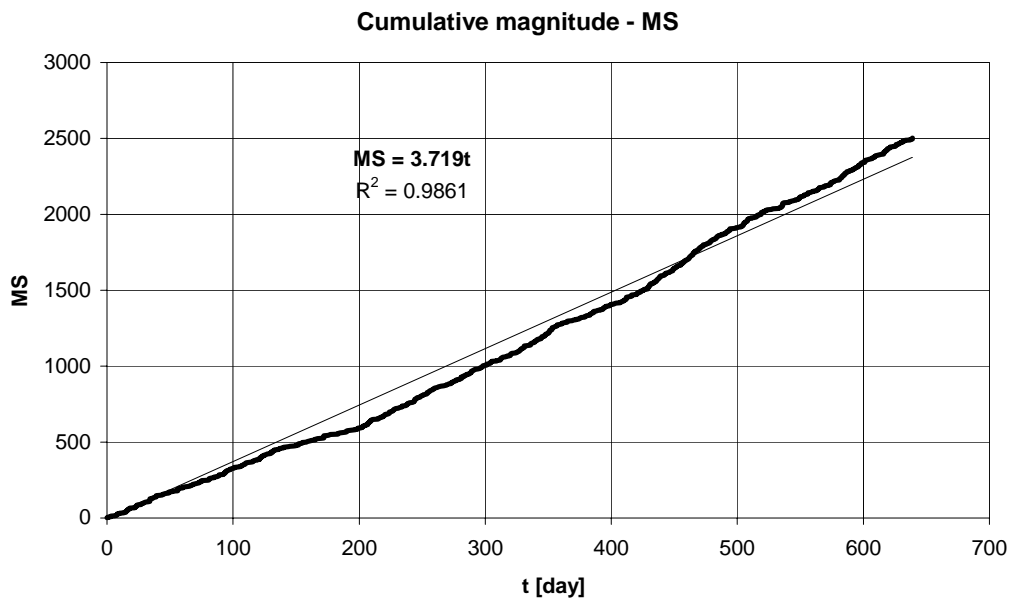


Fig. 3. Energy release of mining tremors – measured values (bold line) and linear regression.

This is shown in Fig. 4.

Comparison of acceleration values calculated from all three above-mentioned relations with measured values at distances  $R = 100$  km and  $R = 160$  km is shown in Figs. 5 and 6. The new AB–ML relation appears to be the most suitable relation for the conditions of the Bohemian Massif and small magnitudes.

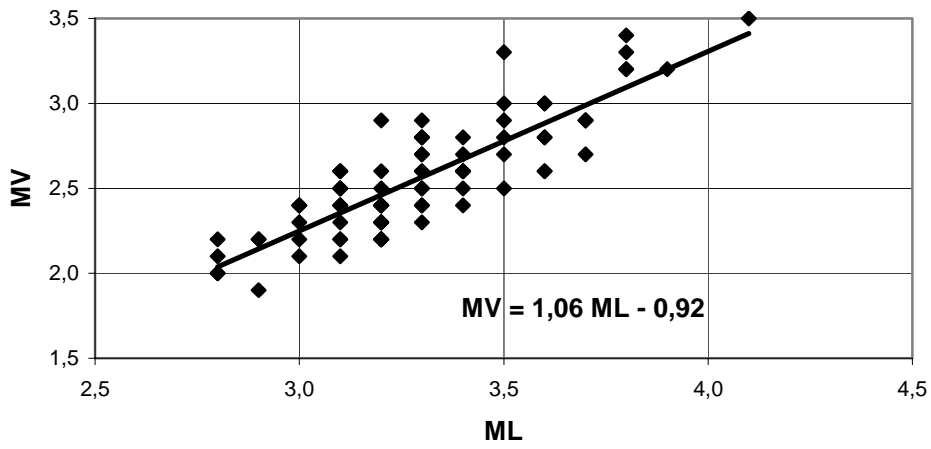


Fig. 4. Correlation diagram ML–MV for mining tremors.

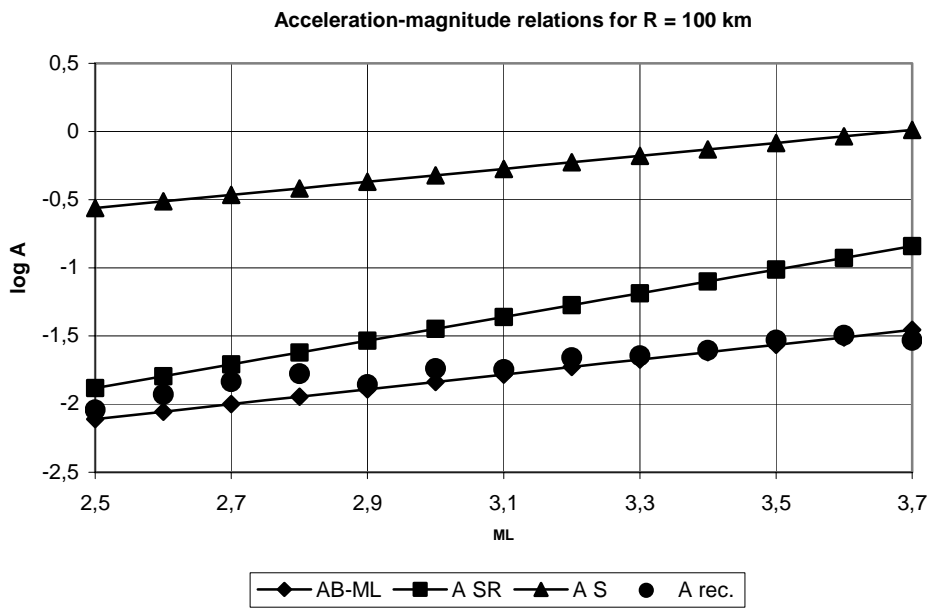


Fig. 5. Recorded values A rec. and calculated accelerations from relations AB–ML, A SR and A S for a distance of 100 km.

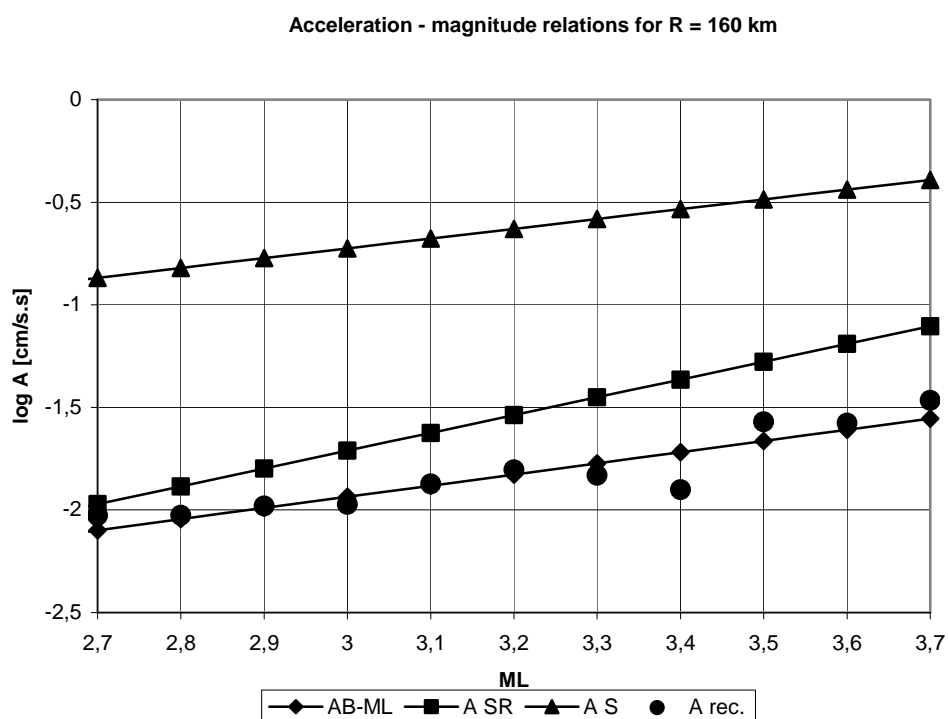


Fig. 6. Recorded values  $A_{rec.}$  and calculated accelerations from relations AB-ML, A SR and A S for distance 160 km.

## 5. Results

Accelerographs dislocated along Profile I recorded about 70 mine tremors from the source zone Legnica-Głogów (Poland) in the period since July 2003 to December 2004. Recorded values of peak ground motion acceleration were analyzed as a function of local magnitude and focal distance. The preliminary attenuation relation was established and compared with some relations derived for abroad seismic and geologic conditions. The newly derived relation is illustrated in Fig. 7. Both calculated and measured values of acceleration are marked in this figure. Here, the measured values were preprocessed by averaging.

The considerable dispersion of values appears, analogical to that obtained in abroad formulae. This problem can be solved in greater generality only after gathering more recorded data, especially as concerns data of regionally stronger earthquakes.

**Acknowledgment.** This paper was supported by project No S3046201 “Experimental determination of the ground motion acceleration attenuation in the Czech massif” of the grant agency of the Czech Academy of Sciences.

## Attenuation graphs

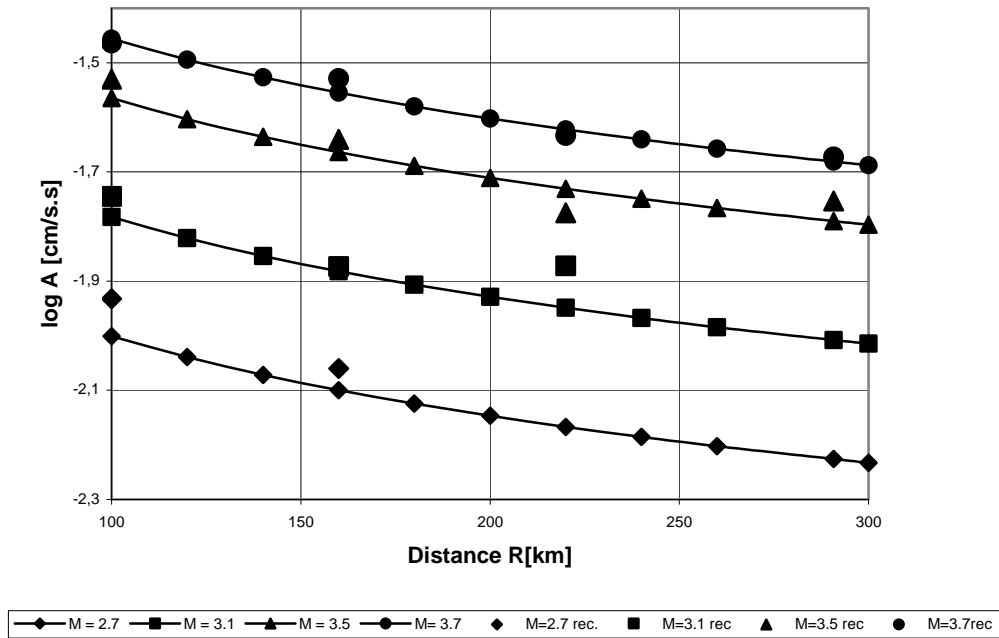


Fig. 7. Attenuation acceleration relation AB-ML.

## References

- Rudajev, V., and J. Buben, 2002, *Vyhodnocení seismického ohrožení JE Temelín na základě zrychlení registrovaných akcelerařem na stanici Struha seismické sítě Temelín*, Expertíza pro JE Temelín.
- Sadigh, K., J. Egan and R. Youngs, 1986, *Specification of Ground Motion for Seismic Design of Long Period Structures (abs.)*, Earthquake Notes **57**, p.13.
- Smit, P., and E. Rüttener, 1998, *Spektrale Beschleunigungs-abminderung in der Schweiz*. Bau-technik, Jahrgang 75, Heft 10, pp. 34-46.

Accepted October 16, 2006

## Field Measurements of Surface Seismic Vibrations Provoked by Mining in the Karvina Region

Zdeněk KALÁB<sup>1,2</sup> and Jaromír KNEJZLÍK<sup>1</sup>

<sup>1</sup> Institute of Geonics, Academy of Sciences of the Czech Republic  
Studentská 1768, CZ-70800, Ostrava-Poruba, Czech Republic  
e-mails: kalab@ugn.cas.cz; knejzlik@ugn.cas.cz

<sup>2</sup> VSB – Technical University of Ostrava, Czech Republic

### Abstract

Mining activities in the Karvina region, Czech Republic, provoke seismic events. Some of them may have amplitude values high enough to cause macroseismic effects on the surface. Generalized information about seismic effect on the surface is presented in the form of calculation of contours of maximum values of vibrations velocity for a given event. Measured values from permanent surface seismic stations are input parameters. A small number of these stations and generalized geological pattern of area under study result in local variances between the computed values and values measured using solitaire temporary stations. Therefore, main parameters influencing vibration on the surface are looked for.

Results of registration in the years 2003-2004 and experimental measurements are presented in this contribution. High differences in the thickness of sedimentary layers of both the Quaternary and Tertiary ages in a small region make it impossible to derive common relations or to use results from other areas.

**Key words:** mining induced seismicity, Karvina region, spectral ratio.

### 1. Introduction

The factor responsible for damage of structures on the surface in undermined areas can be the impact of mining, both in the form of surface deformation and strong mining induced seismic events. The mining induced seismic events can cause damage to elements of a building and accelerate its usual technical wear. This frequently occurring seismic load is comparable with an earthquake of lower intensity, so it is reasonable to pay attention to earthquake load impacts on structures. Since in this case

the repetitiveness of dynamic impact plays the major role, the overall seismic activity which affected a building throughout its life span needs to be taken into account.

In the Karvina region, Czech Republic, the mining activity is a source of induced seismicity. The frequently occurring seismic events, hardly manageable, and sometimes very intensive vibrations observed on the surface are its significant features. The most powerful mining related seismic event was registered at the CSA Mine in Karvina coal basin in 1983. Its local magnitude ( $M_l = 3.6$ ) reached the level of a lower intensity earthquake. The whole area of Karvina coal basin is effected permanently by mining induced seismicity due to concentrated deep coal mine excavation (depth of exploitation about 800 m). Annually, up to 40 thousand events are detected in the Karvina area, up to 500 of them being of local magnitude higher than 1.

Results of registration in the years 2003-2004, experimental measurements and first results from spectral ratio calculations will be presented in this contribution.

## 2. Present State

Detailed study of seismic loading in the Karvina region has been made by the Institute of Geonics of the ASCR (IGN) in Ostrava since 1999. Temporary seismic stations were located in buildings; some of them still operate. However, recorded data are used mostly for evaluation of maximum velocity amplitudes only. This measurement proved the existence of a very complicated distribution of vibration velocity at the surface, mostly due to the mechanism of sources. However, the maximum values measured at particular nearby sites show variable amplitudes from the same distant epicenter area. This indicates that the radiation and geometrical attenuation related to any focal event is strongly directional and that surface sedimentary layers in the surroundings of the recording station, together with the soil-structure, influence the seismic behavior (site effect). This is well documented in seismological studies from different regions, and has been experimentally confirmed.

Current methods of evaluation of seismic effects provoked by mining seismicity in the Karvina region are:

- Calculation of contours (isolines) of vibration velocity on the surface in Seismic Polygon of Ostrava-Karvina Collieries (seismological service for mines).
- Experimental measurement of vibration velocity by solitaire seismic stations (ORL1, ORL2, STO1, DAR1, DOU1 and KAR1) operated by the IGN according to recommendation from Czech technical standard CSN 73 0040 (Kaláb and Knejzlík 2002, Doležalová et al. 2004); sensors are mounted into cellars of buildings to obtain records of good quality (seismic response of building in these points is insignificant and appears at the end of records, usually).

The first step of calculation of contours of vibration velocity on the surface in Seismic Polygon was the estimation of attenuation of seismic waves (according to Holečko and Knotek, unpublished). Using classical statistical methods and extensive set of records of mining induced seismic events, the coefficient of absorption was determined as follows:

$$v_i = v_0 \cdot r_i^{-1} \cdot e^{-\alpha(r_i-1)}, \quad (1)$$

where:  $v_i$  is the absolute value of total vector of velocity on station signed  $i$  [ $\text{ms}^{-1}$ ],  $v_0$  is the same value in referential distance 1 km,  $r_i$  is the distance of station  $i$  from the source [km],  $\alpha$  is the coefficient of absorption [ $\text{km}^{-1}$ ].

To obtain more precise results, multiplicative function  $F(\text{azim})$  was added. Then we obtain

$$v_i = v_0 \cdot r_i^{-1} \cdot e^{-\alpha(r_i-1)} \cdot F(\text{azim}), \quad (2)$$

where  $F(\text{azim})$  is Fourier function up to 4 terms determined according to the azimuth of station.

Using  $F(\text{azim})$  and eq. (2) for given coordinates of the event, it is possible to calculate velocity values for a given point  $(x, y, z)$ . Usually, isolines are calculated from a set of calculated points.

Three-component velocity sensors SM-3 are used for experimental measurements of building seismic loadings. Sensors are connected to seismic apparatus of PCM3-EPC type. This apparatus provides digital records of measured signals in frequency range 0.5–30 Hz and sampling frequency up to 250 Hz (e.g. Knejzlík and Kaláb 2002). Data are interpreted on a personal computer using special seismological software developed in the IGN.

Almost 3000 and 4400 mining induced seismic events were recorded by solitaire seismic stations operated by the IGN in 2003 and 2004, respectively. The maximum velocity amplitude, amounting to  $0.4 \text{ mm} \cdot \text{s}^{-1}$ , was obtained from record on station DOU1 (village Doubrava) on September 16, 2003 at horizontal component. However, much more events were recorded because the buildings in which seismic sensors were installed were subject to high seismic vibrations produced, first of all, by the nearby traffic and other anthropogenic activities.

A selective set was prepared for detecting regions with amplifying or dumping zones of seismic effect on the surface. This set represents 36 events from the year 2003. Detailed isolines of surface vibration velocities were calculated on Seismic Polygon for these events. Related velocities were approached for all positions of experimental seismic stations of the IGN. For this set, only seven events show discrepancy between measured and calculated values greater than  $1 \text{ mm} \cdot \text{s}^{-1}$  (Fig. 1). Measured values were greater for all those cases. All these readings were made at a small distance from epicentral areas of the discussed events.

If we assume that the deep basin geometry can be a dominant factor in determining amplification at sites within sedimentary layers, then we are able to make the following:

- Experimental measurements.
- Calculation of H/V spectral ratio.
- Modeling of changes in the sedimentary thickness (Hrubešová and Kaláb 2005).

The first results of modeling were recently published, so this topic will be not presented in this contribution.

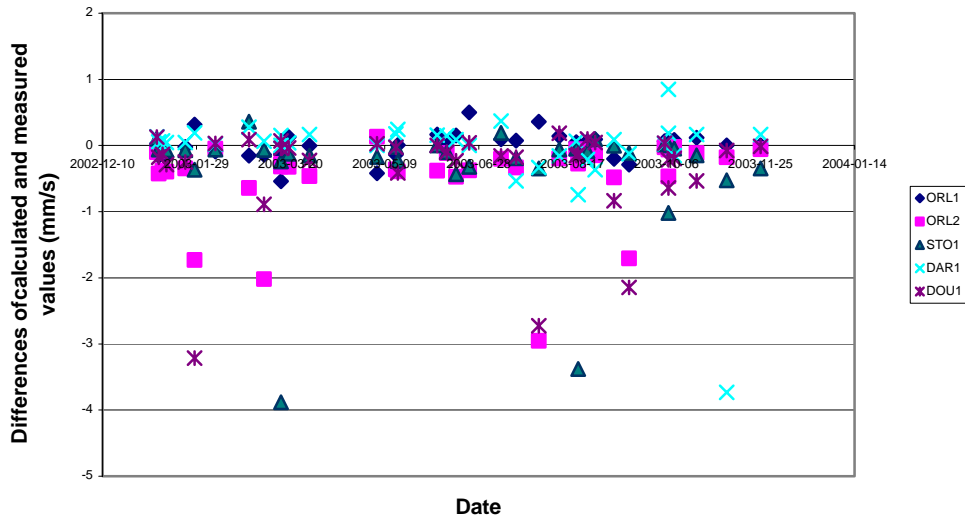


Fig. 1. Relation between maximum values of measured and calculated velocities for selected set of mining induced seismic events from 2003 (symbols represent individual stations).

### 3. Experimental Measurements in 2004

Solitaire seismic stations described above were complemented by eight additional stations to obtain two perpendicular profiles. Crossing of these profiles was situated at the epicenter of source area (Fig. 2) in which two distress-blasting operations were planned in the exploited coalface as a part of safety of mining works (October 15-24, 2005). Mechanism of explosive source is spherical in isotropic medium, so it is not possible to take into account direction from source to station. Generally, mining induced seismic events have very complicated mechanism with prevailing component of double-couple.

All stations were established in small houses, except of the point of profile crossing, in which buildings do not exist. Therefore, only short time measurements were made there and sensors were placed on unmade ground. Digital three-component seismic recorders with natural frequency 0.5 Hz were used for all stations, sampling frequencies were in the range of 100-250 Hz. The selection of measurement points on the profiles results from the local geological pattern. Thicknesses of sedimentary layers that cover the Carboniferous rocks are very different on the N-S profile, e.g., from zero value (outcrop of the Carboniferous rocks) up to 700 m in northern part of the area under investigation. However, the W-E profile has approximately stable value of covering rocks, except of the last point to the east. Our first study evaluates the measured seismic effects with thickness of covering rocks only.

The seismic effect on the surface that was provoked by distress-blasting operations was unfortunately very small; therefore, this vibration has not been detected on most of our seismic stations. Fortunately, three more intensive mining induced seismic events occurred during the experiment time. One of them (Oct. 16, 2005, 23:57) was located above coalface, in which distress-blasting operations were made. Its seismic

energy was  $2 \times 10^5$  J, hypocentral distances from 1.9 up to 5.9 km and a total of 8 records were interpreted (Fig. 3).

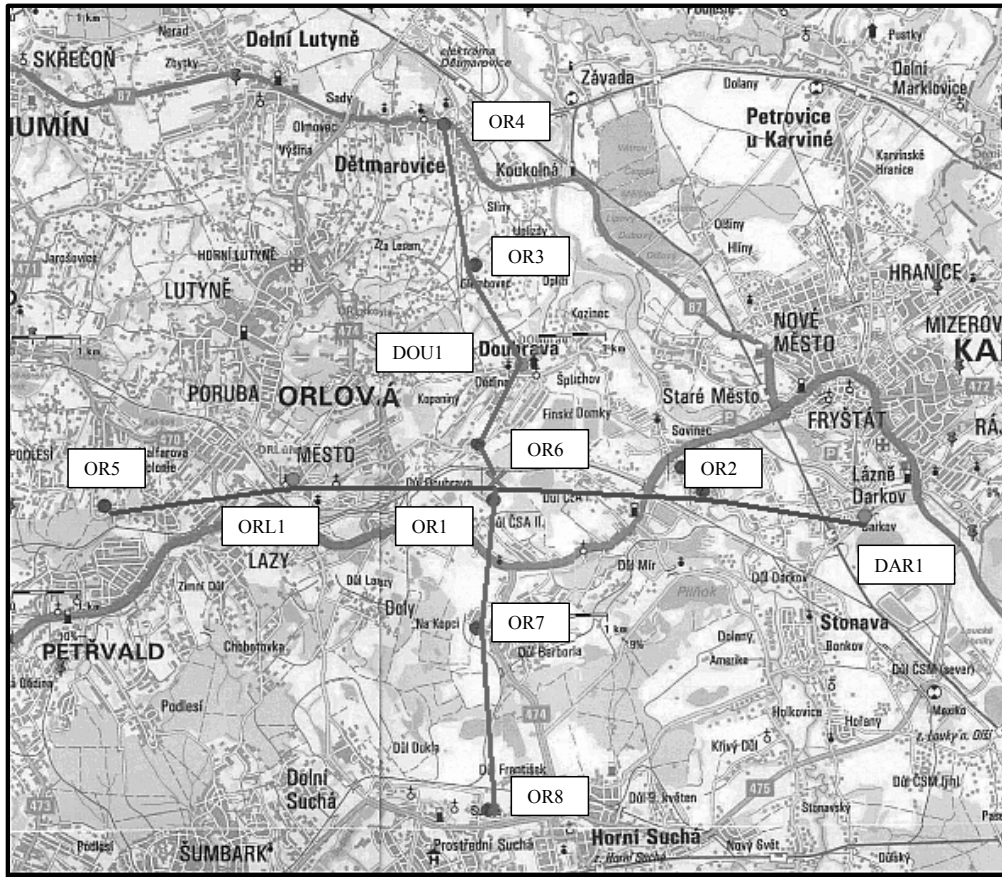


Fig. 2. Sketch of position of profiles for experimental measurements in 2004.

Detailed analysis of the maximum recorded velocities of mining induced seismic event of Oct. 16 gave the following results. The N-S and W-E components correspond to linear relations (log-log scale) with very high values of correlation coefficients; the vertical component has a smaller value of correlation coefficient. Similar relations were obtained also for other events, only the correlation coefficients were smaller. As the local geological conditions, especially the thickness of sedimentary layer, were quite different for the selected profiles, significant differences in the obtained relations were not documented. This means, it will be necessary to take into account next parameters, e.g., the level of underground water, existence of large surface spaces filled by water, local tectonic pattern, polarization of local failures and fissures, and the like. However, the small number of interpreted data for individual relations can result in incorrect conclusions. The same results were obtained also from

an analysis of relations with the summary thickness of the Quaternary and highly failed Tertiary sediments.

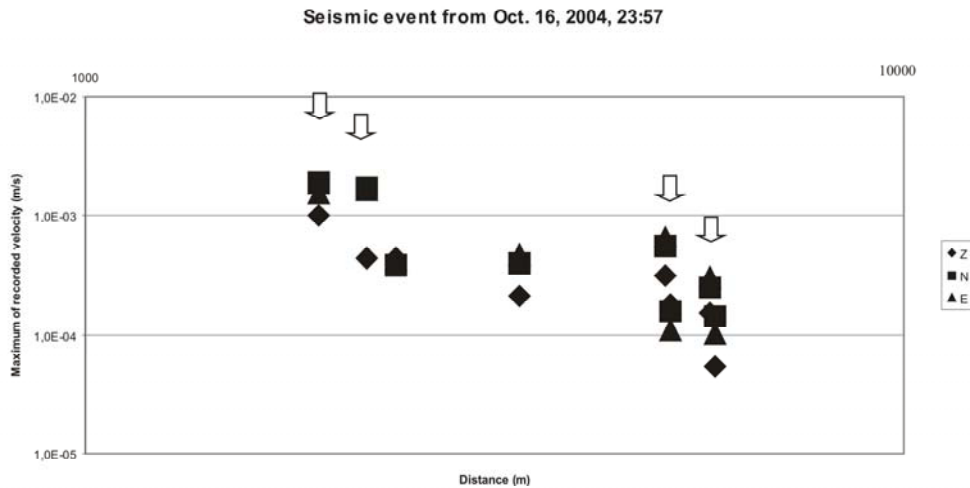


Fig. 3. Example of graph of maximum recorded velocity vs. distance; darts mark stations of the N-S profile.

#### 4. Initial Study in Frequency Domain

Two main causes of site amplification are usually taken into consideration: the effect of unconsolidated layers and the topographic effect. Basically, site effects are associated with the phenomenon of seismic waves traveling into soft soil layers. This is explained firstly by the lower velocity and density between unconsolidated sedimentary layers and the underlying rock (impedance contrast). For conservation of energy, this requires larger amplitudes of the seismic waves in sediments. Secondly, for a structure composed of sub-horizontal layers, body waves, which travel up and down, are the chief inputs. Due to heterogeneity of the sedimentary layer thickness, the surface waves generated by the structure are also trapped. Resonance patterns are created when trapped waves interfere. The shape and frequency content of such waves depend on the geometry and physical properties of the structure. The degree of complexity of predicting a seismic response increases with the complexity of the structure (Rosset et al., 2002).

Abbott et al. (2001) described basic steps for computing the H/V spectral ratio as follows: Nakamura (1989) proposed that the vertical component spectrum of ground motion being uninfluenced by sedimentary layers and therefore containing uncontaminated information about the source, could be used to deconvolve source effects from site effects. In the frequency domain, this is accomplished by simply dividing the horizontal component spectrum of a site by the vertical component spectrum of the same site (H/V – single-station spectral ratio). The technique has proved useful in predicting resonance frequencies of sediments using ambient noise or mi-

crotremor as a source. Lermo and Chavez-Garcia (1993), in modification of Nakamura's technique, showed that it is possible to use S-wave spectra to estimate site response. They find "very good" agreement between the H/V technique and standard spectral ratios (spectral ratios are computed by dividing the horizontal spectra of a station for which you wish to know the site response, by the horizontal spectra of a nearby reference station on rock).

Nakamura's method is at present the most popular tool for estimating the site effect in natural seismicity; the use of this method for estimating the site characteristics of ground motion caused by mining induced seismicity was described by Olshewska and Lasocki (2004).

The described technique was used for initial spectral study for data set from solitaire seismic stations in Karvina region. Data set for new software developed in the IGN was collected from digitally recorded three-component seismograms. Usually, accelerograms are used for the described spectral ratio technique but we use velocity records, likewise, e.g., Abbott et al. (2001). The interpretation of event starts by selecting a signal segment with length  $2^n$  (completed by zero, if necessary), that is, a time window modified by Hamming (or different). The next step is computation of spectra (Fast Fourier Transform) for all three components. Using spline function, the spectral curves are smoothed and, after that, the NS/Z and EW/Z ratios are computed. Useful spectra are added to the averaged summary graph.

The basic station for our study was station ORL1. Sensors of this station were installed in the area in which the outcrop of the Carboniferous rock exists. Therefore, spectral ratios cannot practically contain frequencies due to traveling through sedimentary layers, e.g., the spectral ratios H/V have to be approximately 1 (except of higher frequencies, but it is probably a resonant effect of building or its elements). Figure 4 represents averaged ratios calculated from 21 spectra.

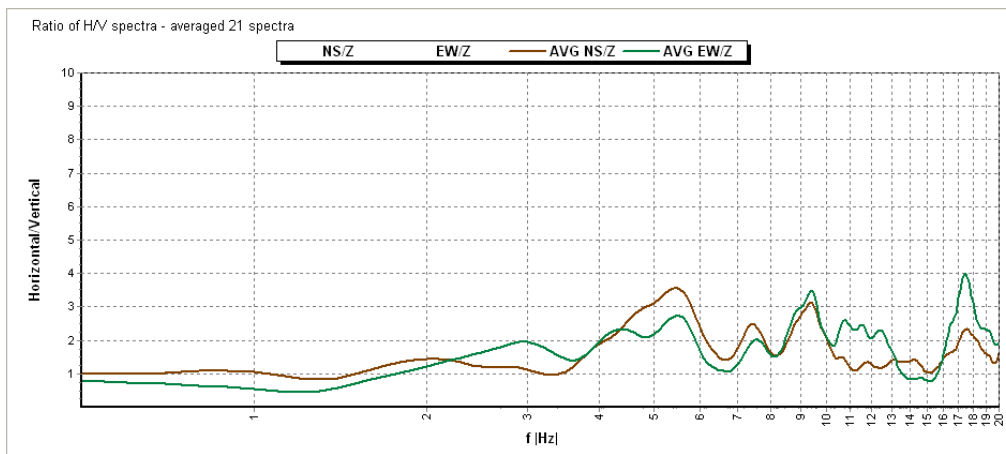


Fig. 4. Averaged spectral ratios H/V (horizontal to vertical component) calculated from spectra of station ORL1 (Carboniferous rock).

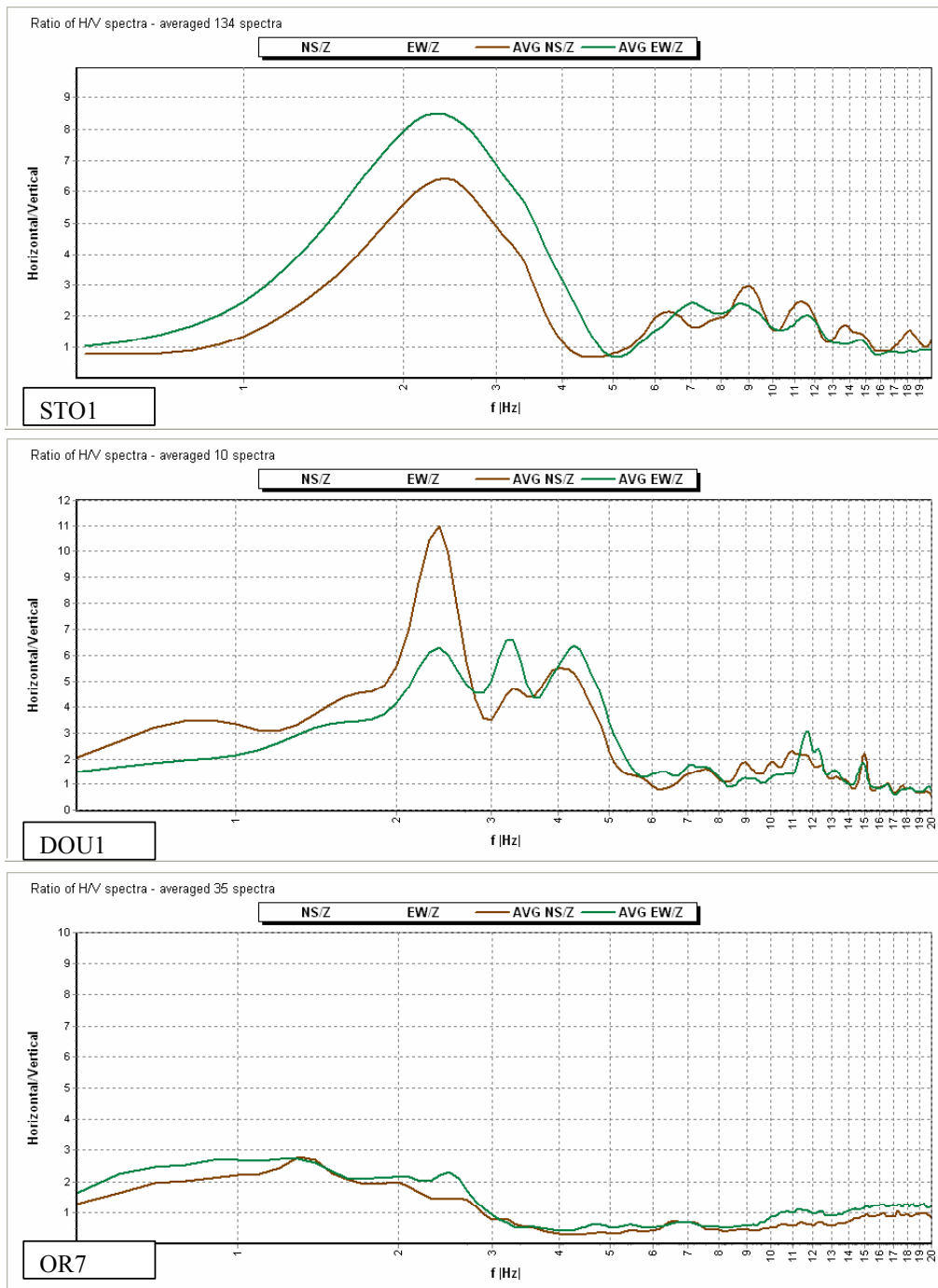


Fig. 5. Averaged spectral ratios H/V (horizontal to vertical component) calculated from spectra of locations with sedimentary layers (stations STO1, DOU1, OR7).

As mentioned above, the thickness of sedimentary layers (Tertiary and Quaternary soils and rocks) in the Karvina region ranged up to 700 m. Three examples from these areas are presented in Fig. 5. Seismic stations STO1, DOU1 and ORL7 have Carboniferous massif covered by 550 m, 400 m and 300 m, respectively. Spectral ratios for these locations have a shape that is quite different from that in the first discussed place. Peaks in these averaged spectra can represent site effect. However, the number of measurement points is still too small to give possibilities for drawing conclusion about amplification of seismic waves resulting from the site effect.

## 5. Conclusions

Experimental measurement plays very important and unsubstitutable role for reliable prediction of seismic loads, which is a crucial information for solution of seismic impacts on buildings and other structures. The measured values obtained from temporary station operated by the IGN and experimental section measurement (situated in selected localities on the surface) have been collected and analyzed.

The commonly used interpretation of measured data in the time domain does not enable us to prepare the evaluation of seismic effect of mining induced seismic events in correlation with the thickness of sedimentary layers. The number of useful data is not sufficient.

The methods of analysis in the frequency domain enable us to assess the effects of actually occurring vibrations. Using Nakamura's technique, spectral ratios for selected measurement points were calculated (this calculation is a test; at present, we do not have a possibility to calculate the total horizontal component). In step with the results of different authors, the point without sedimentary layers (ORL1) has a comparatively low ratio, other points that are situated in areas covered by sedimentary layers show spectral ratios with some significant peaks. They probably represent an increase of seismic effects due to the sedimentary cover. Detailed evaluation will be presented after extended geological and seismological interpretation.

The correctly designed response determines a rational design of structure, i.e., a harmonious utilizing of strength and elastic properties of the structure assuring the demanded function abilities, both during extraordinary loads and after their disappearance. It is evident that seismic loading of surface objects by mining induced seismicity is indispensable and therefore it is necessary to establish a systematic seismic monitoring.

**Acknowledgements.** This paper has been prepared in the frame of grant project of the Czech Science Foundation No. 105/04/1424 "Response of structures and buildings to technical seismicity"; the experimental measurements was performed in the frame of project of the Czech Science Foundation No. 105/03/0078.

## References

- Abbott, R., et al., 2001, *Analysis of Shallow Site Response to LARSE-2 Blasts at Precarious Rock Sites Near the San Andreas Fault*. Final Report, <http://quake.seismo.unr.edu/ftp>.

- Hrubešová, E., and Z. Kaláb, 2005, *Example of Modeling of the Mining Induced Seismicity Impact on the Building Using Numerical System Plaxis*. In: Pa. Konečný (ed), "EUROCK 2005 – Impact of Human Activity on the Geological Environment", A.A. Balkema Publisher, Leiden, 213-218.
- Doležalová, H., J. Holečko, Z. Kaláb and J. Knejzlík, 2004, *Analysis of Influence of Mining Induced Seismicity on Surfáře at Karvina Region*. *Transactions of the VSB-Technical University of Ostrava, Civil Engineers Ser.*, Vol. IV, No. 2, 85-93 (in Czech).
- Knejzlík, J., and Z. Kaláb, 2002, *Seismic Recording Apparatus PCM3-EPC*, *Publs. Inst. Geophys. Pol. Acad. Sc.*, **M-24(340)**, 187-194.
- Kaláb, Z., and J. Knejzlík, 2002, *Systematic Measurement and Preliminary Evaluation of Seismic Vibrations Provoked by Mining Induced Seismicity in Karviná Area*, *Publs. Inst. Geophys. Pol. Acad. Sc.* **M-24(340)**, 95-103.
- Lermo, J., and F.J. Chavez-Garcia, 1993, *Site Effect Evaluation using Spectral Ratios with only One Station*, *Bull. Seismol. Soc. Amer.* **83** (5), 1574-1594.
- Nakamura, Y., 1989, *A Method for Dynamic Characteristics Estimation of Subsurface using Microtremor on the Ground Surface*. QR Railway Technical Research Institute, 30, 1.
- Olszewska, D., and S. Lasocki, 2004, *Application of the Horizontal to Vertical Ratio Technique for Estimating the Site Characteristics of Ground Motion caused by Mining Induced Seismic Events*, *Acta Geophys. Pol.* **52**, 3, 302-318.
- Rosset, P., A. De la Puente, L. Chouinard, D. Mitchell and J. Adams, 2002, *Site Effects Assessment at Small Scales in Urban Areas: A Tool for Preparedness and Mitigation*. <http://www.grif.umontreal.ca/pages/i-rec%20papers/philipros.PDF>

*Accepted October 16, 2006*

## **Characterization of Rock Temperature Changeability in the Halemba Coal Mine Deposit (the Upper Silesian Coal Basin)**

Sławomir KĘDZIOR and Wojciech DROBCZYK

University of Silesia, Faculty of Earth Science, Department of Applied Geology  
Będzińska 60, 41-200 Sosnowiec  
e-mail: slawekkedzior@poczta.onet.pl

### **A b s t r a c t**

The main geological element influencing the temperature changeability within the Halemba Mine area is Kłodnica fault, which divides this area into two parts with different rock temperatures. The area lies to the north of the fault (the upthrow) and is characterized by a higher temperature than in the area located to the south (the downthrow). The same trend is shown in the case of geothermal gradient and geothermal heat flow. The reason for the higher rock temperatures in the upthrow of the Kłodnica fault might be the occurrence of many smaller accompanying faults which could cause the better transport of radiogenic heat from the deeper parts of the rock mass towards the surface and in consequence make the rock temperature higher in the area of Halemba I. The rock temperature rises in the north-east direction. The distribution of temperature in the area of the Halemba Mine is an element of a regional trend, not only the local changeability.

### **1. Introduction**

Rock temperature is one of the important parameters of rock mass physical properties resulting in both temperature mining hazards and possibilities of geothermal energy utilization.

The Halemba Coal Mine is located in the central part of the Upper Silesian Coal Basin (the USCB) within the Main Saddle in the zone of the Kłodnica fault. This fault divides this mine area into two parts: the north part (Halemba I) in the upthrow of the fault and the south part (Halemba II) in the downthrow of the fault. The Kłodnica dislocation of NW-SE direction is one of the largest dislocations in the USCB of the throw of about 280-480 m. There are many smaller faults accompanying the Kłodnica fault of NNW-SSW direction.

Geological structures in the studied area contain the Saddle, Ruda and Załęże Beds which consist of sandstones, mudstones and claystones with coal seams belonging to the coal-bearing Carboniferous system. The Carboniferous is covered by Triassic limestones and Miocene clays of about 200 m thickness, especially in the south part of the area (the downthrow of the Kłodnica fault).

The Halemba Mine is one of the deepest coal mines in the USCB. The coal is exploited at a depth of 1000 m.

The aim of this paper is to investigate rock temperature changeability in the area of the Halemba Mine and to present the natural factors influencing rock temperature distribution in the studied area.

The question of rock temperature changeability and the influence of geological factors on it within the USCB was presented by Karwasiecka (1996, 2002), Plewa and Plewa (1992) and Buła *et al.* (1995). In these publications, it is widely assumed that the large dislocations such as Kłodnica, Bzie-Czechowice and others affect the geothermic field and the isotherms are parallel to the direction of these dislocations. That is why the influence of tectonics and other geological factors on rock temperature is a problem worth studying in the case of small areas. The Halemba Mine, which is characterized by the occurrence of Kłodnica fault and temperature measurements at a considerable depth around 1000 m, seems to be a good example.

## 2. Method

In order to investigate rock temperature changeability in the area of the Halemba Mine, the data obtained from rock temperature measurements were used. The temperature was measured in surface bore-holes using a maximum thermometer 120 hours after the end of drilling and in underground mine excavations using a TC-150 digital thermometer. The temperature measurements in the bore-holes were carried out pointwise in three horizons: 525 m, 830 m and 1050 m, similar to the measurements done in mine excavations on three working floors given above. The measurements of temperature were carried out regularly in the mine in order to define the temperature mining hazards occurring on working floors. The measurements were done by mine workers who made it possible to realise this work (Janik and Kuś 1994, 1996).

On the grounds of rock temperature data taken from the bore-holes, the values of geothermal gradient as well as the values of geothermal heat flow were calculated. The heat flow density [ $\text{W}/\text{m}^2$ ] was calculated using the following formula:

$$q = -\lambda \text{grad} T, \quad (1)$$

where  $\lambda$  is the thermal conductivity, and  $T$  is the geothermal gradient.

The geothermal heat flow density was calculated separately for both areas of the Halemba Mine (Halemba I and Halemba II) because of the different geological structure and different types of rocks, which are characterized themselves by various heat flow values. In the area of Halemba I, Triassic and Miocene formations do not occur and the formation of the Carboniferous lies just under the Quaternary, whereas in the area of Halemba II the overburden consists of Triassic, Miocene and Quaternary for-

mations. The geothermal gradient is different in the two areas; in Halemba I it amounts to 3.44°C/100 m and in Halemba II – 2.83 °C/100 m. In order to calculate the geothermal heat flow density, the following values of heat flow were adopted (Plewa and Plewa 1992, Karwasiecka 2001):

- For the Quaternary: 2.2 W/m°C
- For the Miocene: 1.9 W/m°C
- For the Triassic: 2.2 W/m°C
- For the Carboniferous: 2.1 W/m°C

The heat flow density values given above with each rock stratum thickness and their percentage share are shown Table 1.

Table 1

The average values of thermal conductivity for the USCB and the thickness of rock formations in the area of the Halemba Mine (after Plewa and Plewa 1992)

Formations	$\lambda$	Halemba I		Halemba II	
		average thickness [m]	%	average thickness [m]	%
Quaternary	2.2	88	8	74	4
Miocene	1.9	lack	–	208	12
Triassic	2.2	lack	–	53	3
Carboniferous above 1000 m	2.1	1033	92	1393	81

The percentage thickness was used in order to calculate a weighted average of thermal conductivity. The average value of thermal conductivity for the Halemba I area amounts to 2.1 W/m°C and for the Halemba II area to 2.1 W/m°C too. Using the obtained data, the heat flow density was calculated for both areas:

- Halemba I

$$q_I = 2.1 \times 0.03437 = 0.07218 \text{ W/m}^2 = 72.18 \text{ mW/m}^2$$

- Halemba II

$$q_{II} = 2.1 \times 0.0283 = 0.05943 \text{ W/m}^2 = 59.43 \text{ mW/m}^2$$

### 3. Results and Discussion

#### *The surface bore-holes*

On the grounds of the results obtained from the surface bore-holes, the graphs of vertical temperature changeability were drawn (Fig. 1). In all the analysed bore-holes the rock temperature rose with the increase in depth. Based on the temperature graphs, the geothermal gradient was calculated for the bore-holes. The highest value of geothermal gradient in the area under study, 4.50 °C/100 m, was noted in bore-hole

Halemba 88, in the south part of Halemba I area, whereas the lowest value, 2.5 °C/100 m, occurred in Panewniki 16. This bore-hole is located in the south part of the area of Halemba II.

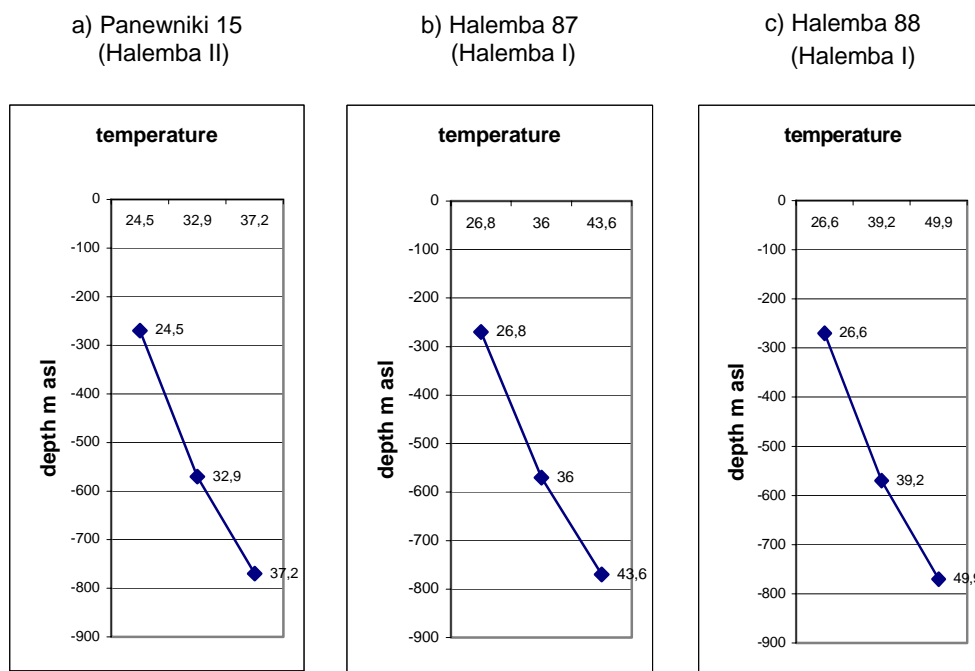


Fig. 1. The vertical changeability of rock temperature in chosen bore-holes.

Table 2 shows the temperatures measured in the bore-holes at three levels (525, 830 and 1050 m) and the geothermal gradient for each bore-hole. Some bore-holes, such as Panewniki 9, Mikołów 1, Mikołów 2 and Mikołów 3 are situated outside the area of the Halemba Mine.

Bore-holes Halemba 87 and 88 are characterized by the highest rock temperatures at all investigated levels (Table 2) and they are located in the area of Halemba I (central and south part). The lowest rock temperatures were noted in the Panewniki 19 bore-hole located in the south part of the Halemba II area.

In the area of Halemba I, to the north of Kłodnica fault, the rock temperatures are generally higher than in Halemba II, to the south of Kłodnica fault, the temperature difference being about 5-6°C.

### ***The geothermal gradient***

The differences in geothermal gradient between the areas of Halemba I and Halemba II divided by the Kłodnica fault were clearly visible. The clear change of geothermal gradient is strongly marked along this fault.

Table 2  
Rock temperatures in the bore-holes in the area of Halemba Mine  
(Janik and Kuś 1994)

Bore-hole	Rock temperature [°C]			Geothermal gradient [°C/100 m]
	level 525 m	level 830 m	level 1050 m	
Kłodnica 1	24.2	33.6	38.2	2.80
Kłodnica 4	23	30.5	37.8	2.95
Kłodnica 5	23.7	31	37.7	2.79
Panewniki 9	23	29.9	35.5	2.50
Panewniki 15	24.5	32.9	37.2	2.82
Panewniki 16	25.1	32	37.6	2.50
Panewniki 18	22.9	32.1	39.5	3.32
Panewniki 19	20.7	28.9	35	2.85
Halemba 87	26.8	36	43.6	3.35
Halemba 88	26.6	39.2	49.9	4.50
Mikołów 1	23	31.8	39.9	3.21
Mikołów 2	20.8	28.4	36.9	3.48
Mikołów 3	22.1	31.9	39.5	2.50

To the north of the Kłodnica fault (Halemba I) the geothermal gradient is higher than to the south of this dislocation (Halemba II). This means that the rock temperature rises faster with depth in the area of Halemba I (2.8-4.5 °C/100 m), than in Halemba II (2.5-3.2 °C/100 m).

In the area of Halemba II the decrease in geothermal gradient towards the north-west direction was observed, while the minimum value was noted in the central part of this area in the vicinity of the Panewniki 15 bore-hole as well as in the north-west part near the Panewniki 16 bore-hole.

#### ***Rock temperature at levels of 525, 830, and 1050 m in the mining excavations***

Rock temperature values at the level of 525 m are varied and fluctuate between 21°C and 32°C (Table 3). The clear temperature boundary between the areas of Halemba I and Halemba II is not visible, but in the area of Halemba I the temperature of rock is slightly higher than in the area of Halemba II (Table 3). There are two positive and one negative geothermal anomalies in the area of Halemba I, while in the whole area of Halemba I and Halemba II the rock temperature generally rises from west to east.

At the level of 830 m the boundary of rock temperature between the areas of Halemba I and Halemba II is clearer than at the level of 525 m. This boundary is al-

most compatible with the Kłodnica fault direction and it is interpreted as the result of the fault presence. In the upthrow (to the north of the fault) the rock temperature is higher than in the downthrow (to the south of the fault). Similarly, at the level of 525 m the rise in temperature from west to east is noted, the rocks of the lower temperature are located close to the west boundary of the area, whereas the warmer ones appear to the east of the studied area.

The level of 1050 m is characterized by the clearest boundary of temperature, which changes along the Kłodnica fault – in the downthrow, the rock temperature is much lower than in the upthrow. The maximum range in the highest temperature (48°C) and lowest one (36°C) occurring there is 13°C (Table 3). Within the areas of Halemba I and II the temperature of rocks rises from west to east just as at the levels lying above. The location of the positive and negative geothermal anomalies at this level is the same as at other levels, while the areas of the negative ones are smaller than in levels lying above.

Table 3 shows the maximum, minimum and average temperatures obtained from the three analysed levels in the area of Halemba I and II.

Table 3

The minimum, maximum and average rock temperature in the areas of Halemba I and II

Level [m]	Halemba I (the upthrow of the Kłodnica fault)			Halemba II (the downthrow of the Kłodnica fault)		
	temperature °C			temperature °C		
	maximum	minimum	average	maximum	minimum	average
525	32	21	26.5	26	21	23.5
830	42	32	37	35	30	33
1050	49	37	43.5	41	36	38.5

***The natural factors influencing the distribution of rock temperature in the area under investigation***

The main factor affecting the rock temperature changeability in the area of the Halemba is undoubtedly the Kłodnica fault, which makes a boundary between the area of much colder rocks to the south and the warmer ones to the north. Within the area of Halemba I, to the north of Kłodnica fault, accompanying faults in large numbers are located which are orthogonal to the Kłodnica fault. These faults could cause a better transport of radiogenic heat from the deeper parts of the rock mass towards the surface and in consequence make the rock temperature higher in the area of Halemba I (Leśniak and Leśniak 1994). The area of Halemba II is characterized by a small number of faults, and that is why the pathway of the heat transport was probably more difficult that could cause the lower rock temperatures related to the Halemba I area.

***Temperature distribution in the Halemba Mine in comparison with geothermal field of the USCB***

The average geothermal gradient for the area of Halemba I amounts to 3.44 °C/100 m, therefore it is approximate to the typical temperature gradient for this part of the USCB (3.4 to 4.0 °C/100 m), whereas the gradient calculated for the area of Halemba II amounts to 2.83 °C/100 m and differs widely from the regional gradient. But the local gradient distribution within the area of Halemba is conformable to the regional geothermal gradient rise presented on maps from the south to the north (Karwasiecka 1996).

The geothermal gradient values in the Halemba region is approximate to the average ones appearing in this region of the USCB; therefore, the values of the area of Halemba I are more compatible to the regional geothermal gradient than the values noted in the area of Halemba II.

The analysis of the heat flow density shows the same trend which was obtained for both areas separately. For the area of Halemba I the heat flow density value (72 mW/m<sup>2</sup>) is closer to the regional values (65-75 mW/m<sup>2</sup>) than the value in Halemba II (59 mW/m<sup>2</sup>).

The horizontal distribution of rock temperature at the three analysed levels (525, 830 and 1050 m) is consistent with the main trend of temperature rise from the south-west to the north-east. The distribution of temperature in the area of the Halemba Mine is an element of regional trend, not only the local changeability. The main reason for the observed temperature distribution in this region of the USCB is probably the Kłodnica fault, which occurs not only in the Halemba area, but it is a regional dislocation in the USCB and its influence on the geothermal field is significant.

**4. Conclusions**

1. The Kłodnica fault divides the Halemba Mine area into two areas of different rock temperature values; in the upthrow of this fault (the area of Halemba I), rock temperatures are higher than in the dowthrow (the area of Halemba II).

2. The trend presented above is confirmed by the analyses of temperature distribution in the bore-holes and in the mining excavations (levels of 525, 830 and 1050 m) and also by calculation of such factors as geothermal gradient and heat flow density.

3. The Kłodnica fault strongly influences the temperature distribution. In the area of Halemba I, the large number of small faults accompanying the Kłodnica fault causes a better transport of radiogenic heat from the deeper parts of the rock mass towards the surface and in consequence they increase the rock temperature.

4. The distribution of temperature in the area of the Halemba Mine is compatible to the regional trend of the temperature rise in the north-east direction; therefore, this distribution becomes a significant element of the regional trend, not only the local changeability.

## References

- Buła, Z., D. Botor, M. Karwasiecka and P. Kosakowski, 1995, *Zarys budowy geologicznej i warunki geotermiczne utworów węglonośnych górnego karbonu w Górnośląskim Zagłębiu Węglowym*. W: R. Ney and M. Kotarba (red.), „Opracowanie modeli oraz bilansu generowania i akumulacji gazów w serii węglonośnej Górnośląskiego Zagłębia Węglowego”, Wyd. Centrum PPGSMiE PAN, Kraków.
- Janik, G., and R. Kuś, 1994, *Dokumentacja Geologiczna Złoża KWK Halemba*, Przedsiębiorstwo Robót Geologiczno Wiertniczych S.C, praca nr 9502.
- Janik, G., and R. Kuś, 1996, *Dokumentacja Geologiczna Złoża KWK Halemba II*, Przedsiębiorstwo Robót Geologiczno Wiertniczych S.C, praca nr 9602.
- Karwasiecka, M., 1996, *Atlas geotermiczny Górnośląskiego Zagłębia Węglowego*, Wydawnictwo Kartograficzne Polskiej Agencji Ekologicznej S.A. Warszawa.
- Karwasiecka, M., 2001, *Nowe wyniki badań gęstości powierzchniowego strumienia ciepłego Ziemi w obszarze Górnośląskiego Zagłębia Węglowego*. W: S. Plewa (red.), „Rozpoznanie pola ciepłego Ziemi w obszarze Górnośląskiego Zagłębia Węglowego dla potrzeb górnictwa i ciepłownictwa”, Studia Rozprawy Monografie nr 90, Wyd. IGSMiE PAN, Kraków.
- Karwasiecka, M., 2002, *Pole ciepłe Górnośląskiego Zagłębia Węglowego*. W: Z. Małolepszy (red.), „Energia geotermalna w kopalniach podziemnych”, Wydział Nauk o Ziemi, Sosnowiec.
- Leśniak, L., and A. Leśniak, 1994, *Modelowanie rozkładu temperatur w strefie uskoku w rejonie Czechowic*, Zesz. Nauk. AGH, Geologia **20**, 2, Kraków.
- Plewa, M., and S. Plewa, 1992, *Petrofizyka*, Wydawnictwo geologiczne, Warszawa.

*Accepted 10 April 2006*

## **Relationship between Seismic Activity and Mine Gas Emissions**

Stanisław LASEK and Bogusław SYREK

Katowice Coal Holding  
ul. Damrota 18, 40-022 Katowice, Poland  
e-mail: zagrozenia@khw.pl

### **A b s t r a c t**

Katowice Coal Holding which groups 9 collieries is a large producer of high quality steam coal. Mines are generally affected by rockbursts, methane and fires. The paper presents the impact of rockburst hazard on methane hazard and gas emissions. The magnitude of the seismic events and their location are also discussed. The relationship between the above-mentioned hazards for strong events is proved. In the next step, the paper attempts to find a relationship between weak seismic activity and mine gas emissions. Typical exploitation tremors with energy of the order of  $10^3$  J, which were localized in the direct vicinity of the longwall face, were used for the analysis. Apart from CH<sub>4</sub> and CO measurements, the air flow velocity in the area was also analysed. Only for several per cent of cases, an increase of CH<sub>4</sub> emissions was registered after the occurrence of seismic phenomena. These phenomena had no impact on CO emissions and air flow velocity. A big group of unexplained phenomena was observed (30 per cent of cases), where the occurrence of tremors was preceded by distinct drops of air velocity in the area.

### **1. Introduction**

The Katowice Coal Holding is a large producer of steam coal of the best quality. The Holding incorporates 9 collieries which are affected by rockbursts, methane, and mine-fires. At two plants of the Holding, i.e. at Śląsk and Wesoła collieries, the highest levels of methane and rockburst hazards occur simultaneously in the same areas. The influence of seismic activity on intensity of methane release into mine headings is known and has been repeatedly reported. Such studies have been presented among others by Matuszewski (1979), Konopko *et al.* (1994) as well as Kutkowski and Badura (1998). In a decisive majority of cases, the interest has been focused on

seismic tremors of large or very large energy and it was found that they potentially influenced methane hazard.

Similar conclusions were also put forward by commissions assigned for the purposes of investigating mine accidents and catastrophes. Similarly, at the Ślask colliery during longwall 3J advancing in seam 502 strong seismic events were several times followed by considerable methane emissions. Lasek *et al.* (2002) performed a detailed analysis of that relation for this longwall. Although almost 4000 tremors with an energy of the order of  $10^2$ - $10^7$  J ( $M_L \approx 0.1$ - $3.1$ ) occurred in the area of the longwall, only 5 of them caused a considerable release of methane into mine headings (concentration increase over 0.2%). Those tremors are presented in Table 1.

Table 1  
Methane emission caused by seismic events in the area of longwall 3J  
in seam 502 at the colliery Ślask

Ord. No.	Tremor			Methane emission		
	Date	Hour	E(J), $M_L$	Concentration increase [%]	Duration of the increase [min.]	Methane increase [m <sup>3</sup> ]
1	21.05.99	08:25.	$3 \times 10^6$ J 2.46	0.2-4.6	935	16456
2	25.08.99	23:39	$4 \times 10^6$ J 2.53	0.1-1.6	14	74
3	29.01.00	00:01.	$4 \times 10^7$ J 3.0	0.2-0.4	214	214
4	07.02.00	23:33	$9 \times 10^5$ J 2.19	0.2-0.6	1	4
5	25.01.02	15:22	$3 \times 10^7$ J 3.1	0.8-18.0	2478	54516

From the above table was found that in some cases (tremors 1 and 5), high-energy seismic events resulted in dangerous methane releases, the results of which stayed in the occurrence place for many hours or even days.

That fact has repeatedly been confirmed, so the authors of the present paper further assumed a somewhat different attitude.

An attempt was made to investigate the relationship between typical, mining-induced, low-energy seismic events occurring in direct vicinity of longwall and emission of mine gases. Longwall 42 extracted in 1998-1999 in field D-west in seam 510 at the Wesola colliery, was chosen as the investigation object, because of the very precise location of foci in that area and potentially high methane and rockburst hazard.

## 2. Mining-Geological Conditions

Field D of seam 510 is located in the north-eastern part of the mining area of the Wesola colliery, at a depth of about 700 meters. The area is bordered by faults with considerable throws.

The geological structure of coal deposit in field D is very diverse. There are two saddle seams, 501 and 510, which are characterised by a very changeable thickness and distance between them.

Seam 510 in field D has a variable thickness that ranges from 6.8 m in its eastern part to 12.6 m in its south-western part. In the most part of field D the seam's thickness ranges, in average, from 8.0 to 10.0 m. According to profiles of boreholes drilled from headings in seam 510, directly in the seam's roof in majority of cases there are sandstone strata of thickness ranging from 1.5 to 25.3 m. The strata form an interbedding that separates seams 501 and 510. Seam 501, lying above them, has a very changeable thickness – ranging from 0 to 5 m. In connection with the geological structure it was necessary to keep the height of longwall 42 at 2.2 m all along its panel in order to protect seam 501 where it is suitable for extraction.

Longwall 42 was developed in the roof slice of seam 510, started in October 1998 with caving. It was the first longwall operated in this field in the saddle seams.

The panel of longwall 42 from its start to 1 April 1999 is presented in Fig. 1. Seam 510 in the area under consideration has been classified as follows:

- Methane hazard category: IV (highest),
- Rockburst hazard degree: III (highest),
- Water hazard degree: I and III (low and highest),
- Dust explosion hazard class: B (h),
- Spontaneous combustion inclination: very high.

## 3. Rockburst Hazard

Seismic activity has held at low and medium levels. During development operations, in principle, no seismic events were recorded. Only while driving gallery Vawest in the vicinity of cavings of longwall 43 (field D-east) and the fault zone connected with fault Wanda, three seismic events with a total energy of  $4.3 \times 10^3$  J were recorded.

In field D-west, where longwall 42 was operated, seismic activity was slightly higher. From the longwall's start to 8 April 1999, 136 seismic events with a total energy of  $2.53 \times 10^5$  J were recorded in its vicinity. Every tremor had energy of the order of  $10^2$ - $10^3$  J. Other examination methods (drilling, seismoacoustics) did not indicate any increase of rockburst hazard.

## 4. Methane and Mine-Fire Hazard

At the time of longwall start, methane hazard remained at a low level. Next, a distinct increase was noted during extraction operations. In total, regular methane re-

lease showed a gradually increasing trend to reach a value of  $22.24 \text{ m}^3\text{CH}_4/\text{min}$ . In turn, effectiveness of methane draining was low at the beginning but increased with time, up to over ten per cent. The regular methane release into the longwall was determined on the basis of laboratory analyses of air samples. Charts of methane gauges exceeding peaks showing the number and time of dangerous concentrations featured a high similarity. At the beginning an increase corresponding to extraction increase was observed. Then, even though output did not increase, an increase tendency in exceeding peak duration appeared.

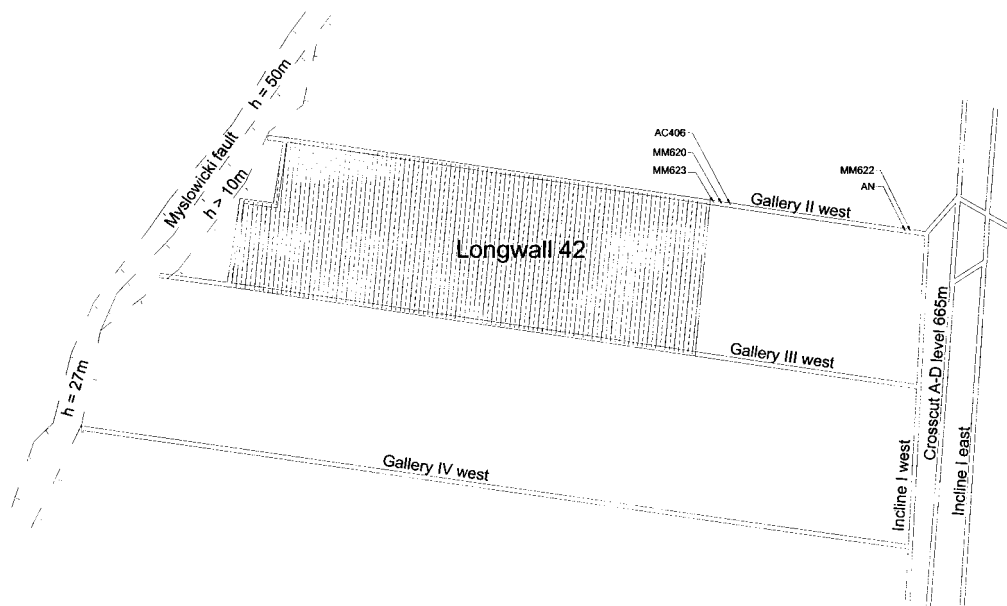


Fig. 1. Fragment of a map of seam 510 showing the panel of longwall 42.

Spontaneous combustion index of coal from seam 510, field D-west,  $Sz^a_{(273)}$  amounts to  $92^\circ\text{C}/\text{min}$  and activation energy of coal oxidation  $A$  amounts to  $36 \text{ kJ}/\text{mole}$ , which qualifies the seam among the spontaneous combustion group IV, which means a strong inclination for spontaneous combustion.

Current control of carbon monoxide and carbon dioxide concentrations in mine air performed by means of hand-operated and automated sensors as well as Graham index determined on the basis of mine air analyses did not indicate any increase of mine fire hazard.

## 5. Results of Examining Relation Between Seismic Activity and Emission of Mine Gases

26 seismic events with energy of the order of  $10^3 \text{ J}$  ( $M_L \approx 0.63-1.1$ ) located in direct vicinity of the longwall face were used for the purposes of the examination. Characteristics of the tremors are presented in Table 2.

Table 2  
Examined seismic events from longwall 42

Ord. No.	Date	Hour	Energy $A_S$ [J]
1	20.10.98	18:39	$4 \times 10^3$
2	23.10.98	14:13	$1 \times 10^3$
3	24.10.98	16:48	$6 \times 10^3$
4	26.10.98	11:43	$5 \times 10^3$
5	14.01.99	23:33	$5 \times 10^3$
6	19.01.99	18:30	$3 \times 10^3$
7	19.01.99	22:56	$2 \times 10^3$
8	20.01.99	20:58	$3 \times 10^3$
9	21.01.99	09:36	$2 \times 10^3$
10	27.01.99	22:14	$8 \times 10^3$
11	28.01.99	01:10	$2 \times 10^3$
12	28.01.99	04:46	$3 \times 10^3$
13	02.02.99	03:38	$8 \times 10^3$
14	02.02.99	18:08	$3 \times 10^3$
15	04.02.99	01:07	$4 \times 10^3$
16	05.02.99	12:42	$3 \times 10^3$
17	06.02.99	07:26	$3 \times 10^3$
18	08.02.99	20:19	$4 \times 10^3$
19	12.02.99	07:07	$7 \times 10^3$
20	15.02.99	18:04	$9 \times 10^3$
21	16.02.99	19:56	$5 \times 10^3$
22	19.03.99	08:43	$1 \times 10^3$
23	19.03.99	11:38	$1 \times 10^3$
24	01.04.99	08:08	$1 \times 10^3$
25	02.04.99	17:15	$2 \times 10^3$
26	03.04.99	01:27	$8 \times 10^3$

In order to examine a possible relation between seismic activity and methane or mine-fire hazards, the following five indicators working in a methanometer system (see Fig. 1) were used:

- Indicator MM623 (methanometer) installed in gallery II-west at the tail gate of longwall,
- Indicator MM622 (methanometer) installed in gallery II-west, west of incline I-west,

- Indicator MM620 (methanometer) installed in gallery II-west, 10 m east of longwall 42,
- Indicator AC406 (CO-analyser) installed 20-30 m from longwall 42 in gallery II,
- Indicator AN (anemometer) installed 10-20 m west of incline I-west in gallery II-west.

Observation diagrams were drawn up for each of the indicators with measurement results recorded through eight hours before registered seismic events. Such a time enables to observe changes in indications and eliminate, to a minimum, recording disturbances of an indicator's function.

### ***5.1 Analysis of indications of methanometer indicator MM623***

Indicator MM623 was placed directly in the tail gate of longwall 42 in gallery II-west, near cave line, in front of an air curtain. The indicator recorded all changes that took place in this area, among others, changes caused by shearer-loader operation, crew passage, damage of the air curtain, roof-rock caving in and seismic events. Thus, the indicator recorded first of all production-process cycles. Its operation was in general unstable and characterised by large indication changes. A careful analysis of its records allows to conclude that in none of analysed cases was an increase or decrease in methane release observed in the time preceding a tremor occurrence, which could not be connected with the longwall's technological process. After seismic events a slight increase of methane emission occurred in only 3 out of 26 analysed cases which make up merely several per cent of the total.

### ***5.2 Analysis of indications of methanometer indicator MM620***

Indicator MM620 was installed in gallery II-west directly before the longwall face so that its location allowed immediate recording of methane concentration in air flowing out of the longwall area, as well as assessing the influence of shearer-loader operation and changes occurring during mining. Like in the case of indicator MM623, the records showed very strong susceptibility to production-process-induced changes, air volume flow changes, and crew travel. In three out of 26 analysed cases, methane release increases were appeared after seismic events. The increases were small, they did not exceed 1 per cent, and were recorded immediately after events.

In Figure 2 it can be seen how tremor No. 15 (see Table 2) with energy  $E = 4 \times 10^3 \text{ J}$  resulted in a methane concentration increase from 0.7% to 1.3%. The tremor occurrence has been marked as an arrow. It can be seen that the methanometer reacted immediately after the tremor.

### ***5.3 Analysis of indications of methanometer indicator MM622***

Methanometer MM622, installed in gallery II-west close to the crossing with incline I-west, played the role of a district indicator of longwall 42. Its indications were characterized by regular changes, enabling the analysis of changes of methane hazard and its dependence on operations currently executed in the longwall district. Concluding from the performed analysis, it cannot be, in general, stated that the

changes resulted from seismic activity. Only in one case (tremor No. 6, see Table 2) an inconsiderable methane emission increase was observed immediately after a tremor. Indicator MM623 also noted an increase of methane concentration after this tremor.

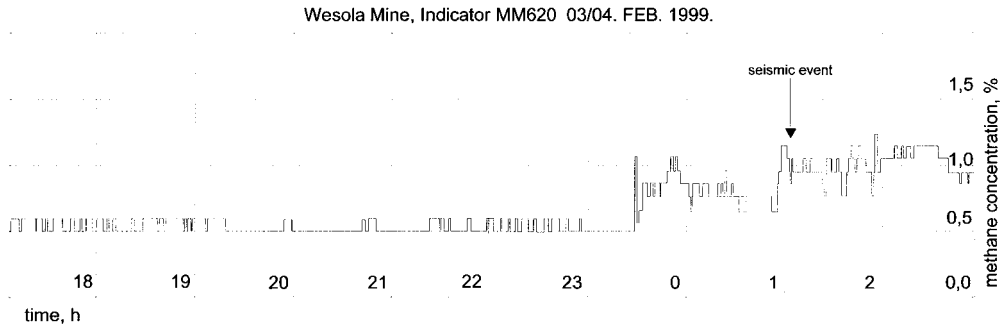


Fig. 2. Methane concentration increase after a seismic event of  $E = 4 \times 10^3 \text{ J}$  ( $M_L = 0.95$ ).

#### 5.4 Analysis of indications of carbon-monoxide recorder AC406

The analysis of fire hazard in the context of recorded seismic events was performed on the basis of records of an ACO-type carbon-monoxide recorder installed in gallery II-west, located east of longwall 42. Indications of the recorder were very stable, some slight changes in its operation during mining work in longwall 42 can be precisely explained based on other parameters recorded by remaining measuring and signalling instruments. All analysed cases showed a homogeneous and stable record. It was only minimally deformed by sensitivity of the measuring instrument itself. In the course of analysing the recorder's indications some peaks drew attention, which suggested calibration periods of the instrument, and sometimes increases of carbon-monoxide content caused by damage or malfunction of accessory devices in the area of the longwall tail gate or alternatively by blasting operations. In no case was any relation found between seismic activity and changes in CO-content records.

#### 5.5 Analysis of air velocity plots made by an AN404-type anemometer

In the analysis of records made by the ultrasonic indicator, type AN404, attention was drawn to changes that did not show connections with production processes, crew travel or changes in the ventilation system. In this analysis there were abstracted recurring, momentary decreases of air velocity in headings by a value of up to 1m/s, occurring with some regularity several hours before a seismic event. In 8 out of 26 cases such a relation has been found. It is difficult to determine whether or not the noted decreases have any connection with seismic activity, or opening air doors during crew passage and haulage exclusively caused them. A relatively large number of such phenomena (almost 30%) proves a need for carrying on further careful observations focused on the aforementioned issue. Yet, it is possible to state with certainty that no distinct changes of air velocity followed the tremor occurrences.

## 6. Conclusions

1. A serious increase of methane hazard may only be caused by seismic events of considerable seismic energy. For collieries of Katowice Coal Holding the energy limit is of the order of  $10^6$  J ( $M_L \approx 2.2$ ).

2. The investigations did not show any certain relations between the natural hazards under investigation. Slight increases in methane emission were noted after tremors but only in several per cents of all seismic events. Those increases were measured by different methanometers for many tremors. In general, the greater the distance between an indicator and a longwall front, the lower the probability of noting increasing methane emission after a tremor.

3. No relation has been affirmed between seismic activity and recorded carbon-monoxide content in mine air.

4. A considerable number of cases (almost 30%) of air velocity decrease in headings was observed, that preceded a seismic event by several hours. It is not explained whether or not it has any connection with seismic activity or it is caused by other things like: opening air doors for the purpose of crew passage or transport, or changes of potentials in the ventilation system. A relatively large number of such cases proves a need for further observations aimed at explaining the aforementioned phenomena. No changes of air velocity in mine headings were observed after tremors.

## References

- Konopko, W., J. Kabiesz and J. Cygankiewicz, 1994, *Wstrząsy i tąpnięcia jako inicjatory zagrożenia metanowego (Tremors and Rockburst as Agents Initiating Methane Hazard)*, Przegląd Górniczy Nr 2 (Mining Review No 2).
- Kutkowski, J., and H. Badura, 1998, *Wpływ wstrząsów sejsmicznych na zagrożenie metanowe (Influence of Seismic Events on Methane Hazard)*, Przegląd Górniczy Nr 3 (Mining Review No 3).
- Lasek, S., G. Stacha and S. Trenczek, 2002, *Doświadczenia uzyskane w trakcie eksploatacji ścian 3J w pokładzie 502 w partii „J” w KWK „Śląsk” w zakresie wpływu zagrożenia tąpnięciami na eskalację zagrożenia metanowego (Experiences Obtained in the Course of Mining Operations on Longwall 3J in Seam 502 in Area J at Colliery Śląsk Regarding Influence of Rockburst Hazard on Increase of Methane Hazard)*, Materiały sympozjum „Tąpnięcia 2000”, Wydawnictwo GIG-Katowice 2002 (Symposium Materials “Rockburst 2000”, Publication House of the Central Mining Institute, Katowice).
- Matuszewski, J., 1979, *Kryteria zagrożenia wybuchami metanu i pyłu węglowego w następstwie gwałtownych przemieszczeń górotworu (Criteria of Methane and Coal-Dust Explosion Hazard as a Result of Violent Rock-Mass Displacements)*, Prace GIG, Katowice (Works of the Central Mining Institute, Katowice).

Accepted 10 April 2006

## **Anisotropy of Seismic Wave Velocity in a Chosen Rock Mass**

Iwona STAN and Adam IDZIAK

Silesian University, Faculty of Earth Sciences  
Będzińska 60, 41-200 Sosnowiec, Poland

### **A b s t r a c t**

In the present research, a relationship between seismic wave velocity anisotropy and the distribution of crack orientation parameters was studied using interpretation methods based on tensor calculus. Objects of the research were basalt deposit located within the Sudetian Monocline and diabase deposit located within the Carpathian Foothill. The relationship between velocity and azimuth of seismic profile was established. It was found that the average strike azimuth of separated vertical crack systems determined by direct fracture measurements agreed with the direction of maximum velocity. Results of the present research were compared with the results of earlier measurements carried out in limestone and sandstone deposits located within the Polish Carpathians.

The existence of relationships between seismic wave velocity anisotropy and fracture parameters makes it possible to use seismic methods for determining the fracture density and the orientation of fracture systems.

### **1. Introduction**

Fracturing is one of elementary features which decide about many physical properties of rocks. Cracks have an essential influence on the elastic properties of rocks, especially on velocity of seismic waves propagation. This dependence, in the rock mass, was used in seismic methods for establishing the orientation and density of cracks. The results were compared with the orientations of cracks from direct measurements. Special attention has been paid to define the relationship between crack anisotropy and anisotropy of seismic waves velocity using interpretation methods based on tensor calculus.

Investigations were carried out in two quarries localized in the south part of Poland (Fig. 1). The first of studied deposits – Tertiary basalt – is located in Gracze quarry within the east part of the Sudetian Monocline. This deposit has the form of mild domed hill about 45 m high and having a shape of elongated irregular ellipse. The length of ellipse is about 1100 m and its width is about 250 m. The Tertiary sandstone and gravel cover the basalt deposit.

The second deposit investigated, the Permian diabase, is located in Niedźwiedzia Góra quarry within the Kraków-Częstochowa Upland. A syntectonic sill of hypersthene-quartz diabase intruded there the Upper Carboniferous clastic sediments.

Earlier measurements of seismic anisotropy were done within the Polish Carpathians (Stan and Idziak 2005). Objects of research were Devonian limestone (site 3) and also Cretaceous and Paleocene sandstone (sites 4 and 5).

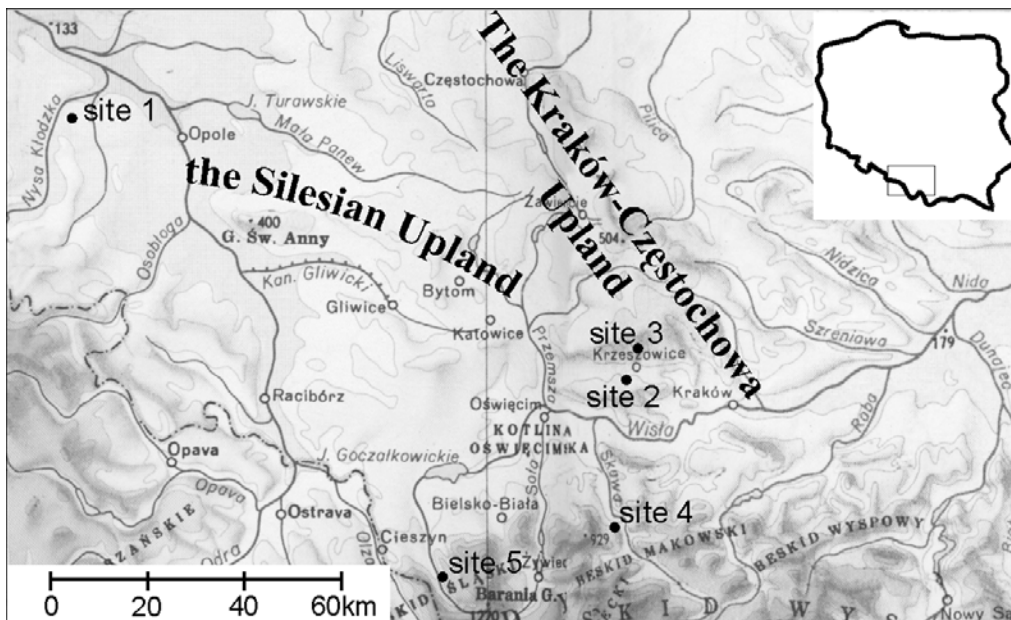


Fig. 1. Location of investigated rock mass: site 1 – basalt deposit, site 2 – diabase deposit, site 3 – limestone deposit, sites 4 and 5 – sandstone deposits.

## 2. Crack Tensor

The number and orientation of cracks in a rock mass are very important while considering the distribution and density of cracks. To give a mathematical definition for the crack geometry including all its elements, the tensor quantity called “the crack tensor” (Oda 1982, Oda *et al.* 1984, 1986) can be employed. Because it is not possible

to determine parameters of all the cracks existing in a rock mass, one has to estimate the crack tensor using mathematical expectation of crack parameters treated as random variables.

To estimate components of crack tensor, a statistical distribution of crack diameters,  $a$ , and orientation vectors  $\mathbf{n}$  normal to the crack plane must be known. The distribution is represented by a density function  $E(a, \mathbf{n})$  which satisfies the condition:

$$\int_0^{a_{\max}} \int_{\Omega} E(a, \mathbf{n}) da d\Omega = 1, \quad (2.1)$$

where  $\Omega$  is the solid angle corresponding to the entire surface of a unit sphere and  $a_{\max}$  is the maximum diameter of existing cracks.

Assuming the cracks are “penny shaped” and their crack aspect ratio  $\alpha = c/a$  is constant ( $c$  is the fracture aperture), the crack volume will be equal to:

$$v_c = \frac{1}{4} \pi \alpha a^3. \quad (2.2)$$

A bulk crack density is calculated from the formula:

$$N = \frac{K(V)}{V}, \quad (2.3)$$

where  $K(V)$  is the number of cracks in a rock mass of volume  $V$ . Crack density parameter  $\varepsilon$  can be introduced as a total crack volume in a rock volume unit:

$$\varepsilon = \frac{\sum_{i=1}^{K(V)} V_c^{(i)}}{V} = N \langle V_c \rangle = \frac{1}{4} \pi \alpha N \langle a^3 \rangle, \quad (2.4)$$

where  $\langle V_c \rangle$  is the expected value of crack volume. If we assume that only vertical cracks occur in rock mass, crack density parameter can be defined on the basis of surface density of crack traces on the plane perpendicular to the crack planes:

$$\varepsilon = \ell M \langle l^2 \rangle, \quad (2.5)$$

where  $M$  is the surface density of crack traces,  $\ell$  is a factor depending on the shape of crack and  $\langle l^2 \rangle$  is average square of crack trace length.

The crack density parameter can be estimated for the established crack model if we take into account the probability of cutting the measurement plane by crack plane. Let us consider a single crack system of identical parallel cracks of diameter  $a$ . The cracks form traces on the measurement plane if their centers are located at a distance  $r$

from the plane smaller than  $a/2$ . The probability  $dP$  that the crack plane cuts the measurement plane is:

$$dP = \frac{1}{C} dr, \quad (2.6)$$

where  $C$  is normalizing factor calculated from the equation:

$$C = \int_{-a/2}^{a/2} dr = a. \quad (2.7)$$

Distribution function of crack traces has the form:

$$P = \frac{1}{a} \int_{-a/2}^{a/2} dr. \quad (2.8)$$

The average square of crack traces length is given by:

$$\langle l^2 \rangle = \frac{1}{a} \int_{-a/2}^{a/2} l^2 dr = \int_{-a/2}^{a/2} (a^2 - 4r^2) dr = \frac{2}{3} a^3. \quad (2.9)$$

If the volume density of crack is  $N$ , the surface density of crack  $M$  is  $M = Na$ . The relationship between volume and surface parameters which describe the density of cracks is the following:

$$M \langle l^2 \rangle = \frac{2}{3} Na^3. \quad (2.10)$$

If instead of cracks of the same diameters, we consider the cracks of different diameters, which are characterized by distribution  $g(a)$ , then:

$$M \langle l^2 \rangle = \int_{a_{\min}}^{a_{\max}} \frac{2}{3} Na^3 g(a) da = \frac{2}{3} N \langle a^3 \rangle. \quad (2.11)$$

We can state, according to equation (2.4), that:

$$\langle \varepsilon \rangle = \frac{\pi\alpha N}{4} \langle a^3 \rangle = \frac{3\pi\alpha}{8} M \langle l^2 \rangle. \quad (2.12)$$

In the case of several crack systems of different orientation we can appoint the density of traces  $M_i$  and average square of crack trace length  $\langle l^2 \rangle_i$ , and we can calculate the total crack parameter:

$$\langle \varepsilon \rangle = \sum_i \frac{3\pi\alpha}{8} M_i \langle l^2 \rangle_i. \quad (2.13)$$

The crack tensor of rank  $k$  can be defined as:

$$\hat{F}^{(k)} = \langle \varepsilon \hat{A}^{(k)} \rangle , \quad (2.14)$$

where  $A$  is a random tensor variable of crack orientation obtained as the tensor product of unit vector  $\mathbf{n}$  normal to the principal plane of crack. Crack tensor can be estimated from the relation:

$$F_{ij\dots l} = \int_0^{a_{\max}} \int_{\Omega} a^3 \cdot n_i \cdot n_j \dots n_l \cdot E(a, \vec{n}) da d\Omega , \quad (2.15)$$

where  $n_i, n_j, \dots, n_l$  are directional cosines of vector  $\mathbf{n}$  in the assumed coordinate system.

The zero-rank tensor is equal to crack density parameter and has the physical sense of crack porosity. The tensor  $F_{ij\dots l}$  is invariant for the change of the sense of vector  $\mathbf{n}$ . This means that only the symmetric tensor whose rank is even has the non-zero components.

Two-dimensional crack tensor can be defined as:

$$\hat{F}^{(k)} = \frac{3\pi\alpha}{8} M \int_0^{l_m} \int_0^{2\pi} l^2 (n \otimes \dots \otimes n) dl d\phi , \quad (2.16)$$

where  $l$  is the length of crack trace on crack plane  $M$ .

When measuring the orientation and length of crack trace on plane  $S$ , we can estimate components of the crack tensor of rank  $k$ :

$$\langle F_{h_1\dots h_k} \rangle = \frac{\ell}{S} \sum_{i=1}^{N(S)} l_i^2 m_{h_1}^{(i)} \dots m_{h_k}^{(i)} , \quad (2.17)$$

where  $N$  is the number of crack traces on the area  $S$ ,  $l_i$  is the length of  $i$ -th trace,  $m_h^{(i)}$  is the directional cosine of the orientation vector of  $i$ -th crack and  $h_1 \dots h_k$  are 1 or 2.

When there is no correlation between the length of crack trace and its orientation, the components of  $\hat{F}$  tensor will be:

$$\langle F_{h_1\dots h_k} \rangle = \frac{\ell M \langle l^2 \rangle}{N(S)} \sum_{i=1}^{N(S)} m_{h_1}^{(i)} \dots m_{h_k}^{(i)} . \quad (2.18)$$

To estimate the crack tensor precisely, a large sample of crack population is needed ( $N > 150$ ).

### 3. Velocity Tensor

The velocity tensor was introduced to describe anisotropy of seismic wave velocity (Oda 1982, 1984). Tensor of rank  $k$  influencing the collection of unit directional vectors  $\mathbf{m}$  marks the  $k$ -rank surface in three-dimensional space. The equation describing this surface has the form:

$$u(\mathbf{m}) = V_{i_1 i_2 \dots i_k} \cdot m_{i_1} m_{i_2} \dots m_{i_k} \quad , \quad (3.1)$$

where  $m_{i_1}$  are the directional cosines of vectors  $\mathbf{m}$  and  $V_{i_1 i_2 \dots i_k}$  are the components of tensor  $\mathbf{V}$ .

Function  $u(\mathbf{m})$  can describe the position of wave front which propagates from point source after definite time  $t$ . For  $t = 1$  the distances are numerically equal to velocity of seismic wave in direction according to vector  $\mathbf{m}$ .

Calculations are simpler if the velocity tensor is non-dimensional. To underline the seismic anisotropy and elastic properties of rock, it is good to assume the function  $u(\mathbf{m})$  defined accordingly to the formula:

$$u(\mathbf{m}) = \left( \frac{v(\vec{m})}{v_0} \right)^2 \quad , \quad (3.2)$$

where the wave velocity  $v_0$  measured for the crack-free samples of rock can be used as a normalizing factor. Equation (3.2) expresses directional distribution of squared wave velocity. In the case of seismic refraction measurements, velocity tensor can be two-dimensional and can be calculated from velocity measurements in  $N$  independent directions. The tensor components are calculated from the set of equations:

$$\left( \frac{v_p}{v_0} \right)^2 = V_{i_1 i_2 \dots i_k} \cdot m_{i_1}^{(p)} m_{i_2}^{(p)} \dots m_{i_k}^{(p)} \quad p = 1, 2 \dots N \quad (3.3)$$

using the least square method.

In case of analysis of velocity changes, the velocity distribution on measurement plane can be defined as:

$$\left( \frac{v}{v_0} \right)_\phi^2 = V_{11} \cos^2 \phi + 2V_{12} \cos \phi \sin \phi + V_{22} \sin^2 \phi \quad , \quad (3.4)$$

where  $\phi$  is the azimuth of wave vector, and  $V_{11}$ ,  $V_{12}$ ,  $V_{22}$  are the components of symmetrical two-dimensional velocity tensor.

#### 4. Experimental Study

Studying the relationship between seismic anisotropy and cracks anisotropy in basalt and diabase, we were only interested in fractures perpendicular to the layering. This allowed us to calculate two-dimensional crack tensors and velocity tensors in planes parallel to the layer surface. The rocks under study are fractured with different fracture densities, depending on rock ages and conditions in which they are formed. Several predominant fracture systems were observed in every quarry under study (Figs. 2 and 3).

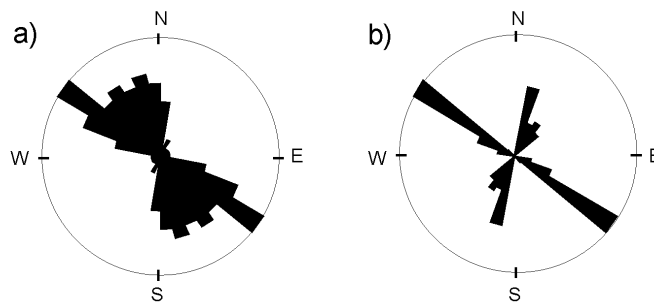


Fig. 2. Rose diagrams of strike directions of cracks: (a) site 1, (b) site 2.

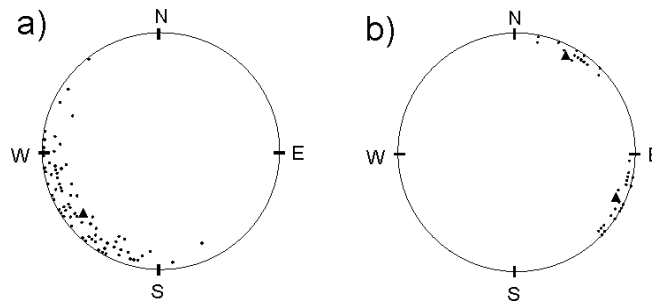


Fig. 3. Point diagram of crack orientations (dots) with distinguished resultant vectors (triangle): (a) site 1, (b) site 2.

Resultant azimuths of observed fracture sets calculated by the ROCKWORK computer program are presented in Table 1.

Seismic measurements were made in the same quarries where the fracture data were obtained. The research was made along precisely oriented radial seismic profiles. The first break times of P-waves were read from the recorded seismograms. Besides the P-waves, also the S-waves were identified on the seismograms.

Table 1

The main fracture system orientations

Investigated area	Predominant fracture sets	Mean strike azimuth of the set
site 1	SE-NW	144°
site 2	NNE-SSW SE-NW	24° 118°

Wave velocities were calculated from a slope of rectilinear refraction hodographs. The obtained P-wave and S-wave velocity data were used for calculating the velocity tensors. The spatial distributions of cracks and velocity data were compared.

## 5. Results

In the investigated rocks, relationships between velocity and azimuth of seismic profile were determined (Figs. 4 and 5). The distribution of seismic wave velocity characterizes the occurrence of some maximum velocity directions which are similar to the resultant direction of the main crack system obtained from direct fracture measurements.

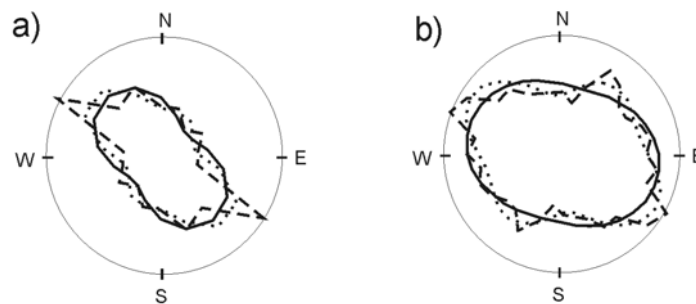


Fig. 4. The relationship between azimuth of seismic profile and measured P-wave squared velocity (solid line), velocity distribution based on the tensor of rank two (dashed line) and on the tensor of rank four (dotted line): (a) site 1, (b) site 2.

The resultant strike azimuth of separated vertical crack systems assigned from the direct fracture measurements are in good agreement with the directions of maximum velocity for basalt deposit occurring in site 1 (Fig. 6a) and diabase deposit (Fig. 6b). The small differences are related to the precision of measurements. The direct measurements were carried out using geological compass with precision which takes two degrees whereas the azimuths of radial seismic profiles differed from themselves by ten degrees.

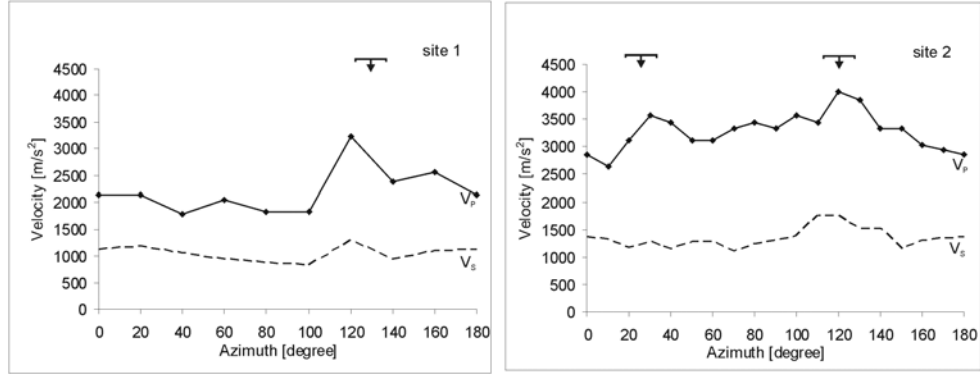


Fig. 5. The relationship between azimuth of seismic profile and measured S-wave squared velocity (solid line), velocity distribution based on the tensor of rank two (dashed line) and on the tensor of rank four (dotted line): (a) site 1, (b) site 2.

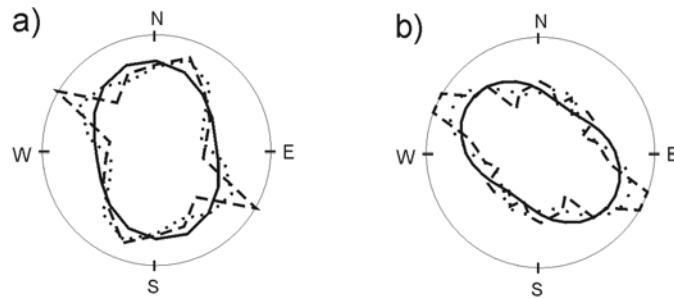


Fig. 6. Comparison of azimuth of maximum P-wave and S-wave velocity directions and resultant strike azimuth of crack systems: (a) site 1, (b) site 2.

The results of seismic wave velocity measurements were used to calculate two-dimensional velocity tensors which were calculated from the set of equations (3.4) using least squares method. The values of maximum P- and S-wave velocity were used as normalizing factors because there were no data of seismic wave velocity in unfractured rock mass. The eigenvalues and eigenvectors of tensors of rank 2 were determined. The degree of seismic anisotropy and azimuth of main tensor axes were calculated on the base of eigenvalues and eigendirections. The fourth rank tensor components were calculated to describe the directions of local velocity maxima showing direction of crack systems in the rock mass. The results of calculations for P and S waves are shown in Table 2 (see also Figs. 4 and 5).

Table 2  
Characteristic values of second rank velocity tensors

Investigated area	The kind of wave	Eigenvalues		Azimuth of tensor axis		Mean values	Anisotropy factor
		max	min	longer	shorter		
site 1	P	0.685	0.291	138°	48°	0.488	0.404
	S	0.777	0.517	170°	80°	0.647	0.201
site 2	P	0.817	0.563	105°	15°	0.690	0.184
	S	0.758	0.437	124°	34°	0.597	0.269

From the geological data of fractures aperture, spacing and orientation, crack tensor could not be calculated at full for investigated rocks because there was no correlation between length and opening of cracks. This made it impossible for us to establish crack density parameters dependent on geometrical parameters. We only succeed in defining the part of crack tensor characterising spatial distribution of cracks basing on rose diagrams of crack orientation (Fig. 7). The results of calculations of the crack tensor components are shown in Table 3.

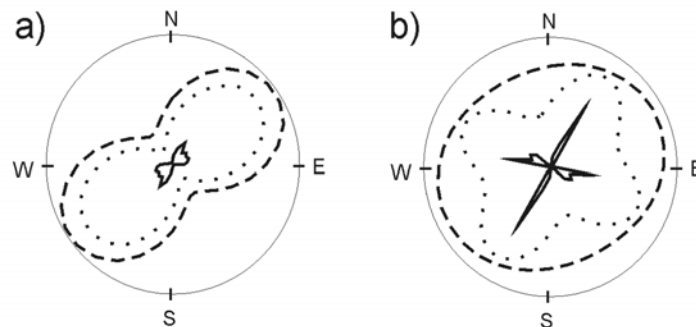


Fig. 7. Spatial distribution of cracks based on rose diagrams of crack orientation (solid line), spatial distribution based on the tensor of rank two (dashed line) and on the tensor of rank four (dotted line): (a) site 1, (b) site 2.

Table 3  
Characteristic values of second rank crack tensors

Investigated area	Eigenvalues		Azimuth of tensor axis		Mean values	Anisotropy factor
	max	min	longer	shorter		
site 1	0.782	0.218	54°	144°	0.500	0.563
site 2	0.548	0.563	63°	153°	0.500	0.096

## 6. Discussion

Similar studies were carried out for limestone and sandstone deposits located within Polish Carpathians (Stan and Idziak 2005). On the whole area, one predominant fracture orientation SE-NW was observed. In sites 3 and 5, NE-SW oriented crack system was observed. In site 5 the third SSE-NNW oriented crack system exists. Two other predominant crack systems existing in site 4 are N-S and W-E oriented.

In all sites seismic anisotropy is strongly connected to the orientation of the crack systems (Table 4).

Table 4

Azimuth of maximum P-wave velocity directions and resultant strike azimuth of crack systems for sites 3, 4 and 5.

Investigated area	Fracture orientation	Azimuth of maximum P-wave velocity	Average strike azimuth of crack system
site 3	SE-NW	140°	152°
	NE-SW	40°	30°
site 4	N-S	350°	355°
	W-E	90°	91°
	SE-NW	130°	135°
site 5	NE-SW	40°	45°
	SE-NW	140°	130°
	SSE-NNW	160°	–

The comparison of crack tensor calculated for limestone deposit with velocity tensor showed that the axes of both tensors are similarly oriented. The longer axis of crack tensor is rotated by 90° in relation to the longer axis of velocity tensor (Table 5). The accordance of tensor axes for the P-wave is bigger than for the S-wave.

Table 5

The comparison of crack tensor with velocity tensor for basalt deposit (site1), diabase deposit (site 2) and limestone deposit (site 3)

Investigated area	The kind of wave	Azimuth of velocity tensor axis		Azimuth of crack tensor axis	
		longer	shorter	longer	shorter
site 1	P	138°	48°	54°	144°
	S	170°	80°		
site 2	P	105°	15°	63°	153°
	S	124°	34°		
site 3	P	59°	149°	142°	52°
	S	66°	156°		

The obtained results show that it is possible to notice an empirical relationship between orientation of both tensors and their average parameters of isotropy and anisotropy for studied rocks.

The present research showed the similar dependence between velocity tensor and crack tensor for basalt deposit occurring in site 1. Distinct correlation between second rank velocity tensor and second rank crack tensor is not observed in site 2. The correlation is not observed because the crack tensor is calculated for two perpendicular crack systems having similar density of fractures. In that case, the second rank velocity tensor generalizes the course of both crack systems and only the fourth rank crack tensor represents the directions of both crack systems and correlates with the fourth rank velocity tensors (Figs. 4, 5 and 7).

## 7. Conclusion

Decomposition of seismic wave velocity characterizes the occurrence of maximal velocity direction, which agrees with main crack systems direction.

The theory of seismic wave propagation in fractured rock mass predicts that the axes of velocity tensor should be rotated by  $90^\circ$  in relation to the axes of crack tensor, when we neglect non-linear effects connected with wave propagation in fracturing centre.

The obtained results for site 1 confirm that the directions of major axes of second rank velocity tensor prove the relationship consistent with predictions of the model. In the case of site 2 we have to consider the crack tensor of rank four and velocity tensor of the same rank because two perpendicular crack systems existing in this deposit cause more complex anisotropy of the rock mass.

## References

- Oda, M., 1982, Fabric tensor for discontinuous geological materials, *Soils Fdns.* **22**, 4, 96-108.
- Oda, M., 1984, Similarity rule of crack geometry in statistically homogeneous rock masses, *Mech. Mater.* **3**, 119-129.
- Oda, M., K. Suzuki and T. Maeshibu, 1984, Elastic compliance for rock-like materials, *Soils Fdns.* **24**, 3, 27-40.
- Oda, M., T. Yamabe and K. Kamemura, 1986, A crack tensor and its relation to wave velocity anisotropy in jointed rock masses, *Int. J. Rock Mech. Min. Sci. Geomech. Abstr.* **23**, 6, 387-397.
- Stan, I., and A.F. Idziak, 2005, *Anisotropy of seismic wave velocity due to the fracturing in chosen rock mass*. In: P. Konecny (ed.), „Impact of Human Activity on the Geological Environment”, Balkema Publishers, Leiden-London, 579-586.

*Accepted 10 April 2006*

## **Calculation of Block Divisibility Using Structural and Refraction Seismic Methods in Dębnik and Imielin Raw Material Deposits**

Zbigniew MIRKOWSKI, Radosława TOMASZEWSKA and Adam IDZIAK

University of Silesia, Faculty of Earth Sciences, Department of Applied Geology  
ul. Będzińska 60, 41-200 Sosnowiec, Poland

### **A b s t r a c t**

The structural research was done in the Silesian-Kraków Upland in two open-cuts of building stone: Dębnik (limestone) and Imielin (dolomite). As a result of the investigations, the directions of fracture systems were delineated and block divisibility was calculated, as principal parameters in the documentation of building stone.

Simultaneously, geophysical methods were applied using shallow seismic refraction. According to the azimuthal velocity of wave propagation, the orientation of fracture was estimated. In Dębnik a strong anisotropy of seismic waves occurred and there was an excellent correlation between structural and seismic measurements, whereas in Imielin this correlation was rather weak, which was probably caused by using explosives for mining in the open-cut. The calculation of block divisibility using a seismic method was not possible in this case.

### **1. Description of Research Area**

Dębnik and Imielin raw material deposits are situated in the southern part of the Silesian-Kraków Upland. They belong to different structural formations: the Dębnik anticline which is built of Paleozoic deposits of the Kraków-Lubliniec zone, and the Imielin monocline, which includes the Mesozoic formation of the Kraków-Częstochowa Monocline (Fig. 1). The Dębnik deposit is composed of dark grey to black Devonian limestone, mostly granulated as well as crumbly and pelitic limestones with wavy beds (Bednarczyk and Hoffman 1989). Dębnik limestones (Dębnik “marble”) were used as famous and prized decorative building stones for a few centuries. At present, the quarry in Dębnik village is idle, though some blocks of stone are sometimes manually excavated. The Imielin deposit is composed of yellow and grey Triassic dolomite which is a massive and fine-grained structure (Smulikowski 1946).

The open-cut in Imielin works and it is a significant producer of crushed stone. In the past, blocks of stone were occasionally excavated at this site.

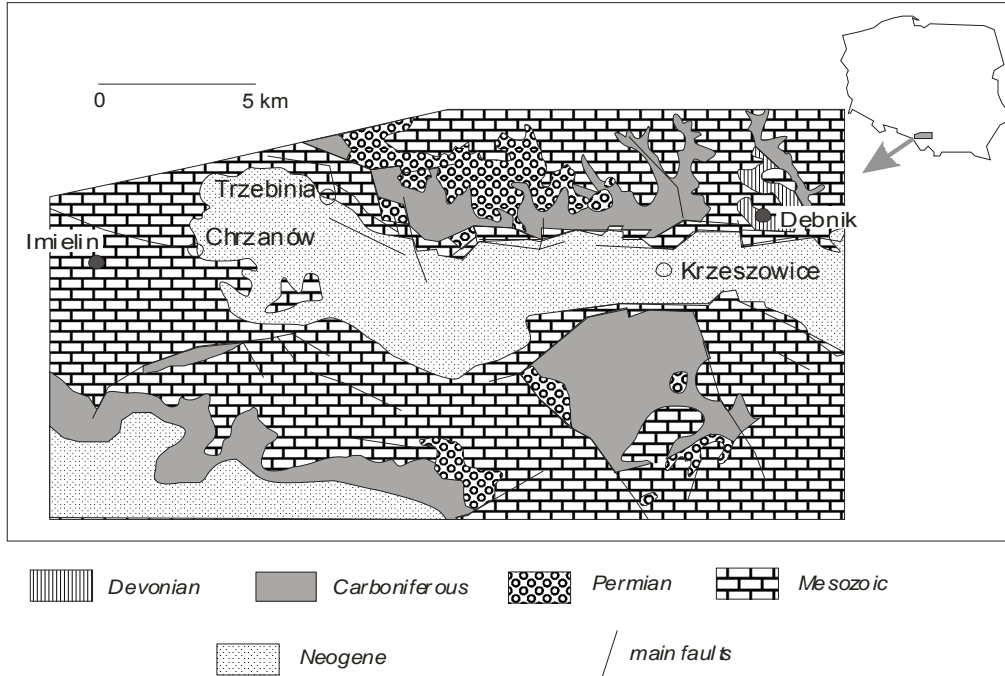


Fig. 1. The geological map of the Silesian-Kraków region with measurement site locations (after Gradziński 1972).

## 2. Block Divisibility and Structural Measurements

The definition of block divisibility has two meanings – in a geological and a mining sense (PN-88/B-04120). Geological block divisibility is characterized by rock materials in an outcrop or a bore-hole profiles. Mining block divisibility is the output of stone blocks in all materials excavated in an open-cut. Mining block divisibility is a principal parameter for using rocks as a building stone and is applied in geological documentation of the deposits. Block divisibility is calculated according to structural measurements using the formula (Bromowicz and Karwacki 1982):

$$b = P_x \cdot P_y \cdot P_z \cdot 100\%$$

where  $P_x$ ,  $P_y$ , and  $P_z$  are the probabilities that  $x$ -,  $y$ - and  $z$ -dimensions are higher than or equal to the limit. The dimension probabilities are shown in the diagram of cumulated frequency. When the three main fracture sets are not perpendicular to each other (blocks are non-orthogonal) the correction coefficient must be used:

$$k = f(d, \beta)$$

where  $d$  is the form index and  $\beta$  is the angle deviation.

The structural measurements were done by using a compass along a perpendicular line on the wells of the open-cut. In the Dębnik deposit two main fracture sets were observed: A – in azimuth range of  $130\text{-}160^\circ$  (average  $144^\circ$ ) and B –  $30\text{-}80^\circ$  (Fig. 2). The fracture of the B-set is composed of two secondary sets of fractures:  $B_1$  –  $30\text{-}40^\circ$  (average  $32^\circ$ ) and  $B_2$  –  $50\text{-}80^\circ$  (average  $63^\circ$ ). This is a typical case for anticlinal forms. Dimensions of the average block from this deposit were  $121\text{ cm} \times 127\text{ cm} \times 57\text{ cm}$  and the volume of this block was  $0.88\text{ m}^3$ . In the Dębnik deposit, blocks of stone have a non-orthogonal shape, so in this case a correction coefficient must be used and thus the block volume is  $0.6\text{ m}^3$ . The marginal volume of the block for this type of limestone established by Polish standard PN-B-11200 is  $0.25\text{ m}^3$ . The block divisibility in Dębnik is equal to 41%.

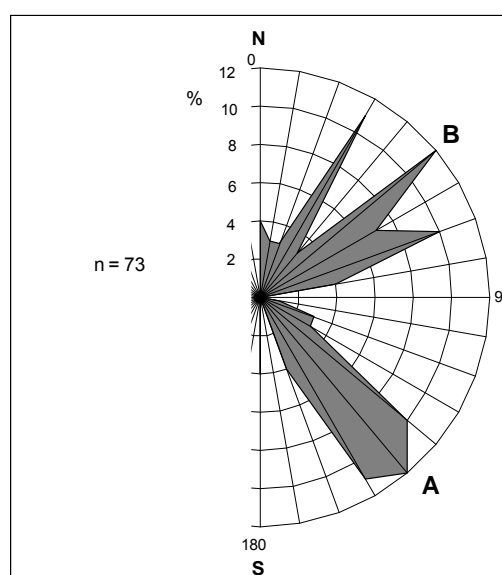


Fig. 2. Rose-diagram of fractures in the Dębnik deposit.

In the Imielin deposit two distinct directions of fracture occurred:  $120\text{-}160^\circ$  (average  $144^\circ$ ) – system A and  $40\text{-}80^\circ$  (average  $53^\circ$ ) – system B (Fig. 3). The block from this deposit has average dimensions of  $134\text{ cm} \times 132\text{ cm} \times 124\text{ cm}$  and its volume is  $2.2\text{ m}^3$ . The marginal volume of the block for dolomite is  $0.3\text{ m}^3$  (PN-B-11200). In the Imielin deposit, block divisibility is equal to 84%.

### 3. Method and Analysis of Seismic Measurements

Seismic measurements were performed using a Terraloc MK6 (ABEM) seismograph. Measurement points were set up inside the quarry in Dębnik and outside the open-cut in Imielin. The oriented profiles were 36 m long in Dębnik and 44 m long in Imielin. The seismic waves were induced using a hammer. Shot-points were located at the initial, central and final points of the measuring profile. After each measurement cycle the profile was rotated by  $20^\circ$ .

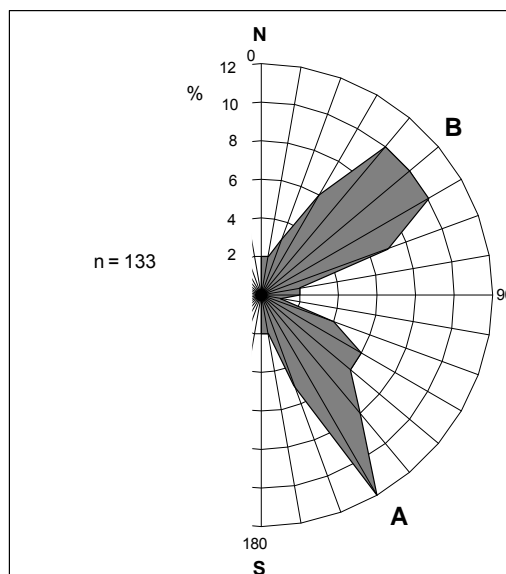


Fig. 3. Rose-diagram of fractures in the Imielin deposit.

As a result of seismic measurements the values of the seismic wave velocity ( $V_p$  and  $V_s$ ) were interpreted for each profile (Table 1). In the Dębnik deposit, wave velocity varied and the maximum of  $V_p$  (2626 m/s) was obtained for profile direction of  $40^\circ$ , whereas the maximum of  $V_s$  (1726 m/s) was at  $60^\circ$ . The velocities of seismic waves in Imielin are considerably less than in Dębnik, the maximum of  $V_p$  (1462 m/s) was at  $60^\circ$  and  $V_s$  (940 m/s) was at  $40^\circ$ .

Table 1

Velocities of seismic waves in the Dębnik and Imielin deposits  
( $V_p$  – velocity of longitudinal wave,  $V_s$  – velocity of distortional wave)

Azimuth	Dębnik		Imielin	
	$V_p$ [m/s]	$V_s$ [m/s]	$V_p$ [m/s]	$V_s$ [m/s]
$0^\circ$	2372	1328	1218	744
$20^\circ$	1978	1018	1346	706
$40^\circ$	2626	1466	1424	940
$60^\circ$	2406	1726	1462	876
$80^\circ$	2520	1228	1390	888
$100^\circ$	1958	1130	1296	732
$120^\circ$	2170	1476	1184	782
$140^\circ$	2224	1252	1068	548
$160^\circ$	1412	992	1158	778

The velocity of wave propagation is strongly determined by direction of fractures in the rock mass and this phenomenon has been described in many papers (i.e., Crampin 1976; Oda 1984; Marcak and Mortimer 1986; Idziak 1988, 1992). The maximum velocities of seismic waves conform to the main directions of set fractures. Thus, in Dębnik (Fig. 4) three strong maxima of velocity of seismic wave (of  $V_p$  in particular) occurred, that conform to the three main directions of fractures:  $40^\circ$ ,  $80^\circ$  and  $140^\circ$ . A comparison of these directions with the orientation of fracture obtained as a result of structural measurements indicates their good correlation. In Imielin the anisotropy of seismic waves is much weaker and there is only one indistinct maximum at the point of azimuth  $60^\circ$  (Fig. 5). This maximum can be correlated with only one fracture set obtained from the structural measurements. Using explosives for mining in the quarry is possibly the main reason for the poor result of seismic investigations in the Imielin deposit because of the occurrence of additional, randomly oriented cracks.

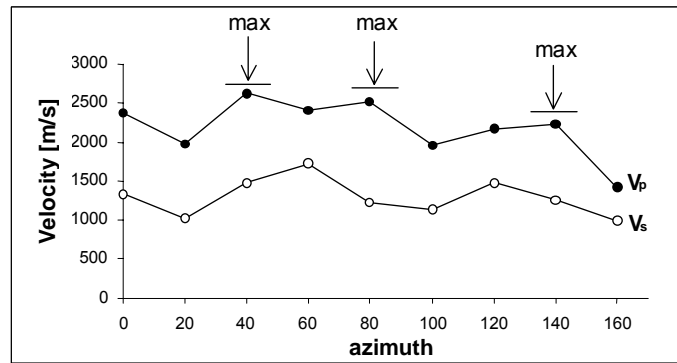


Fig. 4. Azimuthal distribution of seismic wave velocity [m/s] in Dębnik deposit ( $V_p$  – velocity of longitudinal wave,  $V_s$  – velocity of distortional wave).

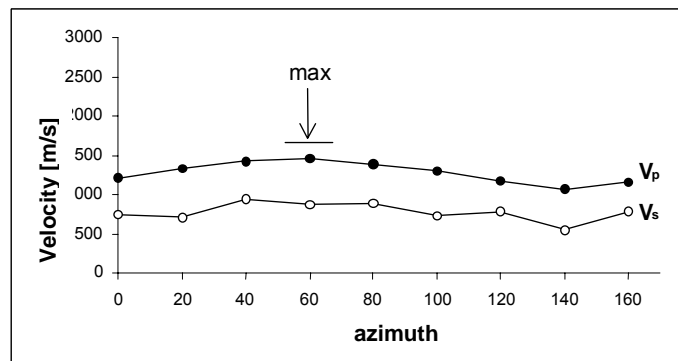


Fig. 5. Azimuthal distribution of seismic wave velocity [m/s] in Imielin deposit ( $V_p$  – velocity of longitudinal wave,  $V_s$  – velocity of distortional wave).

An application of the seismic refraction method to the calculation of block divisibility in these cases is not possible. The calculation of block divisibility is applica-

ble only when the fracture system is orthogonal and measurements of the linear density of fractures along the line for many different directions are made. The above conditions in Dębnik and Imielin were not suitable. As a result of a comparison of the velocity of seismic waves and the linear density of fractures it is possible to create the functions that allow us to approximately calculate the block divisibility index (Badera et al. 2005).

#### 4. Conclusions

In the investigated deposits, a good correlation of structural and seismic measurements was observed. In the Dębnik deposit the maximum of azimuthal distribution of seismic wave velocity (particularly the velocity of the longitudinal wave) is consistent with the measurement of the bearing of the strike of the main fracture. Unfortunately, in the Imielin deposit the anisotropy of the seismic wave is not strong and its correlation is less precise.

The analysis of block divisibility using the seismic method is not good for this case. The calculation of block divisibility using this method may be possible but it must be made on the ground of the linear density of the fracture. Unfortunately, the result of this calculation is approximate. The seismic refraction method is very suitable for indicating the fracture systems before cutting a new portion of the deposit.

#### References

- Badera, J., S. Niemczuk and R. Tomaszewska, 2005, *The use of shallow refraction seismic method for analysis of block divisibility of the Carpathian sandstones in the "Górka-Mucharz" deposit* (in print).
- Bednarczyk, J., and M. Hoffmann, 1989, *Wapień dębnickie*. In: J. Rutkowski (red.), „Przewodnik LX Zjazdu PTG”, Wyd. AGH, Kraków.
- Bromowicz, J., and A. Karwacki, 1982, *Metodyka badań bloczności złóż budowlanych materiałów kamiennych [English summary]*, Zeszyty Nauk. AGH, Geologia **8**, 2, 51-76.
- Gradziński, R., 1972, *Przewodnik geologiczny po okolicach Krakowa*, Wyd. Geol. Warszawa.
- Crampin, S., 1978, *Seismic wave propagation through a cracked solid: polarization as a possible dilatancy diagnostic*, Geophys. J. R. Astr. Soc. **53**, 467 – 496.
- Idziak, A., 1988, *Seismic wave velocities in fractured sedimentary Carbonate rocks*, Acta Geophys. Pol. **36**, 2, 101-114.
- Idziak, A., 1992, *Anizotropia prędkości fal sejsmicznych i jej związek z orientacją systemów spękań masywów skalnych [English summary]*, Prace Nauk. Uniw. Śląskiego 1328, Katowice.
- Marcak, H., and Z. Mortimer, 1986, *Modele związków prędkości fal sejsmicznych ze stopniem szczelinowatości górotworu*, Publ. Inst. Geophys. Pol. Acad. Sci. **191**, 39-51.
- Oda, M., 1984, *Similarity rule of crack geometry in statistically homogenous rock masses*, Mech. Mater. **3**, 119-129.

- Smulikowski, K., 1946, *O dolomicie z Imielina na Górnym Śląsku*, Roczn. PTG t.16.
- Polish standard PN-B-11200, 1996, *Materiały kamienne. Bloki, formaki, płyty surowe*, PKN, Warszawa. Polish standard PN-88/B-04120, 1988, *Kamień budowlany. Podział, pojęcia podstawowe, nazwy i określenia*, PKN, Warszawa.

*Accepted October 16, 2006*



## **Application of the Shallow Refraction Seismic Method for Analysis of Block Divisibility of Carpathian Sandstones in the Górk-Mucharz Deposit**

Jarosław BADERA, Sławomir NIEMCZUK and Radosława TOMASZEWSKA  
University of Silesia, Faculty of Earth Sciences, Department of Applied Geology  
ul. Będzińska 60, 41-200 Sosnowiec  
e-mail: jbadera@wnoz.us.edu.pl

### **Abstract**

The application of the shallow refraction seismic method for analysis of block divisibility of natural building stone is presented for an example of the Górk-Mucharz sandstone deposit (Polish Carpathians). Geological block divisibility is a relative participation of the block material in a deposit, profile etc. The applied method reflects the main fracture directions to the satisfactory degree but the estimation of fracture linear density has only an approximate character. The authors suggest the possibility to set the volume of average block as an additional (geophysical) index of the block divisibility.

### **1. Location and Geological Structure of the Deposit**

The Górk-Mucharz deposit (Fig. 1) is located in the Mucharz village, south of Wadowice, in the eastern part of the Beskid Mały Mts. (Western Carpathians). It consists of the Paleogene sandstones of the Lower Krosno beds belonging to the Silesian nappe (Outer Carpathians). There are four sandstone complexes in the deposit (Znańska 1974). Their total thickness is about 60 m and they dip slightly toward the NE at an angle of 0-6°. The raw material (a natural building stone for blocks and slabs) is excavated by a quarry with five exploitation levels which reflect the complexes mentioned above.

### **2. Block Divisibility**

The block material is defined as blocks of raw material with a subrectangular shape and volume higher than a minimal limit. For example, the marginal size for sandstones is 0.5 m<sup>3</sup> (according to the Polish standard PN-B-11200).



Fig. 1. Schematic geological map of the Carpathians in the Skawa valley region (Książkiewicz 1972).

The block divisibility can be considered as a geological or mining one (according to the Polish standard PN-88/B-04120).

The geological block divisibility is a relative participation of block material in a deposit, profile etc. The mining block divisibility is a participation of extracted blocks in the total excavation. For economic deposits of block sandstones, the geological block divisibility should be equal to at least 20% (Nieć 1994). In the case of geological documentation, the block divisibility index is the most often used measure. It is calculated according to the formula (Bromowicz and Karwacki 1982):

$$b = P_x \cdot P_y \cdot P_z \cdot 100\%,$$

where  $P_x$ ,  $P_y$  and  $P_z$  are probabilities that  $x$ -,  $y$ - and  $z$ -dimensions are higher or equal to the limit. They are estimated on the basis of the cumulated frequency diagrams. In the case of non-orthogonal systems, the minimum values of  $x$ ,  $y$  and  $z$  must be increased by a linear correction coefficient:

$$k = f(d, \beta),$$

where  $d$  is the form index and  $\beta$  is the angle deviation.

### 3. Structural Analysis

Structural measurements made by means of a compass in a fragment of the quarry and then analysed within the *RockWorks* program reveal the presence of two distinct sets of fractures (Fig. 2). The resultant vector of strike is  $101^\circ$  for the sublongitudinal set (A) and  $41^\circ$  for the subtransversal one (B).

The linear density of fractures was calculated for measuring lines traced along an exploitation wall and differing in the azimuth (Table 1).

In the studied fragment of deposit, the block divisibility is significant. It is 96% for  $x$ -,  $y$ - and  $z$ -dimensions equal to at least 0.8 m.

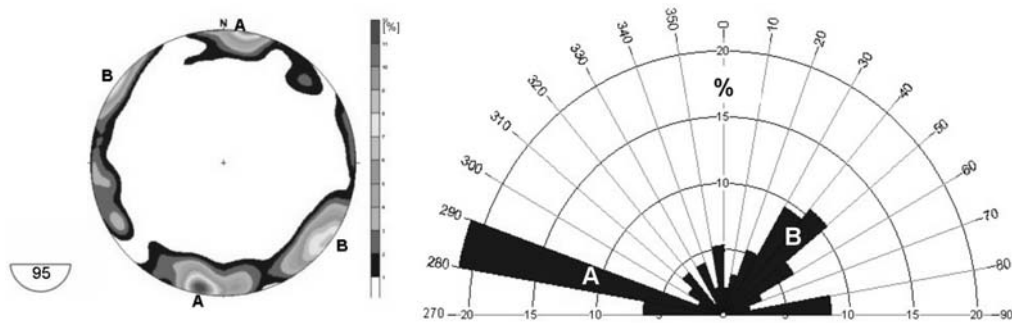


Fig. 2. Orientation of the fractures in the Górk-Mucharz deposit: *left* – contour scheme, *right* – fracture rose (strikes); the main set of fractures: A – sublongitudinal, B – subtransversal; diagrams made within the *RockWorks* program.

Table 1

Linear density of fractures according to different directions of profiles in the Górk-Mucharz deposit

Azimuth of profiles	Linear density of fractures [fr./m]
0°	1,04
20°	0,49
30°	0,57
70°	0,44
80°	0,40
90°	0,21
110°	0,51
140°	0,79
150°	0,70
160°	0,61

#### 4. Seismic Analysis

Seismic measurements were done in accordance with the widely known methodology (Reynolds 1997) using an Terraloc MK6 (ABEM) along profiles, azimuths of which changed every 20° around a common central point (Fig. 3). Seismic waves were induced in the central point and at the ends of measuring lines. The total length of profiles was 40 m and geophones were situated every 4 m. A similar scheme of measuring station has already been applied during other researches of anisotropy in rock massives (for example Idziak 1992). The measuring data were afterwards converted with the *WinSism 9.0 GeoSoft* program.

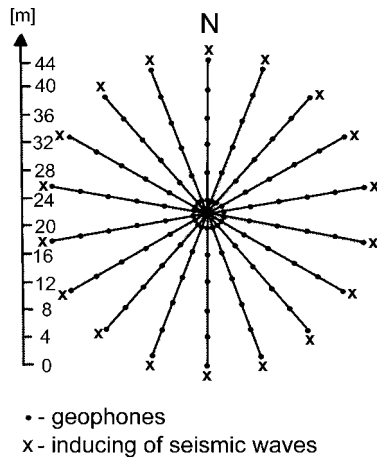


Fig. 3. Scheme of the measuring station in the Górká-Mucharz deposit.

The velocities of seismic waves calculated on the basis of non-cracked rock samples from Mucharz (Dziedzic 2003) are  $V_{op} = 4031$  m/s for longitudinal wave (P) and  $V_{os} = 2698$  m/s for transversal wave (S). The velocities of P and S seismic waves calculated “in situ” for the studied massive are obviously lower and change according to the azimuth of profiles (Table 2). They have been recounted in relation to the velocities in non-cracked samples and raised to the second power to emphasize differences in particular directions.

Table 2

Anisotropy of velocities of seismic waves in the Górká-Mucharz deposit

Azimuth	$V_P$ [m/s]	$V_P/V_{op}$	$(V_P/V_{op})^2$	$V_S$ [m/s]	$V_S/V_{os}$	$(V_S/V_{os})^2$
0°	2158	0.539	0.291	1418	0.523	0.273
20°	2430	0.607	0.369	1476	0.544	0.296
40°	2738	0.684	0.468	1916	0.706	0.499
60°	2576	0.644	0.414	1868	0.689	0.474
80°	2512	0.628	0.394	1522	0.561	0.315
100°	2780	0.695	0.483	2040	0.752	0.566
120°	2266	0.566	0.321	1142	0.421	0.177
140°	2302	0.575	0.331	1306	0.482	0.232
160°	2294	0.573	0.329	1372	0.506	0.256

## 5. Seismic Analysis vs. Structural Data and Block Divisibility

The phenomenon of seismic wave propagation through fractured rock-masses and models describing this process have been the subject of investigation for many

years (Crampin 1976, Oda 1984, Marcak and Mortimer 1986, Idziak 1988 and 1992). In the examined case the comparison of structural and geophysical data shows (Fig. 4) that seismic waves reach maximum velocities in the directions of minimum density of fractures (maximum density of fractures clockwise rotated by  $90^\circ$ ) i.e. in accordance with strikes of the main fracture sets. It is consistent with the results of some previous investigations (for example Idziak 1988, 1992).

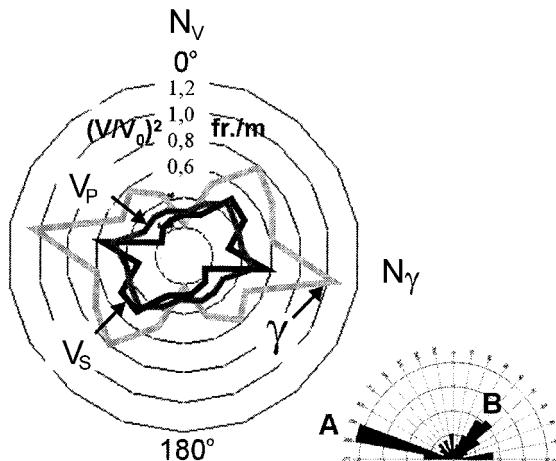


Fig. 4. Azimuthal distribution of velocities of seismic waves and linear density of fractures.  $V_P$  – velocity of longitudinal wave,  $V_S$  – velocity of transversal wave,  $\gamma$  – linear density of fractures clockwise rotated by  $90^\circ$ , A and B – the main fracture sets.

Functional interdependences between the linear density of fractures and the velocities of P and S seismic waves were calculated by means of the empirical data (Fig. 5). Involution functions approximate the empirical data in the best possible degree but absolutely high determination ( $R^2$ ) and statistical validity ( $\alpha = 0.95$ ) were obtained only for the P waves.

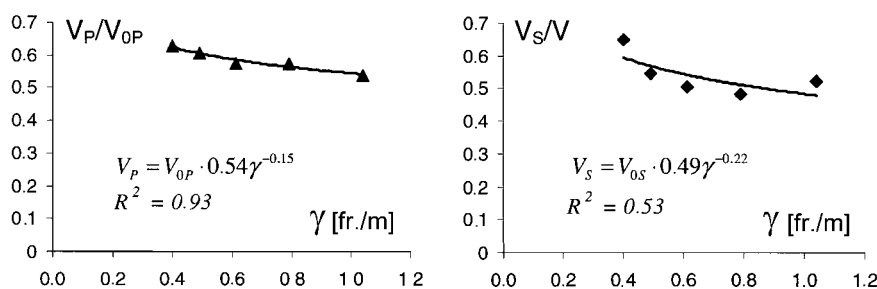


Fig. 5. Relationships between velocities of seismic waves and linear density of fractures.

One can assume that the most significant minimums of P-wave velocity ( $V_{Pmin1}$ ,  $V_{Pmin2}$ ) correspond with the highest densities of fractures ( $\gamma_{max1}$ ,  $\gamma_{max2}$ ), i.e., the average densities of the main fracture sets ( $\gamma_A$ ,  $\gamma_B$ ). Thus, the volume of an average subrectangular block limited by three fracture sets can be characterized by the following function:

$$b_{vg} = f(\gamma_A, \gamma_B, \gamma_C, k),$$

where (after transformations of formulas from Fig. 5):

$$\gamma_{A(\max 1)} = 0.0165^{0.15} \sqrt{\frac{V_{0P}}{V_{P\min 1}}},$$

$$\gamma_{B(\max 2)} = 0.0165^{0.15} \sqrt{\frac{V_{0P}}{V_{P\min 2}}},$$

$\gamma_C$  is the thickness of rock beds valued from drill-cores or outcrops,  $k$  is a linear correction coefficient.

However, there is no direct translation on the block divisibility index, and that is why the authors suggest the possibility of setting the volume of an average block ( $b_{vg}$ ) as an additional (geophysical) index of the block divisibility. In the case of the Górká-Mucharz deposit,  $b_{vg}$  amounts to  $4.1 \text{ m}^3$  – therefore, it is considerably more than the limit.

## 6. Conclusions

1. The refraction seismic method reflects the main fracture directions in Carpathian sandstones to a satisfactory degree. Velocities of seismic waves are the highest in the directions of strike of the main fracture sets.

2. The estimation of fracture linear density shows only an approximate character. However, it seems that empirical functions calculated on the basis of P seismic wave are more precise and can be useful in the case of a simple orthogonal fracture system.

3. The described method allows calculations of sizes of the average block, but there is no direct translation on the block divisibility index. The authors suggest the possibility of setting the volume of an average block as an additional (geophysical) index of the block divisibility.

## References

- Bromowicz, J., and A. Karwacki, 1982, *Metodyka badań bloczności złóż budowlanych materiałów kamiennych* (English summary), *Zeszyty Nauk. AGH, Geologia* **8**, 2, 51-76.
- Crampin, S., 1978, *Seismic wave propagation through a cracked solid: polarization as a possible dilatancy diagnostic*, *Geophys. J. R. Astr. Soc.* **53**, 467-496.
- Dziedzic, A., 2003, *Structural control on fracture toughness (brittle cracking) in the Krosno sandstone of Mucharz, southern Poland*, *Geol. Quart.* **47**, 1, 21-28.
- Idziak, A., 1988, *Seismic wave velocities in fractured sedimentary carbonate rocks*, *Acta Geophys. Pol.* **36**, 2, 101-114.

- Idziak, A., 1992, *Anizotropia prędkości fal sejsmicznych i jej związek z orientacją systemów spękań masywów skalnych* (English summary), Prace Nauk. Uniw. Śląskiego 1328, Katowice.
- Książkiewicz, M., 1972, *Budowa geologiczna Polski t. IV, Tektonika cz. 3, Karpaty*, Wydawnictwa Geologiczne, Warszawa.
- Marcak, H., and Z. Mortimer, 1986, *Modele związków prędkości fal sejsmicznych ze stopniem szczelinowatości górotworu*, Publ. Inst. Geophys. Pol. Acad. Sci. **191**, 39-51.
- Nieć, M. (ed.), 1994, *Zalecane kryteria bilansowości złóż kopalin*, Min. Środ., Kom. Zasobów Kop., Warszawa.
- Oda, M., 1984, *Similarity rule of crack geometry in statistically homogenous rock masses*, Mech. Mater. **3**, 119-129.
- Reynolds, J.M., 1997, *Seismic refraction surveying*, In: *An Introduction to Applied and Environmental Geophysics*, John Wiley & Sons, Chichester.
- Znańska, M., 1974, *Dokumentacja geologiczna złoża piaskowców krośnieńskich Górka-Mucharz w kat. B+C<sub>1</sub>*, Przedsiębiorstwo Geologiczne, Kraków.
- PN-B-11200, 1996, *Materiały kamienne. Bloki, formaki, płyty surowe*, PKN, Warszawa. PN-88/B-04120, 1988, *Kamień budowlany. Podział, pojęcia podstawowe, nazwy i określenia*, PKN, Warszawa.

*Accepted 10 April 2006*



## **Application of Resistivity Imaging to the Recognition of Landslides in the Flysch Carpathians**

Krzysztof JOCHYMCZYK<sup>1</sup>, Jolanta PIERWOŁA<sup>1</sup> and Grzegorz STĄPOREK<sup>2</sup>

<sup>1</sup> University of Silesia, Department of Earth Sciences  
ul. Będzińska 60, 41-200 Sosnowiec, Poland

<sup>2</sup> ProGeo,  
ul. Głowackiego 34A, 33-300 Nowy Sącz, Poland  
e-mails: jochym@ultra.cto.us.edu.pl; pierwola@wnoz.us.edu.pl

### **A b s t r a c t**

This paper contains the results of preliminary study of landslides located in the Polish Flysch Carpathians. The resistivity imaging method in connection with direct geological and geodetic methods was applied to investigate five small landslides situated in Nowy Sącz. The goal of this work was to test the resistivity imaging method for identifying the geological structure of landslide, especially the weathered cover of the flysch. Marking out the slip plane was also an object of interest. Measurements were carried out during the long period of drought which resulted in significant decrease of ground water table. Very dry rock mass and horizontal variability of the landslide structure caused considerable difficulty in the explicit interpretation of the geoelectrical tests.

### **1. Introduction**

Landslides are detected in many places in Poland. Most commonly they appear in the Carpathians and the Sudety Mountains. Landslides can also be generated by sea waves. According to data collected by the Geological Institute, the intensive rains of 1997 triggered more than 20 000 landslides (Poprawa and Rączkowski 2003).

The structure of the sediments of sea origin occurring in the Carpathian flysch is similar to that of sandstones, mudstones and limestones. When weathered, the sediments create a loam mix sensitive to changes in humidity. Higher humidity has an important influence on their strength.

## 2. The Aim of the Work

Landslides present a great danger to humans, especially in the mountain areas. Their structure is recognized using direct geological methods, supplemented by geophysical and geodetic tests. The geophysical methods used so far were seismic refraction, geoelectrical and electromagnetic measurements.

The aim of this work was to investigate the application of resistivity imaging in identifying the geological structure of a weathered cover in the Flysch Carpathians. The difficulty in the interpretation of the geoelectrical tests performed in the landslides comes from vertical and horizontal changeability in the structure of the landslides.

The weathered cover usually consists of layers of clay and rubble. In these structures, the dry layers are separated by more wet ones. Additionally, the weathered layers may also contain dry or wet cracks triggered by landslide movements. Small landslides near Nowy Sącz were chosen for preliminary tests.

## 3. Literature Analysis

Various methods are used to investigate the structure of landslides and the processes occurring inside them. Shallow seismic refraction tests, geoelectrical and electromagnetic methods are among the most commonly used. These methods are recommended by the International Society for Rock Mechanics to test the landslides (Takahashi 2004). Usually, they are utilized to determine the depth of the solid rock base. They are also used to distinguish between distinct blocks separated by the crack zones. These methods generate two and three dimensional data and are non-invasive, which is very important to the landslide areas.

Recently, the most frequently used geoelectrical method has been the resistivity imaging. It has several advantages over other measuring methods, including high vertical and horizontal resolution and relatively low costs of the tests. Resistivity imaging can be used to investigate even the complex geologic structures or to detect water content in the rocks.

Changes in the water saturation of rocks due to intensive rains are the main factors triggering landslides in the Flysch Carpathians (Poprawa and Rączkowski 2003).

Perrone et al. (2004) used two methods: resistivity imaging and induced polarization to study the Varco d'Izzo landslide in Italy. Their aim was to differentiate between rocky substratum and loose sediments, as well as to carry out the hydrogeological tests. The measurements were performed using the dipole-dipole array, which provides high horizontal resolution (Rudzki 2002). The group also demonstrated the applicability of the geoelectrical methods in the determination of slip zones. The method was not reliable in the investigation of the surface erosion which took place in some landslides. Induced polarisation method was useful to investigate the water relations in the landslide.

Godio and Bottino (2001) investigated landslides with the use of two methods: resistivity imaging and electromagnetic measurements. Both methods showed the presence of slide surfaces, which was confirmed by inclinometric measurements. Ad-

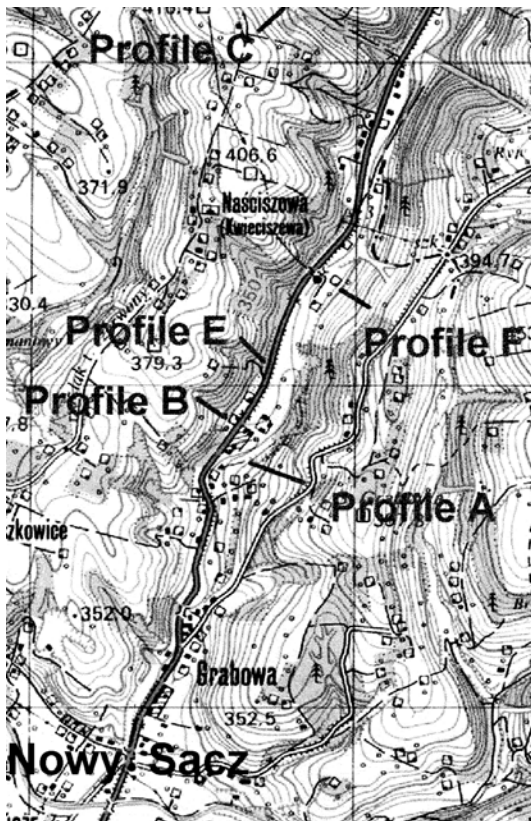
ditionally, using the resistivity imaging, it was possible to detect almost vertical water filled cracks.

The geoelectrical, seismic refraction and electromagnetic methods were tested by Mauritsch et al. (2000) to assess the landslide movements in the Alps. The methodology used did not precisely determine the location of the slide surface because the changes in physical parameters of the rocks were insufficient.

Krejčí et al. (2002) studied landslides in the Flysch Carpathians (east part of the Czech Republic) triggered by intensive rainfalls. Applying the methods of shallow seismic refraction, geoelectrical soundings and electromagnetic profiling in the site of a landslide, they managed to separate the distinct stone blocks.

To sum up, the geophysical methods, including resistivity imaging, become an attractive tool to recognize the geological structure of the landslides. A positive result depends on the knowledge of geological structure in the landslide area.

It is recommended to use several geophysical methods independently. This enables to compare the geophysical and the geological data collected. It is difficult to analyse the data derived from the geoelectrical methods because the changes in resistivity of rocks are too low. The second difficulty lays in the heterogeneity of the landslide.



#### 4. Location of the Area

A survey was carried out in the northern part of Nowy Sącz–Naściszowa district (Fig. 1). Measurements were performed on the slopes of east and west sides of Barska Street which leads to Tarnów and Bobowa. Barska Street is situated in the valley of Naściszówka stream. East and west, it is surrounded by longitudinally oriented ridges. Within the years 1997–2002, landslides of the hillsides along the Barska Street took place. They resulted in the damage of residential and farm buildings.

Fig. 1. Location of survey profiles.

The area chosen for measurements is full of very steep slopes. These slopes are characterized by sharp morphological edges that turn to a flat bottom of the valley. These scarps are up to 30 m in height. Sometimes, morphological forms typical to areas of earth movements are visible on the scarps. These include irregular niches, bulges, and breaks of continuity, localized in the upper parts of the slope.

## **5. Geological and Hydrogeological Characteristics of the Area**

Geological substratum of the analyzed area consists of the Cretaceous and Paleogene flysch deposits. Mostly, they form loam slates containing layers of sandstones. Their thickness varies from 10 to 20 cm. The roof part of the flysch is strongly weathered and usually creates a slide surface. There are younger sediments directly on the flysch. They consist of weathered deposits: sandy clays and rubbles. The sediments' thickness varies according to the slope of the hillside. Sediments tend to slip and flow down the hillside surface.

Two water levels were detected in the analyzed terrain. The deeper, Cretaceous-Paleogene level is present in the cracked sandstones, among dry slates. This level is supplied with two water sources: by rain water infiltrated through the weathered layer and by surface water which is locally present. The shallow level, which has a Neogene origin, is supplied with filtrates from the rubble sediments. This level is mainly present in places where impermeable layers are in contact or within the gravel-sandy layers. Increase the water saturation of the clayish and rubble soil creates a danger of the landslide occurring. A presence of the underground water level was detected in one of the excavations. It was located 3.1 m under the surface level.

## **6. Methods of Investigation**

Resistivity imaging was the main method used in this study. Terrametr SAS 4000 equipment with LUND Imaging System was used. The measurements were performed in the first decade of August after a long drought period. Five profiles of measurements were prepared. They were designed to run along the dip of potentially endangered hillsides. The first profile, A, was 175 m long, the remaining profiles, B, C, E and F, were 100 m in length. Existing conditions were difficult for measurements – they were performed on steep, cracked hillsides covered with bushes.

To perform the survey, the Wenner array was used. The distance between the electrodes was 2.5 m. A minimal current intensity was 50 mA. Data was analyzed using RES2DINV 3.4 Geotomo Software.

Geoelectrical tests were followed by the geological survey. It included research excavations and shallow hand drilling which was 4-5 m deep. For further geotechnical analysis, samples of the rocks were collected.

## **7. Results and Discussion**

The measurements were performed within 3 days without any weather changes. No rainfalls were reported in the period preceding the survey. It resulted in fall of the ground-water level and drying of the surface layers of the landslide.

Among 19 research excavations and drillings, underground water was detected in one case only; it was excavation 3a located on the 49th meter of the B profile. All the remaining excavations were dry. It was supposed that the resistivity of the weathered layer would be higher than in the background.

The laboratory tests of the samples of clayish deposits confirmed a low saturation of the ground. Despite the close localization of the profiles, differences in the geoelectrical cross-section were found.

### ***Profile A***

Profile A was of a clear low-resistivity character. It was lacking a high-resistivity zone present in the four remaining profiles: B, C, E and F (Figs. 2 and 3). The geoelectrical cross-section of the profiles did not display any presence of rocks with the resistance values over 210  $\Omega\text{m}$ . Geological data suggests that in this section, at depths between 2 and 2.5 m, a layer of damp sandy clay containing small pieces of sandstone was present. Below, there is a clayish layer with sandstone blocks. A flysch roof was determined at 22th and 90th m at depths of 3.2 and 3.4 m, respectively. A roof is hardly visible in the geoelectrical profile.

### ***Profile B***

The upper high-resistivity layer of profile B (Fig. 2b) is not homogeneous in terms of the electrical properties. Its thickness is varied which might be a result of the existing vertical cracks in the falling landslide body. The eluvium was divided into the blocks which had the borderline on the 20th, 28th, 40th and 78th meter of the profile. Maximal resistivity value detected in this profile reached 650  $\Omega\text{m}$ . In the site of a high-resistivity layer, there were locally present zones of rocks which displayed low resistivity. They are situated between 17-30 and 76-86 meter of the profile. It is suspected that they contain cracks filled up with damp clay. A presence of water lens was detected in the low-resistivity zone. It was situated at 3.1 m in depth. Flysch sediments were detected on the 94th meter of the profile, at a depth of 1.5 m.

### ***Profile C***

The resistivity value of profile C fluctuated within the range of 15 to 2600  $\Omega\text{m}$  (Fig. 2c). Flysch was localized on the 52nd meter of the profile, at a depth of 3.7 m.

The presence of low-resistivity zone between the 50th and 70th meter of the profile is probably due to a local water table in the flysch rocks.

The landslide body is divided into two blocks with the borderline lying on the 70th meter of the profile.

### ***Profile E***

A high-resistivity surface layer was found along profile E (Fig. 3a). This layer is continuous and rather homogeneous. Maximal resistivity values in this layer reached 2700  $\Omega\text{m}$ . The excavations situated on 27th and 93rd meter of this profile did not reach the roof of the loam-sandstone sediments which indicated it was localized at a depth below 5 m.

**Profile F**

The maximal resistivity value detected in this profile was found to be 1200  $\Omega\text{m}$ . The depth of the roof was measured in the excavations on 20th and 78th m, at a depth of 3.6 and 2.5 m, respectively (Fig. 3b).

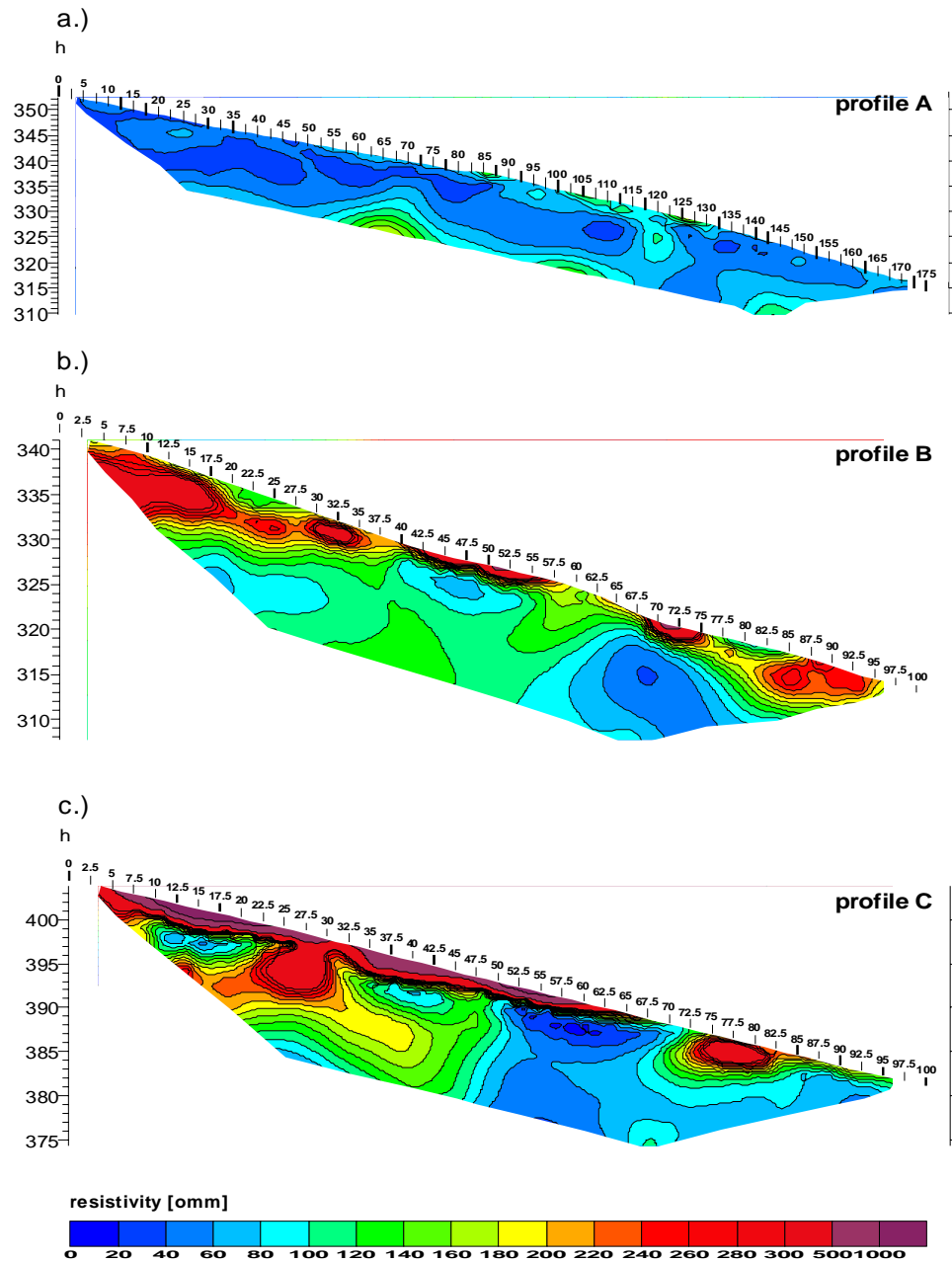


Fig. 2. The results of resistivity imaging for the recognition of landslide structure.

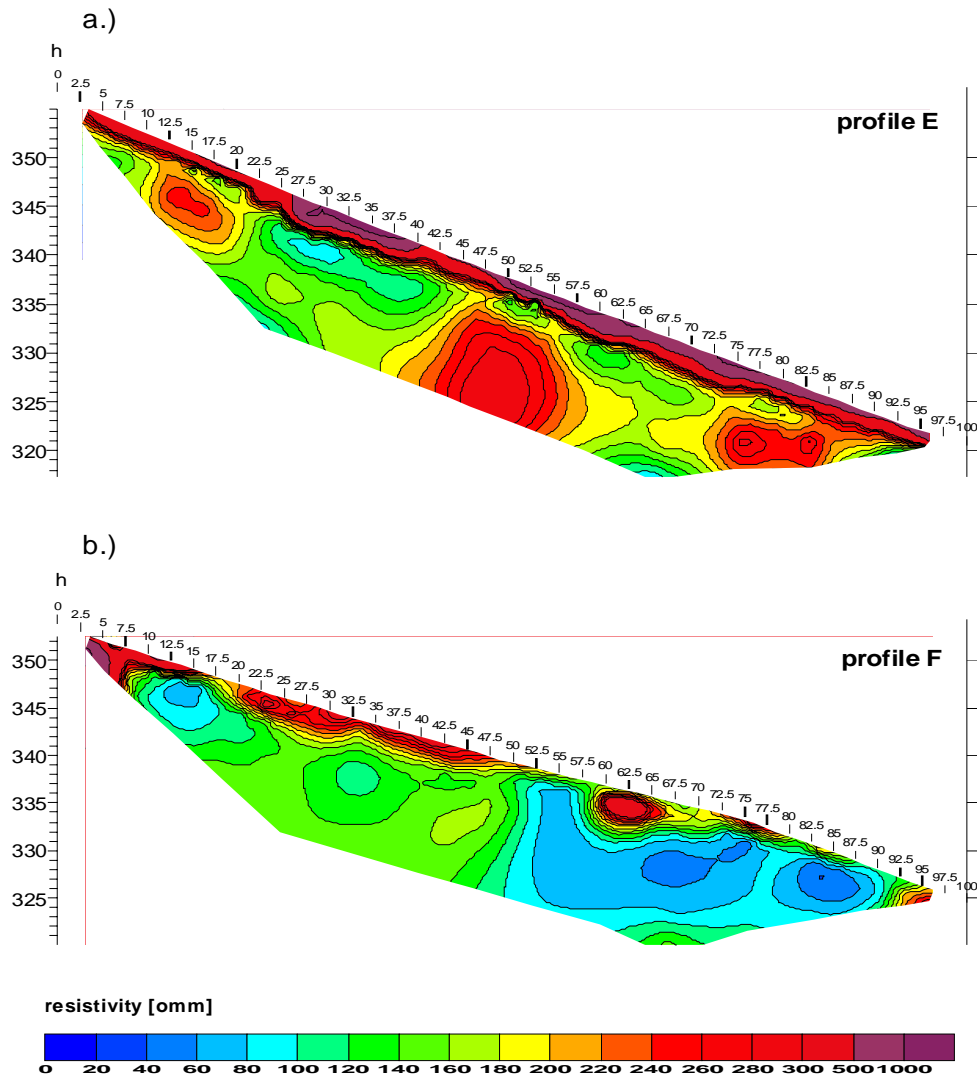


Fig. 3. The results of resistivity imaging for the recognition of landslide structure.

## 8. Conclusions

A field survey during a long drought period was performed. The drought caused a big drop in the ground-water level. For this reason, it was not possible to apply the resistivity imaging in characterizing the slide zones within the eluvium covering the Flysch Carpathians. Usually, a borderline between the weathered layer and the flysch corresponds to the slide surface. By using LUND Imaging System it was very difficult to precisely characterize the depth of the above-mentioned borderline. The resistivity contrast between flysch and residual clay soil is too small. Additionally, the presence of water strongly influenced the values of the resistivity. To detect the depth of borderline, further local geological or geophysical research is required.

Cracked zones in landslide body seen in all the profiles were easy to interpret on profiles B, C, E and F, but not so on profile A.

To obtain more reliable results it is suggested to repeat the measurements when substratum is damper. It is also advised to use Schlumberger or dipole array what would provide a better resolution of the measurements. Also, a closer distance between the electrodes seems to be beneficial.

#### References

- Godio, A., and B. Bottino, 2001, *Electrical and Electromagnetic Investigation for Landslide Characterisation*, Phys. Chem. Earth **26**, 705-710.
- Krejčí, O., I. Baroň, M. Bíl, F. Hubatka, Z. Jurová and K. Kirchner, 2002, *Slope movements in the Flysch Carpathians triggered by extreme rainfalls in 1997: a case study*, Phys. Chem. Earth **27**, 1567-1576.
- Loke, M.H., 2004, *Tutorial: 2-D and 3-D electrical imaging surveys*, www.geoelectrical.com
- Mauritsch, H.J., W. Seiberl, R. Arndt, A. Römer, K. Schneiderbauer and G.P. Sendlhofer, 2000, *Geophysical investigation of large landslides in the Carnic Region of southern Austria*, Engineering Geology **56**, 373-378.
- Perrone, A., A. Iannuzzi, V. Lapenne, P. Lorenzo, S. Piscitelli, E. Rizzo and F. Sdao, 2004, *High-resolution electrical imaging of the Varco d'Izzo earthflow (southern Italy)*, J. Appl. Geophys. **56**, 17-29.
- Poprawa, D., and W. Rączkowski, 2003, *Osuwiska Karpat*, Przegląd Geologiczny **51**, 685-692.
- Rudzki, M., 2002, *Zastosowanie metody tomografii elektrooporowej do wykrywania podziemnych obiektów antropogenicznych*, Publ. Inst. Geophys. Pol. Acad. Sc., **M-27** (352), 195-208.
- Takahashi, T., 2004, *Suggested Methods for Land Geophysics in Rock Engineering*, International Journal of Rock Mechanics and Mining Sciences **41**, 885-914,

*Accepted October 16, 2006*

## Seasonal Electric Resistivity Variations of Rock Formation at an Abandoned Mining Shaft Site

Andrzej KOTYRBA, Łukasz KORTAS and Sławomir SIWEK

Central Mining Institute  
Pl. Gwarków 1, 40 166 Katowice, Poland  
e-mails: bhxak@gig.katowice.pl; l.kortas@gig.katowice.pl;  
slasiwek@gig.katowice.pl

### Abstract

Abandoned shafts, even if backfilled, create a potential hazard for the environment and safe use of post-mining lands. The hazardous phenomena depend on the shaft tube structure and the extent of mining activity in the vicinity and, on the other hand, the dynamic processes which occur within rock strata. Among the processes which affect the rock mass structure is the rainfall water migration and erosion. The amount and rate of water flow within soil and bedrock in the specific area depend on time. The water saturation in rock formation is the main factor which determines the electric properties of geological environment. These phenomena can be used for monitoring erosion processes by electroresistivity or conductometric measurements. In the paper, experimental results of the tests carried out in an abandoned shaft site are described. The tests were performed in three series of measurements conducted using vertical electroresistivity sounding method (VES) in autumn, winter and spring. The results indicate significant changes of rock formation resistivity values due to change in seasonal conditions. This impacts the interpretation of the data collected in geoelectrical measurements.

### 1. Preface

The electroresistivity method uses variations in electrical properties of geological medium to visualize the geological strata arrangement and medium structure. The parameter obtained from the field data in this method is the apparent electrical resistivity  $\rho_p$  of the rocks (the reverse of electrical conductivity  $\sigma$ ) as a function of the interval/spacing AB between the current electrodes. The measured values of the parameter depend on the real values (specific resistivity, depth) and could be calculated using inversion methods. The voids in the dry rock layers are the elements that cause strong

positive anomalies in the visual representation of the data recorded in electroresistivity measurements. Water-filled voids generate negative anomalies. For these reasons, the electroresistivity method is applied to detect and localize the voids of different origin in rock formations and in particular the old shafts. In this application of the method, measurement data characterize a geological medium for a definite moment of time (stationary case). The electrical properties of this medium are mainly affected by water content due to seasonal changes. Due to low compaction of the material used for shafts backfilling, the ground surface in such sites could always become unstable. The possibility of vertical electroresistivity sounding (VES) method application for subsidence hazard monitoring in time domain was the aim of tests conducted in the Triassic carbonate massif in a site located in Olkusz region (Poland). In this nonstationary (time dependent) case, the measurement data strongly depend on water content in the surveyed geological strata.

## 2. Resistivity of Porous Media with Fluctuating Water Content

In theoretical approach, the resistivity of porous media, where part of pores are filled with water of resistivity  $\rho_w$ , can be expressed by Archie's formula (Miltzer *et al.* 1978)

$$\rho = F \cdot \rho_w \cdot \delta^n, \quad (1)$$

where:  $F = a p^{-m}$ ;  $a$ ,  $m$ , and  $n$  are empirical parameters;  $p$  is the fractional pore volume parameter ( $V_p/V$ );  $\delta$  is the fraction of pore volume filled with water ( $V_w/V_p$ ); and  $a$  is the formation factor. Empirical values of  $a$ ,  $m$  and  $n$  for dolomite and limestone can be taken as follows:  $a = 0.6-0.8$  (coarse grained – fine grained);  $m = 2.15-2.30$  (coarse grained – fine grained);  $n = 1.3-2.2$ .

Formula (1) determines the static case in which parameters  $\rho$  and  $\delta$  are time independent. In a dynamic case, both parameters depend on time. Therefore, formula (1) can be written in the form:

$$\rho(t) = F \cdot \rho_w \cdot \delta^n(t). \quad (2)$$

Performing temporary measurements at a specific site we gather data sets which can be expressed in the form:

$$\begin{aligned} \rho_1(t_1) &= F \cdot \rho_w \cdot \delta_1^n(t_1) \\ \rho_2(t_2) &= F \cdot \rho_w \cdot \delta_2^n(t_2) \\ \rho_3(t_3) &= F \cdot \rho_w \cdot \delta_3^n(t_3) \\ &\dots \\ \rho_i(t_i) &= F \cdot \rho_w \cdot \delta_i^n(t_i). \end{aligned} \quad (3)$$

If we neglect the mass transport within the shaft tube (**case 1**), it can be assumed that in the test area parameters  $F$  (porosity factor) and  $\rho_w$  (water resistivity) are constant. Introducing the time dependent fractional parameter  $Q_n$ , the resistivity changes di-

rectly depend on the pore volume filled with water, which can be expressed by the equation:

$$Q_n = \frac{\rho_i(t_i) - \rho_1(t_1)}{\rho_1(t_1)} = \frac{\delta_i^n(t_i) - \delta_1^n(t_1)}{\delta_1^n(t_1)}. \quad (4)$$

The above equation reflects in fact the water balance in rock formation. It is free from primary resistivity value of rock formation. The resistivity data sets from the test site can be directly used as the analog of water volume fluctuations, if the quantitative rainfall record is known. The resistivity variations balance should be similar to the water content variations balance. In the case of mass transport in a shaft tube, porosity parameter ( $F$ ) is not constant, which leads to the set of equations:

$$\begin{aligned} \rho_1(t_1) &= F_1 \cdot \rho_w \cdot \delta_1^n(t_1) \\ \rho_2(t_2) &= F_2 \cdot \rho_w \cdot \delta_2^n(t_2) \\ \rho_3(t_3) &= F_3 \cdot \rho_w \cdot \delta_3^n(t_3) \\ &\dots \\ \rho_i(t_i) &= F_i \cdot \rho_w \cdot \delta_i^n(t_i). \end{aligned} \quad (5)$$

In **case 2** the fractional parameter  $Q_n$  is described as

$$Q_n = \frac{\rho_i(t_i) - \rho_1(t_1)}{\rho_1(t_1)} = \frac{F_i \cdot \delta_i^n(t_i) - F_1 \cdot \delta_1^n(t_1)}{F_1 \cdot \delta_1^n(t_1)}, \quad (6)$$

$$Q_n = \frac{F_i \cdot \delta_i^n(t_i)}{F_1 \cdot \delta_1^n(t_1)} - 1. \quad (7)$$

In **case 2**, the resistivity fluctuations balance is not equal to water content balance and depends on fractional pore volume parameter  $F$ . The mass transport in shaft tube disturbs the spatial porosity distribution (parameter  $F$ ), which can be monitored by various techniques of geoelectrical measurements.

### 3. Description of Test Site and Measurements Performed

The vertical electroresistivity sounding method was applied to collect field data in the test site. The measurements were performed in six points called  $S_1$  to  $S_6$ , localized in the studied area as shown in Fig. 1.

The primary goal in the first series of field works (autumn) was to determine the model of geological structure of the tested ground. The secondary goal was to outline the places in which the electrical properties of the Triassic strata are abnormally exaggerated or lowered. Data collected in the next series (winter and spring) were supposed to determine whether and what changes in the resistivity values take place in the test site area. The important issue here was to estimate the shape of anomalous zones during the whole experiment and to specify their possible influence on the assessment of surface stability.

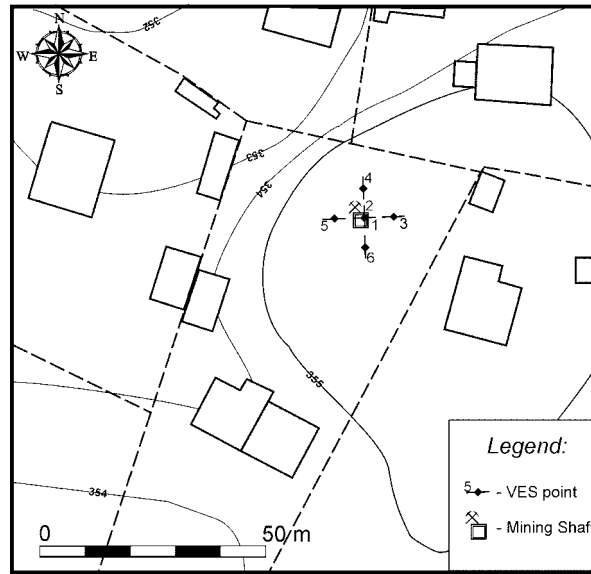


Fig. 1. Location of VES points in the test site.

The electroresistivity soundings  $S_1$  and  $S_2$  were performed within the precincts of the abandoned shaft and had perpendicular directions. The rest of the soundings ( $S_3$ – $S_6$ ) were conducted at 6.5 m distances from soundings  $S_1$  and  $S_2$  in the following directions: N ( $S_4$ ), S ( $S_6$ ), E ( $S_3$ ) and W ( $S_4$ ). Electrode arrays for soundings  $S_1$ ,  $S_3$  and  $S_5$  were oriented in direction WNW-ESE, and for  $S_2$ ,  $S_4$  and  $S_6$  in direction NNE-SSW, which was connected with the existing buildings placement and urban infrastructure. In the points  $S_1$ – $S_4$ , fifteen data points were collected for  $AB/2$  spacing from 1.5 to 72.5 m and in  $S_5$  and  $S_6$  sixteen data points were measured for  $AB/2 = 1.5$  to 95 m.

The field works were performed with application of digital geoelectric apparatus CMG-01, made in Poland. Altogether during data acquisition process 312 data points were recorded (104 data points in each series). Each value registered by the operator was the average value from a couple of instrument readings.

### 3.1 Geology and mining

The test area lays in the southern part of the large Tertiary monocline of diversified lithology and tectonics. This formation is strongly cracked and tectonically dislocated. Tectonics of the area has been formed during the Alpine orogenesis in Saxon phase. In that time, the dense net of normal faults has been created. They divided the area into numerous blocks with different displacement and inclination. The prevailing number of faults has azimuths ranges from  $10^\circ$ – $30^\circ$  to  $95^\circ$ – $120^\circ$ . Dislocations in directions NW-SE and NE-SW or NNW-SSE or WSW-ENE are also sometimes observed.

The net of faults belonging to various systems makes separate blocks which are the units of lower level inclined independently of the general direction of the upper

unit throw. The inclination of layers in blocks is conditioned by the faults of the lowest order. The inclination values range from  $4^{\circ}$ – $5^{\circ}$  to  $20^{\circ}$ – $40^{\circ}$ .

The soils near surface are of anthropogenic origin (mine wastes). Below them, the Quaternary sediments (clays and sands) should be present. They are not seen on VES curves. This is the reason for assuming that in the test site the Triassic sediments are cropping out on the surface, as frequently observed in Olkusz area. They are composed of limestone, marbles and dolomites of the lower and middle Triassic strata. In this formation, the lead and zinc bearing veins occur. They were the subject of shallow mining exploitation in the past (Fig. 2). At present, two mines (Pomorzany, Olkusz) operate in ore deposit. In the Triassic rocks, the Karst phenomena are frequently observed.

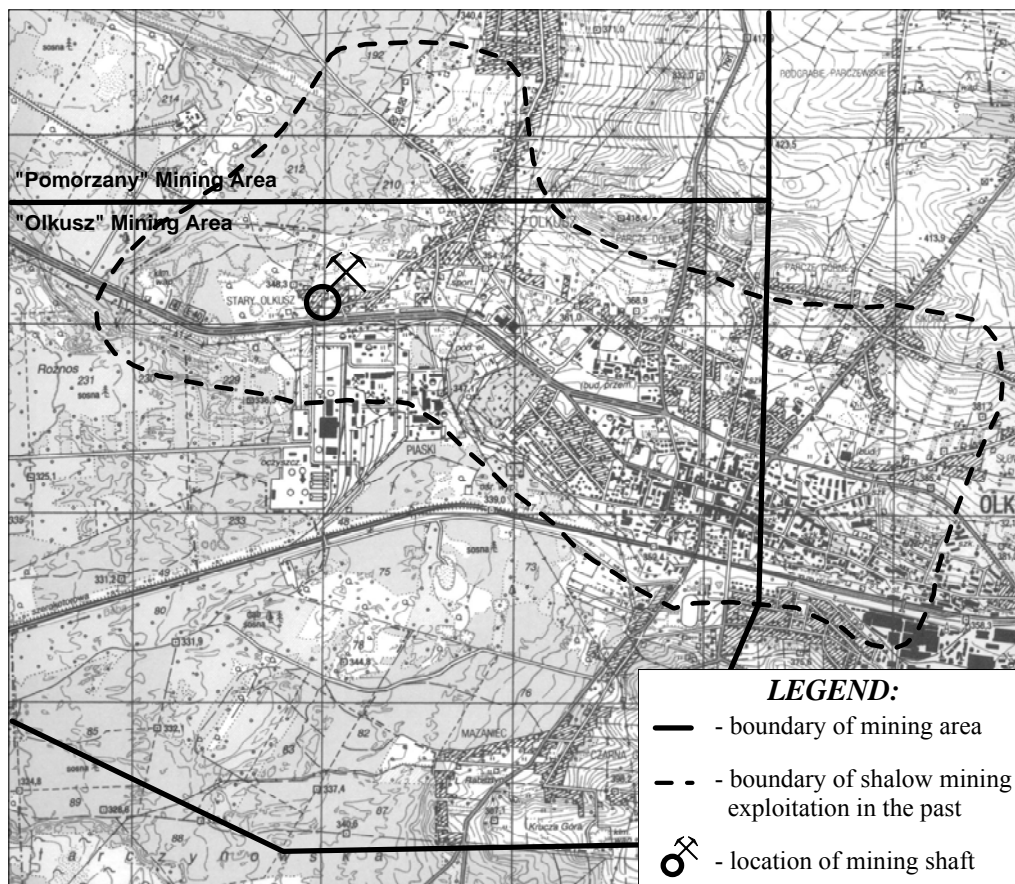


Fig. 2. Test site location on the background of topographic map of the region.

### 3.2 Water conditions

The description of water conditions in test site area is based on the hydrographical map elaborated and published in 1987 (Mapa hydrograficzna Polski). According to

this source, the test area lies in Biała Przemsza and its tributaries river basin. Watersheds dividing river basin of Biała Przemsza are of IV<sup>th</sup> order (i.e. Bobrka, Sztoły, Kozi Bród). Natural water conditions in the area are highly disturbed by mining activity of deep mine Pomorzany (about 1 km to the north) and sand open pit mine Szczakowa (about 6 km to the south). Those mines drain the Quaternary-Triassic water horizon. In the area located to the north from the test site, the water level is lowered approximately to a depth of 100 m b.g.l.

South of the test site, the water level is at a depth of approximately 20 m b.g.l. In the area located on the eastern side of the test site, ground water table is observed at a depth of approximately 10 m b.g.l. The drainage pattern allows to assess that in the test site area the underground water flows generally in northern direction. It is not clear at what depth the water table occurs there. The hydrographical data are too old to estimate the water table depth in the test site, provided that other mines operating in the vicinity of the test site (Olkusz, Bolesław) have been demolished since 1987. This could affect the water conditions and lead to water table recovery in the test site.

The local water conditions in the test site are influenced by rainfall feed and depth of water table in Triassic sediments. Water table divides the bedrock into aeration and saturation zones. The water content in aeration zone is shaped mainly by rainfall. The precipitation rates during the testing period are shown in Fig. 3 (IMGW bulletins 2004-2005).

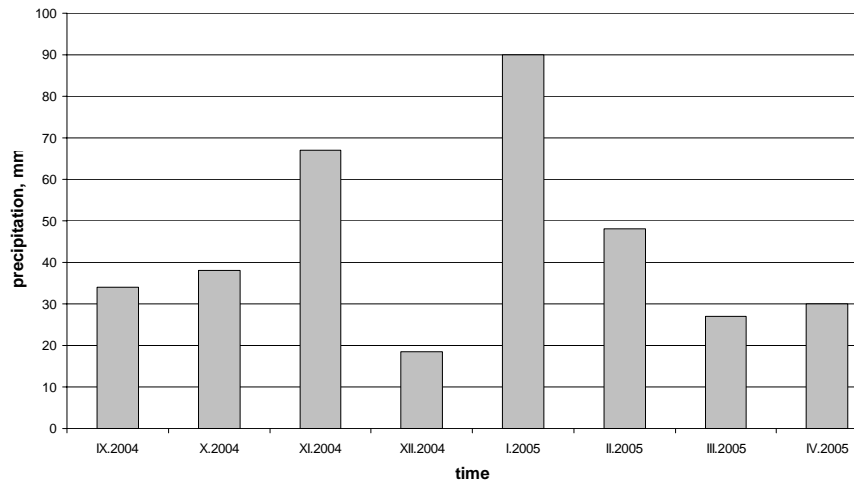


Fig. 3. Precipitation in the test area during testing period (monthly rates).

The percentage of atmospheric rainfalls that infiltrate in the rock formation in Poland ranges between 16 and 25%. The average for Poland is equal to 18.2% (Rogoż 2004). In the active mining areas this percentage is higher and ranges between 30 and 50% (Sztelak 1965). It could be assumed that in the areas where the mining exploitation has ended, this value is still exaggerated in comparison to other regions in Poland and is of the order of 30%.

### 3.3 Hydrogeological Model of Backfilled Shaft

The common practice of shafts liquidation is to backfill them with waste material from exploitation of ore bearing strata. In ancient mining, the waste material from digging works was stored on the surface around the shaft. A mass volume excavated exceeded the shaft volume. The stored waste formed an anthropogenic hill. The primary material usually had a high content of cobble fraction. In weathering process only a small part of dolomite or limestone cobbles changed the size, altering to clay and gravel. Therefore, the prevailing part of mining waste remained in the form of coarse rock fraction. This material had substantially higher porosity and related permeability compared to rock basement. After completion of mining works at a specific area, part of the waste has been transferred to the shaft. Due to irregular form of cobbles, it can be assumed that the porosity of backfilling material remained primary, i.e., similar to the material stored on the surface. Nevertheless, underground openings in shaft vicinity enable the processes of washing out and erosion within the backfilling material, by migrating rainfall waters. Those processes are probably responsible for mass transport within old shaft's tube and surface displacements. The acting force of washing out and erosion is dependent on the volume of percolating water, which is time dependent. Therefore, the model depicted in Fig. 3 can be used for water and mass balance analysis.

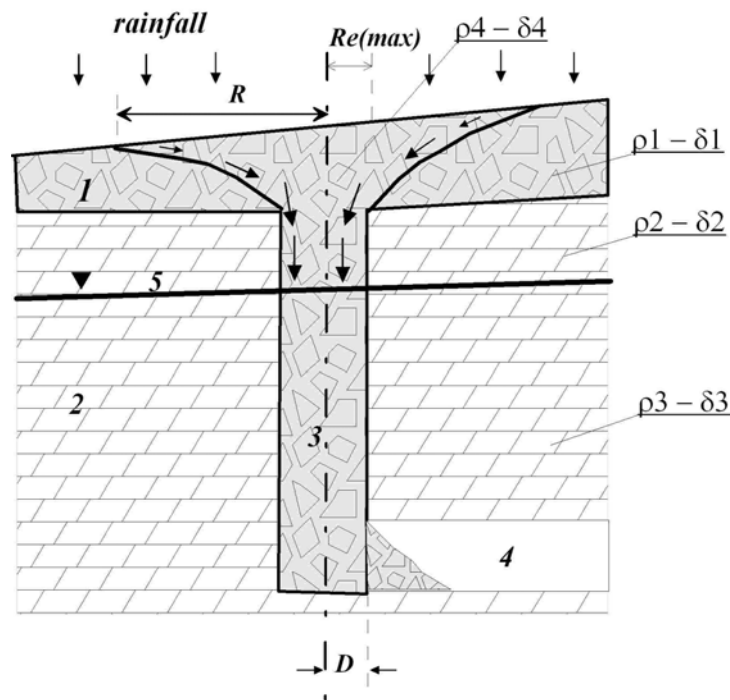


Fig. 4. Hydrogeological model of old backfilled shaft with aeration and saturation zones (1 – waste, 2 – rock basement, 3 – shaft's tube, 4 – mine void, 5 – water table,  $D$  – shaft radius,  $R$  – radius of local catchment area,  $Re(max)$  – radius of zone with maximum water action).

According to the model presented in Fig. 4, an old shaft forms a local catchment area, due to higher permeability of the backfilling material. The power of water erosion and suffusion processes is the highest inside the shaft's tube. The particles eroded or washout from the backfilling material can be transported to the mining voids in the vicinity (mass transport). It should be noted that the water action is highest in the aeration zone. In the case of percolation, the resistivity values ( $\rho_i$ ) of model layers are proportional only to water content ( $\delta_i$ ). The resistivity variations in time should be similar to rainfall rates. In case of mass transport within shaft's tube, the above relation should be disturbed. This finding can be used for prediction of surface displacements, based on continuous or temporary resistivity (conductivity) measurements data, gathered in the site.

#### 4. Test Results

Data collected in field measurements ( $I, \Delta V$ ) were recalculated to obtain apparent resistivity  $\rho$  in each data point of the studied area. Using this data, the bilogarithmic plots of dependence  $\rho$  [ $\Omega\text{m}$ ] vs.  $AB/2$  (m) called the sounding curves were made. Those plots apart from documenting the conducted measurements are the basic materials for analysis of temporary variations of rock formation electric resistivity as well.

Additionally using Surfer/Golden Software, horizontal contour maps were made showing the distributions of resistivity values in halfspace. A parameter for horizontal cuts was half of the  $AB$  spacing of current electrodes. To all plots a point kriging method of interpolation (with parameters shown in Table 1) was used.

Table 1  
Point kriging parameters used in interpolation scheme

Kriging parameters	
Number of sectors to search	1
Max. number of data to be used from all sectors	5
Max. number of data to be used from each sector	5
Min. number of data to be used from all sectors (node is blank if fewer)	1
Blank node if more than this many sectors are empty	1

Sounding curves recorded in autumn, winter and spring series are set in Fig. 5. One can observe that the shape of the plots of all three series is similar and for greater  $AB$  spacing depends on the measurement line azimuth. Soundings with azimuth line ESE-WNW in terms of electrical properties show four-layer medium structure of HK type (the last layer on the curve has a low resistivity value). Soundings performed in spreading line NNE-SSW show five-layer medium structure of HKH type (the last layer on the curve has a high resistivity value). This indicates an anisotropy of the electrical properties of deeper parts of rock formation at the test site. Despite those

differences, the measured values of electroresistivity on VES curves change in the interval from about 100 to 1800  $\Omega\text{m}$ .

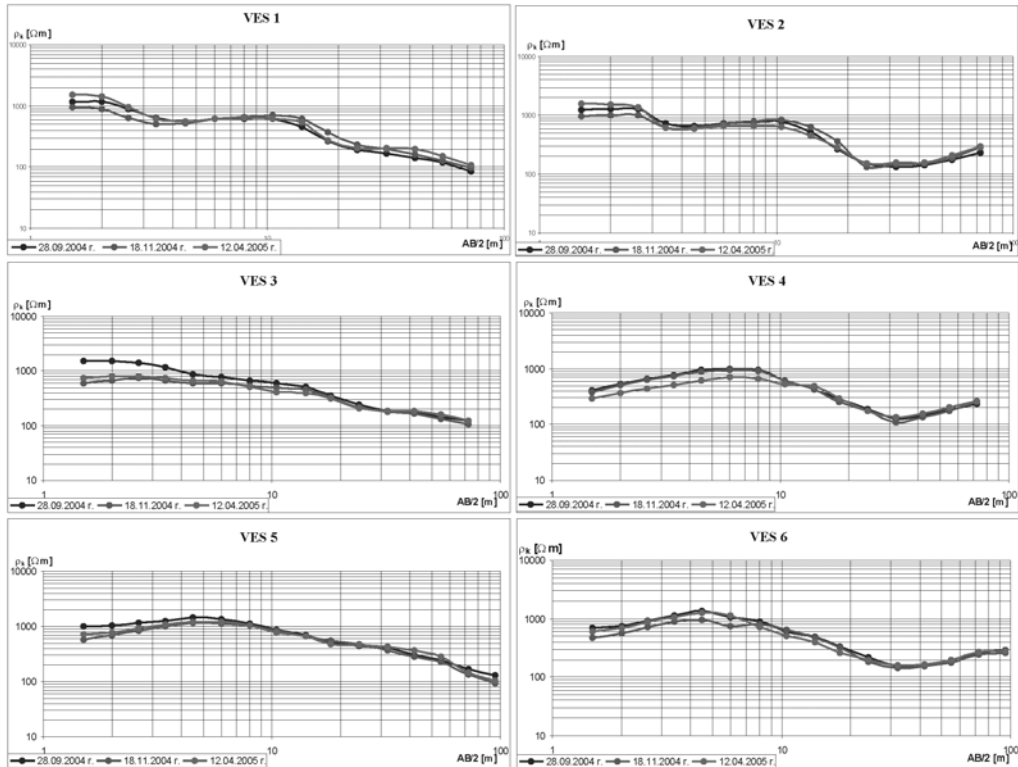


Fig. 5. VES curves  $S_1 - S_6$ . Series: 1 (autumn), 2 (winter), 3 (spring).

Analyzing VES curves one can observe that depending on location they differ in electroresistivity value of subsurface geological layers. While comparing curves for all three series, significant differences are visible also in these parts of the VES plots which correspond to subsurface formations of studied medium (especially plots for  $S_3$  and  $S_4$ ). As concerns the medium structure, the VES curves analysis provided the following geoelectrical layers specification (Popiołek *et al.* 2005):

**Layer I** – apparent electroresistivity values range from 700 to 1600  $\Omega\text{m}$ , depth of deposition 0–1m. Corresponds to the soils in aeration zone.

**Layer II** – apparent electroresistivity values range from 500 to 1500  $\Omega\text{m}$ , depth of deposition 1–4 m. Corresponds to embankment grounds in aeration zone.

**Layer III** – apparent electroresistivity values range from 300 to 900  $\Omega\text{m}$ , depth of deposition 4–8 m. Corresponds to position of weathered Triassic rocks in aeration zone.

**Layer IV** – apparent electroresistivity values range from 100 to 300  $\Omega\text{m}$ , depth of deposition 8–30 m. Corresponds to Triassic rocks formation in saturation zone.

**Layer V** – apparent electroresistivity values range from 100 to 400  $\Omega\text{m}$  in N-S direction and 100–200  $\Omega\text{m}$  in W-E direction, depth of deposition > 20 m. Corresponds to Triassic rocks in saturation zone with characteristic cracking pattern with W-E extent.

Because of the fact that geological structure of the substratum is not essential the model calculations in this work were not conducted with application of inversion methods to obtain exact, quantitative interpretation of the VES curves. For the purpose of this work, an approximate estimation is sufficient.

Due to the types of the recorded VES curves (mainly H and K) one can assume that apparent resistivity and depth values given above are close to their real values.

While analyzing the VES curves, an important issue is the remarkable anisotropy of electrical properties of the Triassic rock formations deposited at greater depths in the studied area. The longer axis of the anisotropy ellipsoid extends in the N-S direction and is probably caused by tectonics of the rock base of studied area which provides the W-E direction of the layers cracking.

Horizontal contour maps showing distribution of resistivity values of rock formation in series 1, 2 and 3 are illustrated in Figs. 6, 7 and 8, respectively.

At the vertical isoohm sections, a decrease of resistivity values with increasing depth is generally observed. More information about the medium can be obtained from the horizontal isoohm sections analysis. At these pictures, positive and negative anomalies connected with the presence of the shaft tube in medium are visible. In the first/autumn series plot, the tube is marked in the subsurface strata as a positive anomaly of electroresistivity (for  $AB/2 = 1.5, 2.0$  and  $2.6$ ) and negative anomaly (for  $AB/2 = 3.4; 4.5; 6.0$  and  $8.0$  m). In deeper parts of the rock formation, the shaft was not clearly visible but could be localized in the zone of lower values of resistivity.

At the horizontal isoohm pictures of second/winter and third/spring series the shaft tube is marked similarly as at the first/autumn series pictures. The only significant difference concerns the subsurface zone ( $AB/2 = 1.5; 2.0$  and  $2.6$  m) and is most visible in the data from third/spring series. At the isoohm maps mentioned earlier, the shaft tube is marked as a positive anomaly of resistivity with significant amplitude, which indicates relatively smaller watering of the soil in the tube than the rock. In any case, if we construct contour maps showing relative changes of resistivity between series, the shaft's tube is clearly visible on all pseudo depth levels (Fig. 9).

Comparison of autumn, winter and spring series from qualitative point of view indicates the time variations of electrical properties of the grounds in the studied area. On resistivity contour maps, variations concern the shape, sign and amplitude of the anomaly. The changes are significant in the aeration zone (about 0-8 m b.g.l.). In the formations deposited at the depth that corresponds to saturation zone, the changes of electroresistivity were insignificant. On resistivity change contour maps, the shaft's tube is visible on almost all depth levels. It is well marked especially in the images corresponding to deeper parts of the rock formation.

The analysis of variations shows that in the studied area the backfilled shaft tube plays a role of drainpipe for rainfall water, which infiltrates from the surface down in the medium. Variation in lithology and permeability of the soil used to back-fill the shaft helps the tube to play the role of reservoir able to retain rainfall water during the dry periods.

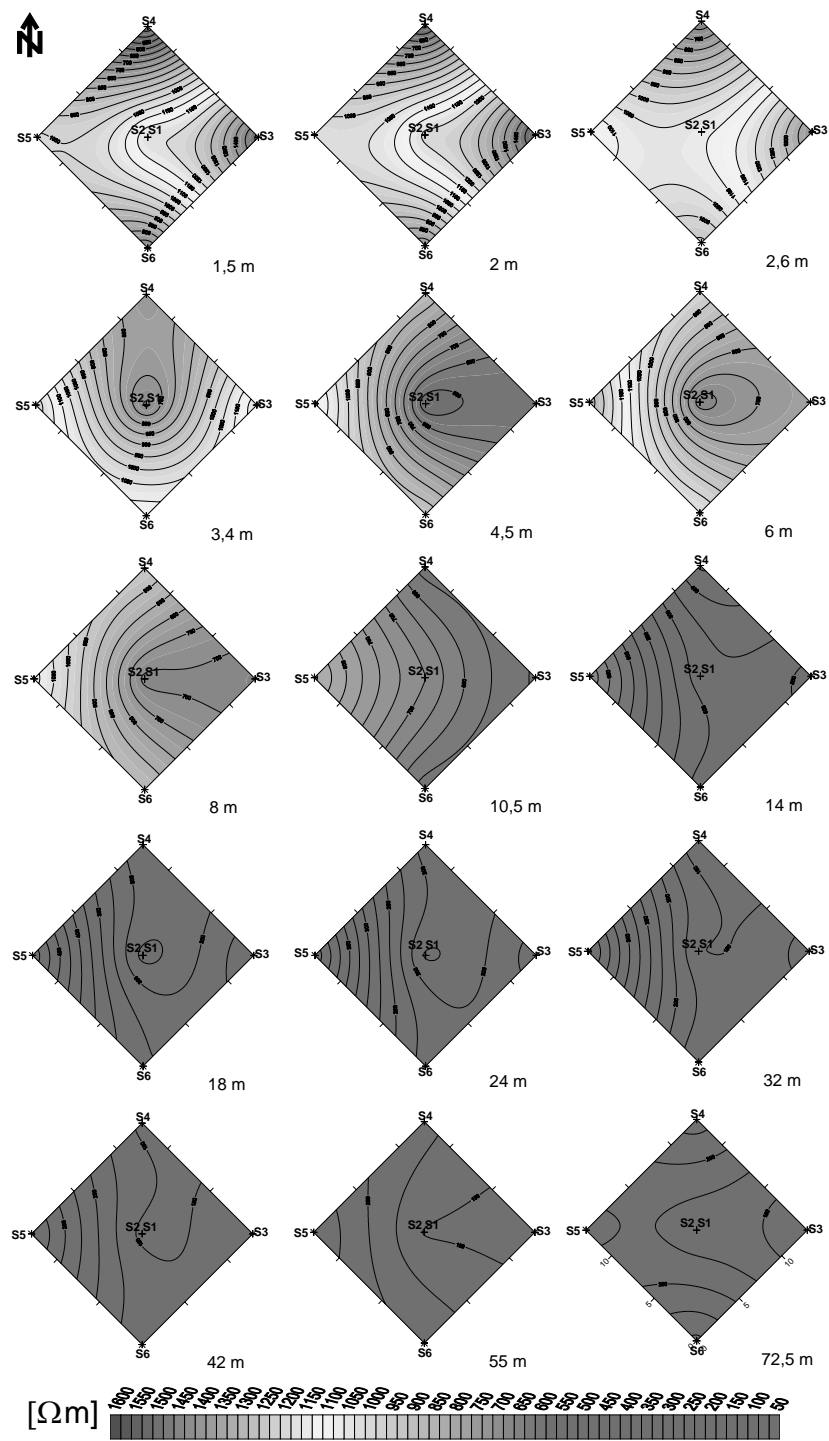


Fig. 6. Resistivity contour maps of the first series of measurements (autumn).

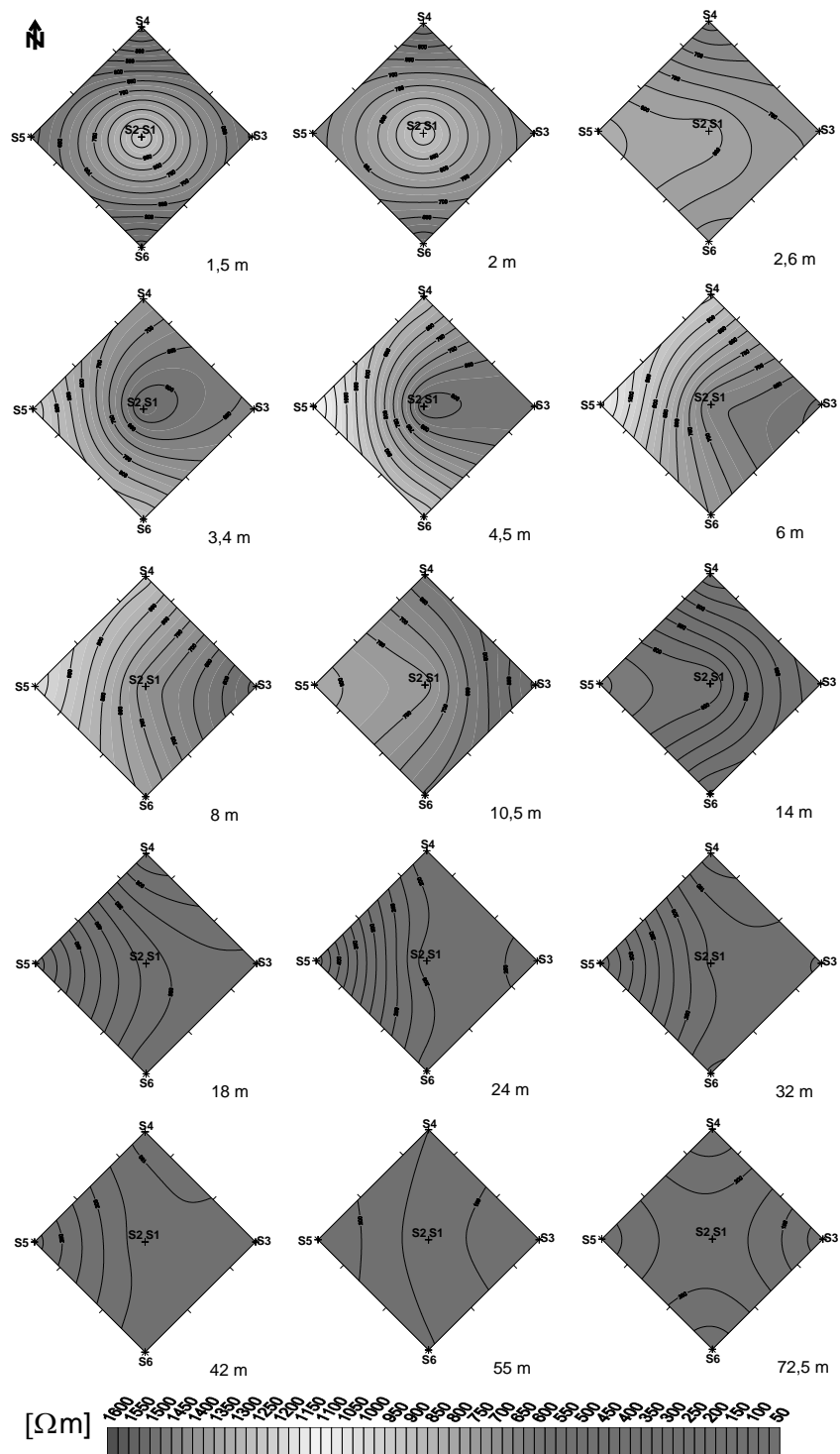


Fig. 7. Resistivity contour maps of the second series of measurements (winter).

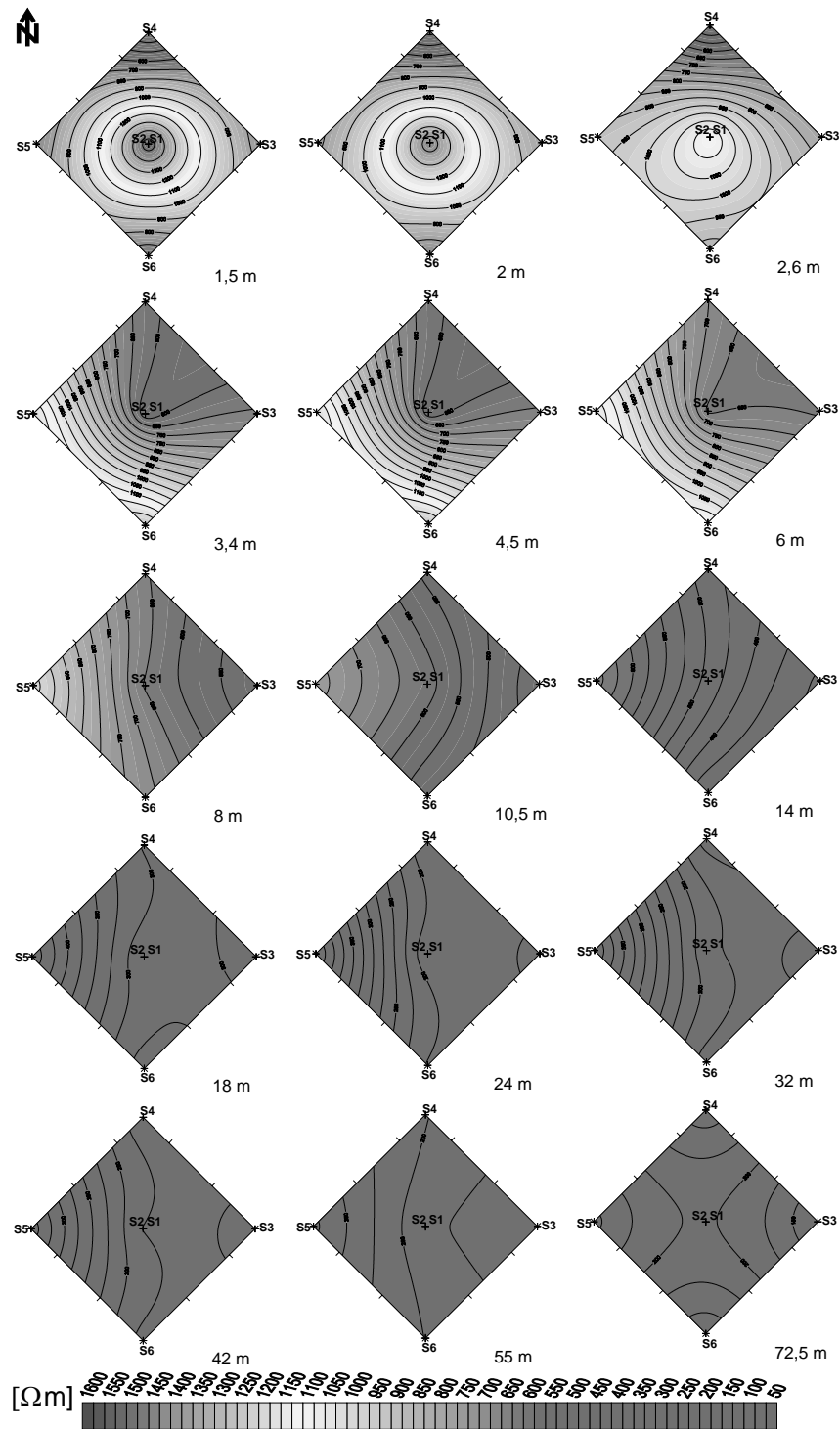


Fig. 8. Resistivity contour maps of the third series of measurements (spring).

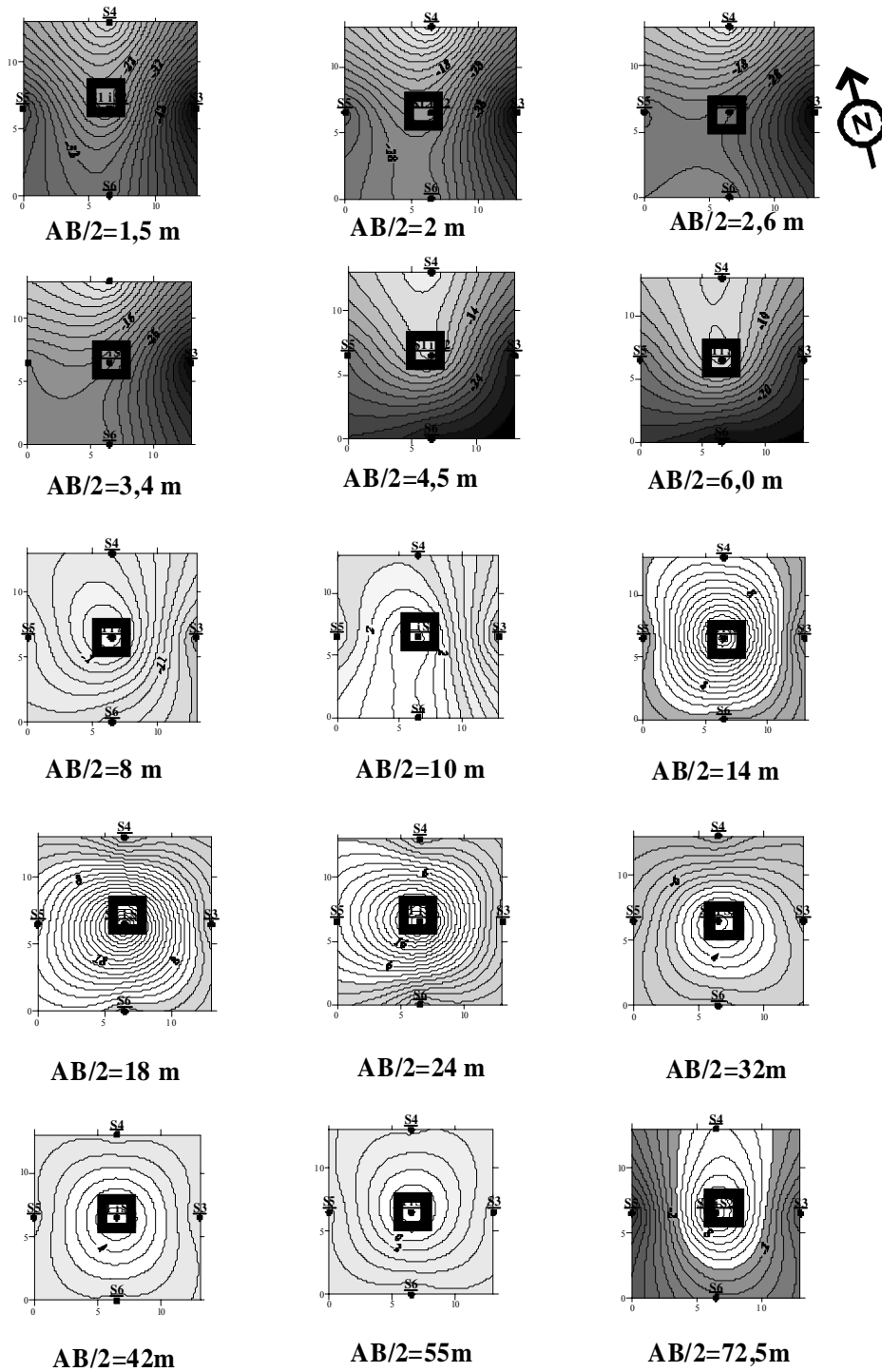


Fig. 9. Contour maps of the resistivity changes between second and first series of measurements (%) drawn in 2% intervals.

Direct analysis of data sets was performed to obtain quantitative characteristics of the resistivity changes in time interval between each series of measurements. The parameters of analysis were as follows:

- The change of resistivity in each sounding point for given AB/2 spacing, calculated in percent:  $\frac{\rho_{s2} - \rho_{s1}}{\rho_{s1}} \cdot 100\%$ ;
- The average change in resistivity value for given AB/2 from 4 points of soundings localized outside the shaft tube ( $S_3, S_4, S_5, S_6$ );
- The average change in resistivity value for given AB/2 from 2 points of soundings localized inside the shaft tube ( $S_1, S_2$ ).

Results of calculations are plotted in Fig. 10. It can be observed that the resistivity changes in shaft's tube are higher than in rock strata. Especially significant changes occurred in the second series of measurements in the range of 10–20 m of AB/2 spacing. The resistivity of that zone increased, which can be assigned to local mass disturbance, not observed in the next series. Nevertheless, in the third data series it can be observed that the resistivity values increased moderately also in deeper parts of strata. This phenomena is visible more clearly, if the changes are shown for individual geoelectrical layers (Fig. 11).

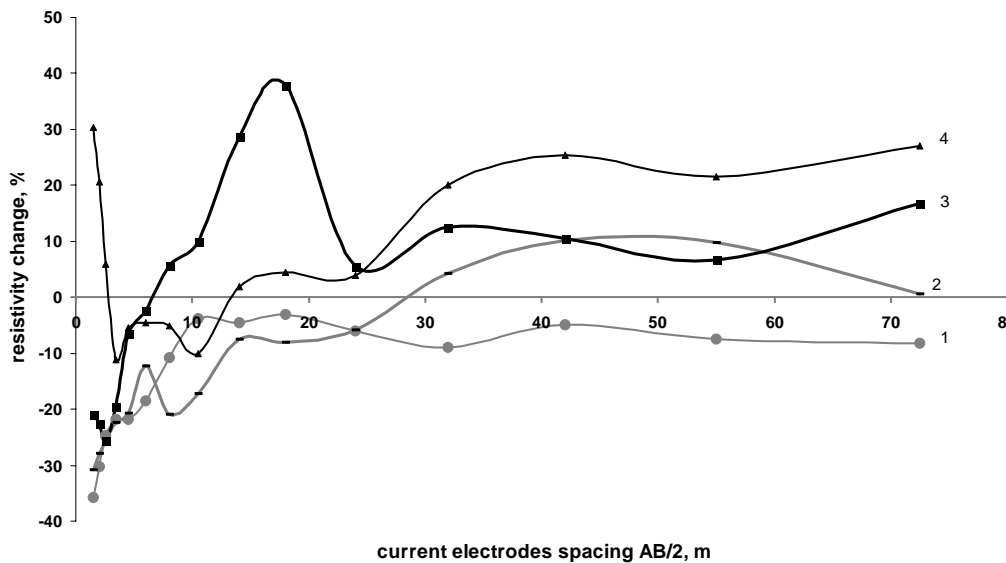


Fig. 10. Comparison of resistivity variations in shaft's tube and rock basement in relation to first series data as a function of current electrodes spacing (1, 2 – rock formation resistivity changes in series 2 and 3; 3, 4 – shaft's tube resistivity changes in series 2 and 3).

One should pay special attention to zones where the resistivity values increase. On the curve shown in Fig. 10, the zone has a form of local maximum in second/winter series in AB/2 range from 10 to 20 m (depth interval 4–8 m). In the estab-

lished geoelectrical model of the medium, this interval corresponds to the weathered Triassic rocks layer. The observed changes of this layer resistivity are connected with lower watering in the period between first/autumn and second/winter series. It is also possible that part of material filling the shaft was washed out from this formation in the time interval between series 1 and 2 (the loosen ground zone was formed). At the same time, the increase of watering in the upper layer (embankments) has taken place what causes the soil particles to more downward. This anomaly was not recorded in the third/spring series of measurements but an increase in resistivity of lower parts in shaft tube was observed, which is clearly seen in Fig. 11. Those changes indicate that within shaft's tube also mass transport phenomena have occurred.

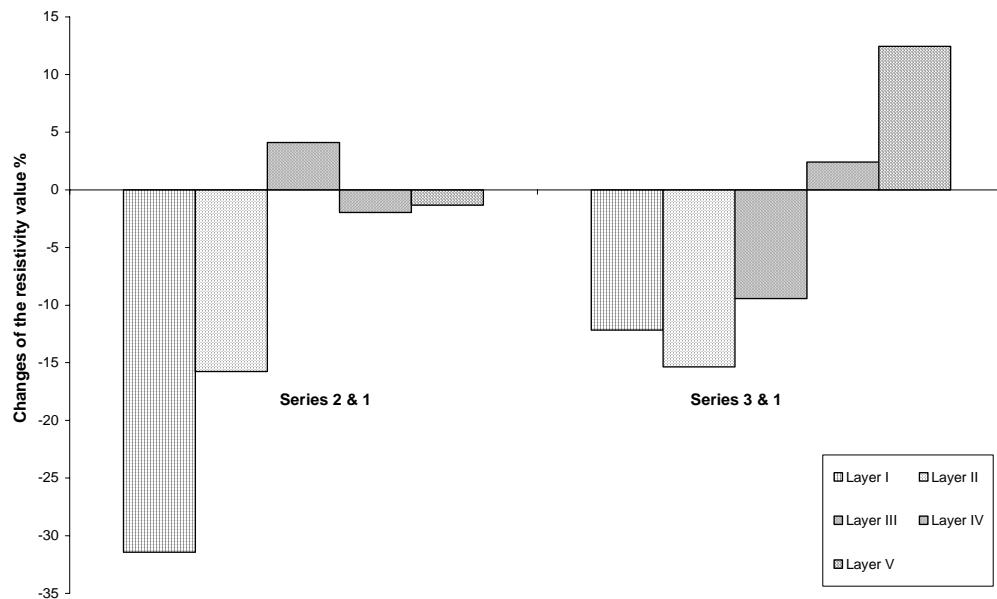


Fig. 11. Changes of the resistivity data recorded in series 2 and 3 in relation to data of the first series (%).

## 5. Conclusions

An analysis of test results shows that during the testing period relatively high quantitative changes took place in the subsurface zone of the studied area ( $AB/2 = 20$  m, down to estimated depth of 8 m). The relative changes reached here the level of 35%. This value is close to the estimated fraction of rainfall which inflows to the geological environment impacted by mining operations. The amplitude of changes in the shaft tube is relatively higher but generally follows the trend of changes in the surrounding medium. All observations pointed out above indicate that within the boundaries of the test site, the cause of the surface deformation hazard is the washout and erosion phenomena taking place in shaft's tube material in accordance with hydrogeological model of the site. Hence, it should be noted that the depth of water table

(estimated in preliminary interpretation of VES data) was not correct. This became obvious when the data of second series of measurements have been collected.

It can be also concluded that in contour maps of resistivity changes the shaft's tube is much better visible than in traditional resistivity isoohm maps. This conclusion can be used in methodology of geoelectrical measurements aimed for old shaft detection. The data sets gathered in two or more series of measurements can significantly reduce the interpretation errors.

The results of the study point out that the electric resistivity is a sensitive indicator of time dependent changes in medium and may be used to monitor various geodynamical processes in rock strata, in particular the surface deformation hazard over abandoned shafts. The temporary changes of rock resistivity reflect the precipitation rates in case of free percolation of water within the geological environment. If the percolation process induces mass movements, the above relation is disturbed, which can be detected by temporary or continuous geoelectrical measurements. For proper interpretation of geophysical data, an exact record of precipitation at the site has to be known.

#### References

- Biuletyny IMGW. Oddział w Katowicach. 2004-2005.*
- Mapa hydrograficzna Polski w skali 1:50 000. Arkusz 532.1. Jaworzno. Główny Urząd Geodezji i Kartografii. OPGK. Poznań 1986/1987.*
- Militzer, M., J. Schön, U. Stotzner and R. Stoll, 1978, *Angewandte Geophysik*, VEB Deutscher Verlag für Grundstoffindustrie, Leipzig.
- Popiołek, E., Z. Pilecki, J. Ostrowski, J. Kłosiński, M. Koster, Z. Fajkiewicz, A. Kotyrba, G. Mutke, E. Stewarski, A. Wróbel, J. Chodacki, Ł. Ortyl, J. Radomiński, R. Siata and A. Wójcik, 2005, *Ocena przydatności do zabudowy terenów zagrożonych deformacjami nieciągłymi za pomocą metod geofizycznych*, Wydawnictwo IGSMiE PAN, Kraków.
- Sztelak, J., 1965, *Promień zasięgu drenażu wyrobisk górniczych lub ujęć wód podziemnych*, Rudy i Metale Nieżelazne nr. 3. Katowice.
- Rogoż, M., 2004, *Hydrogeologia kopalniana z podstawami hydrogeologii ogólnej*. Główny Instytut Górnictwa, Katowice.

*Accepted 13 June 2006*



## **Utilization of Geoelectrical Methods in Order to Identify Places of Pollution and Contamination on the Example of Former Military Camp**

Monika RUSIN-ŻOGAŁA, Adam FREJ, Krystian WZIENTEK  
and Anna MACHALICA

University of Silesia, Faculty of Earth Sciences  
ul. Będzińska 60, 41-200 Sosnowiec, Poland

### **A b s t r a c t**

The article shows the results of an application of geoelectrical methods for identifying places of pollution and contamination in the area of former military fuel base located 2 km west of Borne Sulinowo.

### **1. Introduction**

Areas of former military bases of the Soviet Union Army are strongly degraded in a wide range. You can find there both denaturations with the oil and chemical substances (e.g., phenols) and pollutants, e.g., ferroconcrete constructions and other elements of military infrastructure, which are often located under the surface of the ground. Denaturations and pollutants are the reason of geophysical anomalies connected with modifications of physical features of the source. As the degradation of the natural environment changes the physical features of the medium, there is a chance to localize the focuses of denaturations and pollutants, and also to observe them using geophysical methods. This article shows the results of research carried out in the area of former military fuel base "A", located about 2 km west of Borne Sulinowo. The area under investigation covers about 23 ha and has a diversified morphology.

### **2. Geology of the area**

The investigated region lies on the borderland of two geostructural units: Middle Polish Anticlinorium in the south-west part and hollow Synclinorium that lies close to the above structure from the north-east. On the consolidated Permian-

Mesozoic complex of the Middle-Polish Anticlinorium, there is a cover (of variable thickness) of Cenozoic deposits: sandstones and mudstones of Oligocene, clays, muds and sands of Miocene, and also lithologic variable complex of formations of Pleistocene and Holocene. Miocene deposits are diversified. There were three sedimentation cycles, which begin with sands and end with mud-clayey formations or clay ones, often with brown coal in the roof. The thickness of Miocene formations is estimated at about 160 m at most.

In the area, five glacial horizons – boulder clays and deposits – were registered. Two lower horizons represent the South Polish Glaciation (San I and San II). The next two horizons match the Middle Polish Glaciation (Odra and Warta). The highest North Polish Glacial complex is represented by two or three horizons of boulder clays, which belong to the main (upper) Wisła Glacial. Boulder clays, especially in marginal zones, are accompanied by sandy-gravelly deposits and sandy-mud limo deposits (Żogała et al. 2005). The Holocene deposits are fluvial sands and gravel, mud and sands, gytja, lacustrine chalk and peat, occurring nearby.

The thickness of Pleistocene and Holocene deposits is diverse and changes from 60 to over 200 m; however, generally speaking, it is of 100-120 m.

The profile of Pleistocene substratum is considerably varied. In the general outline you can observe that this area has a tendency to decreasing towards the northwest, according to decreasing tectonic blocks of the Pomerania Levee in relation to themselves. The underclay of Pleistocene deposits most often covers the depth of about 20-50 m (Dobrcka and Piotrowski 2002).

The geological profile is also a result of irreversible vertical glacial movements. This profile, to a high degree, refers to structures of Zechstein-Mesozoic substratum, modified by processes of erosion, denudation and glacial tectonics (Maksiak et al. 1978, Dobrcka and Piotrowski 2002).

In the investigated region, subterranean water of the first water-bearing horizon occurs in sands and gravels that cover on boulder clays. The water level settles down at depths from 3 to over 20 m, which depends on the shape of the ground surface (Madejski and Madejska 1995). As the impermeable substratum is shaped in the diversified way, and the values of filtering factor are variable within permeable formations; the flow direction of this water can change locally. Generally, it is accepted that it is directed towards the Lake Pile or Piława River (Sołtysik and Rybka 1993).

According to documentation of the hydrogeological hole (No. 1638 Liszkowo PGR), in the discussed area there are still three lower situated water-bearing horizons with tense mirror. Their roof was drilled at depths of 103, 84, and 78 m b.s.l (Żogała et al. 2005). The first three horizons were drilled right under boulder clays, and the fourth one – under the muds. Electroresistivity measurements, that we carried out, did not let us identify hydrogeological conditions so precisely.

The water-bearing horizon, which covers in Miocene formations right under boulder clays of Pleistocene, appears distinctly. One can suppose that it corresponds to the third and the fourth water-bearing horizons which were drilled in the hydrogeological hole in Liszkowo (Żogała et al. 2005).

### 3. Aim and methodology of measurements

Denaturations cause modifications of physical features of the soils. In the case of electrical resistivity, denaturation of oil substances causes its increase, and in the case of electrical conductivity – its decrease. The size of anomalies depends on the concentration of contaminative substances in geological formations. In the case of pollutants, e.g. ferroconcrete constructions or elements of military infrastructure, the situation is opposite. They cause a decrease of electrical resistivity and an increase of electrical conductivity.

The aim of our work was to localize the anomalies of electrical conductivity and electrical resistivity at the chosen fragment of “A” base of the former military firing ground, and to test their correlation (Fig. 1).



Fig. 1. The former base „A”.

In order to realize the plans, the following geoelectrical methods were applied:

- Electromagnetic inductive prospecting, using EM34-3XL conductometer and applying two aerial spacings of transmitter and receiver coils: 10 m and 20 m. Horizontal position of measuring dipole was utilized. Research was conducted along 6 profiles, about 20 m apart, with automatic recording every 5 seconds. This gave measuring points at the given profiles at a distance of 0.2 – 0.4 m from each other. This helped to define the apparent electrical conductivity of shallow superficial layers in two depths ranges: to 7.5 and to 15 m. The results of field measurements were inter-

preted and described with the help of graphical program called GEOSOFT OASIS MONTAJ.

– Electroresistivity method – multielectrode resistivity imaging, using apparatus of ABEM Lund Imaging System. The measurement was made along one 450 m long profile, with the continuous prospecting method, using measuring symmetrical system of Schlumberger (protocol Schlumberger L and Schlumberger S ). The spacing of electrodes was 5 and 2.5 m. The output current was programmed for: max. 20 mA and min. 2 mA. The results of field measurements were interpreted with the specialist computer program Res 2Dinv. The electroresistivity section was obtained to a depth of about 30 m b.t.s. It was described with the help of graphical program GEOSOFT OASIS MONTAJ.

#### 4. Analysis of the results. Conclusions

The maps of modifications of apparent ground conductivity to a depth of about 7.5 m (Fig. 2) and 15 m (Fig. 3) were made. The values of conductivity from 5 to 8 mS/m to a depth of about 7.5 m, and values of about 11 to 15 mS/m to a depth of about 15 m, were obtained. Very high values of resistivity were obtained on the electroresistivity section (Fig. 4).

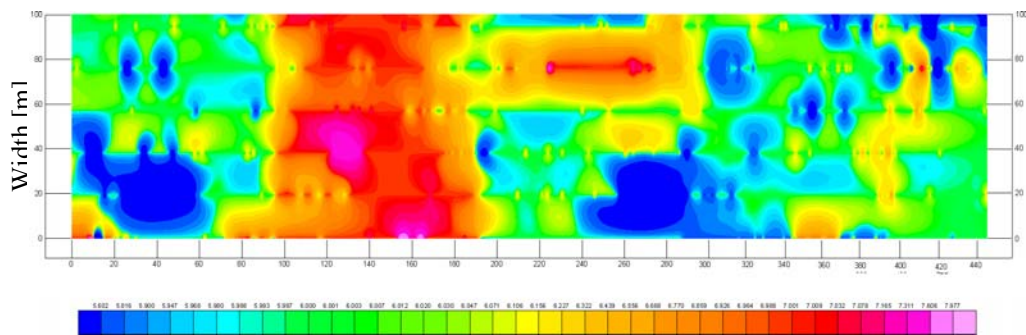


Fig. 2. Change of apparent conductivity of soil to depth  $h = \sim 7.5$  m (conductometr EM34-3XL, HD10).

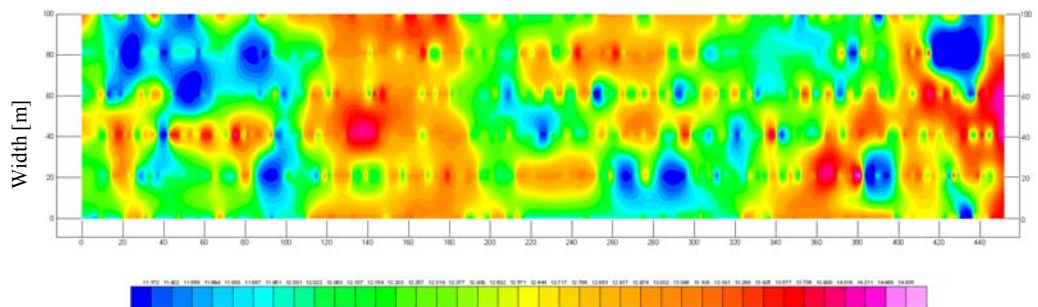


Fig. 3. Change of apparent conductivity of soil to depth  $h = \sim 15$  m (conductometr EM34-3XL, HD20).

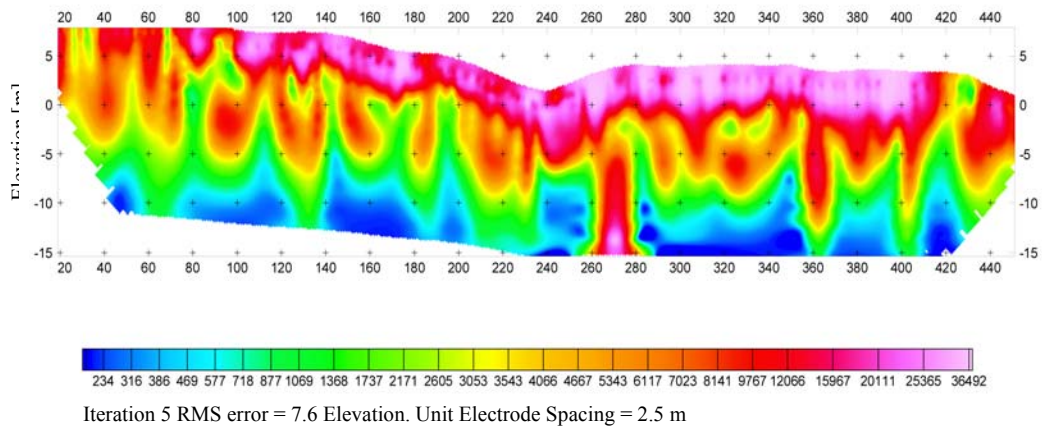


Fig. 4. Model resistivity with topography.

The high-resistivity zone (over  $10 \text{ k}\Omega\text{m}$ ) appears on the map of electroresistivity section, with very irregular underclay. It reaches the depth of about 7.5 m, except of one place where the underclay was not reached. Within this zone, a very high-resistant zone (over  $20 \text{ k}\Omega\text{m}$ ) was assigned. Its thickness is about 2.5 m b.t.s. It may be connected with the following factors:

- A very high-resistant layer of hardpan, with a thickness of 1 m, occurs in the studied area. This caused a flow of very low currents (about 2-5 mA) in the course of realization of electroresistivity measurements (electrodes had to be hammered very deeply).

- In the area where the electroresistivity section was realized, there are remains of concrete foundations and debris which are visible in the area.

Irregular underclay of the layer (with resistance of  $10 \text{ k}\Omega\text{m}$ ) may be connected with containers that were found in the area of electroresistant and electromagnetic studies. The so-called “icicles” (“sopelki”), which are visible on the electroresistant section, can be followed on the map of apparent electrical conductivity in the depth of both 7.5 and 15 m. In most cases, these anomalies correlate with each other (stronger ones – to a depth of 7.5 m and weaker ones – to 15 m).

We can think that the anomalies that have high electrical resistivity correlate with the anomalies that have lower conductivity. This can be connected with oil denaturations because it is proved that there were containers in this area. At the same time, you can not always separate whether these anomalies are connected only with denaturations or also with pollutants with military infrastructure, because the containers were found in places where there are also some traces of foundations.

## References

- Dobracka, E., and A. Piotrkowski, 2002, *Budowa geologiczna i rzeźba powierzchni podczwartorzędowej*. IX Konferencja "Stratygrafia plejstocenu Polski", Borne Sulinowo, 85-92, Wydawnictwo Uniwersytetu Śląskiego.
- Madejski, C., and E. Madejska, 1995, *Raport o zanieczyszczeniach gruntu, wód podziemnych i powierzchniowych produktami ropopochodnymi i innymi substancjami chemicznymi wraz z wyceną szkód ekologicznych na terenie opuszczonego przez wojska Federacji Rosyjskiej poligonu wojskowego "Borne Sulinowo"*, Przedsiębiorstwo geologiczne Polgeol, Warszawa.
- Maksiak, S., W. Mróz and M. Nosek, 1978, *Objaśnienia do mapy geologicznej Polski w skali 1:200 000, arkusz Szczecinek*, Wydawnictwa geologiczne, Warszawa.
- Sołtysik, J., and A. Rybka, 1993, *Raport o zanieczyszczeniach gruntu i wód podziemnych produktami ropopochodnymi i innymi substancjami chemicznymi na obiekcie opuszczonym przez wojska Federacji Rosyjskiej Borne Sulinowo*, Wojskowa Akademia Techniczna, Exbud – 22 Hydrogeotechnika, Warszawa, Kielce.
- Żogała, B., K. Wzientek, W.M. Zuberek, R. Dubiel and M. Rusin-Żogała, *The Resistivity Imaging Survey of the Chemical Waste Dumping Site*, Proc. of the 11<sup>th</sup> Meeting Environmental and Engineering Geophysics, Palermo, P-008.

*Accepted October 16, 2006*

## **Estimation of Dimension of a Regular-Type Sinkhole Activated by Abandoned Shafts**

Zenon PILECKI<sup>1,2</sup> and Adam BARANOWSKI<sup>2</sup>

<sup>1</sup>AGH University of Science and Technology  
Mickiewicza 30, 30-025 Kraków, Poland  
e-mail: pilecki@min-pan.krakow.pl

<sup>2</sup>Mineral and Energy Economy Research Institute  
Polish Academy of Sciences  
Wybickiego 7, 31-261 Kraków, Poland

### **A b s t r a c t**

Sinkholes are natural phenomena in the landscape that cover the majority of old mining sites of shallow hard coal and zinc-lead exploitation in the Silesian Coal Basin and in the Olkusz area. Each sinkhole has unique characteristics due to the mechanism of its occurrence. Some of them are related to old, abandoned shafts, often not quite well closed.

Dependence of sinkhole diameter upon overburden soil parameters has been established by numerical modelling. This dependence correlates quite well with the hypothesis of Professor Chudek, which has not been proved yet.

The paper discusses some theoretical aspects of sinkhole occurrence in the conditions of the Silesian Coal Basin. In the core part, basic assumptions and results of numerical calculations are presented. Finally, the calculated dependence and the resultant graphs are compared to the analytical ones.

### **1. Introduction**

The origin of discontinuous surface deformations can be traced back not only to post-extraction voids, but also to inadequately safeguarded or abandoned shafts collapsing. The knowledge of the old small mine shafts used in the long past to extract shallow coal and ore deposits in the Upper Silesian Coal Basin (GZW) and in the Olkusz area is poor. The information on their locations is incomplete and the preserved old mine plans do not warrant finding their outlets on the surface.

Only a small portion, mere 5%, of all discontinuous surface deformations observed in the GZW area occurred due to improper closure practices of shafts and small pits (Chudek 2002). This does not mean that the hazard they pose, mainly for civil engineering, is insignificant. The areas threatened by the possibility of sinkhole formation can be identified, but it is impossible to forecast the time of their occurrence. For instance, the probability of destruction of a shaft closed to the relatively modern standard, by being covered by a reinforced concrete plug, increases with time due to developing degradation of both its lining and the surrounding rockmass. It could also happen that the material filling a closed shaft shifted, creating voids. The fill material may be drawn off into the excavations adjacent to the shaft if the seal separating them from the shaft pipe is damaged or was not installed.

The surface area around the shaft may gradually settle down or form a sinkhole in an abrupt manner. The following can be named as the major factors influencing the process of formation of shaft-related sinkholes:

- Unfavourable groundwater conditions resulting from heavy rainfalls, which may cause shaft fill to be washed away, suffosion of the medium surrounding the shaft barrel or physical or chemical corrosion of the shaft lining;
- Progressing disintegration of the shaft or pit lining;
- “Washing out” of the shaft fill material;
- Increased load on the ground surface from newly erected structures;
- Dynamic loads caused by traffic-related vibrations or seismicity.

One of the most important parameters determining the level of risk for the land surface users is the maximal dimension of the sinkhole area. This work describes one of the methods, based on numerical modelling, of determining sinkhole size. The method may be used to forecast the diameter of a sinkhole not only when it is shaft-related but also when it stems from other underground voids of more or less known dimensions.

Available are also analytical methods, described in the works of Chudek (2002) or Bell (1988), allowing to calculate the extent of a sinkhole and linking it to the properties of loose overburden. In this paper the authors compare the results obtained by numerical modelling with those calculated analytically.

## **2. Analytical Method of Calculating the Ground Level Size of a Sinkhole**

Discontinuous surface deformations are defined by Chudek (2002) as such changes to the structure of the surface that break its continuity. To avoid misunderstanding, because of numerous meanings and understandings of the term, let us accept that in this paper a sinkhole shall mean such discontinuous deformation of the surface that is characterized by sinking of the ground surface.

The rockmass prone to form sinkholes has to be divided into two distinct zones directly influencing the type and extent of discontinuous deformations (Chudek 2002):

- The strata of competent rock (base rock), containing the void,
- The layer of loose overburden.

The process of deformation of the rockmass leading to the formation of a sinkhole on the surface has been described in numerous Polish and foreign publications, e.g. by Chudek (2002), Fajkiewicz *et al.* (2004) or Popiołek and Pilecki (2005). From these works the formation of a sinkhole may be outlined to proceed as follows:

- A zone of fractured rock is formed by tensile stresses occurring in the immediate roof of the void. Its shape is in general similar to that of a “stress dome”. Its height depends on the void’s volume, the support and the properties of the surrounding rock (base rock),
- With time, the fragments of fractured and loosen rocks fall down, forming a fall at the bottom of the excavation. The position of the excavation’s roof moves upward towards the surface. A secondary void is created between the roof and the collapsed rock,
- The developing rheological processes, which are usually intensified by water–weathering, cause the fracture zone in the roof of the excavation to move towards the ground surface. At the same time, the volume of the void diminishes because the bulk volume of caved rock is greater than that of solid rock,
- If the thickness of the base rock strata through which the void “travels” on its way up is adequate, the secondary void may become completely filled. If it is too small for the void to be completely filled until its roof reaches the loose overburden, it is quite likely that a sinkhole will form on the land surface.

If the overburden comprises loose soil, one has to expect the horizontal size of the sinkhole to be greater than that of the void propagating through the base rock. The size of the sinkhole will depend on the thickness of the loose soil overburden, soil strength properties, groundwater conditions and the criterion for the void to fill itself. In the case of old, closed shafts, sinkhole hazard exists if the shaft’s lining installed in the loose soil layer disintegrates, or in the simplest cases if the plug closing the shaft’s mouth collapses.

The greatest diameter  $D$  of a sinkhole on the ground surface can be calculated from the equation (Bell 1988):

$$D = 2 \cdot Z \tan(90^\circ - \Theta) + 2r, \quad (1)$$

where  $Z$  is the thickness of the loose overburden,  $\Theta$  is the angle of internal friction of the loose overburden material, and  $r$  is the radius of the shaft.

The relationship (1) is illustrated in Fig. 1. The greater the thickness of the layer of loose overburden, the greater the area of the sinkhole.

### 3. Numerical Method of Calculating the Ground Level Size of a Sinkhole

#### 3.1 Methodology of the calculations

The quality of results obtained by numerical modelling to a great extent depends on a number of complex issues, beginning with the size and shape of the model, boundary and initial conditions, material property constants or the accepted calculation methodology. The numerical calculations were done for the small, old, closed

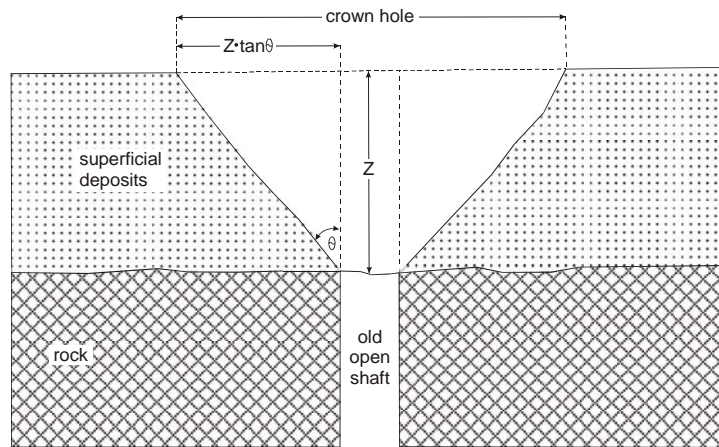


Fig. 1. Method of calculating the diameter of a sinkhole formed in loose overburden above an old shaft (Bell 1988).

shaft “Andrzej” situated in the Olkusz area. Normally, the input data collection consists in establishing the geomechanical properties of the rock medium. In the case of “Andrzej” shaft the material constants were obtained from the results of archival tests and complemented by the information available in the literature. The shaft was the cause of a medium-sized sinkhole (diameter of the funnel 6 m, depth 2 m). The shaft’s probable depth was 32 m and its cross-section was a square with a side of 2 m.

The calculations were made assuming plain strain conditions in an elastic-plastic medium and the Mohr-Coulomb failure criterion. The modelling procedure consisted of the following basic stages:

- constructing the model,
- obtaining the equilibrium of forces in the field of primary stresses,
- calculating the model in several steps of shaft’s constructing, obtaining in the end the equilibrium of forces in the field of secondary stresses,
- conducting a what-if analysis of stress and deformation for various overburden thickness and different types of overburden material.

Figure 2 shows the geometry of the model and its boundary and initial conditions. Axial symmetry of the model was assumed in order to increase the efficiency of the calculations. The values of the vertical and horizontal stress components were assumed as variable within the range defined by the model’s depth, with the vertical to horizontal stress ratio assumed as  $\lambda = 0.42$ . The model had the shape of a 150 m high and 100 m wide rectangle. The computation zone size was 0.5×0.5 m.

When analyzing the relationship between the diameter of the sinkhole and the depth of the overburden it was assumed, according to eq. (1), that the value of the shaft diameter does not influence the behaviour of the overburden material but only the diameter of the sinkhole.

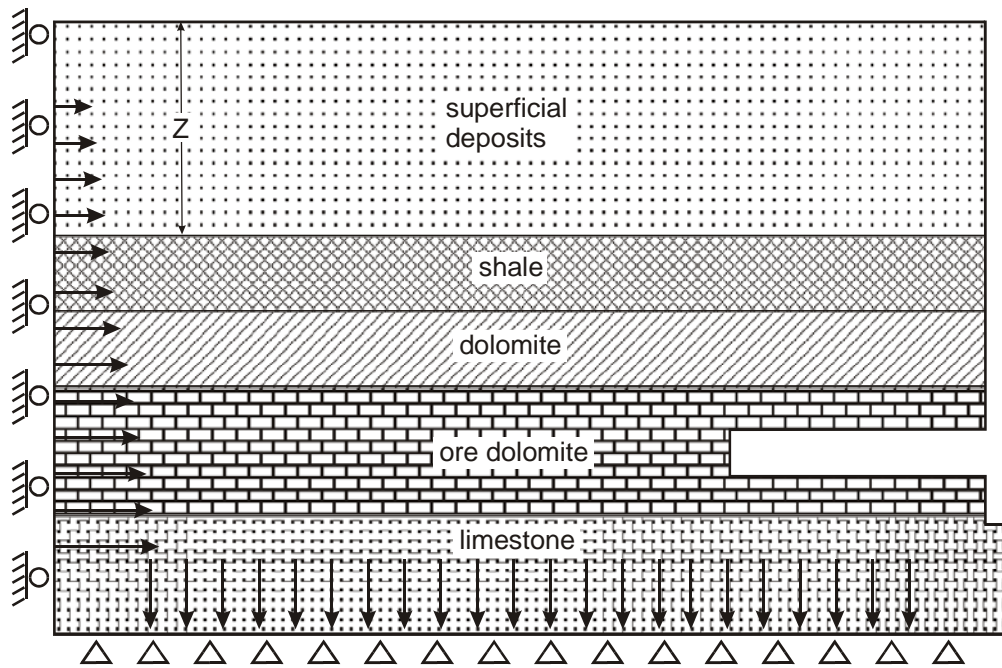


Fig. 2. Computational model with the boundary and initial conditions.

Geological structure of the model was compiled from archival information. The base rock zone comprised four layers and the overburden – one. The parameters of the overburden material were varied according to soil type. The model did not take ground water into account as the rockmass was assumed to be self-draining. The influence of the seeping water on the behaviour of the medium was also disregarded as a separate issue to be considered.

The numerical modelling was done with the use of *FLAC 2D v.4.0.* developed by Itasca, USA, which utilizes the finite difference method.

### 3.2 Material constants

It was assumed that the overburden was composed of one type of material and separate calculations were conducted for three types of soil (Table 1). The base rock was taken to comprise four strata (Table 2).

### 3.3 Analysis of the results

Figure 3 shows an example of calculation results of predicted behaviour of the overburden (sand and gravel) in the shaft's influence zone. The diameter of the formed funnel was approx. 6 m, which matched the field observations (Fig. 3a). Increasing the thickness of the overburden, the funnel's diameter increased up to a certain boundary value (critical), above which a "chimney" effect took place (Fig. 3b). This effect is illustrated by the graph of the dependence of normalized sinkhole diameter on the overburden thickness (Fig. 4). Character of the changes is bimodal. The dependence is

Table 1  
The overburden material properties assumed for the calculations

Soil type	Density [kg/m <sup>3</sup> ]	Bulk modulus [Pa]	Shear modulus [Pa]	Friction angle [deg]	Cohesion [Pa]
Sand and gravel	1500	1.50E8	6.92E7	39	0
Clay	2060	2.00E7	9.23E6	15	2.60E4
Loam	2090	1.80E7	5.11E6	9	1.12E5

Table 2  
The base rock material properties assumed for the calculations

Stratum number	Density [kg/m <sup>3</sup> ]	Bulk modulus [Pa]	Shear modulus [Pa]	Poisson ratio	Friction angle [deg]	Tensile strength [Pa]	Cohesion [Pa]
2 layer	1900	8.33E9	3.85E9	0.30	13.0	1.2E+07	7E4
3 layer	2550	7.11E9	5.33E9	0.20	36.3	6.2E+06	9E6
4 layer	2650	7.84E9	5.96E9	0.20	36.3	6.9E+06	9E6
5 layer	2100	2.26E0	1.11E0	0.20	36.3	1.5E+06	9E6

strata: 2 – (Keuper series) serpentine silt and mudstone; 3 – (Middle Triassic) dolomite; 4 – (Middle Triassic) ore-bearing dolomite; 5 – (Middle Triassic) limestone

nonlinear up to critical depth and linear below it. For example, the behavior of the model in the nonlinear mode can be approximated by polynomial or logarithmic equations (Fig. 5):

- for sands and gravels

$$y = -0.0204x^2 + 2.4355x - 0.7549; \quad R^2 = 0.9984 \quad (2)$$

- for clays

$$y = 9.4168 \ln(x) - 1.4107; \quad R^2 = 0.9169 \quad (3)$$

- for loam

$$y = 6.4244 \ln(x) + 3.6114; \quad R^2 = 0.9068 \quad (4)$$

where  $y$  is the maximum sinkhole diameter within the analyzed range  $x$ , and  $x$  is the overburden thickness.

For comparison Figs. 4 and 5 show the graphical presentation of sinkhole diameter obtained by means of the analytical method from eq. (1). It can be seen in Fig. 4 that after the thickness of the overburden comprising loose material – sand and

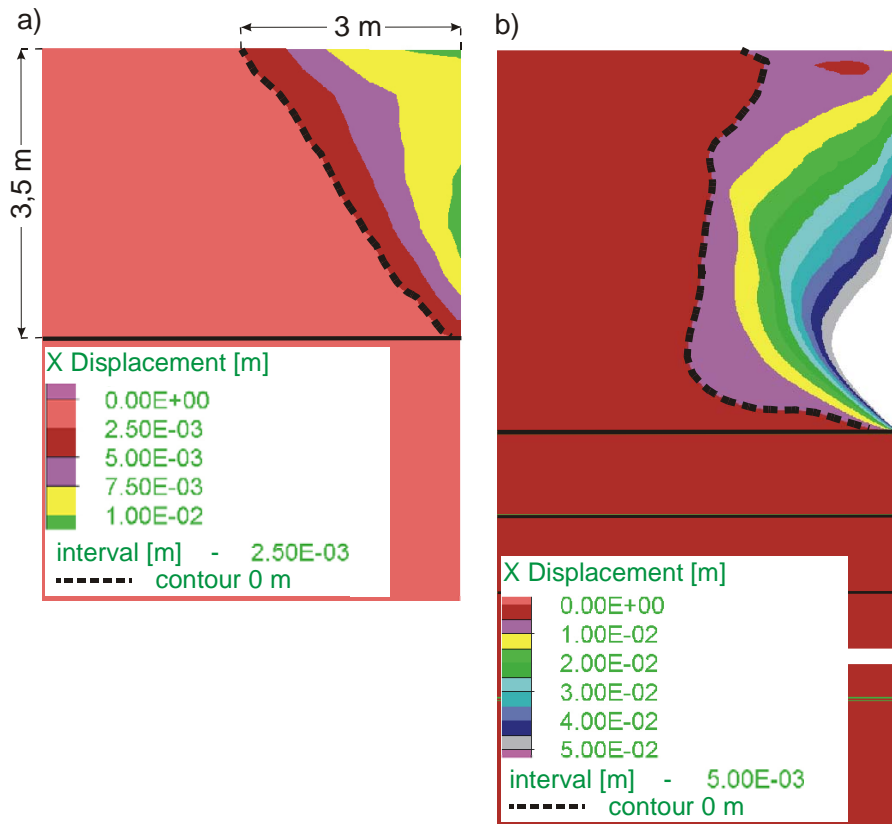


Fig. 3. An example of the distribution of horizontal displacements in the area of sinkhole formation above the shaft pipe for overburden thickness of 3.5 m (a) and greater than the boundary value, which is variable and depends on material type (b).

gravel – exceeds 45 m, the diameter of the sinkhole remains constant. The results obtained for a specific sinkhole diameter by analytical and numerical methods are roughly the same up to the overburden width boundary value. Figure 5 shows the dependence of sinkhole diameter on the overburden thickness for all the types of overburden material considered (Table 2). In the case of clay and loam the boundary condition values of overburden thickness is approx. 10 and 13 m and the sinkhole diameter does not exceed 25 m.

#### 4. Conclusions

The results of numerical calculations show that if the overburden comprises loose material and the base rock formations are competent, the factors determining sinkhole size are the overburden thickness and properties. For the overburden thickness greater than a certain (critical) boundary value, the diameter of the sinkhole remains more or less constant. For typical loose sand-and-gravel formations this limit value is approximately 45 m. It may be assumed that when the overburden thickness

exceeds the limit value, a “chimney formation” process begins. During the process a characteristic bell-shaped deformation appears in the overburden foot.

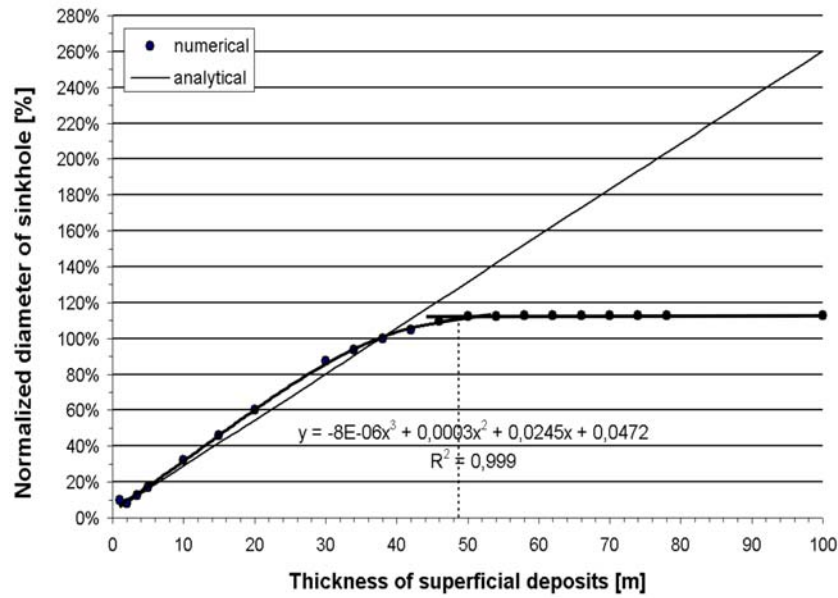


Fig. 4. Dependence of normalized sinkhole diameter on the thickness of overburden comprising sand and gravel.

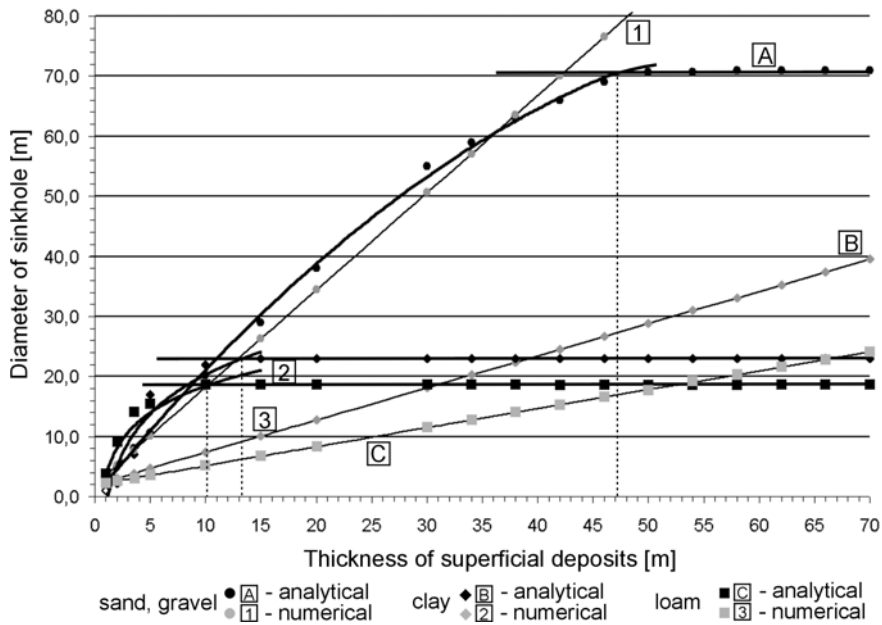


Fig. 5. Dependence of sinkhole diameter on the overburden thickness for various types of material.

The presented numerical analysis was conducted on a relatively simple model of rock mass. Numerical calculations can be used to analyze models of much greater complexity, specifically, the overburdens comprising several layers made of loose and competent material.

#### References

- Bell, F.G., 1988, *Land development. State-of-the-art in the location of old mine shafts*, Bull. of the Int. Ass. of Eng. Geology **37**, 91-98.
- Chudek, M., 2002, *Geomechanika z podstawami ochrony środowiska górniczego i powierzchni terenu*, Wyd. Politechniki Śl., Gliwice.
- Popiołek, E., and Z. Pilecki (red.), 2005, *Ocena przydatności do zabudowy terenów zagrożonych deformacjami nieciągłymi za pomocą metod geofizycznych*, Wyd. IGSMiE PAN, Kraków.

*Accepted 10 April 2006*



## **Natural Radioactivity of Selected Rocks from the Vicinity of the Rožná Uranium Deposit**

Aleksandra SITAREK, Jarosław BADERA and Grzegorz LIZUREK

University of Silesia, Faculty of the Earth Sciences  
ul. Będzińska 60, 41-200 Sosnowiec, Poland,  
e-mails: asitarek@us.edu.pl; jbadera@wnoz.us.edu.pl; glizurek@us.edu.pl

The aim of the paper is to present preliminary results of studies of natural radioactivity of selected rocks from the Vysočina region occurring relatively close to the Rožná (Czech Republic) uranium deposit. Measurements allowed to determine the activity concentrations of  $^{40}\text{K}$  and nuclides from  $^{238}\text{U}$  and  $^{232}\text{Th}$  series in investigated rocks and compare the noted activities with average activity concentrations of these radionuclides in the continental crust and soil. Appearance of regional natural radioactivity anomaly could be determined on the basis of the obtained results.

### **1. Geological Setting and Description of the Samples**

All the sampled places are located within the Strážek moldanubicum – metamorphosed volcano-sedimentary complex of the Precambrian age. Two different series of rocks can be identified in this complex. One group is called monotonous or uniform, the other – variegated or diverse. Various types of paragneisses (biotite, sillimanite, muscovite), migmatized to a different extent, are most common in both series. Moreover, the diverse group contains granitogneisses, amphibolites, quartzites, marbles, erlans, serpentinites, piroxenites, granulites, pegmatites and graphite-rich rocks. All the studied rock samples represent the diverse group of Strážek Moldanubicum. Location of sampled places is shown in Fig. 1.

#### ***Dolní Rožinká***

The Rožná uranium deposit is located near Dolní Rožinká, 7 km southwest of Bystřice nad Pernštejnem. It is a typical example of hydrothermal uranium ores connected with dislocation zones (Hájek 2001, Jirásek and Badera 2005) (Fig. 2). The faults in plagioclase-biotite gneisses are filled by brecciated rocks cemented by my-

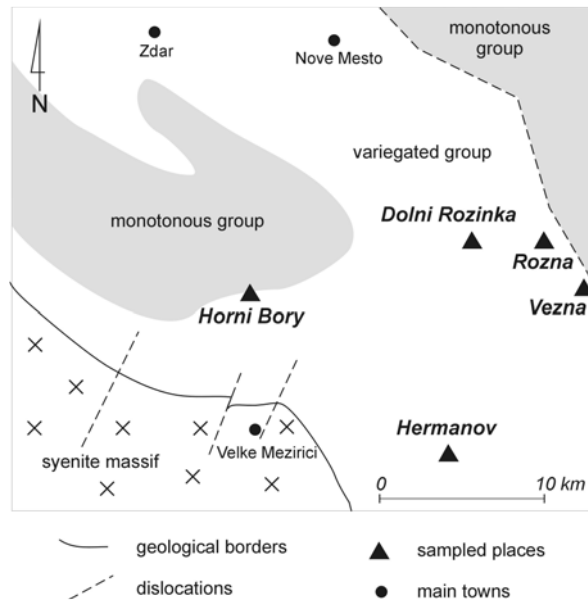


Fig. 1. Location of sampled places on the background of the Strážek moldanubicum.

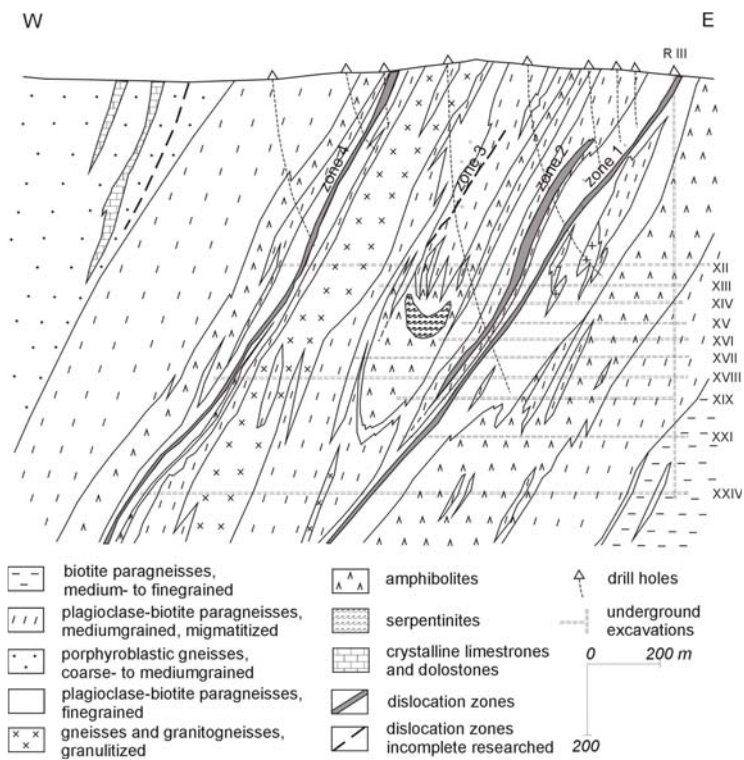


Fig. 2. Cross-section of the Rožná deposit (after Aulický *et al.*, 2003, modified).

lonite with admixture of graphite and pyrite, and cut by carbonate veinlets. Ores have a form of large bodies with disseminated mineralization. Uranium minerals are found in six associations (Šikola 2001). Uraninite and coffinite (rarely brannerite and monroseite) are accompanied with calcite and chlorite. Secondary minerals (liebigite, metaautunite etc.) are found, too. Ore-bearing rocks are metasomatically altered by processes of muscovitization, albitization, chloritization or carbonatization (Arapov *et al.* 1984). Uranium contents in ore bodies differ in the range of 0.01-0.5%, reaching up to 5% in few fragments of the deposit. The average content of uranium in the exploited reserves amounts to about 0.3% (Kavina *et al.* 2004).

Four rock samples were collected from the Rožná uranium deposit. The first one – an uranium ore – is a grey massive finegrained biotite gneiss with single calcite-chlorite veinlets and U-pyrite mineralization. The second sample is a black finelaminated biotite gneiss with numerous porphyroblasts of garnet. Next one is a coarsegrained quartz-actinolite pegmatite and the last – a grey-green finegrained and fine-laminated amphibolite. Sample no. 1 was collected from an underground excavation and no. 2-4 from a heap of barren mining wastes.

### **Rožná**

The Rožná Li-pegmatite deposit is located 6 km south of Bystřice nad Pernštějnem. There is a quarry on the Hradisko hill, where the pegmatite was exploited in the 19<sup>th</sup> and the first half of 20<sup>th</sup> century as a chemical and industrial raw material. The deposit is situated near the contact with the Svratka crystalline complex. The length of pegmatite zone is about 1 km and its thickness reaches 35 m (Pařízek 1999). It is built of several longitudinal bodies striking NW-SE and dipping toward NE at an angle of 50°. The pegmatite contains some textural kinds (blocked, metasomatic etc.). Quartz, albite, microcline, biotite, lepidolite and schörl are the main minerals (Bernard 1981). Among other minerals, monazite and zircon were found, too.

The rock sample collected from the Hradisko hill is a grey-pink coarsegrained massive pegmatite composed of quartz and feldspars, additionally muscovite, biotite, lepidolite and elbaite.

### **Věžná**

The Věžná serpentinite old quarry is situated 8 km south of Bystřice nad Pernštějnem within the contact zone of the Moldanubicum and the Svratka crystalline complex (Zimák 1997). The rock is built mainly of antigorite. Fissures are filled by chrizotile, chlorite, magnezite or silica minerals (Kovář 1998).

From this quarry a grey massive finegrained serpentinite was collected.

### **Horní Bory**

It is an active stone-pit located 8 km north of Velké Meziříčí within the Bory granulite massif. Different kinds of granulites, additionally gneisses, migmatites and pegmatites are exposed there. The main minerals of these rocks are quartz, orthoclase, plagioclase, biotite, muscovite, garnet, cyanite, sillimanite, cordierite, apatite and tourmaline (Bernard 1981).

A finegrained quartz-plagioclase leucogneiss with single biotite lamines was collected from Horní Bory quarry.

### **Heřmanov**

This is a place of occurrence (an excavation made by collectors) of famous Heřmanov “balls”, 12.5 km east from Velké Meziříčí. They are formed within the contact zone of pegmatite and serpentinite and built of compact flogopite cores covered by fibrous anthophyllite. The flogopite makes also a matrix between individual balls and it is often altered to hydroflogopite or vermiculite (Bernard 1981).

From Heřmanov a compact flogopite-anthophyllite aggregate was collected to carry out measurements.

## **2. Materials and Methods**

The natural radioactivity of  $^{40}\text{K}$ ,  $^{208}\text{Tl}$ ,  $^{212}\text{Pb}$ ,  $^{212}\text{Bi}$ ,  $^{214}\text{Pb}$ ,  $^{214}\text{Bi}$  and  $^{228}\text{Ac}$  in the collected rock samples was measured using the Canberra semiconductor detector in the Laboratory of Natural Radioactivity of Faculty of the Earth Sciences in Sosnowiec. The Canberra XtRa (Extended Range) HPGe detector model GX3020 (30% efficiency, crystal length: 58 mm, diameter: 50.5 mm) was used. The resolutions of the detector are excellent and equal 0.86 keV at 122 keV and 1.76 keV at 1.33 MeV. This model of detector was constructed for *in situ* measurements but can be also used in laboratory conditions when shielded with lead bricks to limit surroundings influence. Each rock sample was crushed for homogenization previously. Measurements were carried out in Marinelli (450 ml) geometry. Counting time was set at 24 h for each rock sample. The obtained spectra were analyzed with the use of Canberra Genie 2000 software version 3.0.

## **3. Results and Discussion**

Activity concentrations of  $^{40}\text{K}$ ,  $^{208}\text{Tl}$ ,  $^{212}\text{Pb}$ ,  $^{212}\text{Bi}$ ,  $^{228}\text{Ac}$ ,  $^{214}\text{Pb}$ ,  $^{214}\text{Bi}$  and  $^{226}\text{Ra}$  in rock samples collected from the Vysočina region measured using semiconductor detector (HPGe) are given in Table 1.

### **$^{40}\text{K}$**

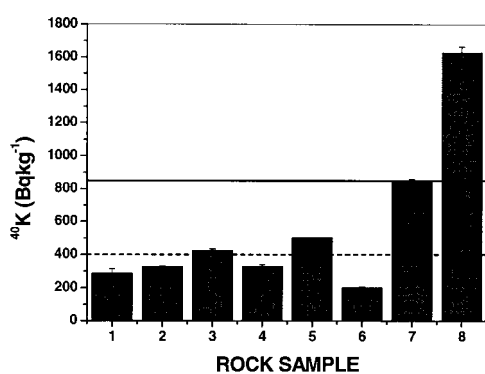
The highest activity concentration of  $^{40}\text{K}$  was noted in flogopite-anthophyllite aggregate from Heřmanov ( $1629 \pm 37 \text{ Bqkg}^{-1}$ ). The obtained value is distinctly higher (almost twice, see Fig. 3) than the average concentration of this nuclide in continental crust that equals  $850 \text{ Bqkg}^{-1}$  (Eisenbud and Gesell 1997). Such high value of activity concentration of  $^{40}\text{K}$  is associated with high contents of flogopite and hydroflogopite in mineral composition of the rock. Only one sample, the quartz-plagioclase leucogneiss from Horní Bory has  $^{40}\text{K}$  activity concentration close to the average concentration in continental crust ( $841 \pm 19 \text{ Bqkg}^{-1}$ ). In this rock, such K-containing minerals as orthoclase, biotite, muscovite and apatite occur. The rest of rocks have activity concentration of  $^{40}\text{K}$  similar or lower than the average concentration of this isotope in soil that equals  $400 \text{ Bqkg}^{-1}$  (Eisenbud and Gesell 1997) with the exception of Li-pegmatite

Table 1

Measured activity concentrations of  $^{40}\text{K}$ , nuclides from  $^{232}\text{Th}$  ( $^{208}\text{Tl}$ ,  $^{212}\text{Pb}$ ,  $^{212}\text{Bi}$ ,  $^{228}\text{Ac}$ ) series and  $^{238}\text{U}$  series ( $^{214}\text{Pb}$ ,  $^{214}\text{Bi}$ ) with calculated  $^{226}\text{Ra}$  activity concentrations in investigated rock samples. Uncertainties are given within one standard deviation

Nuclide	Activity concentration ( $\text{Bqkg}^{-1}$ )							
	Dolní Rožinká				Rožná	Věžná	Horní Bory	Heřmanov
	uranium ore	biotite gneiss with garnets	quartz-actinolite pegmatite	amphibolite	Li-pegmatite	serpentinite	quartz-plagioclase leucogneiss	flogopite-antophyllite aggregate
$^{40}\text{K}$	289±28	326±7	427±10	331±8	504±2	203±5	841±19	1629±37
$^{208}\text{Tl}$	–	3.9±0.4	4.1±0.14	0.3±0.1	1±0.1	2.7±0.1	6.3±0.2	13.7±0.3
$^{212}\text{Pb}$	–	16.5±0.5	13.5±0.8	1.8±0.2	5±0.2	9.8±0.4	25.3±0.8	51.7±2
$^{212}\text{Bi}$	–	9.4±0.8	8.6±1.5	–	3.4±0.5	8±0.6	14.9±0.9	30±1
$^{228}\text{Ac}$	–	13.2±0.3	13.2±0.9	1.4±0.3	4.5±0.2	8.8±0.2	20.5±0.4	43±0.7
$^{214}\text{Pb}$	28754±834	39.9±1.2	1081±56	46.1±1.8	8±0.3	10.5±0.4	23.3±1	60.9±2
$^{214}\text{Bi}$	26350±155	35.7±0.6	975±62	41.1±0.8	7.1±0.3	9.2±0.3	27.1±0.5	52.6±0.8
$^{226}\text{Ra}^*$	27552±1551	37.8±0.9	1028±92	43.6±1.3	7.6±0.3	9.9±0.4	29.7±0.8	56.8±1.4

\* Based on  $^{214}\text{Pb}$  and  $^{214}\text{Bi}$  activity concentrations



No.	Rock sample	
1	uranium ore	Dolní Rožinká
2	biotite gneiss with garnets	
3	quartz-actinolite pegmatite	
4	amphibolite	
5	Li-pegmatite	Rožná
6	serpentinite	Věžná
7	quartz-plagioclase leucogneiss	Horní Bory
8	flogopite-antophyllite aggregate	Heřmanov

Fig. 3. Comparison of  $^{40}\text{K}$  activity concentrations (dark gray bars) in all measured rock samples collected from the Vysočina region with average activities reported for continental crust (solid line) and for soil (dashed line) (Eisenbud and Gesell 1997).

from Rožná in which this value is exceeded and equals  $504 \pm 2 \text{ Bqkg}^{-1}$ . In this pegmatite microcline, biotite and lepidolite occur in mineral composition of the rock. In samples collected from Dolni Rožinka, the  $^{40}\text{K}$  activity concentrations vary in the range from  $427 \pm 10 \text{ Bqkg}^{-1}$  in the quartz-actinolite pegmatite to  $289 \pm 28 \text{ Bqkg}^{-1}$  in the uranium ore. The lowest activity concentration of this isotope was noted in serpentinite from Věžná ( $203 \pm 5 \text{ Bqkg}^{-1}$ ).

### $^{232}\text{Th}$ series

As shown in Table 1, radioactive equilibrium between progenies in  $^{232}\text{Th}$  series can be assumed. There is a slight disequilibrium shown between Tl and Ac in the case of rocks characterized by small activity concentration of Th series (Li-pegmatite, amphibolite), but these exceptions are noted for values of activity concentration at the detection limit levels, that can cause some variations because of small counts for considered lines. Any other signs of disequilibrium between  $^{228}\text{Ac}$  and  $^{208}\text{Tl}$  which can be seen in Table 1 are covered by values of  $^{212}\text{Bi}$  and  $^{212}\text{Pb}$ . The activity concentrations of  $^{232}\text{Th}$  in investigated rocks were estimated on the basis of  $^{228}\text{Ac}$  activity concentration. The highest  $^{228}\text{Ac}$  ( $^{232}\text{Th}$ ) activity concentration was noted in flogopite-antophyllite aggregate from Heřmanov ( $43 \pm 0.7 \text{ Bqkg}^{-1}$ ). The obtained value is at the level of the average activity concentration of thorium in continental crust that equals  $44 \text{ Bqkg}^{-1}$  (Eisenbud and Gesell 1997) and exceeds clearly the average Th series activity concentration in soil that equals  $37 \text{ Bqkg}^{-1}$  (Eisenbud and Gesell 1997).

No other measured rock is characterised by activity of thorium series at the level of the average activity concentration of that series in both continental crust and soil.

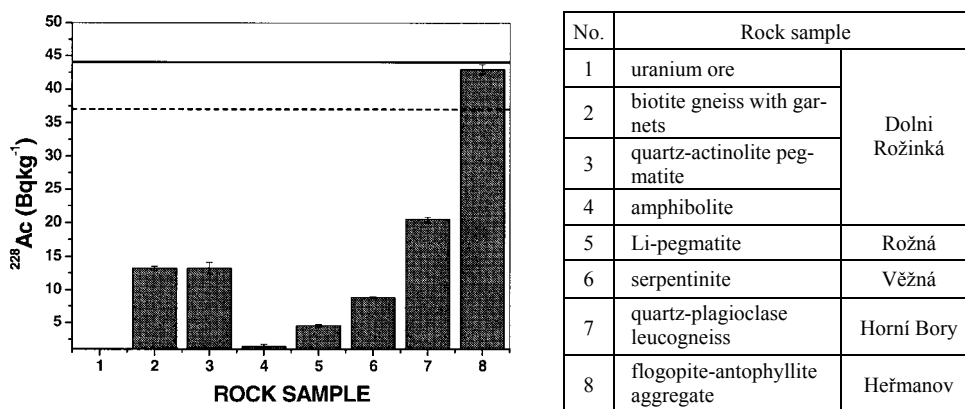


Fig. 4. Comparison of  $^{228}\text{Ac}$  ( $^{232}\text{Th}$ ) activity concentrations (gray bars) in all measured rock samples collected from the Vysočina region with average activities reported for continental crust (solid line) and for soil (dashed line) (Eisenbud and Gesell 1997).

The data in Fig. 5 show a good correlation (correlation coefficient  $R = 0.92$ , determination coefficient  $R^2 = 0.85$ ) between activity concentrations of  $^{40}\text{K}$  and  $^{228}\text{Ac}$

( $^{232}\text{Th}$ ) as observed for the studied region. Result of the goodness-of-fit test shows level of significance  $\alpha = 0.01$ . Linear regression for that data can be written as:

$$^{228}\text{Ac} = 0.027 \ ^{40}\text{K} - 2.43 \ [\text{Bq kg}^{-1}]$$

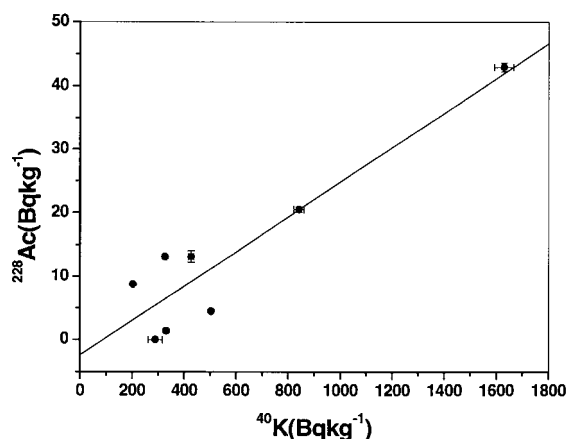


Fig. 5.  $^{228}\text{Ac}$  ( $^{232}\text{Th}$ ) activity concentrations versus  $^{40}\text{K}$  activity concentrations. The solid straight line represents linear regression (correlation coefficient  $R = 0.92$ , determination coefficient  $R^2 = 0.85$ ).

### $^{238}\text{U}$ series

Activity concentrations of  $^{238}\text{U}$  were estimated on the basis of  $^{226}\text{Ra}$  activity concentrations that were deduced from  $^{214}\text{Bi}$  and  $^{214}\text{Pb}$  concentrations with the assumption of radioactivity equilibrium in uranium series. The highest concentration activity of  $^{226}\text{Ra}$  was noted obviously in uranium ore ( $27.6 \pm 1.5 \text{ kBq kg}^{-1}$ ) and then in quartz-actinolite pegmatite ( $1.03 \pm 0.09 \text{ kBq kg}^{-1}$ ). Both of these samples were collected from the uranium mine in Dolni Rožinká. To obtain uranium contents in these rock samples, value of  $^{238}\text{U}$  concentration in ppm was calculated using conversion factors given by Polish Central Laboratory For Radiological Protection ( $1 \text{ Bq kg}^{-1} = 0.08045 \text{ ppm U}$ ). In the uranium ore, the concentration of  $^{238}\text{U}$  equals  $2217 \pm 125 \text{ ppm}$  and in the quartz-actinolite pegmatite it is  $83 \pm 7 \text{ ppm}$ , which means that uranium contents in these samples are about 0.22% and  $< 0.01\%$  respectively.

Comparison of  $^{226}\text{Ra}$  activity concentration measured in all rock samples from the Vysočina region with the average activity concentration of uranium series in continental crust and in soil, that equal  $36 \text{ Bq kg}^{-1}$  and  $22 \text{ Bq kg}^{-1}$ , respectively (Eisenbud and Gesell 1997), is shown in Fig. 6. In the case of two samples, the flogopite-antophyllite aggregate and amphibolite, the activity concentrations of  $^{226}\text{Ra}$  are distinctly higher than the average concentration of  $^{238}\text{U}$  series in the continental crust ( $56.8 \pm 1.4$  and  $43.6 \pm 1.3 \text{ Bq kg}^{-1}$  respectively), whereas in biotite gneiss with garnets the obtained value is close to this average ( $37.8 \pm 0.9 \text{ Bq kg}^{-1}$ ) and in quartz-plagio-

class leucogneiss from Horní Bory the activity concentration of  $^{226}\text{Ra}$  is lower than the average reported for continental crust and equals  $29.7 \pm 0.8 \text{ Bqkg}^{-1}$ . The remaining noted activity concentrations of  $^{226}\text{Ra}$  are clearly below the average concentration of  $^{238}\text{U}$  series in soil ( $9.9 \pm 0.4$  and  $7.6 \pm 0.3 \text{ Bqkg}^{-1}$  in serpentinite and in Li-pegmatite).

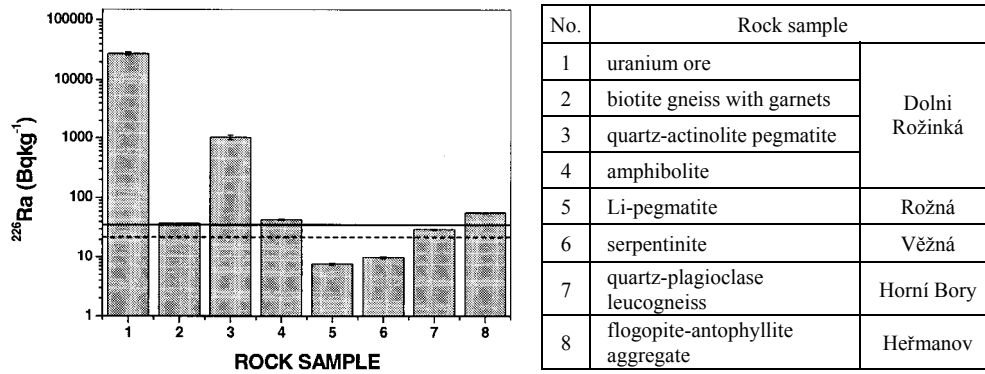


Fig. 6. Comparison of  $^{226}\text{Ra}$  ( $^{238}\text{U}$ ) activity concentrations (light gray bars) in all measured rock samples collected from the Vysočina region with average activities reported for continental crust (solid line) and for soil (dashed line) (Eisenbud and Gesell 1997).

#### 4. Conclusions

The activity concentrations of  $^{40}\text{K}$  depend on mineral composition of rocks to some extent. The highest concentration was noted in K-rich flogopite-antophyllite aggregates from Heřmanov. In the case of leucogneiss from Horní Bory, containing (among others) orthoclase, biotite and muscovite, concentration of  $^{40}\text{K}$  is similar to the average concentration in continental crust. In Li-pegmatite from Rožná, admixtures of microcline, biotite and lepidolite can be a source of this radionuclide. In the other cases, concentrations of  $^{40}\text{K}$  are lower than the average in soil. Curiously, there are very low activity concentrations of  $^{40}\text{K}$  in biotite-rich gneisses from the uranium deposit and its wall-rocks.

In the studied rocks the activity concentrations of  $^{232}\text{Th}$  are very low. The obtained results are smaller than the average concentration of thorium in soil. Only the flogopite-antophyllite aggregate from Heřmanov is characterised by higher value of activity concentration of  $^{232}\text{Th}$  series than the average concentration reported for continental crust and of course soil. There is no thorium content in the uranium ore.

A correlation between concentration of potassium and thorium in all measured rocks can be observed (correlation coefficient  $R = 0.92$ ).

The highest activity concentration of  $^{238}\text{U}$  refers obviously to the uranium ore. Calculated uranium content in measured ore sample equals 0.22%. High activity concentration of  $^{238}\text{U}$  series was noted also in quartz-actinolite pegmatite from the wall-rock of uranium deposit (0.01% of uranium). Concentrations in the other rocks, even from the wall-rock of deposit, are similar or lower than the averages for continental crust and soil.

In the studied area, rocks have greater content of uranium than thorium (whereas the crustal and soil average concentrations of  $^{232}\text{Th}$  are higher than values referring to  $^{238}\text{U}$ ); however, the obtained results (except for the most radioactive samples) do not indicate existence of regional anomaly of natural radioactivity.

#### References

- Arapov, J.A., V.J. Bojcov and N.I. Česnakov (eds.), 1984, *Československá ložiska uranu*, Československý uranový průmysl, Praha.
- Aulický, R., K. Iványi and J. Kafka (eds.), 2003, *Rudné a uranové hornictví České republiky*, Anagram, Ostrava.
- Beck, H.L., J. De Campo and C.V. Gogolak, 1972, *In situ Ge(Li) and Na(Tl) gamma-ray spectrometry*, U.S. Department of Energy, Environmental Measurements Laboratory, HASL-258, New York.
- Bernard, J.H., *et al.*, 1981, *Mineralogie Československa*, Academia, Praha.
- Eisenbud, M., and T. Gessel, 1997, *Environmental radioactivity from natural, industrial and military sources*, Academic Press, San Diego.
- Hájek, A., 2001, *Geologická charakteristika rudního pole Rožná–Olší*, *Minerál* **9**, 2, 118-124.
- Jirásek, J., and J. Badera, 2005, *Rožná – ostatnie eksploatoované zložie uranu w Czechach*, *Prz. Geol.* **11** [in press].
- Kavina, P., J. Starý and M. Vaněček (eds.), 2004, *Surovinové zdroje České republiky*, Nerostné suroviny (stav 2003), ČGS-Geofond, Praha.
- Kovář, O., 1998, *Současné možnosti sběru minerálů v hadcovém lomu u Věžné u Nedvědice*, *Minerál* **6**, 6, 457-458.
- Pařízek, J., 1999, *Objev a těžba lepidolitu v Rožné*, *Minerál* **7**, 4, 299-304.
- Šíkola, D., 2001, *Přehled mineralogických výzkumů rudního pole Rožná–Olší*, *Minerál* **9**, 2, 124–134.
- Zimák, J., *et al.*, 1997, *Průvodce ke geologickým exkurzím, Morava – střední a jižní část*, Vydavatelství Univerzity Palackého, Olomouc, 31-33.

Accepted 10 April 2006



## Natural Radioactivity of Selected Sedimentary Rocks from the Krzeszowice Area

Grzegorz LIZUREK and Aleksandra SITAREK

University of Silesia, Faculty of the Earth Sciences  
ul. Będzińska 60, 41-200 Sosnowiec, Poland  
e-mail: glizurek@us.edu.pl; asitarek@us.edu.pl

### Abstract

Sedimentary rocks from the borders of Krzeszowice graben have been the most popular origin of building materials in the whole Kraków region since the Middle Ages to the present day. Apart from using these rocks for building purposes, they are also used in road construction industry and as a part of sorbent for desulphurisation of combustion gases. It is vital to know the background radiation of these rocks. *In situ* gamma ray spectrometry was used to determine the activity concentrations of nuclides from U series, Th series and potassium  $^{40}\text{K}$  in selected rocks that were mostly of the Paleozoic age.

### Geology of the Krzeszowice Graben

Investigated area is the S-E edge of Silesian-Krakowian monocline, which forms a layered plate whose complex consists of Permian to Cretaceous rocks. This complex is inclined towards N-E. This unit was folded and faulted during geological history and in the Neogene the Krzeszowice graben was formed. The bottom of the graben is filled with the Miocene marine sediments, but the edges of this elongated depression are limited by almost parallel faults. In these edges, different types of rocks belonging to Silesian-Krakowian monocline crop out. The outcrops of sedimentary rocks were selected as measurement sites for *in situ* gamma ray spectrometry. Seven rock surfaces were measured in six locations; one of them is magmatic rock and the rest are sedimentary rocks (five Paleozoic rocks and one Mesozoic).

The first location was the outcrop of Permian Myslachowice conglomerate from Filipowice formed from solid rock particles originated from older rocks surroundings. The conglomerate consists of well rounded particles of Carboniferous limestones mainly, but also Devonian dolomites, limestones, porphyry and sandstone pebbles. The cement has iron compounds (Gradziński 1972).

The second measurement site was Czatkowice quarry of Carboniferous limestone. These rocks are part of coal deposit, and have dark beige colour. This limestone is characterized by variable consistence of CaO, MgO and SiO<sub>2</sub> (Pinińska 1989).

Next location was closed quarry of black bituminous limestone of Devonian age in Dębnik. Black color of this limestone is caused by occurrence of distorted pyrite (Bednarczyk and Hoffmann 1989). This rock, also called “marble”, has been exploited since XVth century.

The fourth measurement site was Dubie quarry of Devonian dolomite, also called dolomite from Zbrza. In this place, two rocks were measured – dolomite and trachyandesite dyke of Permian age, that cut the carbonates.

The dolomites are the oldest formation outcropping in studied area (Silesian-Krakowian monocline). Trachyandesite is the exception of sedimentary rock selection to this work, but it was chosen due to its position – vertical cut through the carbonates, that may influence the surrounding dolomite.

Next rock chosen for measurements was hardly weathered Carboniferous sandstone from Tenczynek, the location is popularly known as “rock below the pine”.

The last investigated rock was Jurassic platy limestone from Nielepice quarry. This is the most popular outcropping rock in the studied area. This rock is currently used for cement and lime production, but formerly it was used for monument construction in the Middle Ages.

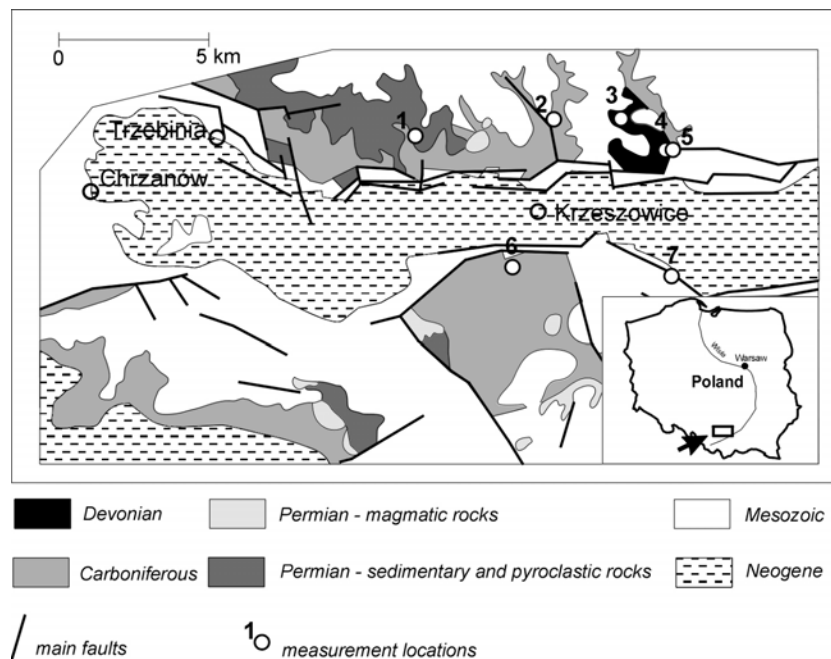


Fig. 1. Location of measurement points on the background of geological map of the Krzeszowice vicinity (according to Gradziński 1972); 1 – Filipowice, 2 – Czatkowice, 3 – Dębnik, 4 – Dubie (dolomite), 5 – Dubie (trachyandesite), 6 – Tenczynek, 7 – Nielepice.

## Methods

The EG&G ORTEC spectrometry system consists of a HPGe detector (30% efficiency, crystal length: 59 mm, diameter: 58.6 mm) with cryostat filled with liquid nitrogen mounted on a tripod, a multichannel buffer DART, and a laptop. The resolutions of the detector are 0.67 keV at 122 keV and 1.73 keV at 1.33 MeV. Software used for determination of the radionuclides and their activity concentration M-1B32 (EG&G ORTEC) use the one-meter geometry, *in situ* analysis methods developed by the U.S. DOE Environmental Measurements Laboratory (Beck *et al.* 1972). The software consists of two parts: the supervisor program which uses the programs M-1 Setup and Gamma Vision-32, and the operator program M-1 for Windows. In field conditions, the detector was placed 1 m above the rock surface. In this case, detector view for gamma emitters was approximately 10 m in radius to a depth of 30 cm, depending on the ground and energy source (Helfer and Miller 1988). The determination of the presence of radionuclides and calculation of their activities was based on the following gamma-ray transitions (in keV):  $^{40}\text{K}$  (1460.8),  $^{208}\text{Tl}$  (583.1 and 860.5),  $^{212}\text{Pb}$  (238.6 and 300.1),  $^{212}\text{Bi}$  (727.2 and 1620.6),  $^{214}\text{Pb}$  (241.9, 295.2 and 351.9),  $^{214}\text{Bi}$  (609.3, 1120.3, 1238.1 and 1764.5) and  $^{228}\text{Ac}$  (338.3, 911.1 and 968.9) (Debertin and Helmer 1988). The energy tolerance for library file (1Meter.lib) was stated as 1.75 keV. Counting live time was set on 3 h for each measurement point. Powdered mixture calibration sources of  $^{40}\text{K}$  (840 Bq),  $^{226}\text{Ra}$  (218 Bq) and  $^{232}\text{Th}$  (127 Bq) were used for calibration of the spectrometer. The vertical distribution of particular radionuclides is described within M-1 software by parameter  $\alpha/\rho$ , where  $\alpha$  is the reciprocal of the relaxation length (flux reduction by factor  $e$ ) for the gamma energy line being observed ( $\text{cm}^{-1}$ ) and  $\rho$  is the soil (rock) density ( $\text{g cm}^{-3}$ ) (EG&G ORTEC 2000). The general source distribution is represented with three cases:  $\alpha/\rho < 0.1$ , uniform source distribution (natural radionuclides),  $\alpha/\rho > 0.5$ , planar source distribution (fresh fallout) and  $0.1 < \alpha/\rho < 0.5$ , not uniform or planar. Values of  $\alpha/\rho$  ranging from 0.1 to 0.5 have been found to describe realistic fallout distributions most adequately, the more aged fallout will be represented by the smaller values. In our work we assumed  $\alpha/\rho = 0$  for distributions of  $^{40}\text{K}$ ,  $^{208}\text{Tl}$ ,  $^{212}\text{Pb}$ ,  $^{212}\text{Bi}$ ,  $^{214}\text{Pb}$ ,  $^{214}\text{Bi}$  and  $^{228}\text{Ac}$  (manufacturer's recommended value), EG&G ORTEC (2000) and ORTEC (2000).

## Results and Discussion

Measured values of  $^{40}\text{K}$ ,  $^{208}\text{Tl}$ ,  $^{212}\text{Pb}$ ,  $^{212}\text{Bi}$ ,  $^{214}\text{Pb}$ ,  $^{214}\text{Bi}$ ,  $^{228}\text{Ac}$  and calculated activity concentration of  $^{226}\text{Ra}$  for all measured rocks are given in Table 1. The uncertainty value (Table 1) consists of the random and systematic errors in all of the factors involved in calculating the final nuclide concentration result (ORTEC 2000). The error can be expressed as:

$$\sigma_t = \sqrt{\sum \sigma_{ri}^2 + \frac{1}{3} \sum \sigma_{si}^2}, \quad (1)$$

where  $\sigma_t$  is the uncertainty,  $\sigma_{ri}$  is the individual random error and  $\sigma_{si}$  is the individual systematic error. The random uncertainties are counting, random summing and ab-

sorption correction, whereas the systematic uncertainties are nuclide uncertainty from library, efficiency fitting uncertainty, calibration source uncertainty and geometry correction. The random summing uncertainty is estimated to be 10% of the Eq. 1 (ORTEC 2000).

Table 1

The results of *in situ*  $\gamma$ -ray measurements of  $^{40}\text{K}$ ,  $^{208}\text{Tl}$ ,  $^{212}\text{Pb}$ ,  $^{212}\text{Bi}$ ,  $^{214}\text{Pb}$ ,  $^{214}\text{Bi}$  and  $^{228}\text{Ac}$  at different locations at the Krzeszowice graben area. The uncertainty means one standard deviation ( $\sigma_i$ ), Eq. (1)

Nuclide	Activity concentration ( $\text{Bqkg}^{-1}$ ) Measurement point						
	Filipowice	Czatko- wice	Dębnik	Dubie	Dubie	Ten- czynek	Nielepice
Rock (age)	Conglomer- ate (C)	Limestone (C)	Limestone (D)	Dolomite (D)	Trachyan- desite (P)	Sandstone (C)	Limestone (J)
$^{40}\text{K}$	423.2±6.1	53±2	473±9	85±4	184±3	129.5±4	82±3
$^{208}\text{Tl}$	11.4±1.1	2.5±0.3	11.4±0.9	2.4±0.3	3.3±0.6	9.2±0.7	3.4±0.5
$^{212}\text{Pb}$	17.8±1	5±0.5	30.3±0.8	< DL	6.9±0.4	18± 0.9	7.8±0.3
$^{212}\text{Bi}$	14.9±1.7	< DL	< DL	< DL	< DL	15.2±2	4.6±0.7
$^{228}\text{Ac}$	34±3.6	6.6±1.4	30.9±5.6	7.2±1.3	9.7±1.7	28.8±3.4	9.5±2
$^{214}\text{Pb}$	19.7±2.4	35.1±1.7	42.2±4.8	20.3±2.6	23.6±4.8	18.3±1.9	13.7±1.8
$^{214}\text{Bi}$	28.5±4.1	36.4±2.2	44.3±6.7	18.1±3.3	20.4±5.7	23.5±2.9	11.9±2.7
$^{226}\text{Ra}^*$	24.1±3.3	35.7±2.4	43.2±6.8	19.2±3.7	22±6.4	20.9±2.4	12.8±2.8

\* Based on activity concentrations of  $^{214}\text{Bi}$  and  $^{214}\text{Pb}$

DL – detection limit

In this work the radioactive equilibrium in  $^{232}\text{Th} \rightarrow ^{228}\text{Ac}$  and  $^{238}\text{U} \rightarrow ^{226}\text{Ra} \rightarrow ^{222}\text{Rn} \rightarrow ^{214}\text{Pb} \rightarrow ^{214}\text{Bi}$  series was assumed. Exhalation of  $^{222}\text{Rn}$  from the rock can produce 10-20% reduction in the gamma emitting  $^{214}\text{Pb}$  and  $^{214}\text{Bi}$  on the surface. However in field conditions that exhalation is compensated in most part by the contribution of the flux from the same nuclides in the ambient air (Helfer and Miller 1988).

<sup>40</sup>K

The highest value of <sup>40</sup>K activity concentration was noted in Devonian limestone from Dębnik and in Carboniferous conglomerate from Filipowice amounting to  $473 \pm 9 \text{ Bqkg}^{-1}$  and  $423.2 \pm 6.1 \text{ Bqkg}^{-1}$  respectively. Limestone (C) from Czatkowice is characterized by the lowest <sup>40</sup>K activity concentration of  $53 \pm 2 \text{ Bqkg}^{-1}$ . In the case of intrusion influence on the dolomite in the Dubie quarry there is no evidence that trachyandesite enriched intruded dolomite in potassium. The activity concentration of <sup>40</sup>K in Permian trachyandesite ( $184 \pm 3 \text{ Bqkg}^{-1}$ ) is distinctly higher than <sup>40</sup>K concentration noted in Devonian dolomite ( $85 \pm 4 \text{ Bqkg}^{-1}$ ). In Fig. 3 the comparison of <sup>40</sup>K activity concentration in rocks of studied area with average concentrations in soil and continental crust is shown. The average activity concentration of <sup>40</sup>K in the continental crust amounting to  $850 \text{ Bqkg}^{-1}$  (Eisenbud and Gesell 1997), was not exceeded by any of measured rocks. In the case of soil average activity of <sup>40</sup>K amounting to  $400 \text{ Bqkg}^{-1}$  (Eisenbud and Gesell 1997), a higher value was noted for two rocks: Devonian limestone from Dębnik and Carboniferous conglomerate from Filipowice ( $473 \pm 9 \text{ Bqkg}^{-1}$  and  $423.2 \pm 6.1 \text{ Bqkg}^{-1}$ ). These values exceed the average concentration clearly above the standard deviation gap, but it can be said that these rocks have activity concentration of <sup>40</sup>K on the soil level.

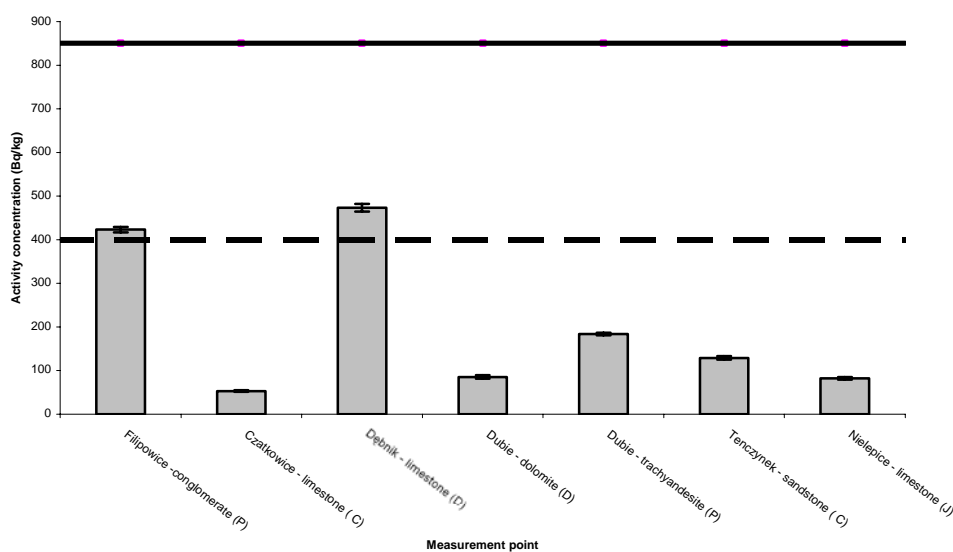


Fig. 2. Comparison of the <sup>40</sup>K activity concentrations (grey bars) with average activities reported for continental crust (solid line) and soil (dashed line) for each measurement point at the Krzeszowice graben area.

**Th series**

Measured activity concentration values of particular nuclides from Th series are presented in Table 1. There is very good radioactive equilibrium between <sup>228</sup>Ac and

$^{208}\text{Tl}$  in  $^{232}\text{Th}$  series at each measurement location. It is clearly visible after multiplying concentration value of  $^{208}\text{Tl}$  by 2.77 factor, that is deduced from the decay channel distribution in Th series. The highest activity concentration was noted in conglomerate (C) from Filipowice ( $34 \pm 3.6 \text{ Bqkg}^{-1}$ ), Devonian “marable” from Dębnik ( $30.9 \pm 5.6 \text{ Bqkg}^{-1}$ ) and sandstone (C) from Tenczynek ( $28.8 \pm 3.4 \text{ Bqkg}^{-1}$ ). The difference between these concentration values is smaller than uncertainty gap. The smallest activity concentrations with values ranging from  $6.6 \pm 1.4 \text{ Bqkg}^{-1}$  to  $9.7 \pm 1.7 \text{ Bqkg}^{-1}$  characterize rest of the carbonates and trachyandesite. In the case of the dyke from Dubie and its influence on the surrounding dolomite for Th series there is not significant difference in activity concentration of  $^{228}\text{Ac}$  and other nuclides from this series noted in dolomite ( $7.2 \pm 1.3 \text{ Bqkg}^{-1}$ ) and in trachyandesite ( $9.7 \pm 1.7 \text{ Bqkg}^{-1}$ ). This difference is within the standard deviation gaps. The lack of difference can be caused by opposite influence of the dolomites on trachyandesite or by the small thickness of the dyke – about 2-3 m. The clastic rocks from the studied area have higher Th series activity concentration than most of the carbonates (except of the limestone from Dębnik). There is no correlation between Th series concentration and the age of the rock observed. The comparison of activity concentration of Th series obtained for sedimentary rocks and trachyandesite with the average activity concentration of Th in continental crust ( $44 \text{ Bqkg}^{-1}$ ) is shown in Fig. 3. This average activity concentration is clearly higher than any noted concentration in sedimentary rocks from Krzeszowice area.

### U series

As it was mentioned above, the activity concentration of U series was based on  $^{226}\text{Ra}$  activity concentration that was deduced from  $^{214}\text{Bi}$  and  $^{214}\text{Pb}$  concentrations. The highest  $^{226}\text{Ra}$  activity concentration was noted in two dark bituminous limestone’s Devonian “marble” from Dębnik ( $43.2 \pm 6.8 \text{ Bqkg}^{-1}$ ) and in limestone (C) from Czatkowice quarry ( $35.7 \pm 2.4 \text{ Bqkg}^{-1}$ ). The lowest U series activity concentration characterises Jurassic limestone from Nielepice:  $12.8 \pm 2.8 \text{ Bqkg}^{-1}$ . The highest concentrations are probably caused by the reductive deposition environment. In such case, uranium comes to the sediment from surroundings (Polański 1979). It is distorted pyrite that produced dark colour and characteristic „bitouminous” smell of the limestone from Dębnik (Bednarczyk and Hoffmann 1989). This appearance of pyrite may be an indication of reductive deposition environment.

Comparison of U series activity concentration measured in the Krzeszowice area with average activity concentration of this series in the continental crust (Fig. 3) shows that the highest noted value exceeds the average ( $36 \text{ Bqkg}^{-1}$ ) and the U series activity concentration value in Carboniferous limestone from Czatkowice is close to crustal average activity concentration value. The other U series activity concentrations presented in this work are clearly lower than continental crust average activity concentration.

At the same figure, a comparison of U series activity concentration measured in sedimentary rocks from borders of Krzeszowice graben with average activity concentration in the carbonates ( $25 \text{ Bqkg}^{-1}$ ) is presented. This comparison shows that two

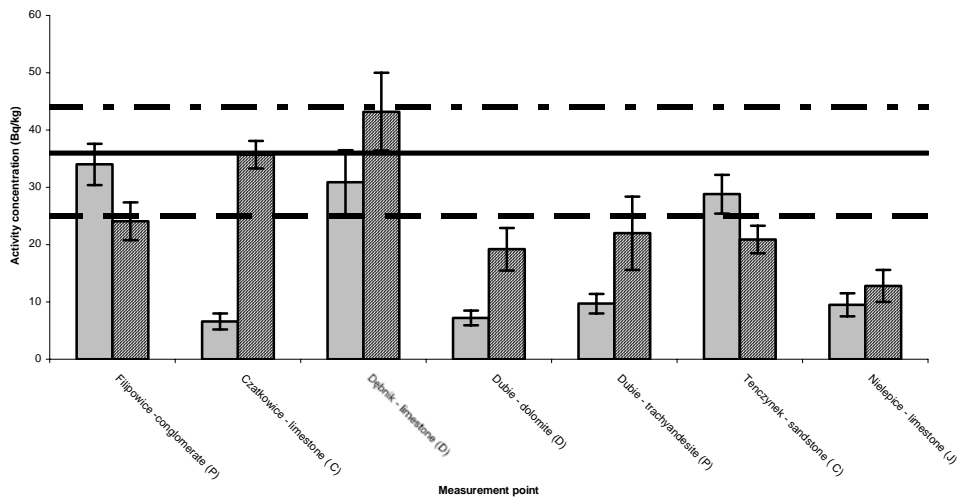


Fig. 3. Comparison of the  $^{232}\text{Th}$  and  $^{238}\text{U}$  activity concentrations (grey and striped bars, respectively) obtained *in situ* in common rocks at the Krzeszowice graben borders with average activities reported for these nuclides in continental crust and average activity concentration of U series in carbonates. Solid line – the average crustal concentration of  $^{238}\text{U}$ , dashed line – the average crustal concentration of  $^{238}\text{U}$  in carbonates, dashed-dotted line – the average crustal concentration of  $^{232}\text{Th}$ .

highest values noted in limestones from Dębnik and Czatkowice clearly exceed the average activity concentration in the carbonates, when other measured activity concentrations of U series in carbonates from studied area are clearly below this average. There is an interesting dependence between the age of limestone from studied area and its activity concentration – the oldest limestone has the highest activity concentration. It is hard to tell whether this connection is global because of small number of measured limestones (only three), but it is more likely that this age–concentration dependence is characteristic for the studied area.

In the case of the influence of dyke from Dubie on the surrounding dolomite for U series, there is no significant difference in activity concentration of  $^{226}\text{Ra}$  and other nuclides from this series noted for dolomite ( $19.2 \pm 3.7 \text{ Bqkg}^{-1}$ ) and trachyandesite ( $22 \pm 6.4 \text{ Bqkg}^{-1}$ ). This difference is again within the standard deviation gaps. It is strange that U series concentration is higher than Th series concentration in trachyandesite from the Dubie quarry; such a situation is common for carbonates but not for magmatic rocks (Eisenbud and Gesell 1997). This fact suggests that dolomites surrounding the trachyandesite dyke have greater influence on it or the size of the dyke is not sufficient to measure the activity concentration of radionuclides *in situ* with the one meter geometry method.

## Conclusions

In most of the studied rocks, the U series activity concentration is higher than the Th series activity concentration. Only clastic sedimentary rocks, such as sandstone

and conglomerate, had higher Th series activity concentration than the U series concentration. The average activity concentrations of U and Th series in the continental crust are  $36 \text{ Bqkg}^{-1}$  and  $44 \text{ Bqkg}^{-1}$ , respectively, so our results contradict the expected prevalence of the Th series concentration. This can be explained by the origin of the rocks. Clastic rocks are composed mostly of grains of other weathered rocks, which were transported to the deposition site. Since the Th minerals are hard to dissolve, the grains composed of thorium minerals are deposited and compose the clastic sedimentary rocks. In the case of carbonates, it is unlikely for thorium minerals to come into deposition in such an amount as in clastic rocks. Carbonates from the Krzeszowice graben borders show an interesting dependence between the age of rock and the activity concentration of nuclides from U series – the older the rock, the higher the U series activity concentration. This dependence characterizes probably only these local carbonates; because of a small number of measurements and lack of similar cases in literature it is impossible to treat this dependence as a global rule. It is to be said that sedimentary rock gamma ray background radiation level in the Krzeszowice area does not exceed the average continental crust gamma radiation level. Therefore, there is no reason to stop using these rocks as building or other industrial material sources even in the case of the rock that is “richest” in U series activity; i.e., the Dębnik limestone. This rock has a higher activity concentration ( $43.2 \pm 6.8 \text{ Bqkg}^{-1}$ ) than the continental crust average activity concentration ( $36 \text{ Bqkg}^{-1}$ ), but the difference between these values is not higher than the uncertainty gap, so in the case of sedimentary rocks from the Krzeszowice area the highest activity concentration level is comparable to average continental crust background radiation level.

#### References

- Bednarczyk, J., and M. Hoffmann, 1989, *Wapienie dębnickie*. W: Przewodnik LX Zjazdu PTG, Kraków. Wyd. AGH: 40-50.
- Beck, H.L., J. De Campo and C.V. Gogolak, 1972, *In situ Ge(Li) and Na(Tl) gamma-ray spectrometry*. U.S. Department of Energy, Environmental Measurements Laboratory, HASL-258, New York.
- Debertin, K., and R.G. Helmer, 1988, *Gamma- and X-ray spectrometry with semiconductor detectors*, Elsevier Science Publishing Company, Inc. Amsterdam.
- EG&G ORTEC, 2000, *In situ spectroscopy M-1-B32 M-1 Setup supervisor program. Software user's manual*, EG&G ORTEC Part No. 779980, Oak Ridge.
- Eisenbud, M., and T. Gessel, 1997, *Environmental radioactivity from natural, industrial and military sources*, Academic Press, San Diego.
- Gradziński, R., 1972, *Przewodnik geologiczny po okolicach Krakowa*, Wyd. Geol., Warszawa.
- Helfer, I.K., and K.M. Miller, 1988, *Calibration factors for Ge detectors used for field spectrometry*, Health Phys. **55**, 15-29.

ORTEC, 2000, *Gamma Vision – 32 for M-1. Gamma-Ray Spectrum Analysis and MCA Emulator for Microsoft Windows 95, 98, and NT*. Software User's Manual. ORTEC Part No. 774780, Oak Ridge.

Polański, A., 1979, *Izotopy w geologii*, Wyd. Geol., Warszawa.

Pinińska, J. (ed.), 1989, *Własności wytrzymałościowe i odkształceniowe skał*. Cz. III – Jura Krakowsko-Częstochowska, t. 5, Warszawa: 79.

*Accepted 10 April 2006*



## **Geophysical Survey of the Archaeological Grave Mounds Site in Cieszacin Wielki**

Artur POREBA

University of Silesia, Faculty of Earth Sciences  
Będzińska 60, 41-200 Sosnowiec, Poland  
e-mail: aporeba@wnoz.us.edu.pl

### **A b s t r a c t**

This paper presents the results of a non-invasive geophysical investigation of an archeological position in Cieszacin Wielki. The study was carried out on a group of ancient ground mounds. The main aim of the present investigation was to recognize the internal structure of one of the selected mounds and delineate the anomalies of the zones which might be related to archaeological objects in the cover of the mound. Three geophysical methods were used: magnetic, electromagnetic and resistivity imaging. The results are presented on the maps of magnetic anomalies  $\Delta T$ , maps of apparent ground conductivity and shallow resistivity inversion up to 2 m in depth.

The results were combined with the geological cross-section and geochemical data obtained from the environs of the mound.

The investigated archaeological site is situated several kilometres south of Jarosław in Kańczuga Plateau loess area. There are four grave mounds. It is assumed that the ground mounds were built during the Neolithic age. Topographic plans for grave mounds were made. These mounds are 1-2 m in height and ca. 20-30 m in cover diameter. One of them was examined in detail. On the basis of a few ground boreholes (made and analysed at the Maria Curie-Skłodowska University, Lublin), a cross-section through the grave mound was determined (Fig. 1).

A clearly laminar structure of the mound was confirmed. On the basis of almost all bore-holes, it has been confirmed that the cover of grave mound can be divided into three units. The light layer of the mound, ca. 30-50 cm in thickness, consists of the material including ca. 9% of the clay fraction and 1.1-1.4% of iron compounds.

The dark/middle layer is characterised by a high content of both clay fraction (about 28%) and iron compounds (to 3.7%) (Łanczont *et al.* 2003, 2004). The possible

archaeological objects can be noticed in the third layer of the cover. A geochemical analysis was carried out for profiles VII and IX (Fig. 2 in Łanczont *et al.* 2003). The content of  $\text{Fe}_2\text{O}_3$ , which can influence the conductivity and magnetic susceptibility, increases outside of the grave mound. This may also be a kind of determinant of clay minerals content.

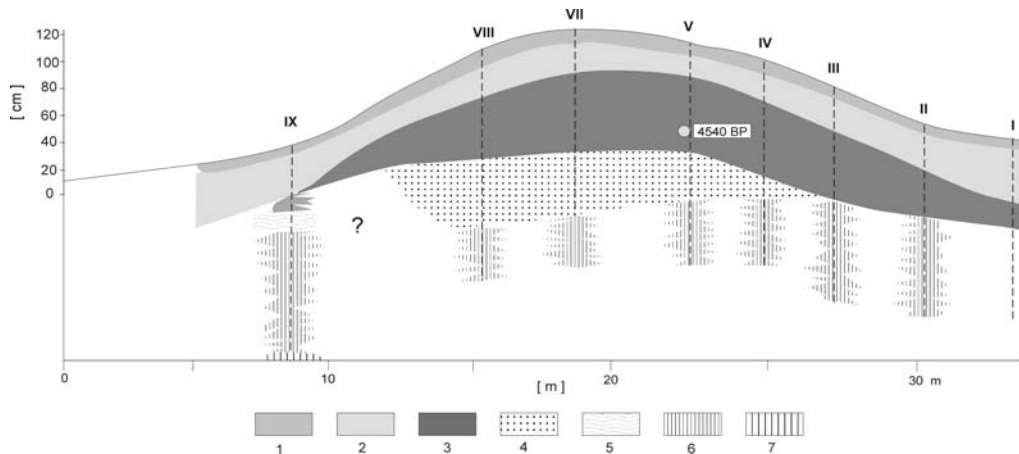


Fig. 1. Schematic geological cross-section of the grave mound in Cieszacin Wielki (Łanczont *et al.* 2003), 1 – humus horizon of soil; 2 – light/upper part of mound cover; 3 – dark/middle part of mound cover; 4 – variegated lower part of mound cover; 5 – eluvial horizon of fossil soil; 6 – illuvial horizon of fossil soil; 7 – parent rock horizon, loess.

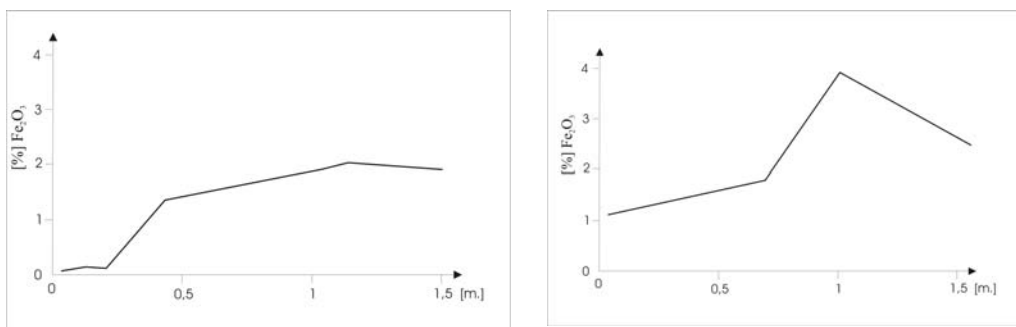


Fig. 2. Content of  $\text{Fe}_2\text{O}_3$  in borehole no. VII (on the left) and no. IX (on the right) in cover of the grave mound.

In the years 2002-2005, non-invasive geophysical investigations were carried out in order to determine the internal structure of the mound, as well as to indicate the zones of anomalies of the measured physical parameters of soil and improve the methodology of investigation of such structures. Three geophysical methods were used: magnetic, electromagnetic and resistivity imaging. The geophysical methods applied are non-invasive.

### **Magnetic prospection**

This is a magnetic method based on the measurement of small variations in the magnetic field. This field is affected by any variation in the distribution of magnetized or polarized objects at different depths. Magnetic investigation involves measurements of the Earth's total magnetic field  $\Delta T$ , or sometimes component  $\Delta Z$  of the total magnetic field (Eppelbaum 2000). Soils compacted by human occupation or disturbed by a burial can also show a variation from background values of magnetic susceptibility. Burials frequently cause localized oxidation creating a void in magnetite content (Wynn 1986).

Two Polish proton magnetometers PMP-5 were used. The magnetometers were applied in two positions of measuring probes – 0 and 1.8 m over the studied area. A regular grid (1×1 m) of measurement points was applied at the investigation site.

The maps of magnetic field  $\Delta T$  for the lower and upper position of the measuring probes were drawn. On these maps, clear anomalies in the central part of the grave mound (co-ordinates: x28, y23) are marked. For the lower position of the measuring probes the value  $\Delta T$  increases up to 20 nT, and for the upper position it increases up to 10 nT. The range of anomaly for these two positions suggests a disorder. A quantitative interpretation of the anomaly was carried out using Łogaczew's method of characteristic points (Fajkiewicz 1972), which showed a depth of ca. 60 cm. This value is not very precise because the curve was approximated using too few points (the distance between the measuring points equals 1 m).

### **Electromagnetic investigation**

A Geonics EM 31-MK2 conductivity meter was used in surveys at the grave-mounds. EM surveys measure contrasts in the electrical conductivity of subsurface deposits. The effective penetration depth is approximately 6 meters (the normal operating mode and vertical dipoles were used) (Dalan 1991). Automatic recording with 0.5 s spacing was used. A map of apparent conductivity was drawn (Fig. 4). The cover of the gravemound is marked on the map (Poręba *et al.* 2003). This may relate to loosening of the soil and rinsing of clay minerals from the region of the mound. One clear anomaly can also be observed at the top of the mound at co-ordinates x23, y22. The value of this anomaly is positive and higher than the background of ca. 1 mS/mm of the grave mound, as marked on the map (Poręba *et al.* 2003). The value of apparent electrical conductivity of soil is ca. 2-4 mS/m and they are lower than the apparent conductivity measured outside of the cover.

### **Resistivity investigation**

The resistivity imaging allows us to follow the changes of physical parameters of medium (electric resistance) in the shallow layer. Multielectrodes equipment – Lund Imaging System – was used for the study. For the chosen combination of electrodes, the measurement of apparent resistance for the type and current geometry of spacing was conducted. The results of this investigation can be visualized, processed and interpreted (Rudzki 2002, Loke 1996). The apparent resistivities measured have to

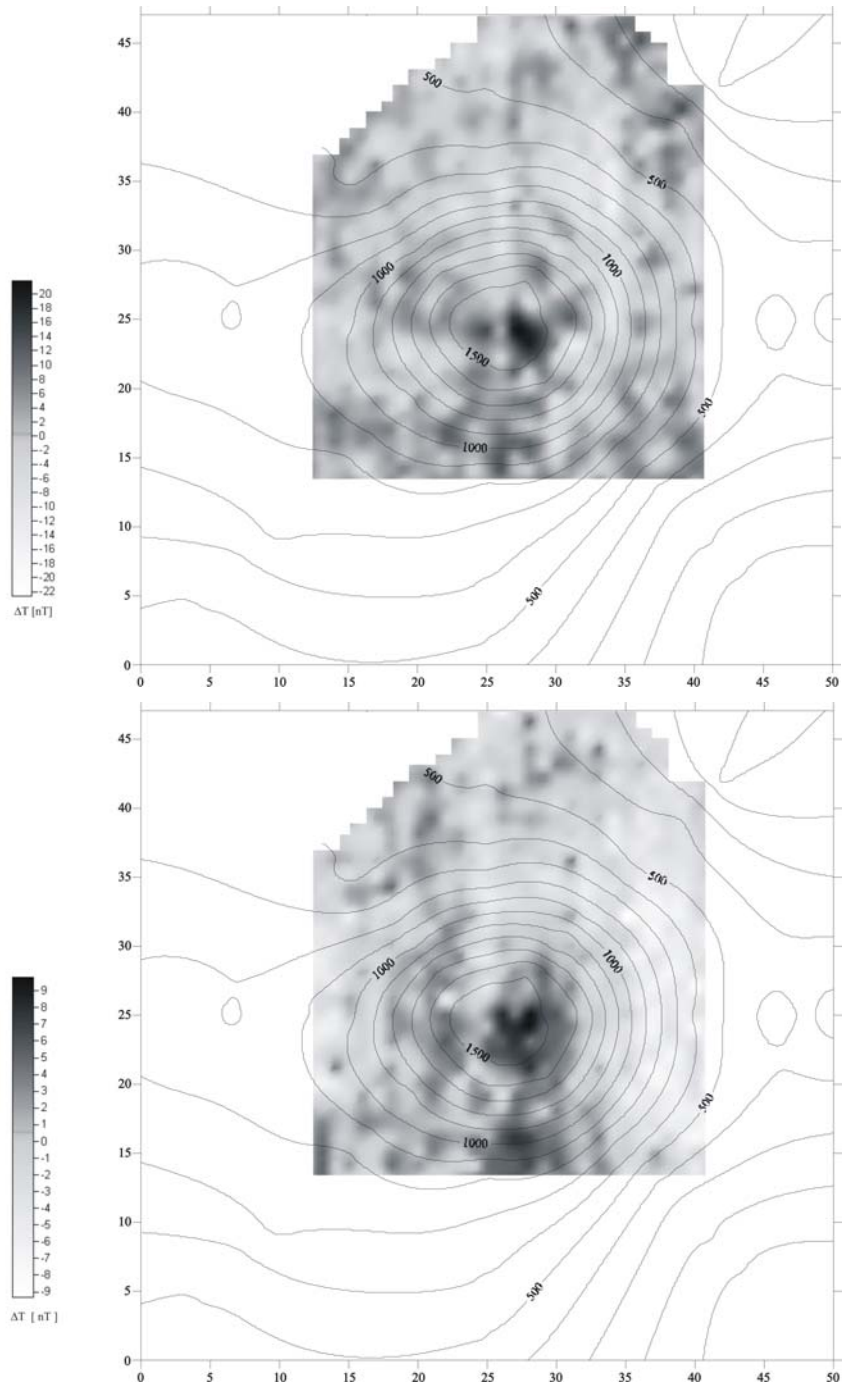


Fig. 3. Maps of magnetic anomalies  $\Delta T$  on topographic plan (isolines are in cm of altitude). The map on the top presents the measurements in the lower position of the measuring probe; the map on the bottom – in the upper position of the measuring probe.

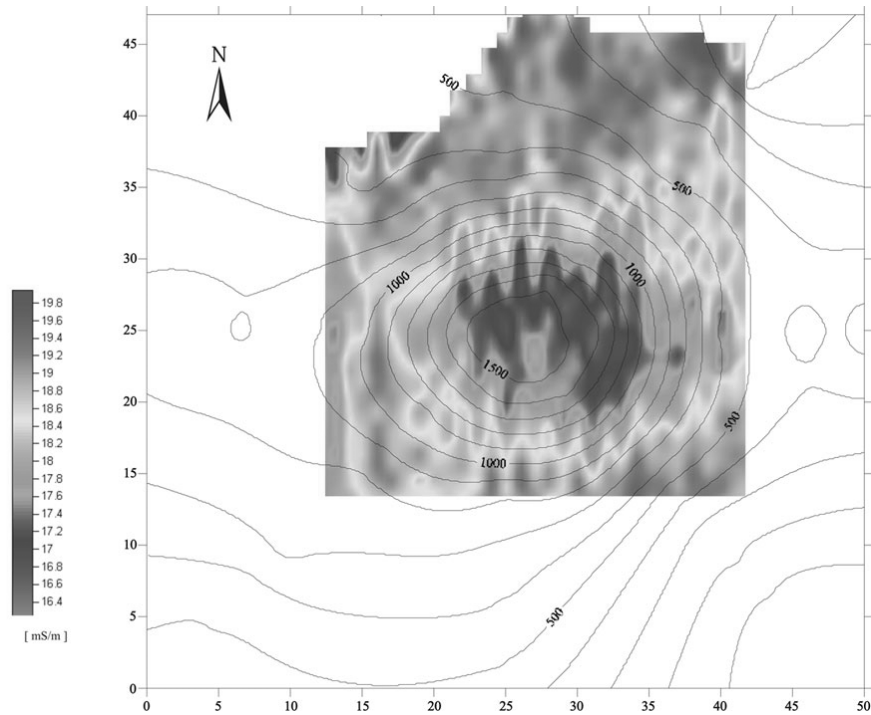


Fig. 4. Changes of soil apparent conductivity.

be inverted to determine a model of the resistivity structure beneath the profile. Where a profile is not made along a flat surface, the topographic relations between the electrodes have to be taken into account (Collier *et al.* 2003). This effect of topography was considered in the investigation of the grave mound. The electrode separation was 0.3 m. Such a small spacing between the electrodes enable us to recognize the soil very precisely. This is a high density resistivity method (HDRM), (Kai 2004).

The electrodes were inserted to a depth of 15 cm. The Wenner-Schlumberger measurement protocol was used. The depth of recognition was obtained at ca. 2.5 m.

One of the intersections is shown in Fig. 5. This is the profile with N-S orientation running across the top of the mound. In this intersection one can distinguish a layer of high resistance, from 100 to 1500  $\Omega\text{m}$ . Probably it is the resistivity of a light layer with humus. Fig. 5 presents a resistivity section shown in two scales to show the variability in a low resistivity layer. The realization of several parallel measuring profiles is planned in order to obtain the full recognition of the resistivity of the mound. The realization of these profiles can be drawn as a 3-D model of the ground.

## Conclusions

The presented results show possibilities of using geophysical methods to recognize the neolithic grave mounds positions in loesses. The magnetic anomaly  $\Delta T$  and the anomaly of apparent conductivity in the culminating part of the mound are situated

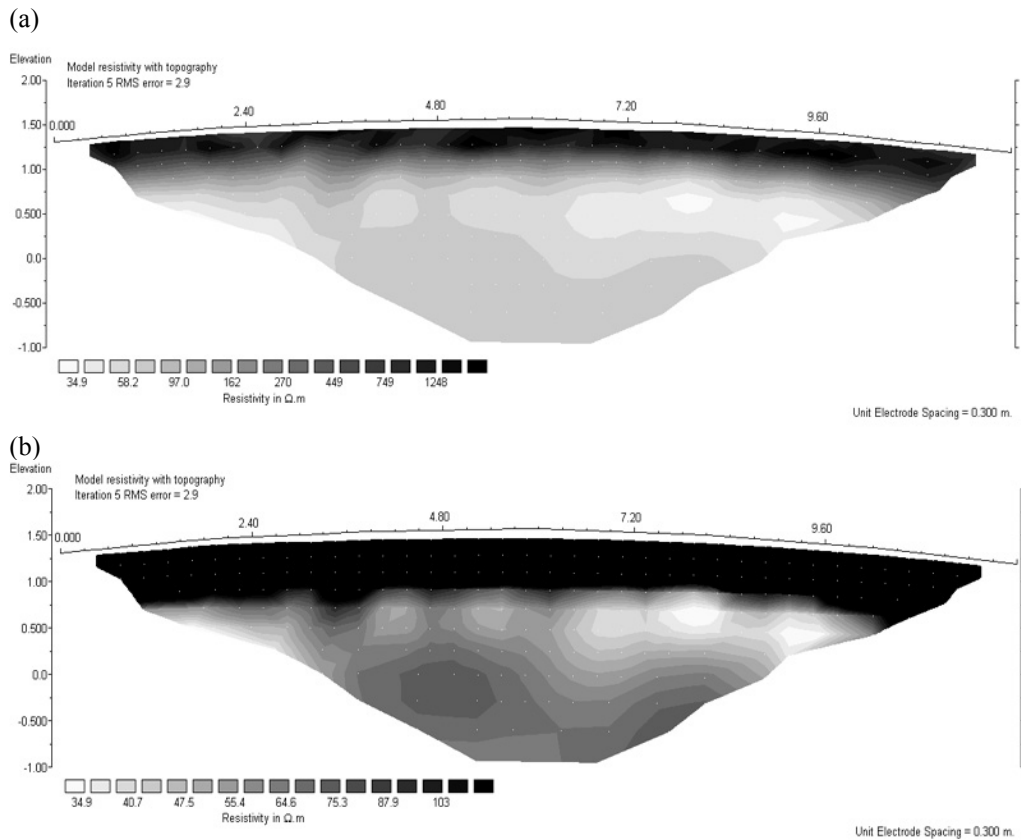


Fig. 5. Grave mound at Cieszaczin Wielki – a modelled resistivity cross-section, topographically corrected, (a) – scale to about 1500  $\Omega\text{m}$ , (b) – transform scale to about 120  $\Omega\text{m}$ .

in the same area. These anomalies may indicate an existing tomb chamber of the grave mound or another shallow archaeological object.

On the maps of apparent conductivity we can also outline the cover of the grave mound. The HDRM method (high density resistivity method) is of great importance when applied to the grave mound. Creating several resistivity sections parallel to each other allows us to construct a quasi 3-D model of such an object. The main future aims of the archaeologists from Maria Curie-Skłodowska University are to excavate works upon that site, which will unequivocally help us to verify the methods used so far.

The development of proper geophysical methods concerning such objects will allow us to quickly and cheaply recognise ground mounds situated on loess deposits in the future.

**A c k n o w l e d g m e n t.** This work has been sponsored by the Polish Committee of Scientific Research – KBN 4T 12B 045 28.

## References

- Aitken, M.J., 1961, *Physics and Archaeology*, Interscience Publishers Inc., New York.
- Collier, L., B. Hobbs, T. Neighbour and R. Strachan, 2003, *Resistivity imaging survey of Capo Long Barrow*, Aberdeenshire, Scotisch Archaeological Internet Reports no 6.
- Dalan, A.R., 1991, *Defining archaeological features with electromagnetic surveys at the Cahokia Mounds State Historic Site*, *Geophysics* **56**, 1280-1287.
- Eppelbaum, L.V., 2000, *Applicability of geophysical methods for localization of archaeological targets: an introduction*, *Geoinformatics* **11**, 1, 25-34.
- Kai, Z., X. Ming-jie, S. Huo-sheng, H. Jian-qiu and L. Liu-gen, 2004, *High density resistivity method in archaeological prospecting: case in Tenghualuo neolithic relict, eastern Jiangsu, China*, International Conference on Remote Sensing Archaeology, Beijing, October 18-21, 2004, 158-161.
- Loke, M.H., 1996, *2-D and 3-D electrical imaging surveys*. In: web site [www.geoelectrical.com](http://www.geoelectrical.com)
- Łanczont, M., K. Klimek, M. Komar, J. Nogaj-Chachaj, A. Poręba and B. Żogała, 2003, *Nieinwazyjne badanie kurhanów (na przykładzie kurhanu nr 2 na stanowisku 37 w Cieszacinie Wielkim)*, *Rocznik Przemyski* **39**, Archeologia, 5-19.
- Łanczont, M., J. Nogaj-Chachaj, K. Klimek, M. Komar, A. Poręba, W. Zuberek and B. Żogała, 2004, *Wybrane problemy badań starożytnych kurhanów z okolic Jarosławia (Wysoczyzna Kańczucka)*, *Rocznik Przemyski* **39**, Archeologia, 7-16.
- Poręba, A., B. Żogała, K. Klimek, M. Łanczont and J. Nogaj-Chachaj, 2003, *The application of electromagnetic profilings in archaeology – case study of Cieszacin Wielki mounds, Poland*, *Archaeologia Polona* **41**, 250-252.
- Rudzki, M., 2002, *Zastosowanie metody tomografii elektrooporowej do wykrywania podziemnych obiektów antropogenicznych*, *Publs. Inst. Geophys. Pol. Acad. Sc.* **M-27 (352)**, 195-208.
- Wynn, J.C., 1986, *A review of geophysical methods used in archaeology*, *Geoarchaeology* **1**, 245-257.

Accepted 13 June 2006

## Contents

Preface .....	3
<b>Seismic Effects and Rotation Waves – The Keynote Lecture</b>	
<i>Roman Teisseyre</i> .....	5
<b>Seismic Doublets and Multiplets in the Polish Copper Mines</b>	
<i>Stawomir J. Gibowicz, Bogusław M. Domański and Paweł Wiejacz</i> .....	15
<b>Energy Distribution of Induced Seismic Events Occurring in Wesola Coalmine, Poland</b>	
<i>Lukasz Rudziński and Adam F. Idziak</i> .....	27
<b>Concordance of Tremor Occurrence with Poisson Distribution in the Jas-Mos Coal Mine</b>	
<i>Krzysztof Bank and Wacław M. Zuberek</i> .....	37
<b>Focal Mechanisms of Mining Induced Seismic Events: Reliability of the Solutions</b>	
<i>Ryszard Dubiel and Agnieszka Górka</i> .....	49
<b>Short-Term Prediction of Approximate Probability of Rockburst</b>	
<i>Jerzy Kornowski</i> .....	55
<b>Resampling Methods for Improving the Accuracy of Probabilistic Seismic Hazard Analysis</b>	
<i>Beata Orlecka-Sikora</i> .....	63
<b>Mining Tremors Registered at Ojców and Książ Observatories: Rotational Field Components</b>	
<i>Krzysztof P. Teisseyre</i> .....	77
<b>Tomography Imaging Through the Monte Carlo Sampling</b>	
<i>Wojciech Dębski</i> .....	93
<b>Tidal and Non-Tidal Frequencies Found in the Seismicity of California</b>	
<i>Pavel Kalenda, Jiří Málek and Lumír Skalský</i> .....	107
<b>Analysis of Displacement Geometry: A Tool for Identifying Kinematic Type of Fault</b>	
<i>Lestaw Teper and Anna Lisek</i> .....	119
<b>SPS – Seismic Signal Processing System</b>	
<i>Janusz Mirek</i> .....	131
<b>Cultural Monument Jeroným Mine, Czech Republic – Contribution to the Geomechanical Stability Assessment</b>	
<i>Zdeněk Kaláb, Jaromír Knejzlík, Robert Kořánek and Petr Žůrek</i> .....	137
<b>Historical Buildings in the Ostrava and Karviná Region and Their Seismic Loads</b>	
<i>Markéta Lednická</i> .....	147
<b>Attenuation Relations of Ground Motion Acceleration Response Spectra for the Polkowice Region</b>	
<i>Dorota Olszewska</i> .....	161

Determination of Authentic Formulae for Seismic Acceleration Decay in the Bohemian Massif <i>Vladimír Rudajev and Jiří Buben</i> .....	175
Field Measurements of Surface Seismic Vibrations Provoked by Mining in the Karvina Region <i>Zdeněk Kaláb and Jaromír Knejzlík</i> .....	185
Characterization of Rock Temperature Changeability in the Halemba Coal Mine Deposit (the Upper Silesian Coal Basin) <i>Sławomir Kędzior and Wojciech Drobczyk</i> .....	195
Relationship Between Seismic Activity and Mine Gas Emissions <i>Stanisław Lasek and Bogusław Syrek</i> .....	203
Anisotropy of Seismic Wave Velocity in a Chosen Rock Mass <i>Iwona Stan and Adam Idziak</i> .....	211
Calculation of Block Divisibility Using Structural and Refraction Seismic Methods in Dębnik and Imielin Raw Material Deposits <i>Zbigniew Mirkowski, Radostawa Tomaszewska and Adam Idziak</i> .....	223
Application of the Shallow Refraction Seismic Method for Analysis of Block Divisibility of Carpathian Sandstones in the Górka-Mucharz Deposit <i>Jarosław Badera, Sławomir Niemczuk and Radostawa Tomaszewska</i> .....	231
Application of Resistivity Imaging to the Recognition of Landslides in the Flysch Carp athians .....	239
<i>Krzysztof Jochymczyk, Jolanta Pierwoła and Grzegorz Staporek</i> .....	239
Seasonal Electric Resistivity Variations of Rock Formation at an Abandoned Mining Shaft Site <i>Andrzej Kotyrba, Łukasz Kortas and Sławomir Siwek</i> .....	247
Utilization of Geoelectrical Methods in Order to Identify Places of Pollution and Contamination on the Example of Former Military Camp <i>Monika Rusin-Żogała, Adam Frej, Krystian Wzientek and Anna Machalica</i> .....	265
Estimation of Dimension of a Regular-Type Sinkhole Activated by Abandoned Shafts <i>Zenon Pilecki and Adam Baranowski</i> .....	271
Natural Radioactivity of Selected Rocks from the Vicinity of the Rožná Uranium Deposit <i>Aleksandra Sitarek, Jarosław Badera and Grzegorz Lizurek</i> .....	281
Natural Radioactivity of Selected Sedimentary Rocks from the Krzeszowice Area <i>Grzegorz Lizurek and Aleksandra Sitarek</i> .....	291
Geophysical Survey of the Archaeological Grave Mounds Site in Cieszacin Wielki <i>Artur Poręba</i> .....	301

PUBLICATIONS OF THE INSTITUTE OF GEOPHYSICS  
POLISH ACADEMY OF SCIENCES

M. MISCELLANEA

Series M contains volumes devoted to various geophysical problems, history of geophysics, conference proceedings and bibliographies. The following volumes have been published since 1990.

- M-17 (266)** Bibliography 1989-1993.
- M-18 (273)** The Hundredth Anniversary of the First Chair of Geophysics (Stulecie pierwszej katedry geofizyki). In Memory of Maurycy Pius Rudzki.
- M-19 (281)** Badania sejsmiczności w kopalniach (Seismicity in Mines). Materiały XXIII Polsko-Czesko-Słowackiej Konferencji, Ustroń-Zawodzie, 21-22 października 1994 r.
- M-20 (294)** Podstawowe problemy głębokich badań geofizycznych i geologicznych obszaru Polski (Basic Problems of Deep Geophysical and Geological Investigations of Poland).
- M-21 (309)** Proceedings of the International Conference "Nuclear Geophysics '97" Kraków, 20-23 October 1997.
- M-22 (310)** Mining Geophysics. Proceedings of the XXVI Polish-Czech-Slovakian Symposium, Wisła, Poland, September 23-25, 1998 (Geofizyka Górnicza. Referaty przedstawione na XXVI Polsko-Czesko-Słowackim Sympozjum w Wiśle, 23-25 września 1998).
- M-23 (314)** Bibliography of Polish Research in Spitsbergen Archipelago. Part I - 1930-1996.
- M-24 (340)** Monographic volume - Mining Geophysics.
- M-25 (347)** Wybrane problemy geofizyki współczesnej (Some current problems in geophysics), Stanisław Kramsztyk (1841-1906) in memoriam.
- M-26 (348)** Bibliography and activity report of the Institute of Geophysics (in print).
- M-27 (352)** Badania geofizyczne środowiska geologicznego (Geophysical research of geological environment).
- M 28 (363)** Geology, Geophysics, Geothermics and Deep Structure of the West Carpathians and Their Basement, J. Golonka and M. Lewandowski (eds.)

ISBN-83-88765-67-1